Simulation of Advanced Materials with Atomic Resolution: Atomistic Modelling of Smectic Liquid Crystal Mesophases

Kristian Poll

PhD

2022

Simulation of Advanced Materials with Atomic Resolution: Atomistic Modelling of Smectic Liquid Crystal Mesophases

Kristian Poll

A thesis submitted in partial fulfilment of the requirements of the University of Northumbria at Newcastle for the degree of Doctor of Philosophy

Research undertaken in the Faculty of Health and Life Sciences

August 2022

Abstract

Fully atomistic molecular dynamics simulations have been used to investigate the mesophase behaviour of three liquid crystal compounds, an (S)-hexyl-lactate derivative, 9HL, 2−{4′−[1″,1″−dihydro−2″−(2″−perfluorobutoxyperfluoroethoxy)−perfluoroethoxy]}phenyl−5′−octylpyrimidine, 3M 8422, and 4-[3’-nitro-4’-(R)-1(methylhexyloxy)phenyl]phenyl 4-(6-heptylmethoxyltrisiloxyhexyloxy)benzoate, TSiKN65. All of these materials, despite their very different structural features, are reported to exhibit de Vries character.

Force constant parameterisation was performed on molecular fragments representing the perfluoropolyether and trisiloxane terminal chains of mesogens 3M 8422 and TSiKN65, respectively, before the subsequent simulations were used to examine the de Vries behaviour exhibited by these two materials.

For all compounds, simulations were carried out across a broad temperature range, encompassing both the SmA and SmC phases. Simulated trends in orientational order parameters, translational order parameters, layer spacings, and tilt angles were compared to results from experimental investigations and were found to be largely consistent. Further analysis of the simulations revealed the simulated results were inconsistent with many of the conventional models proposed to account for de Vries behaviour, but examination of individual sub-units comprising the liquid crystal compounds showed that distinct aromatic and lactate/fluorinated/siloxane sub-layers were formed by all three compounds, and these sub-layers exhibited very different orientational behaviour across the simulated smectic A and smectic C temperature ranges. The aromatic sub-layers exhibited fairly conventional tilt behaviour, aligning along the layer normal in the smectic A phase, but becoming tilted relative to the layer normal when cooled to the smectic C phase. However, in contrast, the orientation of the lactate/fluorinated/siloxane sub-layers were found to remain largely unchanged and retained a smectic A-like configuration even in the smectic C phase, providing a potential explanation for de Vries behaviour, in which only a fraction of the layer structure exhibits an overall tilt in the smectic C phase. In addition, analysis of the phases formed in simulations of the partially perfluorinated compound 3M 8422 showed that the contraction of the aromatic and aliphatic sub-layers caused by the onset of molecular tilt was partially compensated by a simultaneous expansion of the perfluoropolyether sublayers. These observations highlighted that the exact factors that promote de Vries behaviour still remain somewhat unresolved, but a deep insight into molecular behaviour can be gained from atomistic simulations.

Contents

List of Figures

List of Tables

Acknowledgements

Firstly, I would like to thank my supervisor Dr Mark Sims for giving me the chance to work on this project, as well as for his help and support over the duration of this research. His guidance has provided especially valuable throughout the more challenging parts of the project.

I would also like to thank all of the technical staff at Northumbria University, particularly Jimmy Gibson whose expertise in using and maintaining the HPC clusters has been invaluable to the research performed during this project.

Throughout this project, I am extremely glad to have worked with my friends and colleagues in EBA510, who have provided me with considerable inspiration, and with whom I have shared some incredible experiences. Special thanks go to Dr Andrey Zaytsev, Dr Thang Truong, Dr Sotiris Kyriakou, Dr Charlotte Marsh, Joe Watson, Lynn Anderson, Craig Hodgson, Elliot Sharp, Joe O'Sullivan, Lucy Porter, Brad Thomas, James Railton, Hoang Nguyen, Pedro Rivero Ramos, Hannah Baker, and Neave White.

Finally, I would like to my family for their support through the last three years.

Author's Declaration

The research described in this thesis was carried out in the Department of Health and Life Sciences at the University of Northumbria at Newcastle between October 2018 and July 2022. I confirm that, to the best of my knowledge, the work presented in this thesis is my own. In cases where information has been obtained from other sources, this has been indicated in the text. Additionally, this work has not been previously submitted for an award, at this, or any other university.

A section of the research presented within this thesis has been published previously in:

K. Poll and M. T. Sims, *J. Mater. Chem. C.*, 2020, 8, 13040-13052.

K. Poll and M. T. Sims, *Mater. Adv.*, 2022, 3, 1212-1223.

I declare that the Word Count for this Thesis is 45,682 words.

Name: Kristian Poll

Date: 19/08/2022

Chapter 1 – Introduction

The work reported in this thesis concerns the study of liquid-crystalline phase behaviour in three chemically distinct materials reported to exhibit minimal layer contraction at the SmA-SmC transition, commonly referred to as de Vries behaviour, through the application of various computational modelling techniques. The materials studied in this work possess different structural features thought to promote de Vries behaviour, enabling the individual contributions to reduced layer contraction to be explored in a diversity of systems. The design of new devices utilising materials that exhibit de Vries behaviour could undoubtedly benefit from greater insight into the general mechanisms that lead to de Vries character. Consequently, this work aims further to elucidate the fundamental features of de Vries behaviour and probe the materials that exhibit it through atomistic molecular dynamics (MD) simulations.

This introduction chapter introduces the general background of liquid crystal materials, providing background information on the most common liquid-crystalline phases, highlighting the characterisation of partially ordered systems and their applications in technological devices. In this work, there is a particular focus on ferroelectric liquid crystals, their specific applications, and the concept of de Vries character. This chapter also provides a brief overview of the experimental techniques used to study de Vries materials and considers the theoretical models proposed in the literature that attempt to partially or fully rationalise de Vries behaviour. This is followed by a general summary of the development of computational methods relevant to the study of de Vries phases and the use of parameterisation to model such materials with greater accuracy. An outline of the computational techniques utilised in this work is also afforded before, in the final section, the aims of the work performed throughout his project are presented.

1.1 Liquid Crystals

1.1.1 Background, History and Discovery

Liquid-crystalline phases exist at a temperature range between the solid crystalline and the isotropic liquid states. Therefore, the degree of order present in a liquid crystal phase is typically intermediate between that in a solid crystal and an isotropic liquid. The molecules comprising a liquid crystal phase possess orientational order and may have some degree of translational order, neither of which are present in an isotropic phase. However, these liquid crystal phases typically lack the long-range three-dimensional translational order observed in a true crystalline solid and as a result these partially ordered phases exhibit many of the anisotropic properties of a crystal while retaining the various fluid properties associated with the isotropic liquid phase.

The initial discovery of liquid crystals is often credited to Austrian botanist Friedrich Reinitzer in 1888,[1] as he observed two distinct melting points upon the heating of cholesteryl benzoate and cholesteryl acetate. This curious discovery led to subsequent work by German physicist Otto

Lehmann,[2] who noted that the 'cloudy' intermediate phase, while having the fluid properties usually associated with a liquid, exhibited optical properties similar to those observed in a crystal. Subsequent studies confirmed the existence of similar 'liquid crystal' phases in many related compounds before polymorphous materials that exhibited multiple liquid-crystalline phases were reported in the early 1900s. Despite the fast pace of these initial discoveries, the field of research into liquid crystals was slow to develop further throughout the early to the mid-20th century.[3] However, liquid crystals gained greater significance with the discovery of their technological importance in the 1960s,[4] which provided the foundation for numerous modern devices and greatly influenced the field of liquid crystal research as seen today.

1.1.2 Characterisation of Liquid Crystals

Numerous materials with diverse chemical structures exhibit liquid-crystalline phases, which may possess different types and various degrees of order. As a result, the many divisions and subdivisions of liquid-crystalline phases are primarily determined by the specific type and extent of order present within a system, in addition to the observed phases' fundamental symmetries. Perhaps the most widely studied class of liquid crystals are the thermotropic liquid crystals, formed in the absence of solvent and in which the extent of order they exhibit is largely a function of system temperature. The phases formed by thermotropic liquid crystals exist within a specific temperature range, and it is this class of liquid crystals that is considered in this thesis. In contrast, lyotropic liquid crystals, in which phase stability is predominantly dependent on the relative concentration of the liquid crystal species within a solvent, are beyond the scope of this thesis.

Thermotropic liquid crystal compounds may themselves be subdivided based on the specific type of anisotropy they exhibit due to their molecular structure. The first main type is often termed calamitic, referring to rod or lath-like compounds, in which one molecular axis is substantially longer than the other two. While the second, perhaps less ubiquitous, variety are labelled discotic, describing disc-like compounds, in which one molecular axis is considerably shorter than the other two. Additionally, in order to exhibit any liquid crystal phase, these compounds must possess a sufficiently rigid molecular structure to maintain their anisotropic shape, promoting favourable alignment with neighbouring molecules. While calamitic and discotic compounds have the capacity to form a variety of distinct liquid crystal phases, with their own curious and unique properties, this project focuses exclusively on materials composed of calamitic molecules.

1.1.3 Liquid Crystal Phases

The nematic (N) phase is the simplest liquid crystal phase. In the nematic phase, molecules possess no translational order and are largely free to diffuse throughout the phase structure. However, molecules in the nematic phase have short-range orientational order as their principal molecular axes align, on average, along a single axis. In a typical sample, the average direction of this orientational

order is consistent only within relatively small domains of aligned molecules. The alignment direction throughout the bulk phase is generally non-uniform due to the presence of disclinations, which act as boundaries between regions of differently aligned molecules, where the average molecular orientation changes abruptly. Typically, alignment of the bulk material is achieved through the application of an external electric or magnetic field, or alternatively may be induced by applying a surface treatment that promotes molecular alignment. The average orientation of molecules in an aligned sample is described as the director, denoted by the unit vector, **n**, as shown in Figure 1.1. The conventional nematic phase can be characterised as uniaxial, as molecules possess complete rotational freedom around their principal molecular axis, leading to a cylindrically symmetric phase.

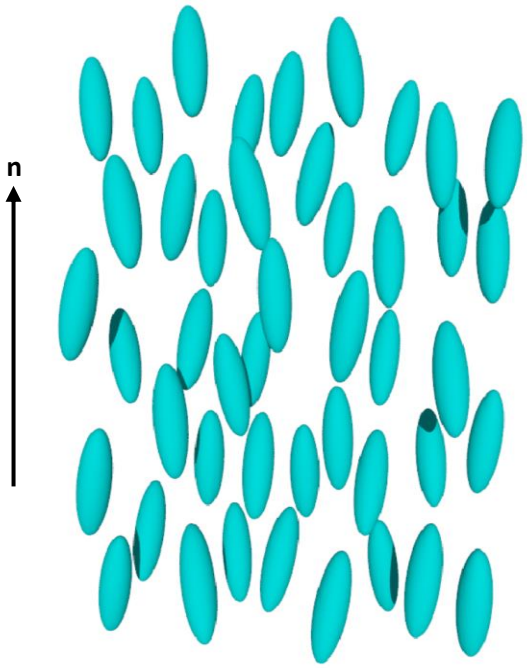

Figure 1.1 Representation of the nematic liquid crystal phase with the director, **n**, defined.

Smectic liquid crystal phases are also commonly exhibited by calamitic molecules. Smectic phases possess a degree of translational order in addition to orientational order similar to that seen in the nematic phase. As a result, molecules in the smectic phase are assembled in a lamellar-like structure, described by a density wave of the molecular centres, which runs perpendicular to the layer plane. Several varieties of smectic mesophase exist, subdivided based on the specific molecular arrangement adopted in the phase, as well as their underlying symmetry. The smectic A (SmA) phase, for example, is considered the simplest smectic phase, as the director sits parallel to the layer normal, **k**, as illustrated in Figure 1.2. In contrast, the director in the smectic C (SmC) phase does not sit parallel to the layer normal, but rather **n** is tilted with respect to **k**, also illustrated in Figure 1.2. Neither the SmA nor SmC phase possess bond orientational order, i.e. a regular molecular arrangement within the plane of the layers. Nevertheless, such highly ordered smectic phases are

observed, namely the smectic B, F and I phases. However, while these low symmetry smectic phases undoubtedly exhibit many properties of interest, they will not be considered further in this thesis.

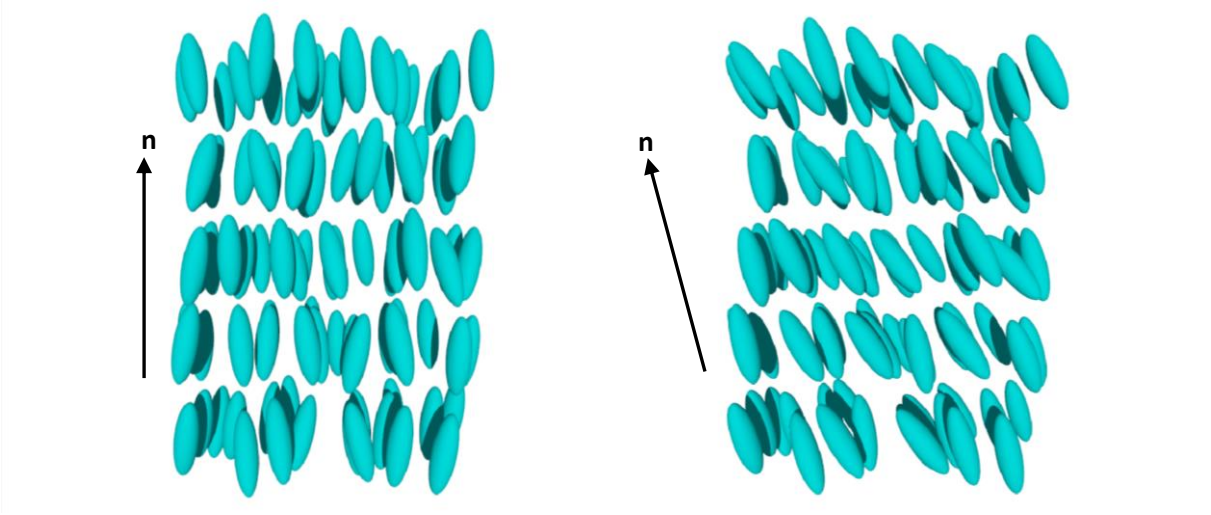

Figure 1.2 Representation of the Smectic A (left) and Smectic C (right) liquid crystal phases, with their relative director orientations, **n**, defined in each case.

Chiral molecules can also form liquid crystal phases similar to non-chiral compounds, and these chiral phases demonstrate a number of unique properties not seen in their achiral equivalents. The chiral nematic phase (N*), sometimes referred to as the cholesteric phase, is exhibited when an optically active substance forms, or is added to, the uniaxial nematic phase. While molecules in the chiral nematic phase possess orientational order comparable to the non-chiral nematic phase, the preferred alignment direction is not consistent throughout the entire phase structure. The chiral nature of the constituent molecules causes the local director to experience a constant small rotation perpendicular to the director axis, resulting in the emergence of a helical structure. The pitch of this helical superstructure is the distance over which the director rotates 360°, and the helical pitch is a crucial characteristic of the chiral nematic phase due to its impact on its optical properties. In the specific case of a nematic phase composed of a racemic mixture, the pitch length is infinite, and as a result, the phase is considered non-chiral.

The chiral smectic A (SmA*) phase does not exhibit a helical structure equivalent to that in the N* phase, as a rotation of the director would necessarily result in a disruption of the smectic layer structure. However, despite this fact, the SmA* phase does differ from its non-chiral counterpart in several fundamental ways. Most significantly, the chiral version of the phase displays less symmetry due to the loss of a mirror plane, as well as a centre of inversion, which facilitates the electroclinic effect upon application of an external electric field.[5] In the chiral smectic C (SmC*) phase, molecules likewise possess orientational and translational order and are tilted with respect to the layer normal, similar to in the achiral SmC phase. However, the influence of molecular chirality causes the tilt direction within the phase to rotate around an axis normal to the smectic layers. The resultant director

rotation generates a helical superstructure throughout the phase, with the helix twisted around **k**, as shown in Figure 1.3. The SmC* phase, together with all other chiral tilted smectic phases, are reported to exhibit ferroelectric character due to their fundamental symmetry properties.[6] Consequently, a spontaneous local polarisation is typically present within the layer structure of the SmC* phase. This thesis will discuss ferroelectric liquid crystals in further detail in the sections below.

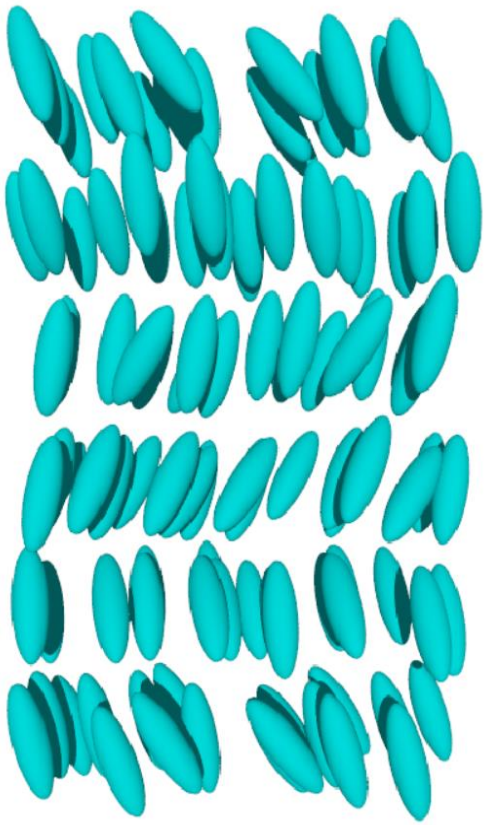

Figure 1.3 Representation of the helical superstructure formed by the chiral Smectic C (SmC*) liquid crystal phase.

The phases described in the section above are considered some of the most common exhibited by calamitic liquid crystals, but numerous other distinct phases have been discovered, displaying a diverse array of properties and a variety of structures. These include blue phases that are observed to exist between the chiral nematic and isotropic liquid phases, highly ordered hexatic phases like the smectic B, F and I phases, mesophases composed of bent-core or banana-shaped molecules, and phases formed from hydrogen bonded dimers.[7,8]

1.1.4 Properties

Liquid crystals have a relatively small amount of order in comparison to crystalline solids, yet this small amount of order clearly distinguishes them from isotropic liquids and greatly influences many of their physical properties. The inherent anisotropic nature of liquid crystal phases manifests as

inequivalent interactions and responses to environmental stimuli in different orientations. Measurement of quantities such as viscosity, elasticity, electric and magnetic susceptibility, and optical properties can, therefore, vary significantly depending on the direction of the measurement relative to the director's orientation. Technological devices that employ liquid crystals regularly exploit a combination of these anisotropic properties, typically relying on the response of liquid crystal materials to external perturbations such as electric and magnetic fields.[9]

1.1.5 Order Parameters

The difference between two liquid-crystalline phases lies in the different types of symmetry they exhibit. This symmetry is the underlying basis of mesophase characterisation, with the transition from one phase into another corresponding to a shift in some fundamental symmetry property. Order parameters offer a means of quantifying the degree of order present within a system, which changes in thermotropic liquid crystals due to an increase or decrease in temperature. The measurement of several different order parameters can provide a detailed insight into the fundamental properties of any liquid-crystalline state. Consequently, the determination of order parameters is a valuable tool to quantify the difference between any two mesophases.

Orientational order is the primary characteristic of all liquid crystal phases, and it is therefore important to quantify accurately. An orientational order parameter can be defined for that purpose, which describes the average orientation of all molecules in a sample. For example, a rod-like molecule's orientation can be expressed as a function of the three Euler angles, α, β and γ, shown in Equation (1.1):

$$f(\Omega) = f(\alpha, \beta, \gamma) \tag{1.1}$$

However, in a phase composed of cylindrically symmetric molecules, rotation around the principle molecular axis, described by angle γ, will not affect the orientational distribution. Likewise, in a cylindrically symmetric system, such as the N phase and SmA phase, all azimuthal angles can be considered equivalent, hence angle α can be ignored. Consequently, the full orientational distribution can be simplified so that only the angle formed by the director and the molecular axis, referred to as β, is relevant. This simplified expression is shown in Equation (1.2):

$$f(\Omega) = f(\alpha, \beta, \gamma) = f(\beta) \tag{1.2}$$

Given the symmetry constraints discussed previously, a complete description of the molecular orientation may be provided by this singlet orientational distribution function, $f(\beta)$. This function can be normalised as defined in Equation (1.3):[10,11]

$$\int_0^{\pi} f(\beta) \sin\beta \, d\beta = 1 \tag{1.3}$$

The symmetry requirements of apolar phases such as the N phase, in which **n** ≡ -**n**, lead to an equivalence between molecules orientated anti-parallel to each other. As a result, the form of the distribution must account for the equality between the angles β and $(\pi - \beta)$, as expressed by Equation (1.4):

$$f(\beta) = f(\pi - \beta) \tag{1.4}$$

Although the complete distribution is theoretically calculable, it is exceedingly difficult to derive experimentally, requiring an infinite number of expansion coefficients. Nevertheless, molecular alignment within a system may still be quantified through more simplified forms of the distribution. For example, through the determination of the second Legendre polynomial, which yields the order parameter, *S*, in Equation (1.5).[12]

$$S = \langle \frac{3}{2}\cos^2\beta - \frac{1}{2} \rangle \tag{1.5}$$

With this description of molecular alignment, $S = 0$ when the system is entirely disordered as in an isotropic liquid, $S = 1$ in a perfectly aligned system in which all molecule orientations are described by $\beta = 0$, and $S = -0.5$ for a system in which all molecular axes sit perpendicular to the director. However, while this quantity can be obtained from the full orientational distribution function, it is often difficult to distinguish between subtly different distributions with the same value for *S*. For example, the same positive value of *S* between 0 and 1 may result from a broad molecular distribution centred around a single angle, β, but may also correspond to a distribution in which all molecules sit at a single non-zero angle, with respect to the director.[13]

Additional order parameters must be considered to obtain a more complete description of the orientational distribution function. This can be achieved by further expansion of the Legendre polynomials, as shown in Equations (1.6) and (1.7).[14] Here, the angular brackets around P_L denote an ensemble average value for the distribution, and odd coefficients need not be considered due to the symmetric nature of the orientational distribution. Equations (1.8) to (1.11) highlight that the second term of the Legendre expansion, P_2, corresponds to the orientational order parameter, *S*, described above, which provides a partial description of the orientational distribution function.[10]

$$f(\beta) = \sum_L f_L P_L(\cos\beta) \; ; (L \text{ even}) \tag{1.6}$$

$$f_L = (\frac{2L+1}{2})\langle P_L \rangle \tag{1.7}$$

$$P_0(\cos\beta) = 1 \tag{1.8}$$

$$P_2(\cos\beta) = \frac{(3\cos^2\beta - 1)}{2} \tag{1.9}$$

$$P_4(\cos\beta) = \frac{(35\cos^4\beta - 30\cos^2\beta + 3)}{8} \tag{1.10}$$

$$P_6(\cos\beta) = \frac{(231\cos^6\beta - 315\cos^4\beta + 105\cos^2\beta - 5)}{16} \tag{1.11}$$

A complete description of the orientational distribution function may be obtained through the infinite expansion of these even Legendre polynomials, represented in Equation (1.12), which entails the substitution of Equations (1.7) to (1.11) into Equation (1.6).

$$f(\beta) = \frac{1}{2} + \frac{5}{2}\big(\langle P_2\rangle P_2(\cos\beta)\big) + \frac{9}{2}\big(\langle P_4\rangle P_4(\cos\beta)\big) + \frac{13}{2}\big(\langle P_6\rangle P_6(\cos\beta)\big) \ldots \tag{1.12}$$

A value of $\langle P_L \rangle$ may be determined from any given orientational distribution function with the application of Equation (1.13).[11] Alternatively, $\langle P_L \rangle$ may be obtained from an ensemble average of molecular orientations with Equation (1.14).

$$\langle P_L \rangle = \int_0^x P_L(\cos\beta) f(\beta) \sin\beta \, d\beta \tag{2.13}$$

$$\langle P_L \rangle = \langle P_L(\cos\beta) \rangle \tag{1.14}$$

Determination of the full orientational distribution function, $f(\beta)$, requires the measurement of high-rank order parameters that are often difficult to derive experimentally. While some x-ray and neutron scattering studies have attempted to calculate such distributions, several approximations are still necessary.[15,16] In contrast, $\langle P_2 \rangle$ is significantly more accessible through experiment because it can be derived from the measurement of properties such as birefringence, magnetic susceptibility, and linear dichromism.[11,17,18] Likewise, several experimental methods are able to obtain $\langle P_4 \rangle$, including polarised Raman scattering[19,20] and fluorescence depolarisation.[21] Measurement of higher-rank order parameters provides increased insight into the distribution function. Still, the exact distribution

function cannot be accessed through a finite expansion of terms, and measurement of high-rank order parameters becomes progressively more complex when calculated from experimental methods.

The orientational order parameter is independent of the layer structure observed in any smectic or lamellar liquid crystal phase. Therefore, the translational order parameter, τ, and layer spacing, d, are often necessary to obtain an insight into the phase behaviour exhibited by smectic systems. While the translational order parameter was initially introduced in simple molecular crystals,[22] specifically in liquid crystals, the smectic translational order parameter was not formally established until work reported by Kobayashi,[23,24] and McMillan.[25,26] These theories assumed that the formation of the smectic layer structure is primarily driven by core-core interactions where the polarisable aromatic cores of molecules are separated from the flexible terminal chains. In the density wave, $\rho(z)$, that results from this separation of sub-units, the smectic layer spacing, d, describes its period length. Therefore, the translational order parameter corresponds to the amplitude of the one-dimensional density wave, which is expressed in Equation (1.15):

$$\tau = \langle \cos(\frac{2\pi z}{d}) \rangle \tag{1.15}$$

Here z refers to the molecular positions along the z-axis, which itself is defined to maximise the amplitude of the density wave in a smectic system.[26]

The translational order parameter is an essential property of smectic and lamellar phases, but it is frequently left unreported in many studies of liquid-crystalline materials. Despite this, a variety of smectic materials have been studied in the context of translational order,[27–29] and in these cases, values were obtained by a method proposed by Leadbetter and Norris,[27] utilising x-ray scattering measurements. However, the application of this method has been limited by several major drawbacks, namely, the requirement to measure second-order diffraction peaks, which may be too weak to be detected in many smectic materials. Additionally, such a method supposes a Gaussian distribution of displacements around the centre of the layer, which has further restricted its utility for routine measurements.[30,31] More recently, Kapernaum and Giesselmann,[30] proposed a seemingly more robust method in which the smectic translational order parameter is obtained from the temperature-dependent intensity, I, of the fundamental smectic layer peak, observed through small-angle x-ray scattering measurements. Still, this method uses a 'Haller-like' extrapolation of I to absolute zero that necessitates a suitably large smectic temperature range. At the same time, its lack of widespread use may also raise questions about its reliability in non-conventional smectic systems. Both approaches discussed above also require an aligned sample of the liquid-crystalline material, typically in an x-ray capillary tube, the preparation of which may be difficult. Additionally, smectic translational order parameters in several materials have been probed using methods based on neutron

scattering,[31] which aim to avoid many of the issues outlined above, but this is a more recent development, and hence questions about the reliability of the method remain relevant.

1.1.6 Design of Liquid Crystals

At first, the molecular structures of compounds known to form liquid-crystalline phases appear rather similar, yet this seemingly narrow selection of compounds may contain a myriad of structural elements that can affect their material properties in diverse ways. The design strategy applied to liquid crystals often focuses on several fundamental structural features that are known to be conducive to liquid crystal phase formation. Consequently, the search for new and improved liquid crystal compounds tends to centre around modifying these key structural elements in an effort to promote or suppress the development of certain phases, or to adjust the temperature range over which a specific mesophase is exhibited. Calamitic liquid crystals are typically composed of structural elements that help maintain the rigidity of molecules, and it is often useful to break these elements down into structural 'groups', which each contribute to the liquid-crystalline behaviour in separate ways.

Perhaps the most important structural feature of calamitic liquid crystals is the core: an inflexible unit typically constructed from two or more aromatic or similarly cyclic structures, and frequently connected by smaller linker groups. Such features contribute to the anisotropic shape of the molecules, while intermolecular interactions between the π-systems of conjugated cores promote an orientationally ordered molecular assembly. Modification of the core structure can result in the expression of different mesophase types, with various core properties theorised to play a crucial role in either nematic or smectic phase formation. A vitally important aspect of research on liquid crystals is therefore the optimisation of liquid-crystalline properties for device applications, which requires an appreciation of how individual structural features contribute to mesophase character. For example, the N phase is typically exhibited when the structure of the compound promotes molecular alignment towards single direction yet lacks the features necessary to stabilise a lamellar-like phase structure. As the liquid crystal core is a key component in the development of such orientational order, small adjustments to the core structure can also have a substantial effect on nematic phase stability. Though it can be difficult to precisely predict whether a certain type of core will produce a nematic or smectic phase, there are several basic features that are widely known to promote either orientational or translational order. For instance, the molecular length to width radio has been identified as a central characteristic of mesogens, so, perhaps unsurprisingly, extension of the linear core is a common strategy utilised to promote orientational order within a phase. Likewise, expansion of the conjugated π-system typically strengthens core-core interactions and elongation of the core tends to increase polarisability anisotropy, both of which contribute to a favourable molecular alignment. The overall effect of these changes on orientational order is illustrated by the nematic phase ranges in Figure 1.4.

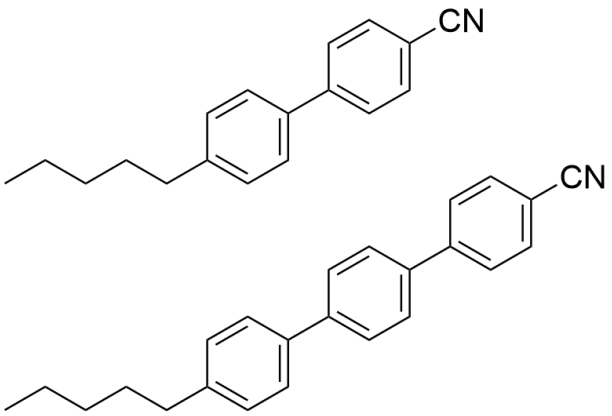

Figure 1.4 Chemical structure of 5-cyanobiphenyl (5CB) (Cr 24°C N 35°C I) and 5-cyanotriphenyl (5CT) (Cr 130°C N 239°C I).[7]

For a material to produce a liquid-crystalline phase, terminal substituents are typically also required on either one or both sides of the core's primary axis. These terminal units are commonly composed of extended alkyl or alkoxy chains that introduce a degree flexibility to the molecular structure, which has the potential to disrupt crystal packing. Small modification to these terminal substituents can result in compounds displaying drastically different types of order. Notably, extension of an alkyl or alkoxy chain usually promotes smectic phase formation, reportedly due to favourable interactions between aliphatic groups, resulting in chain entanglement. This nano-segregation between the flexible terminal chain and the largely inflexible core structures facilitates the development of a layer structure within the phase. In addition, the introduction of chirality into a liquid-crystalline molecule is normally achieved by replacing one of the terminal groups with a branched alkyl chain. However, the inclusion of a branched unit can often disrupt molecular packing, which causes a reduction in liquid crystal phase stability. The substantial impact of such a relatively small structural modification emphasises the complex relationship between liquid crystal structure and mesophase properties, as well as difficulty associated with the formulation of new materials. Frequently, a polar substituent, such as a nitrile functional group, is inserted at one of the terminal positions to increase intermolecular interactions between nearby molecules, which stabilise an orientationally ordered phase structure.

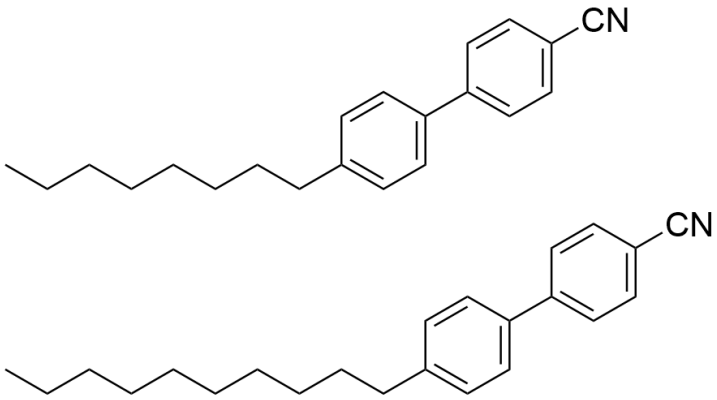

Figure 1.5 Chemical structure of 8-cyanobiphenyl (Cr 21.5°C SmA 33.5°C N 40.5°C I) and 10-cyanobiphenyl (10CB) (Cr 44.0°C SmA 50.5°C).[7]

Lastly, lateral substituents are sometimes incorporated into to the core structure to modify transition temperatures, phase morphology or fine-tune the dielectric properties of the liquid crystal material. Due to the requirement to preserve anisotropy of molecular shape and phase stability, these lateral substituents are typically limited to single atoms, such as halogens, or small di- and tri-atomic functional groups. Despite this, lateral substituents are not an uncommon feature of liquid crystal compounds, with the introduction of a lateral fluorine a fairly routine strategy used to promote the formation of tilted phases, such as SmC, in materials that already exhibit a stable SmA phase.

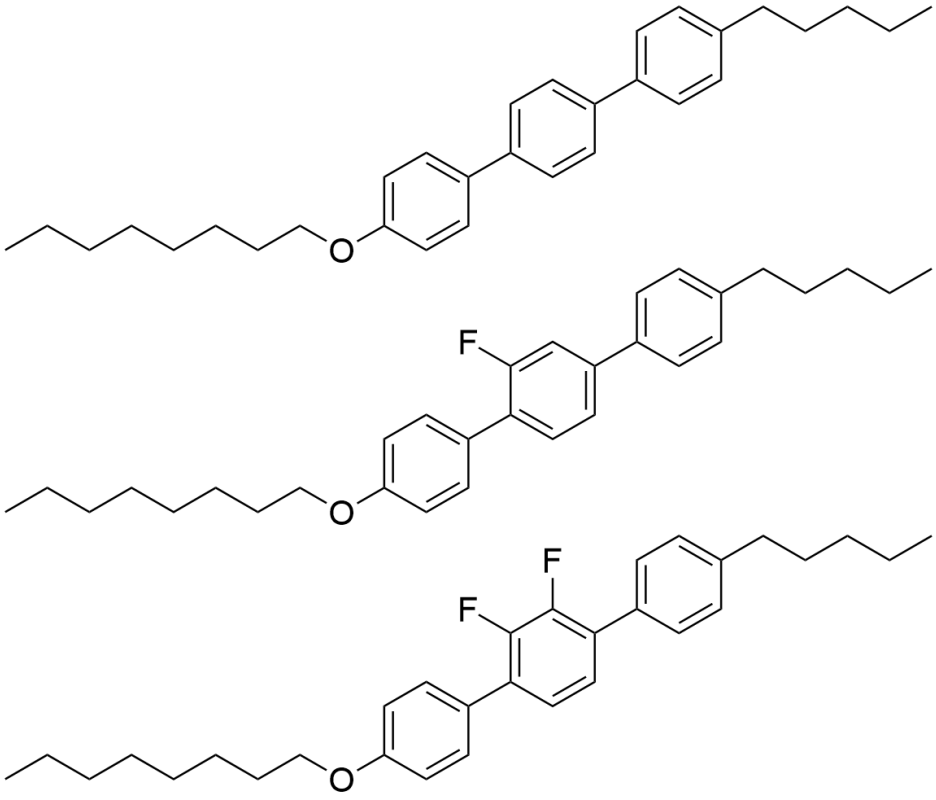

Figure 1.6 Chemical structure of liquid-crystalline materials with different degrees of lateral fluoro-substitution (top) (Cr 194.5°C SmB 211.0°C SmA 221.5°C I), (middle) (Cr 46.0°C SmI 53.5°C SmC 116.5°C SmA 130.0°C N 155.0°C I), (bottom) (Cr 48.5°C SmC 95.0°C N 141.5°C I).[7]

As evident from the discussion above, the specific types of liquid-crystalline order exhibited by any compound result from a seemingly complex interplay between numerous factors related to the underlying chemical structure of a material. However, mesophase formation can perhaps be more intuitively described from a thermodynamic perspective. The characteristic orientational order exhibited by liquid-crystalline phases can be largely considered a consequence of entropic effects, notably the fact that rod-like molecules retain less free volume within the randomly orientated isotropic phase than within an orientationally ordered phase. The reduction in excluded volume between pairs of aligned molecules, results in a substantial negative contribution to the free energy, and hence heavily promotes nematic ordering. Additionally, enthalpic effects such as the balance of repulsive and attractive interactions between sub-sections of adjacent molecules can contribute negatively to a system's free energy, promoting the development of orientational order, as well as translational order.

1.1.7 Applications of Liquid Crystals

Liquid crystals are widely recognised in the modern world for their application in display technology. Such devices employ many different types of liquid crystal phases and can be built upon various architectures. However, all these devices operate based on two 'modes' of alignment that can be switched with the influence of an electric field. Individual pixels in a liquid crystal display are liquid crystal cells. These structures are generally made from the combination of two glass plates that are coated with a thin transparent electrode layer, typically indium tin oxide (ITO), which allows an electric field to form across the internal cell. A surface treatment is similarly applied to the inside surfaces of the glass plates in an effort to promote bulk alignment of the liquid crystal within the cell. Additionally, thin-film polarisers are added to one or both external glass surfaces, dependent on the device's specific mode of operation.

The earliest display devices emerged in the late 1960s,[32] with the first commercially successful LCD utilising an ion-doped liquid crystal mixture. However, while this technology enjoyed some success, the widespread appeal of these devices suffered due to issues with high power consumption and narrow operating temperatures. Many of the problems associated with these early devices were rectified with the development of the Twisted Nematic (TN) display, which operated based on the chiral nematic phase. As a result, liquid crystal displays became increasingly commonplace after a new millennium, eventually all but replacing bulky CRT devices. In more recent years, liquid crystal displays have competed against the growing market of LED-based devices. However, devices based on liquid crystals continue to be utilised in many areas and have the potential for further growth with the development of more advanced liquid crystal-based technology.

The TN mode of operation is based on the interaction between plane polarised light and a nematic liquid-crystalline material in two different states. In the TN display, the surface treatment promotes

molecular alignment parallel to the plane of the glass plates, orthogonally aligned within the cell. Therefore, the alignment direction of molecules points parallel to the glass plates but experiences a 90° rotation between the top and bottom surfaces of the cell. The helical pitch of the nematic liquid crystal within the cell is significantly larger than the wavelength of visible light. Therefore, the polarisation direction of light passing through the cell is rotated through 90°. Thin-film polarisers orientated perpendicular to each other are placed on the external surface of the glass substrates, which means light that has passed through the first polariser is blocked by the second if the polarisation remains unaffected by the liquid crystal within the cell. However, the light will pass through the second polariser if the polarisation direction of light has been rotated by the pitch of the liquid crystal material. In the TN display, the molecular alignment can be switched with the application of an electric field. A voltage applied across the internal cell causes the bulk material to orient perpendicular to the glass substrates. This voltage leads to the destruction of the helix, which results in the plane polarised light retaining its original polarisation and being subsequently blocked by the second crossed polariser. This results in no light transmittance and the 'dark state' of the cell. The TN display often employs a backlight that allows the display to function in low light conditions.

TN display devices overcame many of the problems associated with earlier liquid crystal display architectures, such as high-power consumption and low contrast between 'light' and 'dark' states. Optimisation of liquid crystal material properties has led to subsequent improvements to TN display devices, which have occupied a large proportion of the display market for a number of years.[4]

An alternative liquid crystal device architecture that has become more prominent in more recent years is referred to as in-plane switching (IPS). Devices based on this mode of operation were designed to resolve some of the main issues associated with the TN mode of operation. As a result, IPS devices offer wide viewing angles and improved resolution.[33] IPS technology utilises a nematic liquid crystal, similar to TN devices, but operates by a different mechanism. In the IPS cell, transistors are attached to the same glass substrate, and an electric field is generated across the width of the liquid crystal cell. When a voltage is applied, molecules align parallel to this electric field, which unwinds the helical molecular arrangement. In this device, the thin-film polarisers are aligned parallel to one another. In the 'off' state, polarised light that passes through the first polariser is rotated due to its interaction with the twisted liquid crystal and is subsequently blocked by the second filter. In comparison, the polarisation direction of light in the 'on' state is unaffected because of the untwisted molecular arrangement and passes through the second polarising film. IPS displays, which offer wide viewing angles, can often be found operating in touch screen devices that employ liquid crystal due to their ability to produce less tailing when pressure is applied through touch. However, IPS displays are generally more expensive to produce and still suffer from issues common to other nematic-based devices, such as relatively slow (ms) response times.

As outlined above, displays based on liquid crystals can operate via several different mechanisms, perhaps unsurprisingly due to the large variety of liquid crystal phases with distinct types of order in existence. However, a multitude of factors must be considered to produce a practical liquid crystal display device. The liquid crystal material in question must be sufficiently stable over an extended timescale and many switch cycles. In addition, the liquid crystal phase on which the device is based must exist over a wide temperature range. The material should also be capable of fast switching, typically speeds on the scale of a few milliseconds or less are required. And these switch speeds are often dependent on a combination of dielectric and mechanical properties. The material properties necessary for a commercial display are usually achieved by carefully designing liquid crystal mixtures, as optimisation of one property can have undesired consequences for another. As a consequence, the materials used in modern commercial displays are those that have the most well-balanced properties. Due to this need to perform well in all required categories, new liquid-crystalline materials are often difficult to design, and significant research and development efforts are necessary to be successful.

In addition to their use in display devices, liquid crystals can be found operating in numerous other commercial devices. Such devices often rely on the temperature and electric field dependence of molecules in the liquid crystal phase. For example, temperature sensors that utilise the properties of chiral nematic liquid crystals.[34,35] The pitch length of a chiral nematic liquid crystal is dependent on the system temperature, while the colour of visible light reflected by the liquid crystal corresponds to the pitch length. Therefore, a temperature change is reflected by a shift in the colour of the liquid crystal material. This effect has been exploited in a range of applications such as thermometers, medical thermography,[36,37], and temperature-sensitive clothes and jewellery.[38] Another area where liquid crystals have shown potential is in spatial light modulators (SLMs) that control the transmission of light passing through the device. Liquid crystal-based SLMs have potential applications in optical computing,[39] hologram generation,[40,41] data encoding[42,43] and vision correction.[44] Furthermore, liquid crystals have numerous potential applications in emerging fields such as nano-, bio- and micro-technology,[45] and continue to generate significant academic interest today.

1.2 Ferroelectric Liquid Crystals

1.2.1 Concept, History and Discovery

The liquid crystal phases vary in their structure and order and, therefore, their fundamental symmetries. It is these symmetries that influence the mechanical, optical and electric properties of liquid-crystalline materials. And it was symmetry arguments that were the basis for the prediction of ferroelectricity, i.e. the existence of a spontaneous polarisation that can be reversed with the application of an electric field, in smectic liquid crystals by Meyer, R. *et al.*,[6] in 1974. The

ferroelectric effect was well-known after it was initially identified in solid crystals in 1921 by Valasek.[46]

The achiral SmC phase possesses monoclinic symmetry, which consists of a centre of inversion, a mirror plane normal to the layers and a two-fold axis of rotation parallel to the layers and normal to the tilt direction. In comparison, when chirality is introduced into the SmC phase, it results in the SmC* phase. In the SmC* phase, the mirror plane and the centre of inversion disappear, leaving only the C_2-rotation axis. This loss of symmetry should allow a permanent local dipole moment to form, resulting in a material that exhibits ferroelectric character.[47] This led to the realisation that all chiral tilted smectic phases could exhibit a spontaneous local polarisation, and this was experimentally confirmed with the synthesis of the first ferroelectric liquid crystal *L*-*n*-decyloxybenzylidene-*p'*-amino-2-methyl butyl cinnamate (DOBAMBC), in 1975,[6] the structure of which is shown in Figure 1.7.

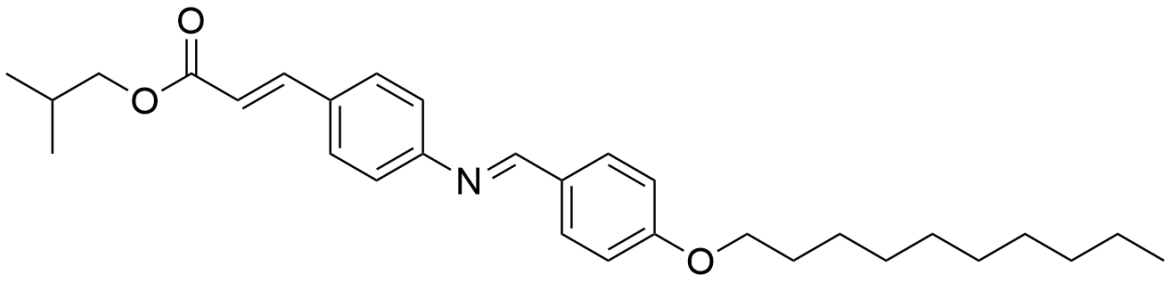

Figure 1.7 Chemical structure of the liquid-crystalline DOBAMBC (Cr 76°C SmC 95°C SmA 117°C I).[6]

The SmC* phase may be formed when chiral molecules form the SmC phase or may be induced in a non-chiral SmC host phase with the addition of a chiral dopant.[48] Due to the symmetry properties described in the previous paragraph, both of these SmC* systems may exhibit a small spontaneous local polarisation when the constituent molecules contain a permanent transverse dipole moment.[48] The molecular chirality also causes a small continuous shift in the direction of tilt throughout the phase, which gives rise to a helical superstructure.[49] The emergence of this helix results from the interactions between chiral molecules that induce a molecular twist perpendicular to the layer normal, **k**. Consequently, the dipole moment rotates through 360° as the azimuthal angle of the director experiences rotation around the layer normal. The precession about **k** causes a compensation of the dipole moments, as the spontaneous polarisation cancels out over one helical pitch length. In a bulk sample, the net spontaneous polarisation is, therefore, reduced to zero.

The helical structure in the SmC* phase can be unwound with the application of an external electric field. The interaction of the permanent molecular dipole moments with the electric field causes the spontaneous local polarisation to align with the direction of the field. If this direction is reversed, molecules reorientate so that the spontaneous polarisation once again corresponds to the field direction. This rapid electro-optic response, which can occur on the scale of a few microseconds,[50]

makes ferroelectric liquid crystal-based devices particularly appealing for various applications in science and technology.

1.2.2 Modes of Operation

Ferroelectric liquid crystals (FLCs) have attracted significant research interest since they were initially proposed by Meyer *et al*.,[6,51] primarily due to their potential for fast electro-optic response times.[50] The development of display devices employing FLCs was swift after this prediction of ferroelectricity in liquid crystals,[52] with the first FLC mode of operation reported in 1980 by Clark and Lagerwall.[50] Throughout the years, several more FLC device architectures have been developed, utilising the fundamental properties of FLCs in many unique and noteworthy ways.[53,54]

The first electro-optic mode of operation for FLCs reported was the surface-stabilised ferroelectric liquid crystal (SSFLC) geometry, commonly referred to as the Clark-Lagerwall effect.[50,54] In the SSFLC cell, the liquid crystal material is sandwiched between two glass plates that are internally coated in an alignment layer. Interactions with the surfaces of the cell cause the helical structure, ordinarily present in the SmC* phase, to unwind. In this arrangement, the formation of the helix is unfavourable because the distance between the glass substrates is considerably smaller than the typical chiral pitch length in SmC* materials. The smectic layers are orthogonally arranged with the glass plates, with molecules aligned parallel to the cell surfaces but tilted away from **k** by the tilt angle, represented by θ. In the FLC cell, two stable molecular arrangements exist and switching between these 'states' can be achieved with an external electric field, in which the sign can be reversed. These two molecular arrangements, separated by an angle of 2θ or twice the molecular tilt angle, provide the device with an intrinsic bistability, which can act as a favourable memory effect, and an essential property for large flat-panel electro-optic displays.[52,55] The SSFLC cell is placed between two thin-film polarisers that are orientated perpendicular to each other. In the first 'state', molecules are aligned parallel to the polariser, resulting in the polarisation direction of light passing through the cell remaining the same. The second polarising film, orientated at a non-zero angle from the first, then blocks the light and gives rise to the 'dark' mode of the device. In the alternative' state', molecules make a non-zero angle with the first polariser, and the polarisation direction of light that passes through the cell is shifted to align with the second polarising film. Consequently, the light is transmitted through the cell, resulting in the 'light' mode of the device.

The SSFLC effect is considered a suitable candidate for electro-optic display devices due to its capacity for high switching speeds and wide viewing angles. Despite the advantages SSFLCs provide over earlier liquid crystal-based display technology, they have yet to supplant nematic-based displays due to several issues that have hindered their development, such as the difficulty in realising different greyscale levels.[54,56] However, the most severe problem emerges due to the contraction of the smectic layer structure as the sample is cooled from the SmA phase into the SmC phase during the

manufacturing process of SSFLC displays. This problem, as well as potential solutions, will be discussed further later in this thesis.

In addition to the SSFLC geometry discussed above, several other device concepts have been proposed for displays that utilise FLCs. For example, the deformed helix ferroelectric (DHF) device relies on the ability to distort the FLC helix with an applied electric field.[57] In this device, the liquid crystal mixture contained between two glass plates possesses a layer thickness that is considerably larger than the helical pitch length of the material. In an FLC material that displays these properties, the helical structure is preserved within the FLC cell. The smectic layers are positioned perpendicular to the glass substrates, while the helical axis runs parallel to the glass surfaces. The application of an electric field can disturb the helical structure in the cell, which results in a variation of properties such as refractive index and birefringence. Electrical control of these properties can be utilised in many electro-optic devices, and the DHF effect has potential applications in spatial light modulators[58,59] and colour sequential displays.[60]

A different mode of operation that has been reported more recently is called the electrically suppressed helix ferroelectric liquid crystal (ESHFLC) device.[61,62] The ESHFLC effect offers high contrast ratios and very fast electro-optic response times, making it particularly suitable for display technology and photonics applications.[54]At low electric field strengths, the ESHFLC device appears similar to the DHF mode, in which the helical structure is preserved within the FLC cell. However, at high electric field strengths, the difference between the two devices becomes apparent. Above a specific threshold voltage, the helix is suppressed entirely by the electric field, and the molecular arrangement resembles that in the SSFLC device. Although the initial conditions in the ESHFLC and SSFLC are different, when the helix is unwound, the dynamics of both are identical.[54] The absence of the surface-stabilised molecular arrangement in the ESHFLC facilitates improved FLC alignment, which results in a superior contrast ratio to that achievable in the SSFLC geometry.

1.2.3 Applications of FLCs

The excitement around the potential applications of SSFLC has decreased throughout the years, as problems associated with the manufacture of large area, passively or actively addressed, fast response displays with wide angles of view became especially apparent. However, devices employing SSFLCs have found a number of niche applications in small devices that are heavily dependent on fast switching speeds for their operation. For example, one device type that frequently utilises FLCs is SLMs. SLMs are most often used in optical devices that employ FLCs for fast processing speeds in various applications such as flexible beam steering,[63] holographic devices,[64] neurocomputing,[65] and image processing and analysis.[66] Like many other areas of science, SSFLCs have also immensely benefited from the miniaturisation of technological devices and the ever-increasing demand for smaller displays. Micro-displays regularly make use of ferroelectric liquid crystal on silicon

(FLCOS) technology,[67,68] and are employed in a range of applications that prioritise high resolutions and fast response times, such as camera view-finders, virtual reality systems, laser material processing and micro-projectors.[68–72] However, outside of these more niche uses, SSFLCs have attracted interest due to their potential application in Field-Sequential Colour displays,[73] which require particularly rapid switching speeds to operate effectively, but offer improved display resolutions and contrast ratios, as well as substantial reductions in power consumption.

1.2.4 Design of FLCs

The design strategy for FLC materials overlaps substantially with the design of LC phases more generally, as rod-like molecules that contain a sufficiently rigid, polarisable core and one or more flexible terminal chains are typically crucial for the generation of FLC phases. The SmC phase, in which molecules are tilted with respect to the layer normal, is often favoured with the addition of ester (-CO_2-) or imine (-CH=N-) functional groups. These structural features promote layer formation and a tilted phase due to the introduction of some amount of lateral polarity within the molecule.[74] Relatively extended terminal chains promote intermolecular interactions that can aid the formation of smectic phases, while the increased flexibility as a result of the terminal chains also contributes to molecular tilt behaviour.[75] Ferroelectric character in the SmC phase is entirely dependent on reduced symmetry, a consequence of chirality present within the system. The introduction of chirality is usually accomplished by the inclusion of a chiral centre in one of the extended terminal chains. DOBAMBC was the first FLC to be synthesised,[6] and provides a fairly typical example of the chemical structure of FLC materials. A considerable amount of the early research that investigated structure-property relationships in FLC materials centred around the development of materials with a high value of spontaneous polarisation, which was thought to be beneficial for device properties.[66] Some standard methods to increase spontaneous polarisation include the addition of one or more polar functional groups to the area around the chiral centre.[76] Additionally, restriction of molecular rotation, generally accomplished by elongating the alkyl/alkoxy chains or by positioning the chiral centre closer to the aromatic core, increases spontaneous polarisation.[76,77] However, as an increase in molecular length also has the inverse effect of reducing spontaneous polarisation, greatly extended terminal chains are rare, despite their ability to decrease rotational freedom. Though the insights gained into structure-property relationships in FLC materials are valuable, the development of functional FLCs has proved difficult due to the numerous properties that must be taken into consideration. Functional devices most often utilise chiral doped FLC mixtures as they provide a better ability to tune properties and phase morphology than those based wholly on chiral molecules.[66]

1.2.5 SSFLC Issues

The initial promise offered in the SSFLC effect attracted considerable attention; however, the development of SSFLC-based flat panel displays in the 1990s suffered from many serious problems caused by the emergence of alignment defects. These problems were related, primarily, to the fact

that smectic layers contract significantly at the transition between the SmA phase and the SmC phase due to the onset of molecular tilt. In the SSFLC cell structure, the SmA phase is contained between two glass plates, with the smectic layers perpendicular to the cell surfaces.[50] In this arrangement, molecules are anchored to the glass plates to promote the preferred alignment direction within the cell. As the SmA phase is cooled, a tilt transition occurs at the SmA-SmC transition that causes the smectic layer structure to contract. In typical smectic materials, an observable molecular tilt, θ, presents at the SmA-SmC transition, causing an associated shrinkage of the smectic layers proportional to $\cos(\theta)$.[78] Due to this, the layer thickness in the SmC phase, d_C, can be considerably smaller than the layer thickness in the SmA phase, d_A. As the layer structure is anchored to the cell surfaces, the smectic layers buckle as they contract, which results in the formation of chevron folds throughout the cell. The development of the chevron geometry was experimentally demonstrated by Rieker *et al*. in 1987.[79] Several optical defects arise because of the chevron configuration, the most common of which are referred to as zig-zag line defects caused by the separation of chevrons with opposite fold directions.[80,81] The emergence of the chevron geometry, and the subsequent zig-zag defects, have been a major barrier to the development and widespread adoption of FLCs in device applications as they severely reduce the optical quality of devices that function using the SSFLC mode of operation. Therefore, the future of FLC applications in display devices is increasingly dependent on finding a solution to the problem caused by layer shrinkage. A potential answer may lie in materials that exhibit minimal layer contraction at the SmA-SmC transition.[78]

1.3 De Vries Behaviour

1.3.1 Concept and History

Materials that exhibit substantially less layer shrinkage at the SmA-SmC transition than predicted by the rigid-rod model of liquid crystals had attracted initial research attention when first reported in 1970.[82] However, this behaviour was primarily regarded as a curious phenomenon with little practical application and interest in these materials lessened as it was discovered that minimal layer contraction was a rare behaviour exhibited by a minority of materials that could form the SmC phase. Nevertheless, these materials offer a potential solution to many of the issues that result from the contraction of smectic layers at the SmA-SmC transition in SSFLC-based devices. This fact has propelled materials that exhibit de Vries behaviour as it is commonly known, in reference to the American crystallographer Adriaan de Vries after he developed one of the first models to account for the effect, into the scientific consciousness. Due to this increased research focus, numerous materials that exhibit near-constant layer thickness at the SmA-SmC transition have been identified.[83–86] Despite the extended search for new materials, de Vries behaviour has still not been fully rationalised, and the question of why these materials exhibit minimal layer contraction is an open area of scientific debate. Progress towards an answer to this question would certainly benefit

the further development of functional FLC materials and electro-optic devices, as well as provide additional insight into the more general topic of phase transitions in smectic liquid crystals.

1.3.2 Experimental Studies of de Vries Behaviour

Experimental investigations have focused on materials that exhibit minimal layer contraction at the SmA-SmC transition in an effort to further elucidate their remarkable behaviour and support the synthesis of new de Vries materials. The observation of an increase in molecular tilt with little or no associated layer contraction appears at first to be illogical and contradictory, and it is this fact that has led to a wide variety of experimental techniques being employed to study de Vries character. In the study of these systems, the orientational order of molecules within smectic phases has become an increasingly significant area of research. Experimental techniques such as Raman scattering, x-ray diffraction, infrared dichroism, NMR spectroscopy and birefringence analysis have all been used to quantify orientational order in smectic systems, particularly at the SmA-SmC transition. However, the results of these experimental studies have tended not to be entirely conclusive.[87–90] Due to the nature of the experimental techniques employed to probe orientational order, no single method is able to provide a complete description of mesophase behaviour, which necessitates the use of multiple techniques in combination. In addition, it is often the case that the results from these methods are not easy to fully rationalise. The difficulty associated with the interpretation of these seemingly disparate experiments may be partially attributed to the inherent limitations of the methods themselves in terms of the number of accessible expansion coefficients of the orientational distribution function, and from the specific molecular feature that is actively measured. For example, birefringence measurements can yield information on the orientational order of the polarisable aromatic core of a mesogen but can offer little information on the orientational properties of the side chains and end groups. Conversely, where x-ray scattering may provide information about the overall orientational order of molecules, it cannot typically provide knowledge about how this relates to the orientational order of individual molecular sub-units.

The fundamental differences between experimental techniques predictably leads to dissimilarities in their resultant orientational order parameters. As a result, separate studies may not necessarily be consistent, generating complexity when comparisons between investigations are made. Furthermore, severe approximations are often necessary when it comes to the calculation of orientational order and interpretation of the data. These approximations are usually of cylindrical molecular symmetry and certain dominant molecular associations.[87] While many experimental methods are able to probe orientational order, x-ray scattering techniques are particularly noteworthy due to their theoretical ability to provide the entire orientational distribution function,[15] yet interpretation is significantly complicated not only by molecular symmetry but also by issues such as data processing after collection.[16,91] Still, a considerable amount of data on orientational order in these system has been obtained, and clear trends in the behaviour of material displaying de Vries character have become

increasingly apparent. Such observations have formed the basis for several models that have been proposed to account for de Vries behaviour, discussed in further detail in section 1.3.3 of this thesis.

The experimental assessment of translational order within smectic system, while not a particularly common practice, can be considered a key component of several studies,[27,29,92] providing an insight into the smectic layer structure in both the SmA and SmC phases. Techniques such as x-ray scattering are able to probe translational order but rely on the interpretation of higher-order diffraction peaks, which can be a challenge to observe in many systems.[27] Like with orientational order, the determination of translational order depends on several assumptions such as Gaussian positional fluctuations of molecules around their equilibrium position and calculations of molecule structure factors derived from assumptions of dominant molecular conformations. As a result, the calculation of translational order in de Vries materials is not commonly performed, and the translational order parameters of only a few materials have been reported.[30]

A strong electroclinic response has also been reported in experimental studies of de Vries liquid crystals.[86,93,94] The electroclinic effect can be observed when an electric field is applied to a system of molecules in the SmA phase, generating a non-zero molecular tilt. This effect is particularly apparent in materials that exhibit minimal layer contraction and has been used to support the concept of a 'de Vries-like' SmA phase, in which molecules are tilted but azimuthally disordered. Birefringence measurements have been utilised to calculate the field induced optical tilt, and a theory for the orientational distribution of molecules has been proposed by Selinger *et al*.[95] Likewise, Spector *et al*.[96] performed optical and x-ray scattering experiments on the same series of chiral organosiloxane mesogens, observing a large induced tilt accompanied by minimal layer contraction. The tilt angle determined from x-ray diffraction measurements was consistently smaller than the tilt angle deduced from the measurement of the optic axis, suggesting that molecules do not act in accordance with the rigid-rod model of liquid crystals.

In addition to the experimental techniques discussed above, many studies have utilised methods such as dielectric spectroscopy to study systems displaying de Vries behaviour.[97,98] The primary focus of dielectric studies is often on tilt angle fluctuations in the vicinity of the SmA-SmC transition, with dielectric characterisation enabling molecular tilt to be probed through measurement of the dielectric constant and relaxation frequency. Typically, the results of dielectric studies performed on conventional smectic liquid crystals, in which molecular behaviour is generally well understood, can provide an insight into how de Vries materials deviate from this 'conventional' behaviour. For example, some studies have probed the temperature dependence of the dielectric constant either side of the SmA-SmC transition, showing that de Vries materials differ substantially from more typical smectic liquid crystals, and proposing that this shift is a result of some parts of the molecule adopting a less tilted orientation, relative to **k**, upon transition to the SmC phase.[97] In other studies, dielectric

absorption spectra have been used to probe the tilt angle fluctuations exhibited by de Vries materials, reported to display a particularly high degree of soft-mode absorption due to the fact that tilt fluctuations are decoupled from variations in layer thickness.[98] Through such investigations, dielectric spectroscopy has proved a practical tool to investigate smectic liquid crystals, with the assessment of the dielectric response and the relationship between various relaxation modes able to provide useful information on the tilt behaviour of liquid crystal compounds.

1.3.3 Models of de Vries Behaviour

From the studies outlined above, several models have been proposed that attempt to explain the mechanism behind the anomalous reduction in layer shrinkage at a molecular level. However, individual molecular contributions that result in supramolecular effects are difficult to isolate and interpret unambiguously. Consequently, a general molecular explanation for de Vries behaviour remains absent.

Adriaan de Vries and his co-workers pioneered the discussion about an explanation for minimal layer contraction when the first, and perhaps still most prevalent, models of de Vries behaviour were proposed.[99,100] Initially, the non-correlation model predicted that molecules were tilted in the SmA phase as well as in the SmC phase. In this model, the tilt direction of molecules in the SmA phase is consistent within individual layers, but there is no correlation in the tilt direction between layers. This model results in a uniaxial SmA phase, as the tilt direction averages out at zero across all of the layer structure, but was subsequently abandoned by de Vries, who recognised that due to the imperfect orientational order typically exhibited by non-layer shrinkage materials a model based around layers of uniformly tilted molecules was not necessary.[78] However, despite this, smectic phases with such a randomly tilted layer structure have since been reported in the literature.[101] The random diffuse cone model was the second model proposed by de Vries,[102] which again suggested molecules were already tilted in the SmA phase. However, in this model, the molecules within the same layer are considered to be azimuthally disordered in the SmA phase, with no correlation in the tilt direction, and it was the random nature of the tilt directions that gave the diffuse cone model its name. In both these models, the SmC phase is composed of tilted molecules that possess a significant degree of azimuthal order, resulting in a phase where the tilt direction of molecules is highly correlated and exhibits a net tilt with respect to **k**. The non-correlation model and the random diffuse cone model both predict that the transition from the SmA phase into the SmC phase is a disorder-order transition of the azimuthal alignment, and the SmA phase in either case can be considered uniaxial. More recently, a model has been proposed by Domenici *et al*.[103] that shares many similar features to the random diffuse cone model. In this model, small molecular clusters form within the smectic layers that are azimuthally ordered. However, there is little correlation in tilt between different clusters of molecules, which results in a uniaxial SmA phase that is globally untilted. The experimental justification for this altered model of molecular order was the observation that

orientational order in the SmA phase increased significantly upon the application of a strong magnetic field.[103–105] This model was later supported by an NMR relaxometry study of the same lactate-based mesogen.[106]

Another model that has been proposed does not assume molecular tilt in the SmA phase, and instead predicts that the layer shrinkage typically observed at the SmA-SmC transition is wholly or partially offset by a shift in the average molecular conformation. This model states that the onset of molecular tilt is accompanied by a simultaneous increase in the effective length of molecules. Several mechanisms have been suggested that account for this increase in molecular length, the first indicating that the terminal chains adopt a different conformation with respect to the mesogenic core in the SmA and SmC phase.[103,107] Alternatively, it has been suggested that the gradual extension of the terminal chains themselves, resulting from the reduced temperature in the SmC phase relative to the SmA phase, can offset the layer contraction caused by tilt. This negative thermal expansion has been observed in recent studies of perfluorinated and siloxane-based de Vries materials performed by Merkel *et al*.[108,109]

A different model has been developed for nano-segregated systems such as semi-perfluorinated and silicon-containing compounds.[83,84] The layer thickness in any smectic liquid crystal is heavily influenced by the degree of interdigitation. This model proposes that the packing arrangement of molecules, which contain both flexible and rigid structural features, in adjacent layers may change as molecules tilt in the SmC phase.[110] A lack of layer shrinkage can then be explained by a simultaneous reduction in interdigitation between neighbouring smectic layers, causing an effective increase in the relative layer thickness that compensates for the tilt transition.

The models outlined above emphasise different aspects of the SmA-SmC transition, and all models provide reasonable explanations for de Vries character on a molecular and sub-molecular level. However, they all assume idealised cases in which only one effect impacts the layer thickness of the system. As a result, while these models provide an excellent indication of the types of factors that could influence the behaviour of the smectic layers, a more realistic explanation of anomalous reduction of layer shrinkage in de Vries materials can be reasonably expected to include aspects from multiple scenarios that contribute to the layer thickness in different ways.[78]

1.3.4 Design of de Vries Materials

Many studies have attempted to successfully synthesise new materials that exhibit some amount of de Vries character. Effective strategies have typically been those that focus on compounds containing one of several similar structural features, such as semi-perfluorinated,[84,111] polysiloxane,[83,112] polysilane,[113] and lactate[85,114] sub-units. The inclusion of these structural elements is reported to strongly promote the formation of smectic layers and the separation of rigid aromatic cores and flexible terminal chains into distinct chemical domains, and the combination of this nano-segregation

with low orientational order in the SmA phase is understood to increase a material's de Vries-like character.[115,116] Several investigations have aimed to design materials that integrate structural elements which promote the formation of the SmA phase with other features that promote the formation of the SmC phase. This design strategy is illustrated in a series of molecules that incorporate polysiloxane-terminated side chains and chloro-terminated side chains,[117,118] as well as in molecules that combine a polysilane chain with a 5-phenyl pyrimidine-based core.[113,119] Materials that exhibit significant de Vries character do not typically exhibit the material properties required for serious applications, leading some studies to focus on the design of de Vries mixtures that incorporate de Vries-like materials and conventional SmC liquid crystals, which allows the mixture's properties of interest to be tuned.[120]

1.4 Computational Methods

Computer simulations have become popular tools used in many academic areas of interest, and liquid crystal research is no different, with numerous theoretical methods readily utilised to study liquid-crystalline systems.[121] In comparison to other techniques, computational methods have a somewhat unique capacity to probe the behaviour of chemical systems with a sub-molecular level of detail, which cannot be easily matched by experimental observations alone. Typically, computational techniques can be classified as either quantum mechanical (QM) or molecular mechanical (MM), with QM methods based on approximate solutions to the Schrödinger equation and MM methods based on classical equations of motion.

1.4.1 Electronic Structure Calculations

Methods with their foundation in quantum mechanics allow for the prediction of chemical properties from first principles. A fundamental postulate of QM techniques is the idea that for any chemical system, there exists an associated wave function, ψ, that contains information about the observable properties of the system. The appropriate quantum mechanical operators, θ, when applied to the wave function, result in a value for the corresponding physical observable. This relationship is expressed in Equation (1.16), where θ denotes an operator and e is a value for a system property. In Equation (1.16), the application of the mathematical operator, θ, yields the same wave function multiplied by a constant, e, referred to as an eigenvalue equation. While this relationship holds, ψ may be referred to as an eigenfunction and e as an eigenvalue.[122,123]

$$\theta\psi = e\psi \tag{1.16}$$

In the eigenvalue equation associated with the energy of a chemical system, the operator in Equation (1.16) yields the eigenvalue for system energy, E, and the operator is referred to as the Hamiltonian operator. This equation, known as the time-independent Schrödinger equation, is shown in its simplified form in Equation (1.17):[122,123]

$$H\psi = E\psi \tag{1.17}$$

The general form of the time-independent Schrödinger equation accounts for numerous contributions to a systems total energy, such as the kinetic energy of the electrons and nuclei, the attractions of the electrons and the nuclei, and the repulsion as a result of interelectronic and internuclear interactions. The Hamiltonian operator is fully described in Equation (1.18), where *i* and *j* represent the electrons, *A* and *B* represent the nuclei, ħ denotes the reduced Planck's constant, i.e. Planck's constant divided by 2π, m_e is the electronic mass, m_A is the mass of nucleus *A*, ∇^2 is the Laplacian operator, *e* is the charge of an electron, Z_A is the atomic number of nucleus *A*, and r_{ln} represents the distance between two particles *l* and *n*.[122,123]

$$H = -\sum_i \frac{\hbar^2}{2m_e}\nabla_i^2 - \sum_A \frac{\hbar^2}{2m_A}\nabla_A^2 - \sum_i \sum_A \frac{e^Z Z_A}{r_{iA}} + \sum_{i>j} \frac{e^2}{r_{ij}} + \sum_{A>B} \frac{e^2 Z_A Z_B}{r_{AB}} \tag{1.18}$$

In Equation (1.18), the first two terms represent the kinetic energy of the electrons and nuclei in the system, respectively. The rest of the Hamiltonian is composed of terms that relate to the system's potential energy. Therefore, the final three terms account for the energy contributions as a result of the interactions between nuclei and electrons, electrons and other electrons, and nuclei and other nuclei, from left to right, respectively.

Exact solutions to the Schrödinger equation are not feasible for most chemical systems. Therefore, to simplify the problem, several common strategies are employed in determining solutions to the Schrödinger equation. For example, the form of the wavefunction may be restricted to those that are physically meaningful and are normalised. Additionally, the Pauli principle requires that the wave function representing electrons be anti-symmetric, with respect to the exchange of any two particles. This results in inversion of the sign of the wave function whenever the positions of two electrons are interchanged, as demonstrated in Equation (1.19):[123]

$$\psi(r_1, r_2, \dots) = -\psi(r_2, r_1, \dots) \tag{1.19}$$

To further simplify the calculation of the wave function, the Born-Oppenheimer approximation is regularly invoked, which allows the electronic and nuclear components on the wave function to be considered independently. This approximation asserts that since the nuclei are considerably more massive than the electrons, they move much more slowly than the electrons. In fact, electronic 'relaxations' may be considered instantaneous relative to the motions of the nuclei in the system. Consequently, the nuclear positions can be frozen, and a wave function can be calculated that depends only on the coordinates of the electrons. In this electronic Hamiltonian, H^{elec}, the second term in Equation (1.18) that considers the kinetic energy of the nuclei can be ignored, while the final term in Equation (1.18) reduces to a constant, dependent only on the charges of the nuclei and their now fixed distances from each other. With these constraints, the electronic Hamiltonian can be used

in the Schrödinger equation to acquire the electronic wave function, ψ^{elec}, which is determined by the positions of electrons (r), in a system of fixed nuclei (R), and its associated electronic energy, E^{elec}, as shown in Equation (1.20):[122,123]

$$H^{elec}\psi^{elec}(\mathrm{r},\mathrm{R}) = E^{elec}(\mathrm{R})\psi^{elec}(\mathrm{r},\mathrm{R}) \quad (1.20)$$

A potential issue with the calculation of this wave function appears as there are possibly infinite acceptable eigenfunctions that satisfy Equation (1.17), each resulting in a different associated eigenvalue, or energy, *E*. Fortunately, the variational principle can be used to determine many approximations to the energy by employing various trial wave functions. The variational principle means that the true wave function of a system in its ground state is that which results in the lowest associated energy. This allows the accuracy of a constructed wave function to be assessed through its associated energy, with a lower energy value representative of an improved description of the ground state system.[122,123]

In molecular orbital theory, the true wave function may be approximated as a combination of one-electron wave functions. This approach relies on the use of one or more Slater determinants, which satisfy the requirement for an antisymmetric function as well as the Pauli principle.[122,123]

In order to mathematically describe the one-electron wave functions, electronic structure calculations utilise a linear combination of basis functions referred to as a 'basis set', which defines how many of each function is used and their orbital exponents. These basis sets commonly rely on the use of atom-centred functions due to their computational efficiency and ease of calculation compared to the computation of Slater-type orbitals (STOs). For example, basis sets such as 6-311G (d) represent each one-electron wave function with six Gaussian functions for each core orbital, while valence orbitals are described by 3 basis functions comprising 3, 1 and 1 Gaussian functions each, with additional d-functions added to all non-hydrogen atoms. Basis sets that use this notation are referred to as Pople-type basis sets,[124] and are amongst the most widely used. With these basis sets, a wave function can be approximated as the combination of basic functions with corresponding coefficients that result in the minimum energy. However, whilst the approximations outlined here provide a means by which the Schrödinger equation can be nominally solved, the determination of the electron-electron repulsion term is particularly complex and necessitates further approximations to be made for multi-electron systems.

The Hartree-Fock (HF) method is one approach used to determine the wave function of a chemical system through approximation of the Schrödinger equation. Modern HF methods utilise matrix equations to calculate the minimum energy. These equations, developed independently by Roothaan and Hall,[125,126] may be represented in the form of a generalised eigenvalue problem, as shown in

Equation (1.21), where F is the Fock matrix, C is a matrix of molecular orbital coefficients, S is the overlap matrix of the basis functions, and ε refers the diagonal matrix of orbital energy values.

$$\mathrm{FC} = \mathrm{SC}\varepsilon \tag{1.21}$$

The Roothaan-Hall matrix equation must be solved self-consistently through the self-consistent field (SCF) procedure. When convergence criteria are met, the matrix equation's solution will produce *N* HF orbitals; however, only the lowest *N*/2 will be occupied with electrons, while the rest act as virtual or unoccupied orbitals.[123]

Although HF methods have had undoubted success, granting chemists the ability to model more complex molecular systems, the method is limited by several severe approximations. The most problematic approximation comes as a result of the disregard for electron correlation, which is not accounted for and can lead to significant deviations from experimental results. Furthermore, HF methods scale poorly with basis set and system size, meaning larger basis sets are challenging to utilise effectively.[122] Nevertheless, HF methods still find use today, and many of its weaknesses have been resolved in post-Hartree-Fock methods that build upon this general approach.[122,123]

One such post-Hartree-Fock method, which is widely applied in electronic structure calculations, attempts to account for correlation energy based on Møller-Plesset perturbation theory.[127] Specifically, second-order Møller-Plesset (MP2) calculations find extensive use as one of the simplest but most effective levels of theory beyond HF, and are utilised within the parameterisation work presented in this thesis. MP methods use the approximate solution to the Schrödinger equation produced by an HF calculation as a start point but then introduce a small perturbation that directly accounts for part of the electronic correlation, as illustrated in Equation (1.22), where H is the exact solution to the Hamiltonian eigenvalue problem, H_0 is the HF solution to the Hamiltonian eigenvalue problem, V is a small perturbation and λ is a dimensionless parameter.

$$H = H_0 + \lambda V \tag{1.22}$$

From this relation, the energy and wavefunction can be expanded as a power series in λ, as shown in Equations (1.23) and (1.24), in which E and Ψ are the exact energy and wavefunction, respectively, and $E^{(n)}$ and $\Psi^{(n)}$ are the nth-order expansion terms associated with the energy and wavefunction, respectively. Most relevant for this work, the zeroth-order, E_0, term corresponds to the base HF energy and in MP2 calculations the expansion series is truncated after the second-order, $\lambda^2 E^{(2)}$ term. Additionally, while MP3 and MP4 methods find occasional use, calculations that include higher order terms become increasingly complex, and hence their solution become computationally prohibitive.[128]

$$E = E^{(0)} + \lambda E^{(1)} + \lambda^2 E^{(2)} + \lambda^3 E^{(3)} + \cdots \tag{1.23}$$

$$E = \Psi^{(0)} + \lambda\Psi^{(1)} + \lambda^2\Psi^{(2)} + \lambda^3\Psi^{(3)} + \cdots \quad (1.24)$$

Electronic structure calculations with their foundation in density functional theory (DFT) provide an alternative to HF and post-HF methods. DFT is based on Hohenberg-Kohn theory, in which the energy and associated properties of a many-electron system may be determined from the probability distribution of the system's electron density. The utilisation of electron density, dependent on only three spatial coordinates, rather than the 3*N* coordinates of the wave function, means DFT remains computationally feasible even for large systems and at higher accuracies.[129] Additionally, just as with molecular orbital theory, the density of a system obeys the variational principle i.e. the true ground-state density of the system is equal to the input density that results in the lowest associated energy.

Further development of DFT by Kohn and Sham resulted in the Kohn-Sham (KS) method that resolves the difficulties associated with the calculation of kinetic energy in a system of interacting electrons, with the approximation of a system of non-interacting electrons. The energy functional in such a system can be divided into specific energy contributions, as shown in Equation (1.25), where E^{T} is the kinetic energy of electrons in a chemical system with an identical density as the real system; however, with no interelectronic interactions, E^{V} is the Coulombic interactions between electrons and nuclei, E^{J} is Coulombic interactions between only electrons, and E^{XC} is the exchange-correlation term, which includes the non-Coulombic electron-electron interactions.

$$E = E^{\mathrm{T}} + E^{V} + E^{\mathrm{J}} + E^{XC} \quad (1.25)$$

The KS orbitals that minimise the energy are determined by a comparable method to that implemented by HF theory, with E^{XC} described by a KS Slater determinant. In addition, the orbitals are similarly described by a combination of basis functions. However, while minimisation of the energy is performed in an analogous way to the HF methods, DFT is typically much more computationally efficient.[130]

Despite the success of DFT-based methods, they are limited by their treatment of the E^{XC} functional in Equation (1.25), for which an exact form does not exist. The E^{XC} is usually split into the individual exchange and correlation contributions and may be further divided into local functionals and non-local functionals. Numerous combinations of these exchange and correlation functions are utilised, and a DFT method may be characterised by the particular functions employed. This work uses the B3LYP functional, a combination of a Becke 3-parameter hybrid functional and the LYP correlation functional.[131,132]

Geometry optimisation allows for the prediction of minimum energy structures from electronic structure calculations, as the position of atoms in the structure may be adjusted until a stationary point is found on the potential energy surface. These geometry optimisation procedures can use numerous different algorithms that calculate the first derivative of the energy, i.e. the gradient, and can locate local energy minima, and in the case of transition structures, saddle points. This optimised structure can then be used to obtain further information about a chemical system. Additionally, mapping the energy while varying coordinates of interest provides a view of the associated energy landscape, from which the relative energy can be used to determine the expected molecular population adopting any state at any given time.[122,123]

1.4.2 Molecular Dynamics

Molecular dynamics (MD) simulations are a computer simulation method employed to model the dynamics of a chemical system. Alder and Wainwright first introduced the MD method in the 1950s,[133,134] but it was not until the early 1970s, with the simulation of liquid water, that MD simulations were applied to model realistic chemical systems.[135–137] MD relies on the ergodic principle, which states that the physical quantities of a dynamic system are equal to the statistical average values of the quantities over an infinite amount of time. In the specific case of a chemical system, the ergodic principle indicates that the evolution of an MD simulation can be used to determine information about the system, for example its macroscopic thermodynamic properties.

Unlike electronic structure calculations, which have their foundation in quantum mechanics, MD techniques are derived from classical mechanics, relying on numerically solving Newtonian equations of motion. The classical systems in MD methods are described by specifying the positions of all particles along with their associated momentum. This relationship between the position, q, and momentum, p, of a particle of mass, m, at times, t_1 and t_2, with acceleration, a, is expressed in Equations (1.26) and (1.27).[122]

$$q(t_2) = q(t_1) + \int_{t_1}^{t_2} \frac{p(t)}{m}\, dt \tag{1.26}$$

$$p(t_2) = p(t_1) + \int_{t_1}^{t_2} a(t)\, dt \tag{1.27}$$

Although these equations may be readily applied to simple systems such as a classical harmonic oscillator, it becomes impractical to apply them to more complex systems. Fortunately, Equations (1.26) and (1.27), relating to position and momentum, respectively, can be approximated as Equations (1.28) and (1.29), which utilise a finite time-step, Δt. These equations, given a set of initial

positions and momenta and a method for calculating the forces acting on each particle, allow a phase-space trajectory to be simulated.[122]

$$q(t + \Delta t) = q(t) + \frac{p(t)}{m} \Delta t \tag{1.28}$$

$$p(t + \Delta t) = p(t) + ma(t) \Delta t \tag{1.29}$$

Sophisticated integration schemes have been developed to deal with the propagation of trajectories. The Verlet method, introduced in 1967,[138] considers the sum of the Taylor expansions for forward and backwards time-steps Δt. In this sum, due to opposite signs, the odd-order derivatives of the Taylor expansion disappear. As a result, Equation (1.30) may be acquired by rearranging the sum of the expansions and cutting off after the second-order coefficient.

$$q(t + \Delta t) = 2q(t) - q(t - \Delta t) + a(t)(\Delta t^2) \tag{1.30}$$

The acceleration, *a*, of a particle can be only calculated by accounting for all the forces acting on that particle. As a result of the interactions between particles, these forces are defined by derivatives of the potential energy functions specified in the force field utilised by the simulation.

The Leap-Frog scheme is a similarly symplectic integrator that is employed in all the MD simulations presented in this thesis. While the Leap-Frog method produces trajectories that are identical to the Verlet algorithm, it differs as it utilises the positions, *q*, at time *t*, but utilises the velocities, v, at time $t - \frac{1}{2}\Delta t$. The positions and velocities are than updated from the calculated forces, F(*t*), at each timestep, with the relations expressed in Equations (1.31) and (1.32):[139]

$$\mathrm{v}\left(t + \frac{1}{2}\Delta t\right) = \mathrm{v}\left(t - \frac{1}{2}\Delta t\right) + \frac{\Delta t}{m}\mathrm{F}(t) \tag{1.31}$$

$$q(t + \Delta t) = q(t) + \Delta t \mathrm{v}(t + \frac{1}{2}\Delta t) \tag{1.32}$$

In all MD simulations, the interactions between particles are described by these potential energy functions. However, what defines a particle may not be consistent throughout all MD simulations. A crucial element of MD setup is choosing how the chemical system should be represented. Molecules and atoms can be described in a number of ways, with the best description for a system dependent on several factors such as available computational resources and the level of detail required to investigate the properties of interest. Coarse-grained methods typically provide the lowest resolution description of molecules, with whole molecules often represented by single particles or by chains of bead-like particles. At the other end of the scale, in fully atomistic MD simulations, every individual atom within a molecule is represented by a particle, providing the highest resolution representation

possible for MD. Finally, united atom methods represent atoms with a level of detail intermediate between that of coarse-grained and that of atomistic simulations. In united atom simulations, hydrogen atoms are often combined with heavier atoms, such that common functional groups such as methyl and methylene groups are represented as one particle. Generally, the higher resolution description used by an MD simulation, the more computationally expensive it becomes. Consequently, coarse-grain and united atom approaches are utilised to reduce the computation time scales required to produce a fully equilibrated system.[140,141]

For atomistic simulations, the potential functions are typically split into bonded terms and non-bonded terms. Bonded terms concern interactions involving chemically bonded particles, while non-bonded terms consider through-space interactions involving no chemical bonds, such as the interactions caused by two charges. In standard force fields, bonded interactions are generally defined to include bond stretching, bond angle bending and dihedral torsional potentials. Non-bonded interactions comprise Coulombic interactions between the assigned charges of particles and long-range attractive and short-range repulsive interactions between pairs of particles. Additionally, force fields such as COMPASS,[142] belonging to the series known as consistent force fields that have been adapted to study a broad variety of compounds, utilise additional cross-coupling terms that consider the interactions between multiple internal coordinates.

The terms outlined above comprise a force field's functional form, which contains all of the equations related to the potential energy of the system. The potential energy functions employed in standard force fields appear similar but are often subtly different. In order to model a system, the coefficients in these terms must be specified for each combination of particles present in the simulation. Many of these quantities can be accessed through experimental methods, but some such as dihedral force constants prove much more of a challenge to obtain. With this in mind, standard force fields frequently define these quantities for the most common groups of atoms, with one value typically used for many different atoms that are in similar chemical environments. The transferability of these atom-types allows force fields to be developed and simulations to be performed more efficiently than if these quantities had to be determined individually for every atom in every different molecule within a system. However, such transferability does have the potential to introduce errors through the improper assignment of some quantities. Nevertheless, these methods have been utilised in a vast array of MD simulations and have proved largely successful. Therefore, the assumption of transferability between different atoms in related chemical environments appears to be valid for many cases.[143] Still, the assignment of values to atoms and particles can be a complicated process, and several factors must be considered at once. Additionally, force fields are usually parameterised against experimental observables to increase their ability to model chemical systems accurately.

An MD simulation can be defined by the type of ensemble employed throughout, with the choice of ensemble determining which properties are fixed and which are allowed to fluctuate. The ensembles that are most commonly used include the canonical (*N*, *V*, *T*) ensemble in which the number of particles, signified by *N*, as well as the volume, *V*, and temperature, *T*, are fixed throughout the simulation, the microcanonical (*N*, *V*, *E*) ensemble in which temperature is allowed to vary, while the energy, *E*, of the system is kept constant, and the isothermal-isobaric (*N*, *P*, *T*) ensemble wherein the pressure and the temperature are static throughout the simulation. In the (*N*, *P*, *T*) ensemble, control over temperature and pressure is typically achieved through the use of a thermostat and barostat algorithm.[144] It is this isothermal-isobaric ensemble employed throughout this project as it is considered to provide the best representation of systems under experimental conditions. However, more generally the properties under investigation primarily determine the most suitable ensemble to use throughout an MD simulation.

Extended MD simulations provide an improved description of the system, and hence the associated statistical properties, but the appropriate time scale for a simulation may also be determined by limitations on computational time and resources. As a result, it is often necessary to ensure an adequate simulation time has been reached before any information about the system can be extracted. The evolution of an MD simulation requires the positions, momenta and forces acting on all particles to be periodically evaluated. The length of time between the evaluation of these quantities is referred to as the time-step. An appropriate choice of time-step is often considered to be a few orders of magnitude shorter than the fastest molecular motion, usually the bond stretching frequency.[122] However, the use of a longer time-step can be justified with the application of some constraints. For example, bonds can be restricted to their equilibrium length to reduce the necessary computation time for a given MD simulation.

The length of an MD simulation determines the time over which the chemical system can evolve, and an appropriate simulation length is largely defined by the time required for the system to adopt an equilibrated configuration. Interpreting when a system is suitably equilibrated is, therefore, an important aspect of simulation analysis, which can provide greater assurance that the measured properties are truly reflective of a relaxed system. The majority of MD simulations start from a state that is unrepresentative of an equilibrated configuration. As a result, the initial trajectory frames are frequently discarded to ensure that the mean values for properties of interest are not influenced excessively by the early system geometry. Many factors determine the optimal point at which the system can be considered equilibrated. For example, neglecting a substantial portion of the early trajectory reduces the impact of the unequilibrated initial system structure on the data, but increases the error associated with the measured values as less data is included in the estimate. Nevertheless, various procedures that aim to define system equilibration have been proposed, providing an efficient route to computing statistical properties from MD simulations.[145,146]

System size plays a central role in the computation time required to run an MD simulation: the larger the number of particles in a simulation, the more computationally intensive it is to complete. Although computer speeds have increased exponentially since the first MD simulations were carried out, the size of the average system is still small enough where the surface interactions at the boundary of the simulation box may well dominate the behaviour of the system. However, periodic boundary conditions can be employed to approximate a pseudo-infinite system, which overcomes many of the problems associated with system size constraints. With periodic boundary conditions, the simulation box is assumed to be an infinite number of identical unit cells in all directions, allowing the bulk properties of a system to be explored. Molecules located at the edge of the simulation box do not interact with the cell's surface; instead, they interact with molecules on the opposite side of the system through the walls of the simulation box. Although utilisation of periodic boundary conditions has been proven to work well for systems of sufficient size, the simulation box must remain large enough so that molecules cannot interact with their own image in any of the neighbouring boxes, as this can result in periodic artefacts. Nevertheless, these issues can be avoided with the use of adequate system sizes and the implementation of the appropriate cutoffs for non-bonded interactions.[122]

1.5 Liquid Crystal Simulations

1.5.1 Concept and History

In recent years, the use of computational methods has become increasingly popular within the field of liquid crystal research. The first attempts to simulate liquid crystals were reported in the mid-1980s, significantly later than the initial development of simulation techniques for molecular liquids,[147] due to the relatively long time scales and length scales necessary to effectively simulation mesogens and the slow equilibration required to probe many of their more interesting properties.[141] Although experimental studies have uncovered a significant amount of information about the mesoscopic and microscopic behaviour of liquid crystals, computational methods have a unique capacity to elucidate behaviours not easily accessible by laboratory-based techniques. The relentless growth of computational power over the years has led to great developments in simulation techniques applied to mesophases, with many different phases and equilibrium observables having been successfully reproduced.[141,148–150]

Various simulation techniques have been used to investigate liquid crystal phases, with Monte Carlo (MC) and MD simulation particularly common. MC methods rely on repeated random sampling techniques to simulate simple particle systems. These systems are typically composed of hard particles, such as spherocylinders or ellipsoids,[151,152] or may utilise Lennard-Jones and Gay-Berne models.[153,154] In comparison, MD techniques can be more computationally intensive but allow for the study of a system's dynamic properties. MD simulations employing coarse-grained, united atom and fully atomistic descriptions of mesogens have been used to elucidate many of the behaviours

associated with the liquid crystal phase.[141,150] Fully atomistic simulations, in which every atom is considered individually, provide the most detailed representation of phase structure and have significant potential to identify some of the underlying causes of complex mesophase behaviour. As a result, such simulations are particularly suited to these partially ordered phases, in which behaviour may be influenced by subtle interactions at both the molecular and sub-molecular levels.

1.5.2 Development of MD Simulations

As the use of computational methods to investigate liquid crystal systems has become more widespread, MD studies of thermotropic liquid crystals have aimed to replicate many of the experimental observables associated with the nematic phase, such as transition temperatures, densities, conformational dynamics and orientational order.[155–158] These early studies laid the foundation for more advanced simulation techniques that enabled reproduction of the odd-even effect,[159] prediction of EPR spectra,[160,161] investigation of the twist-bend nematic phase,[162] and simulation of guest-host systems.[163,164] In contrast, simulations of smectic phases were not initially as prevalent due to the impracticality of accurately modelling long-range translational order in relatively large systems over extended time scales, which required enormous computational resources. Hence, atomistic studies could provide only limited information on the structure and dynamics of lamellar systems.[165,166] However, since these early studies were performed, many factors have led to enhanced MD simulation techniques, such as improvements in force fields designed to model mesophases,[167,168] and increased CPU speeds, as well as GPU use, and the increasing prominence of efficient parallelisation methods.[169–171] These advances have enabled simulations containing a few thousand molecules to be performed, which has provided insight into the molecular origin of layer formation in smectic systems. As a result, more recent simulation studies of translationally ordered phases have reproduced various experimental observables,[172,173] investigated molecular packing within the smectic layers,[174] and demonstrated the influence of bulky terminal substituents on the formation of the smectic layer structure.[175] While such studies highlight the variety of liquid crystal systems that have been investigated using MD simulations, materials that exhibit de Vries character have yet to be studied in any significant detail, emphasised by the existence of only a single MD study, reporting on a coarse-grain investigation of de Vries-type smectics.

1.5.3 Force Fields and Force Field Parameterisation

The desire to more accurately reproduce experimental observables, such as transition temperatures, densities, as well as orientational and translational order parameters, has increased the requirement for more accurate atomistic force fields. As a consequence, many studies have become increasingly focused on the parameterisation and verification of force fields, with the application of both experimental and theoretical approaches.[155,176–179] Although many force fields aim to predict

experimental properties for a range of compounds, force fields that have been parameterised for accurate prediction of a specific family of molecules often perform poorly when applied to a different series of compounds. As a result, while general force fields are known to give less accurate predictions of absolute experimental values, they may be used to model experimental trends in a broader range of compounds, providing a means to assess their phase structure under simulated conditions.

A number of liquid crystal simulations have utilised force fields, such as OPLS[180] and the General Amber Force Field (GAFF),[181] providing insights into mesophase behaviour over various time and length scales. As a result, simulation studies employing such force fields are fairly well established within the literature, and clear benefits and drawbacks associated with the use of OPLS and GAFF for liquid crystals simulations have become apparent. For example, the OPLS force field was primarily developed to predict the properties of molecular liquids and solvents, but has also been applied to model partially ordered systems in studies of liquid crystal compounds.[157,167,182–185] These simulation studies have proved immensely valuable in the examination of certain mesophase properties, but have often been limited by the inaccuracy associated with the prediction of order parameters and transition temperatures when employing the OPLS force field.[167,182–184] Likewise, a few studies have utilised the GAFF force field to simulate liquid crystal compounds,[161] but this was shown to also overestimate the temperature at which the isotropic-nematic and nematic-smectic A phase transitions occur. The failure of default force fields to accurately predict key elements of phase behaviour has led to several efforts to develop optimised force field parameters that are much more suited to simulation of liquid-crystalline materials. In one study, an optimised AMBER-like united atom force field was developed specifically for realistic replication of transition temperatures through optimisation of the Lennard-Jones parameters.[156,158] More recently, a study performed by Boyd and Wilson,[168] has focused on optimisation of the GAFF force field, reporting on a fully atomistic force field that includes refined parameters for liquid crystal molecules. The parameters outlined in this report, in addition to a second study by the same authors,[186] have been shown to more successfully reproduce number of important physical properties of liquid-crystalline materials. The modified GAFF force field, therefore, provides a balance between the precision of bespoke force fields and the transferability of force fields employing general parameters for use in liquid crystal systems. Due to these advantages, this optimised GAFF force field was used throughout the work reported on in this thesis, employing the functional form as expressed in Equation 1.33.

$$E_{pair} = \sum_{bonds} K_r(r - r_{eq})^2 + \sum_{angles} K_\theta(\theta - \theta_{eq})^2 + \sum_{dihedrals} \frac{V_n}{2}[1 + \cos(n\varphi - \gamma)] + \sum_{i<j}[\frac{A_{ij}}{R_{ij}^{12}} - \frac{B_{ij}}{R_{ij}^{6}} + \frac{q_i q_j}{\varepsilon R_{ij}}] \quad (1.33)$$

Here, r_{eq} and θ_{eq} are the equilibrated bond length and bend angle, respectively; K_r, K_θ, V_n are force constants; n is multiplicity and γ is the phase angle for torsional angle parameters. The *A*, *B* and *q* parameters characterise the non-bonded potentials.

1.6 Aims

A set of three rod-like liquid crystal materials formed the basis of this work reported in this thesis. These three compounds, despite their very different chemical structures, are reported to exhibit de Vries behaviour, i.e. minimal layer shrinkage at the SmA-SmC transition.

The overall aim of the project was to apply suitable computational methods to these compounds in order to rationalise their behaviour, gaining an insight into their mesophase properties. The objective was to elucidate the structure-property relationships of these compounds, exploring the fundamental features, which lead to de Vries behaviour, and in a wider context, provide insights that could aid in the design of new de Vries materials intended for electro-optic device applications.

A further aim was to assess the ability of MD simulations to accurately capture subtle properties of smectic liquid crystals, which may arise from the complex interplay between many competing factors. Chapter 4 of this thesis focuses on the parametrisation of perfluoropolyether- and trisiloxane-based compounds for use in standard force fields. The aim of this work was to study the capacity of the GAFF force field to correctly reproduce the key characteristics of these materials, particularly focusing on their bonded parameters.

The optimised parameters from Chapter 4 are then applied in Chapters 5 and 6, probing their ability to predict key mesophase properties, such as orientational and translational order, tilt and layer spacing, as well as investigate de Vries behaviour. Finally, Chapter 7 draws conclusion from the entire project as a whole and outlines potential future work.

Chapter 2 – Experimental

This chapter offers a summary of the methods utilised throughout this thesis, and provides more in-depth information on frequently used software, computational techniques, and simulation parameters. The computational methods and software packages used to perform this work are outlined in the first section, in addition to details associated with MD simulation setup. The scale-up method that enabled the construction of the ultimate 1024-molecule systems from the initial disordered 16-molecule systems is also described. The second section focuses on simulation analysis, and reports on the tools used to obtain the data from each simulation, as well as the software used to analyse the equilibrated phases.

2.1 Computational Methods

2.1.1 Electronic Structure Calculations

The *ab initio* calculations described in this thesis were performed using DFT and MP2 methods and carried out within the Gaussian 09 software package.[187]

DFT geometry optimisations yielding low energy structures of 9HL, 3M 8422 and TSiKN65 employed the B3LYP functional,[188,189] while the basis set used in each case is stated within the individual chapters. The potential energy scans and optimisations described in the parameterisation section of this thesis also utilised the DFT method with the B3LYP functional, and used basis sets at the 6-31G(d) and 6-311G(d,p) for 3M 8422 and TSiKN65, respectively. Single point energy calculations performed on the structures output at each frame of each potential energy scan were carried out the MP2 level of theory,[190] and made use of identical basis sets to those described above for the perfluoropolyether- and siloxane-based molecular fragments, respectively.

2.1.2 MD Simulations

All MD simulations were performed at a fully atomistic level within the GROMACS 5.1.2 software package,[191–196] in combination with the General Amber Force Field,[181] with modified parameters more suitable for simulations of liquid crystal systems,[168,186] except where stated otherwise in the main text. Partial charges for all atoms within each simulated compound were obtained from the lowest energy structures by employing the RESP method,[197] except for in those cases indicated in the main text.

MD simulations were performed using a 2 fs time step and 3-dimensional periodic boundary conditions, while all bond lengths were constrained at their equilibrium value by the LINCS algorithm.[198] The particle mesh Ewald method enabled the calculation of electrostatic interactions,[199] which were cut-off after 1.2 nm. Similarly, short range van der Waals interactions were truncated after 1.2 nm. Except were discussed below, temperature control was achieved by employing a Nosé-Hoover thermostat,[200,201] while a pressure of 1 bar was maintained with a Parrinello-Rahman

barostat.[202] isotropic pressure coupling was preferred for the 16- and 128-molecule systems due to the small number of molecules in these systems, but this was replaced by an anisotropic pressure coupling for 1024-molecule systems to allow the relative dimensions of the periodic box to vary throughout the final simulations.

For all compounds, the initial simulation boxes were constructed via a 4 × 2 × 2 replication procedure, producing a cubic lattice of 16 molecules packed in a random head-tail orientation. In all cases, an isotropic geometry was obtained from an *NPT* simulation, performed at nominal elevated temperature and pressure, specifically 340-500 K and 500-5000 bar, depending on how rapidly order was lost in each system. In each case the specific values were chosen to ensure the compression was sufficiently slow to allow the artificial order present within the 16-molecule lattice to be fully lost before the system reached a stable liquid density. The isotropic system produced by this compression provided a suitably unbiased structure, from which subsequent simulations could be carried out.

All of the MD simulations studied in this thesis were equilibrated using a scale-up method, introduced in an effort to decrease the simulation time required to produce a stable phase structure. Starting from the isotropic configuration described above, MD simulations were performed at various regularly interspaced temperatures. The initial 16 molecule systems were equilibrated for an appropriate time to allow for the development of a phase that exhibited partial orientational order. After this, the 16 molecule systems were scaled up to 128 molecules by way of a two-fold replication of the simulation box in three dimensions. The 128 molecule systems then underwent a similarly lengthy equilibration to ensure that any potential simulation artefacts introduced by the replication procedure were minimised, after which the system was subjected to a second two-fold replication, which provided the initial systems for the full MD simulations. The 1024 molecule simulations were run until the phase structure, characterised through assessment of the orientational and translational order parameters, was considered to be fully equilibrated. Equilibration was determined in an unbiased, quantitative fashion, as described in the following section.

2.2 Data analysis and Processing

For all simulations, the point at which the phase was adjudged to be equilibrated was calculated using a procedure described by Chodera,[146] which insured that the optimal amount of initial data was discarded before evaluating average values and their associated errors. Throughout all of this work, averages and errors were calculated using a 95% confidence interval.

In all simulations, the orientational order parameter, P_2, and the director, **n**, were calculated at each trajectory frame in a way that maintained consistency with previous studies.[156–158] In each case, the axes utilised in the calculation of these order parameters were determined from the minimum moment of inertia (MOI) of either the whole molecule or the aromatic core, with the specifics discussed further in the main text of individual chapters. Similarly, the translational order parameter, τ,

determined for each simulated phase was calculated by employing a method described in several published studies.[158,175]

In each simulation, the calculation of the layer normal, **k**, was achieved through determination of a local layer normal for every molecular reference position, *i*, before the associated ordering tensor was diagonalised, in accordance with reported literature.[203,204] The layer thickness, *d*, was determined as the distance between the maximum density fluctuations of the molecular reference positions, parallel to the layer normal vector. The atom defined as the centre of each molecule was chosen based on its position within the aromatic core structure and is stated specifically for each of the compounds in the chapters below.

Throughout the force constant parameterisation described in Chapter 4 of this thesis, both angle and torsional parameters in all molecular fragments were fitted using the statistical software, *R*.[205] For a number of angles and dihedrals, stated in the main text, a weighted fit was employed in an effort to achieve an improved accuracy in areas of the potential where the relative energy was lowest. The weighting procedure involved the calculation of a Boltzmann distribution at 298 K for each angle and dihedral undergoing parameterisation, while a minimum weighting of 1×10^{-4} was used to maintain a suitable accuracy at high relative energy values.

All visual inspection of molecular conformations and phase structures was achieved by loading the coordinate files and MD trajectories output from the MD simulations performed in this work into the VMD v1.9.3 software.[206]

Chapter 3 – Molecular Dynamics Study of Lactate-Based 9HL

The work reported in this chapter focuses on the MD study of the chiral (S)-hexyl lactate derivative, 9HL. The MD simulation techniques employed throughout the investigation are described, while the analysis performed on the simulated phase of 9HL is also reported. The calculated order parameters, tilt angles and layer spacings are discussed, and comparisons are made to those obtained from experimental investigations of 9HL reported in the literature. All further analysis is also discussed, in which the molecular behaviour of 9HL is assessed over a wide simulated temperature range, and the overall smectic layer structure is characterised. The results of these analyses are interpreted and rationalised with regard to the observed reduction in layer shrinkage, relative to that expected from the rigid-rod model.

3.1 Introduction

This section sets out to briefly introduce the MD simulation techniques relevant to the work reported within this chapter. At the same time, it intends to provide a summary of previous research related to the MD simulation of liquid crystal systems. Ferroelectric liquid crystals are also discussed, with particular focus on the lactate-based mesogen 9HL, which is reported to exhibit de Vries character. A number of experimental studies of 9HL, and their efforts to rationalise its de Vries behaviour, are subsequently reviewed. Finally, the aims of the work presented in this chapter are outlined.

3.1.1 Molecular Dynamics Studies of Liquid Crystals

As introduced in Chapter 1, MD simulations, with their foundation in the classical equations of motion, enable complex material characteristics to be studied across various time and length scales. In MD simulations, the positions and velocities of particles are determined via numerical solutions to the Newtonian equations of motion over discrete time frames, allowing a system's evolution to be modelled with reasonable accuracy. MD techniques are less computationally intensive than *ab initio* and DFT methods, which rely on the determination of a system's electronic structure from the Schrödinger equations. As a result, MD simulations have the capacity to study molecular systems that contain thousands of particles. This ability to model relatively sizable systems means MD simulations are a particularly useful technique in the study of soft materials, such as liquid crystals, in which macroscopic phase behaviour is determined by interactions between a significant number of molecules.

MD simulations of liquid crystals have become much more abundant, in recent years, driven primarily by ever-increasing computer speeds and a greater accessibility to parallel computing systems. Numerous MD simulations have aimed to replicate liquid crystal properties, many of which result from the interactions of molecules in the bulk phase, requiring large system sizes. Additionally, a relatively large number of molecules are often necessary to prevent boundary effects influencing system properties, and to avoid the emergence of artefacts when employing periodic boundary

conditions. The progress of molecular simulations of liquid crystals has also undoubtedly benefited from the development of different molecular models, which has led to a variety of research focused on applying these methods to liquid crystal phases.[141,207] This introductory section aims to briefly summarise the application of MD techniques to liquid crystal systems.

MD simulations have the capacity to model liquid crystal systems at various levels of detail, with the most appropriate simulation method often dictated by the liquid crystal properties under investigation and the available computational resources. Many studies have employed coarse-grained simulation techniques that represent individual molecules as hard particles, such as spherocylinders or ellipsoids, and utilise a variety of interaction potentials.[141,148] The simplest coarse-grained models account for only repulsive interactions between molecules, yet they have still shown the ability to form stable liquid-crystalline phases, playing an important role in studying the influence of molecule shape on mesophase formation. More sophisticated potentials, which consider attractive as well as repulsive contributions to the system energy, may be used to model temperature-dependent mesophase phenomena. One such example is the Gay-Berne potential, which has become somewhat of a standard model for coarse-grained simulation of liquid-crystalline phases.[141] These hard-particle models have successfully replicated a broad range of experimentally observed liquid crystal phases, and have also shown the capacity to exhibit hypothesised mesophases, which have yet to be confirmed through experimental studies. This ability to investigate many of the underlying causes of mesophase behaviour with significantly reduced computational expense, relative to higher resolution MD techniques, makes coarse-grained approaches worthwhile to test theoretical models that attempt to capture mesophase behaviour, and in cases where the properties of interest necessitate the simulation of a particularly large system.

Compared to coarse-grained techniques that operate using a highly generalised description of molecules as hard particles, united atom (UA) methods provide a more faithful representation of real chemical systems. In UA simulations, individual atoms are not treated explicitly, but groups of atoms are instead combined into single interaction sites, where appropriate, enabling shorter simulation times than methods that represent all atoms independently. These UA methods are particularly prevalent in liquid crystal simulations, as such simplifications allow for significantly reduced simulation times in systems comprising large liquid crystal compounds. One of the many advantages offered by UA approaches over lower resolution representations is the capacity to study specific chemical features and the ability to assess their contribution to overall liquid crystal phase character.

Many MD simulations employing UA approaches have focused on the replication of experimental observables in nematic liquid crystals. Such MD simulations have most often centred on the *n*-cyanobiphenyl series of compounds due, in part, to a large amount of published experimental research available on these mesogens. Early UA simulations on cyanobiphenyl compounds were

typically performed with standard force fields, which adopt parameters derived from small organic compounds. Although these simulations successfully reproduced several experimentally observed liquid crystal phases, they also predicted phase transition temperatures and order parameters significantly higher than those observed experimentally.[208–210] These issues associated with standard force field parameters were investigated in a more recent study, which reported that more realistic phase transition temperatures could be obtained by adjusting the Lennard-Jones parameters in the AMBER force field.[156] MD simulation studies employing these optimised parameters have since shown the capacity to reproduce the nematic and smectic phases of 8CB and predict their associated properties with reasonable accuracy.[158]

Despite the undoubted success of coarse-grained and UA techniques in studying liquid crystal behaviour, fully atomistic approaches are frequently preferred due to their ability to provide the most detailed description of mesophases accessible while employing purely MM-based methods. Although a lack of computer power made early atomistic simulations a challenge, these studies offered several valuable insights into the development of orientational order in nematic phases.[211,212] For similar reasons to UA simulations, a significant proportion of more recent atomistic studies have focused on cyanophenyl-based compounds. Several of these investigations have demonstrated the capability of atomistic simulations to form thermodynamically stable liquid-crystalline phases from an initial isotropic geometry.[212] fully atomistic studies have also successfully replicated specific properties, such as rotational viscosities,[213] flexoelectric coefficients[183] and dihedral conformations.[159] In addition, the unique capacity of atomistic models to probe certain intermolecular interactions was highlighted in an investigation concerned with the effects of hydrogen bonding on the local layer structure of nematic liquid crystals.[214] The fully atomistic simulation of the liquid crystal mixture, E7, has also been reported, from which individual dipole correlations and the order parameters of individual components, not accessible experimentally, have been calculated.[157] A set of more recent studies have focused on fully atomistic simulations employing the GAFF force field, reporting a drastic improvement in transition temperature predictions by optimising the force field parameters.[168,186] These studies outline the remarkable progress of fully atomistic simulations as a means of modelling liquid-crystalline phases, and despite the relatively simulation times associated with atomistic simulations, the rapid advances in computational speeds and availability have made atomistic simulations increasingly appealing for the simulation of liquid crystal systems.

3.1.2 Molecular Dynamics Studies of de Vries Materials

Even with the recent advancements in MD simulations of liquid-crystalline phases, materials that exhibit minimal layer shrinkage at the SmA-SmC transition have not been significantly studied through computational methods. The extent of the research related to the application of computational techniques to 'de Vries-type' systems appears to be limited to a single coarse-grained study performed by Jenz *et al*. in 2016.[215] In this investigation, three SmA phases with distinct

orientational distribution functions were simulated before 2D diffraction patterns were calculated upon equilibration of each SmA phase. The possibility of distinguishing between the SmA orientational distribution functions was then studied by comparing the 2D diffraction patterns. Despite this work, materials that exhibit de Vries behaviour could undoubtedly benefit from further investigation by applying computational techniques. One area of interest is the capability of fully atomistic MD simulations to replicate the reduction in layer contraction of an experimentally confirmed de Vries material.

A possible explanation for the apparent lack of reported research related to *in silico* studies of de Vries compounds could be the inherent difficulty associated with accurately modelling materials comprising non-standard structural elements. MD simulations of liquid-crystalline systems typically rely on the atom types defined in standard force fields, which are parameterised to describe the properties of various small non-liquid-crystalline molecules. The use of standard force field parameters presents a potential problem as materials reported to exhibit de Vries character frequently include structural elements such as perfluorinated,[84,111] polysiloxane[83,216,217] and polysilane[110,113,218] chains, the chemical properties of which many molecular mechanics force fields may be unable to accurately model due to an absence of appropriate atom types. As a result, compounds comprising more conventional structural elements are typically the most suitable simulation targets as they are less likely to require significant force field parameterisation. With this in mind, it is notable that several lactate-based ferroelectric liquid crystals have been reported to exhibit considerable de Vries character.[85,114] Such lactate derivatives may well provide suitable simulation targets for an MD study centred on the rationalisation of de Vries behaviour.

3.1.3 Development of Lactate-Based FLCs

Ferroelectric liquid crystals (FLCs) have attracted considerable interest due to their potential for use in electro-optic devices capable of sub-microsecond response times.[50] However, since their initial proposal, several problems related to fundamental device operation have become apparent. While the primary issue associated with FLC devices results from the contraction of smectic layers typically observed at the SmA-SmC transition,[78] the relatively high temperatures at which the ferroelectric SmC* phase generally occurs have led to difficulties associated with the manufacture of devices. As a result, a considerable amount of research has focused on the synthesis of compounds that exhibit the SmC* phase at lower temperatures, typically around 298 K. One strategy commonly employed to lower the temperature at which a liquid crystal phase is expressed involves increasing the flexibility of the mesogenic core through the introduction of specific linking groups. For example, the inclusion of ester linkages in the polarisable core significantly reduces rigidity, making compounds of this structure potentially appealing targets for chemical investigations. In one such study, several new series of lactate-based ferroelectric liquid crystal compounds, all possessing a polarisable core composed of phenyl benzoate groups and four ester linkages, were synthesised by

Kaspar *et al*. in 1998.[219] This study found that a majority of the synthesised compounds exhibited the SmA and SmC* phases over an extended temperature range and at significantly lower temperatures than typically observed in FLC materials.

3.1.4 Experimental Investigations of 9HL

Various experimental techniques have been employed to study the mesophase behaviour of the (S)-hexyl lactate derivative, 9HL. While the *n*HL series of compounds, of which 9HL is included, were initially reported on in 1998, by Kaspar *et al*.,[219] the first study to examine the de Vries behaviour displayed by 9HL was carried out by Giesselmann *et al*., in 1999.[85] In this work, the phase behaviour exhibited by 9HL near the SmA-SmC* transition was characterised, with results of x-ray diffraction indicating that the observed layer shrinkage upon transition to the SmC* phase was significantly less than the reduction in layer thickness predicted by the rigid-rod model, calculated with the equation $d_C = d_A\cos(\theta)$. the same study also reported on the electric field dependence of the optical tilt in 9HL, demonstrating that a considerable tilt angle could be induced in the SmA phase upon application of even a weak electric field. This investigation concluded that the electric field dependence was likely a consequence of the minimal layer shrinkage associated with the tilt transition in 9HL, which resulted in significantly less resistance to molecular tilt fluctuations, and hence a noticeably large electroclinic response in the SmA phase.

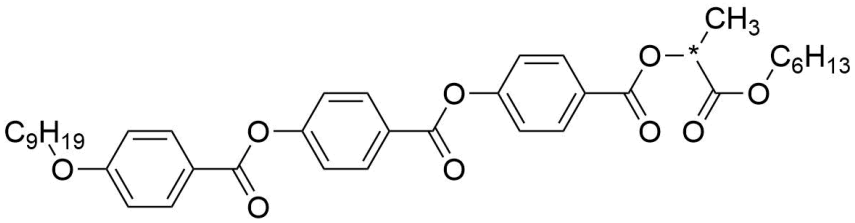

Figure 3.1 The chemical structure of the compound 9HL (Cr 41.0°C SmC* 67.2°C SmA* 134.6°C I).[219]

A second study, carried out by Krueger *et al*.,[98] examined the behaviour of 9HL molecules, as well as several other FLC compounds, at the SmA-SmC* transition through dielectric spectroscopy. In this study, the dielectric absorption spectrum of 9HL was noted to be significantly different from that of a common FLC, displaying a considerably larger soft mode absorption at the SmA-SmC* transition. This soft mode, corresponding to fluctuations of the tilt angle, was shown to be particularly pronounced in materials that exhibit a smaller layer shrinkage upon transition to the SmC* phase, such as 9HL. The study concluded that the large tilt fluctuations in the SmA phase, consistent with the observed electroclinic response discussed previously, were likely due to a decoupling of the tilt angle from variations of the smectic layer thickness in de Vries materials.

Another study that has attempted to assess the de Vries character exhibited by 9HL was reported by Sanchez-Castillo *et al*.,[87] and utilised polarised Raman spectroscopy and x-ray diffraction to probe the orientational order in the SmA and SmC* phases. In this study, the orientational order parameters,

P_2 and P_4, determined from the experimental techniques mentioned above, were found to differ significantly from each other. This discrepancy in the order parameters was proposed to be due to differences between the two techniques, as each probe the orientational distributions of different axes within the molecule. Nevertheless, both the reported Raman spectroscopy and x-ray diffraction results corresponded to a 'sugarloaf-like' orientational distribution in the SmA phase, exhibiting no apparent differences from a conventional SmA phase. The translational order parameter, derived from x-ray diffraction data, was also calculated across the SmA phase. From these results, it was observed that some sections of the 9HL molecule might exhibit high orientational and high translational order, but other sections may be more weakly orientationally ordered. However, while this lack of uniform behaviour may impact the overall smectic layer structure, it was concluded that the role of such individual molecular sub-units in the promotion of de Vries behaviour could not be entirely rationalised.

A series of studies on the ferroelectric liquid crystal 9HL have also been published that have examined liquid crystal phase behaviour through the application of NMR spectroscopy.[103–106] The first of these studies, carried out by Marchetti *et al*.,[104] centred on the measurement of molecular tilt in both the SmA and SmC* phases of 9HL at various magnetic field strengths. In this study, the orientational order was determined for a deuterated phenyl group within the core of 9HL, while the tilt of this same group was obtained directly from ^{2}H NMR measurements. The results of the NMR analysis indicated that 9HL molecules are tilted in the SmA phase, and the change in tilt angle at the SmA-SmC* transition is likely due to a shift in molecular conformation. In addition, an observed increase in orientational order near the SmA-SmC* transition at higher field strengths was proposed to be caused by the alignment of local clusters of tilted molecules that possess the same azimuthal angle. An extension of this study was reported by Domenici *et al*.,[105] which also found that molecules exhibited a slight tilt even in the SmA phase. Likewise, measurements of orientational order at additional magnetic field strengths were consistent with the previous study, supporting the presence of clusters of tilted molecules.

Another NMR study of 9HL was later reported by Domenici *et al*.,[103] in which ^{13}C NMR was used to probe the conformational and orientational properties of 9HL. In this study, the orientational order parameter was determined for all three phenyl groups in the aromatic core of 9HL, with values consistent with the previous two studies. A small molecular tilt was also measured for all three phenyl groups in the SmA phase, while the group closest to the lactate unit was observed to be significantly more tilted than the other two phenyl groups in the SmC* phase. The authors proposed that this observation was likely due to a conformational change near the SmA-SmC* transition. At the same time, they also indicated that the molecular behaviour of 9HL could be explained through a combination of the 'clustered diffuse cone' model and a conformational shift upon transition to the SmC* phase.

A final NMR-based study performed by Gradišek *et al*.,[106] investigated proton NMR spin-lattice relaxation in 9HL. In this study, the dynamic properties of 9HL molecules near the SmA-SmC* transition were explored by analysing several frequencies related to different molecular motions. The results indicated that frequency contributions from tilt angle fluctuations deviated significantly from that of a conventional FLC. The investigation concluded that the presence of small clusters of tilted molecules could explain the increased contribution from these tilt director fluctuations in the SmA phase, consistent with models proposed in the previous NMR studies.

The experimental studies outlined above provide a number of valuable insights into the phase behaviour of 9HL, with results derived from different experimental techniques largely consistent with one another. Most significantly, the results of several x-ray diffraction experiments indicate that the layer contraction observed in 9HL is substantially reduced relative to that expected from the tilt measured in the SmC* phase.[85,220] This minimal shift in the smectic layer thickness is further supported by dielectric spectroscopy studies,[85,98] which propose that the exceptionally high soft mode absorption exhibited by 9HL results from the decoupling of molecular tilt fluctuations and layer spacing. Several studies have focused on exploring the rationale for de Vries behaviour in 9HL, employing a wide array of experimental techniques, and the determination of orientational order parameters in such studies has provided a clearer view of dominant molecular conformations and associations within the SmA and SmC* phases. In these reports, Raman spectroscopy and x-ray diffraction techniques have been utilised to probe the orientational distribution exhibited by 9HL in the SmA phase, described as a broad 'sugar loaf' distribution comparable to that exhibited by conventional smectic materials.[87] In contrast, orientational analysis in a series of studies that centre on NMR spectroscopy has provided evidence that clusters of tilted molecules exist within the SmA phase, and it is these clusters that become azimuthally ordered upon transition to the SmC* phase.[103–106] Such inconsistencies between experimental studies are perhaps predictable due to the fundamental differences between the techniques themselves, but nevertheless highlight the value of complementary techniques, which enable a more complete examination of phase behaviour. In the specific case of 9HL, while some experimental studies appear to be contradictory, more generally the results of x-ray diffraction, dielectric spectroscopy, and NMR analysis indicate that 9HL displays a number of behaviours uncharacteristic of a conventional smectic liquid crystal. As a result, 9HL makes an appealing target for novel investigations into the de Vries character exhibited by various liquid crystal compounds.

3.2 Aims

The overall aim of the work presented in this chapter was to investigate the de Vries character of the (S)-hexyl lactate derivative 9HL, shown in Figure 3.1, through the application of MD simulation techniques. The initial objective was to successfully model the SmA and SmC* phases of 9HL starting from an initial isotropic geometry before quantifying important properties such as

orientational and translational order upon equilibration of these systems. The goal was then to explore the capacity of MD simulations to capture complex mesophase behaviour, such as the anomalous reduction in layer contraction at the SmA-SmC* transition, reported to be exhibited by 9HL.

If successful in this pursuit, a further aim was to assess the individual contributions to the de Vries character exhibited by 9HL simulations on a molecular and sub-molecular level. The intention was to compare the results of this analysis to several of the established models that have been proposed in the literature to account for the behaviour of de Vries materials. A broader aim was to provide further insight into de Vries character more generally that could prove beneficial to future studies focused on de Vries materials.

3.3 Results and Discussion

Input structures for the 9HL molecules used in the initial system set-up were derived from DFT optimisations at the B3LYP/6-31G(d) level. Four geometry optimisations were performed from different initial structures in an effort to establish the lowest energy conformation of 9HL. This lowest energy geometry, corresponding to conformer 4 in Figure 3.2 and Table 3.1, was then used to construct a 16-molecule cubic simulation box, comprising a 4 × 2 × 2 lattice of parallel molecules arranged in a random head-tail orientation.

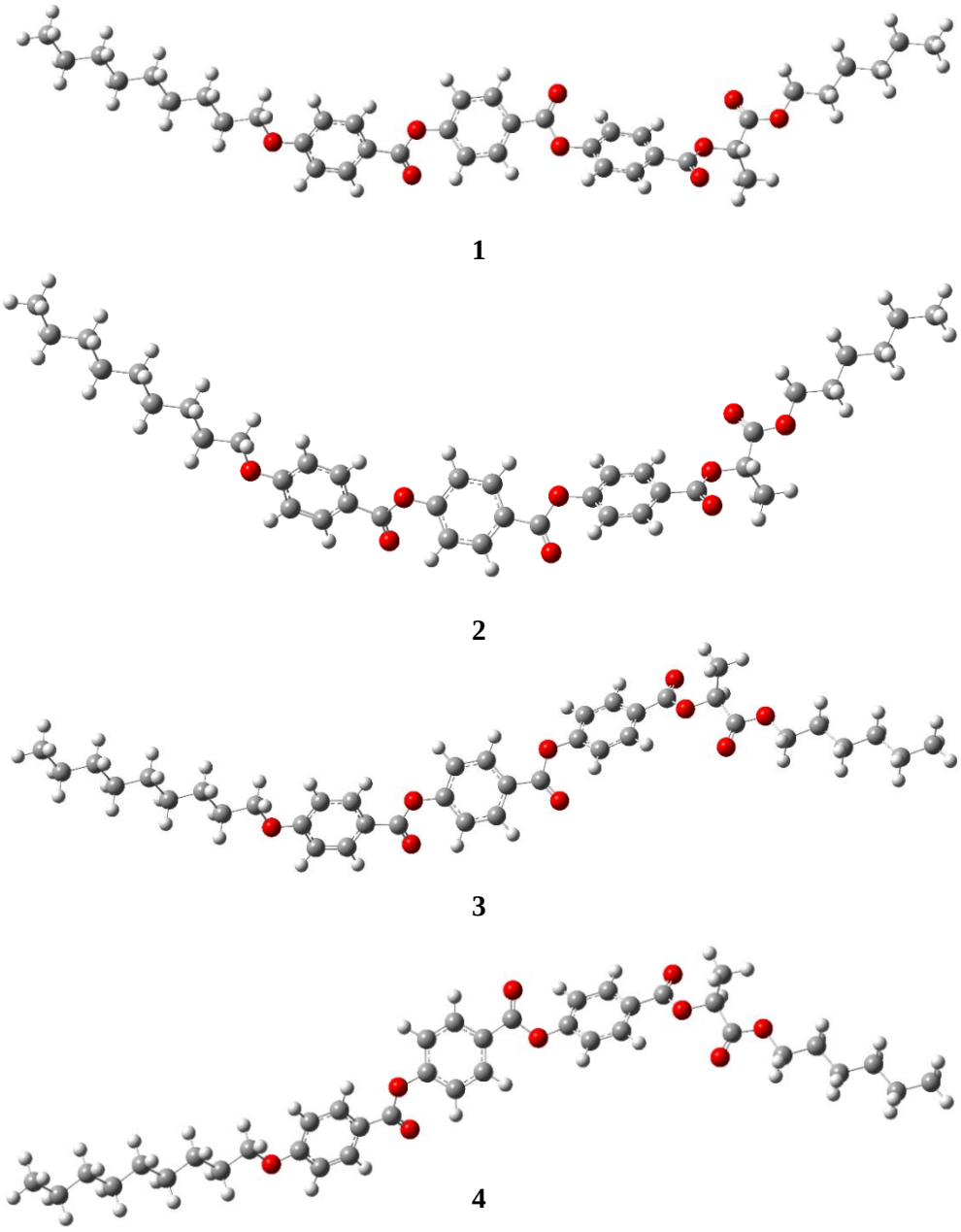

Figure 3.2 The four optimised conformers of 9HL, calculated at the B3LYP/6-31G(d) level

Table 3.1 Energies of the four 9HL conformers calculated at the B3LYP/6-31G(d) level

Conformer	E / Ha	ΔE / kJ mol^{-1}
1	-2192.16583195	0.416
2	-2192.16586777	0.322
3	-2192.16569003	0.789
4	-2192.16599035	0.000

For the MD simulations presented in this chapter, equilibration time corresponded to a minimum simulation time of 500 ns and a maximum simulation time of 800 ns, and it is these equilibrated systems from which the subsequent results are obtained.

Fully atomistic MD simulations were performed on systems of pure 9HL at 10 K intervals between 330 K and 400 K. This simulated temperature range is consistent with the experimentally observed SmA and SmC* phase ranges of 9HL and offers several data points on both sides of the experimentally determined SmA-SmC* transition temperature ($T_{A\text{-}C}$) of 337-346 K.[85,98,219] The analysis carried out on these systems is presented in the sections below, with particular emphasis on the determination of order parameters and quantification of de Vries character. Furthermore, the section below also considers the possible causes of any observed reduction in layer contraction exhibited by the simulated 9HL systems.

3.3.1 Determination of Order Parameters

As orientational order is a fundamental character of liquid crystal phases, its development provides a key indicator of mesophase formation in MD simulations. In this work, orientational order was confirmed at all simulated temperatures, evident from the calculated P_2 values, plotted in Figure 3.3, which show a gradual decrease in the orientational order as the temperature increases. The P_2 values of 0.80-0.85 in the simulated phases match closely with the experimentally reported values of 0.80-0.85, determined from birefringence measurements and polarised Raman spectroscopy,[87] while they are only slightly higher than values of *ca*. 0.70-0.80 obtained from ^{2}H NMR spectroscopy.[103,104] The simulated P_2 values appear substantially higher than the reported values of *ca*. 0.60 derived from x-ray scattering experiments, but these values are reported to be underestimated due to the influence of small molecular associations which have varying orientations within the phase. Accordingly, the simulated P_2 values are much more consistent with the rescaled values of *ca*. 0.80 derived from the same x-ray experimental data.[87] For the data in Figure 3.3, P_2 values were determined using the principle molecular axis, defined as that calculated from the minimum MOI axis of the 9HL molecule.

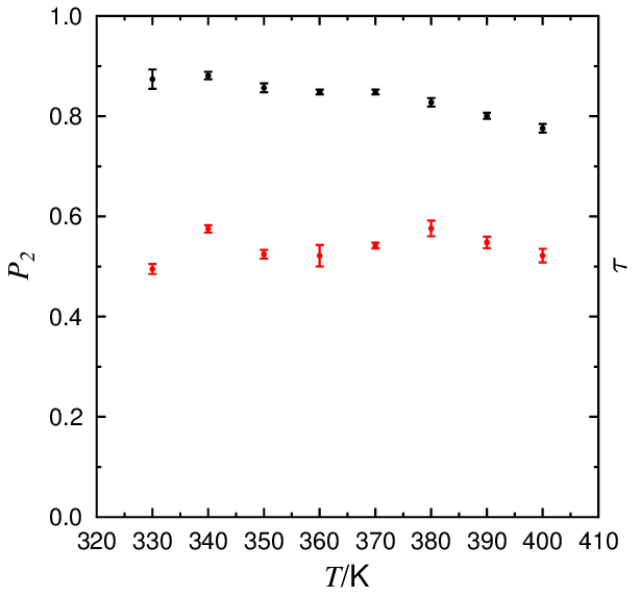

Figure 3.3 Plot of the average orientational order parameter (P_2), with respect to **n**, and the translational order parameter (τ) determined from simulations between 330K and 400 K, with associated error bars.

Figure 3.3 shows the effect of temperature variation on the orientational order is relatively small across the simulated temperature range, consistent with the experimental results from polarised Raman spectroscopy and x-ray diffraction.[87]

Visualisations of the simulations performed at 340 K and 380 K are shown in Figure 3.4, revealing that the orientational order is accompanied by the development of a layer structure at both temperatures. Additionally, Figure 3.4 shows that molecules are noticeably tilted relative to the layer normal at 340 K, while molecules appear to be untilted at 380 K, implying that a simulated SmA-SmC* transition lies between these two temperatures.

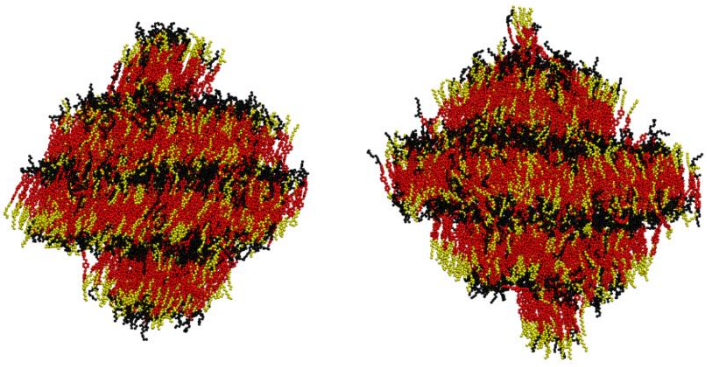

Figure 3.4 Visualisation of the layer structure of 9HL, showing the achiral aliphatic chain (yellow), aromatic core (red), and lactate chain (black), at 340 K (left) and 380 K (right), respectively.

An additional order parameter is usually introduced to characterise the extent of translational order exhibited by the SmA and SmC phases. The translational order parameter, defined as τ, is determined from the density fluctuations of the molecular positions along the layer normal axis,[25,74,221] with τ assuming values between 0 and 1, when molecular positions are wholly disordered, and when a system has a perfectly defined layer structure, respectively.

The τ values at each simulated temperature are also plotted in Figure 3.3, with average values of *ca*. 0.5-0.6, indicating a defined layer structure across the full simulated temperature range. These simulated values for 9HL are significantly lower than those derived from an x-ray scattering investigation of the same compound, in which τ was determined to be 0.50 at $T_{\text{I-A}}$, rising to 0.80 at $T_{\text{A-C}}$.[87] The inconsistency between τ values derived experimentally and computationally may result from the methodology used to determine transitional order from x-ray measurements, which has been reported to yield higher values relative to the results of simulation in previous studies.[16,158] Nevertheless, the high amount of translational order exhibited by 9HL is a fairly common feature in de Vries materials, as the immiscibility between chemically-different moieties is reported to be the primary factor promoting mesophase formation, supported by the direct transition from isotropic to the SmA phase that is observed to take place in many de Vries character materials.[222] While a direct quantitative comparison is difficult due to the inconsistencies associated with the determination of translational order by experiment and computational techniques, the values calculated for 9HL in this work are considerably higher than those of *ca*. 0.15-0.20 calculated from equivalent simulations of more conventional SmA phases formed by cyanobiphenyl liquid crystals.[158,175,223]

3.3.2 Tilt Angles and Layer Spacings

The tilt angle, defined as the angle between the minimum MOI director and the layer normal, was calculated at each simulated temperature and is shown in Figure 3.5, displaying a decrease as the temperature is increased. It can be seen that the most significant change in tilt occurs between 350 K and 360 K, which suggests a simulated SmA-SmC* transition lies between these two temperatures, consistent with the snapshots in Figure 3.4, and nearby to the experimentally determined temperature range of 337-347 K.[85,98,219] The calculated tilt of *ca*. 15-18° in the simulated SmC phase is in good agreement with the spontaneous tilt angle of 15-20°,[85,219] reported in some experimental studies, but appears significantly lower than the 30° tilt measured in the SmC phase of 9HL by NMR spectroscopy.[105]

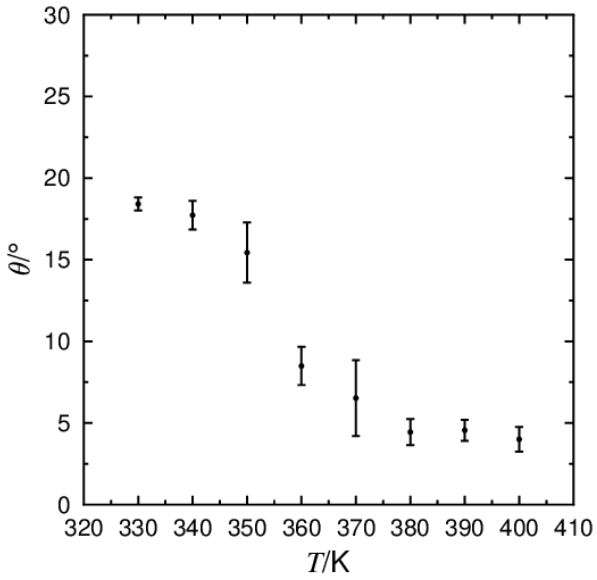

Figure 3.5 The average tilt angle between the layer normal (**k**) and the director (**n**) determined from simulations between 330 K and 400 K.

The non-zero tilt angle calculated above 360 K (i.e. in the simulated SmA phase) may be partially explained by small molecular tilt fluctuations, reported in some studies to account for the strong electroclinic effect observed in 9HL.[85] In addition, the tilt angle of *ca*. 5° in the simulated SmA phase is broadly consistent with the non-zero molecular tilt reported to exist in the SmA phase by studies relying on ^{2}H NMR spectroscopy.[103] A non-zero tilt in the SmA phase may also be an artefact of the small size of the simulated system, relative to the dimensions of a bulk experimental sample, in which small ripples in the layer structure of a SmA phase may be expected to average out over the sample. However, such ripples could manifest as a measurable tilt in a system of limited size, such as the MD simulations reported on here.

The primary indicator of de Vries character in smectic mesophases is the behaviour of the layer spacing at $T_{A\text{-}C}$. The calculated layer spacing, defined as the distance between the density wave maxima of the C16 atom in 9HL, at each simulated temperature is plotted in Figure 3.6, which demonstrates an overall increase as the temperature increases from *ca*. 4.05 nm at 330 K to *ca*. 4.25 nm at 370 K, fairly consistent with the experimentally reported layer thickness values of 3.90 nm[220] and 4.30 nm.[85] The layer shrinkage, commonly used as a quantitative measure of de Vries character, can vary significantly depending on the temperature at which the SmC layer thickness is defined, but the layer thickness determined from the simulations of 9HL below the apparent SmA-SmC transition are all < 3% smaller than the layer thickness at the calculated transition, determined as the average of the layer spacing in the 350 K and 360 K simulations.

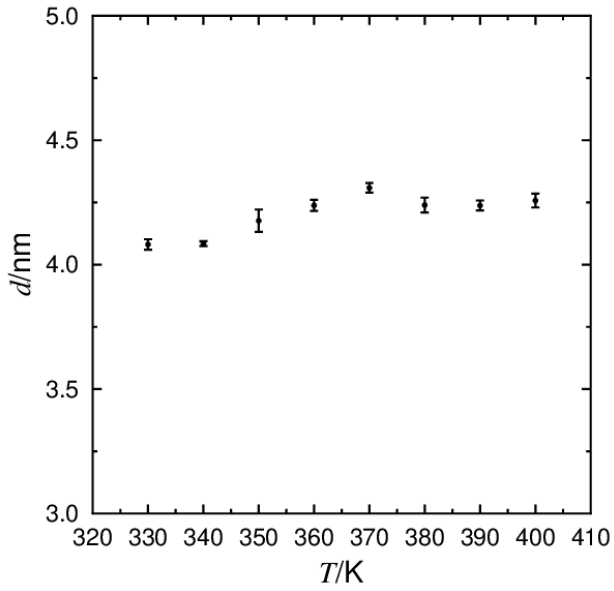

Figure 3.6 The average layer spacing defined by the C6 atom determined from simulations of 9HL between 330 K and 400 K, with associated error bars.

3.3.3 Quantification of de Vries Character

In addition to employing the calculated layer shrinkage to assess the de Vires character exhibited by a particular material, it can also be valuable to account for the molecular tilt exhibited in the SmC phase, which allows the reduction in layer contraction to be quantified relative to that expected from the rigid-rod model. The reduction factor, *R*, defined by Radcliffe *et al*.,[84] relates to the ratio between the tilt angle required to give the observed layer contraction at the SmA-SmC transition and the measured tilt angle, assuming molecules behave as rigid-rods,. As *R* approaches 0, a liquid crystal phase becomes increasingly more de Vries-like, i.e., the phase approaches zero layer shrinkage, whereas an *R* value of 1 corresponds to layer contraction fully consistent with the rigid-rod model. While inconsistency between experimentally derived layer thicknesses and tilt angles results in a considerable uncertainty associated with experimental *R* factors for 9HL, they are generally reported to be less than 1, indicative of some amount of de Vries character. Likewise, the *R* values of 0.76, 0.78 and 0.45 determined from the simulations at 330 K, 340 K, 350 K, respectively, also indicate that MD simulations have successfully captured de Vries character in 9HL. Even after adjusting for the non-zero tilt in the simulated SmA phase, *R* values were calculated to be below 1 in these simulations.

The simulated phases of 9HL were characterised further, as illustrated in Figure 3.7, which shows histograms of the angles between the layer normal and the director at each frame over the final 100 ns of each simulation. The histograms show a significant shift in the angle populations between 350 K and 360 K, again supporting the presence of a simulated SmA-SmC* phase transition between these temperatures, consistent with Figures 3.4 and 3.5. The non-zero tilt angle above 350 K is also evident in Figure 3.7, but whether this tilt is a simulation artefact, or an actual feature of the real

system is still unclear. Nevertheless, the combined data in Figures 3.5-3.7 reveal that there exists a phase transition from a significantly tilted phase at temperatures of ≤ 350 K to a essentially untilted phase at temperatures ≥ 360 K. Furthermore, the layer contraction associated with this transition is less than would be expected from the shift in molecular tilt alone, signifying that the simulations of 9HL, reported in this work, exhibit clear de Vries character.

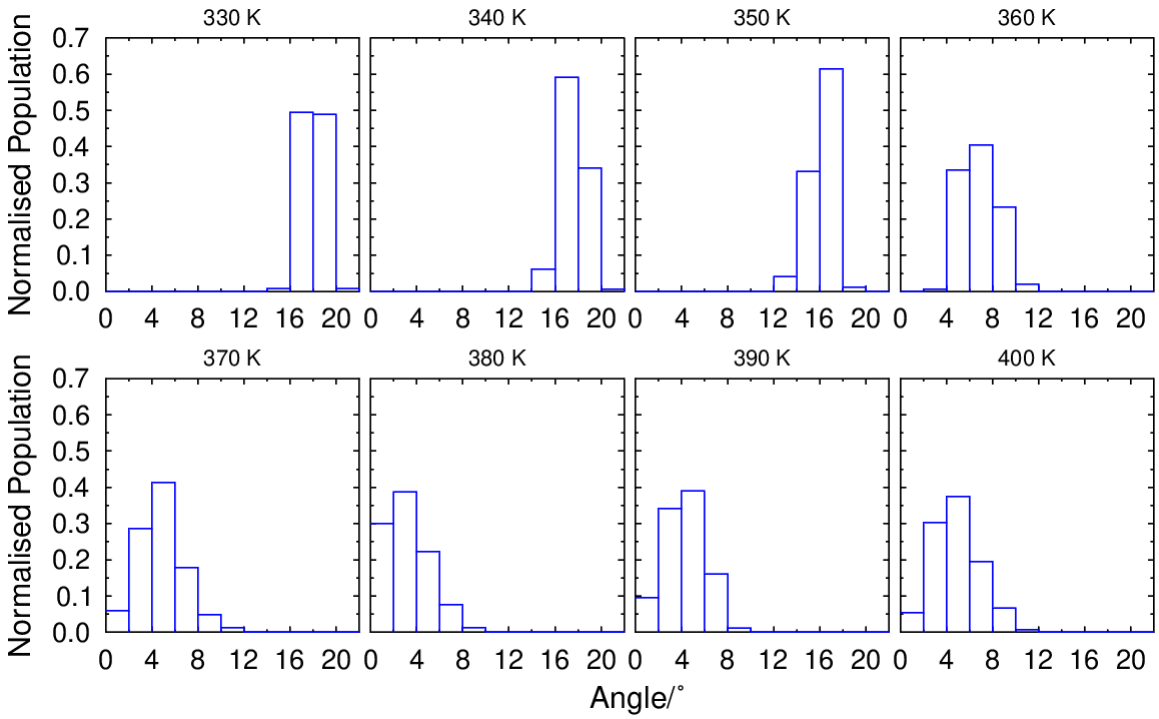

Figure 3.7 Normalised histograms of the angle formed by the vectors **n** and **k** over the final 100 ns of simulations of 9HL, performed every 10 K between 330 K and 380 K, determined with a bin-width of 2°.

3.3.4 Orientational Distribution Functions

Although P_2 values, such as those presented in Figure 3.3, provide a convenient way to quantify orientational order in liquid crystal mesophases, individual second-rank orientational order parameters cannot distinguish between different orientational distributions. The distribution of molecular tilt directions is reported in a number of models to play a significant role in de Vries behaviour, with orientational distributions in the SmA phase described as a 'volcano-like' or broad 'sugarloaf-like' shape.[99,100] the distribution of molecular orientations within a system can be revealed through orientational distribution functions (ODFs). ODFs of the minimum MOI axis of the 9HL molecules are plotted in Figure 3.8, displaying broad distribution functions with non-zero maxima in the simulated SmC* phase (≤ 350 K), but showing distribution functions clearly centred on 0° in the simulated SmA phase (≥ 360 K). Even without additional characterisation of the shape of the ODFs, it is clear that there is a significant change across the simulated transition temperature. The ODFs, as well as visual inspection of the simulated phase structure of 9HL, indicate a fairly conventional SmA phase that is inconsistent with the SmA phase proposed in the diffuse cone model and does not provide a straightforward rationale for the low layer shrinkage.

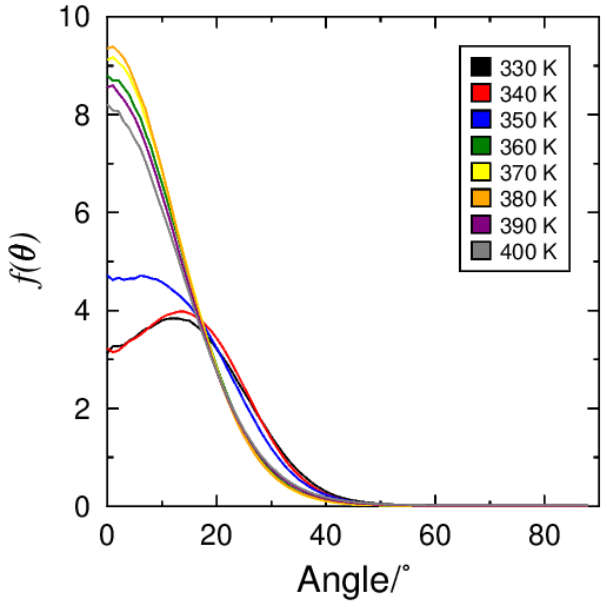

Figure 3.8 Orientational distribution functions (ODFs) of the minimum MOI vectors of the whole molecule, determined from simulations of 9HL at 10 K intervals between 330K and 400 K

3.3.5 Molecular Length

A shift in the mean length of molecules can significantly impact the layer thickness in the SmA and SmC phases, which has led to several proposals that the layer shrinkage is partially or wholly offset by an increase in the effective molecular length in de Vries materials. The distribution of the molecular lengths in 9HL, defined as the length of the vector between the terminal CH_3 carbon atoms on the C_9 aliphatic chain and the C_6 lactate chain, at each temperature is shown in Figure 3.9, together with the average molecular length, which shows an overall decrease as the temperature is increased. This data indicates that any contraction of the smectic layers, caused by an increase in molecular tilt is, at least partially, likely to be offset by a subsequent increase in molecular length. Analysis of the simulations at 350 K and 360 K, either side of the simulated SmA-SmC transition, shows a reduction in layer thickness of 0.62 Å. When the calculated molecular tilt angles are accounted for at these temperatures, the molecular length would have to exhibit a corresponding increase of 0.48 Å if molecular elongation was the only factor compensating layer shrinkage. The average calculated increase in molecular length between 360 K and 350 K is 0.23 Å, implying that whilst molecular elongation appears to contribute to the de Vries behaviour of 9HL, it cannot fully explain the observed reduction in layer shrinkage.

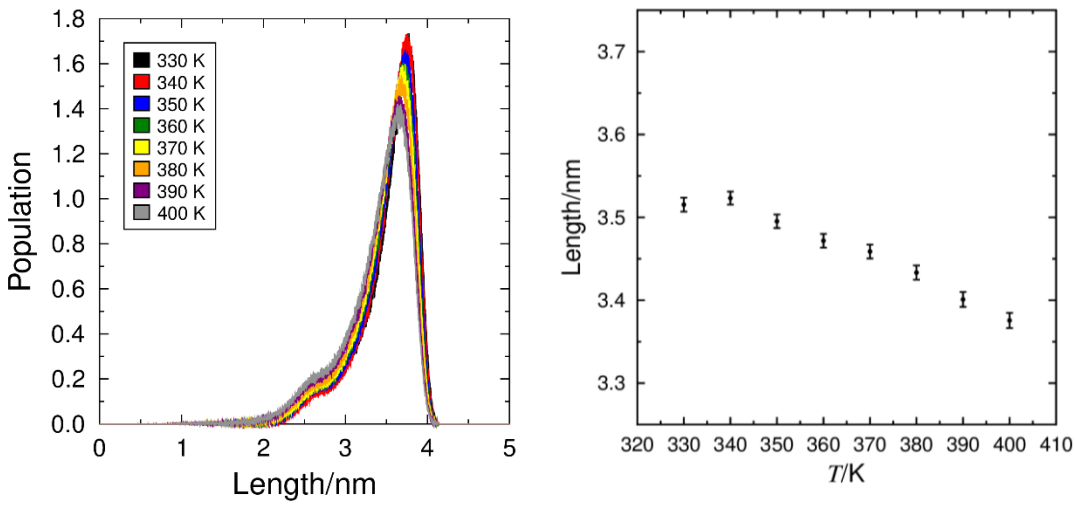

Figure 3.9 Distribution of molecular lengths of 9HL (left) and mean molecular lengths plotted against temperature (right), determined from simulations of 9HL at 10 K intervals between 330K and 400 K

3.3.6 Molecular Interdigitation

A shift in the extent to which molecules overlap within individual smectic layers and between adjacent smectic layers can also considerably affect the overall layer thickness. The percentage interdigitation of the two end groups of the 9HL molecules, defined as the CH_3 carbon atoms on the C_9 aliphatic and the C_6 lactate chain, at each simulated temperature, are plotted in Figure 3.10. These values were determined in accordance with the method laid out in previous work, where an atom is considered interdigitated if it lies beyond the overall layer position defined by all molecules within a layer.[175] A degree of interdigitation of 100% would indicate all atoms in oppositely orientated molecules overlap, whereas a value of 0% would indicate no overlap between the atoms in oppositely orientated molecules.

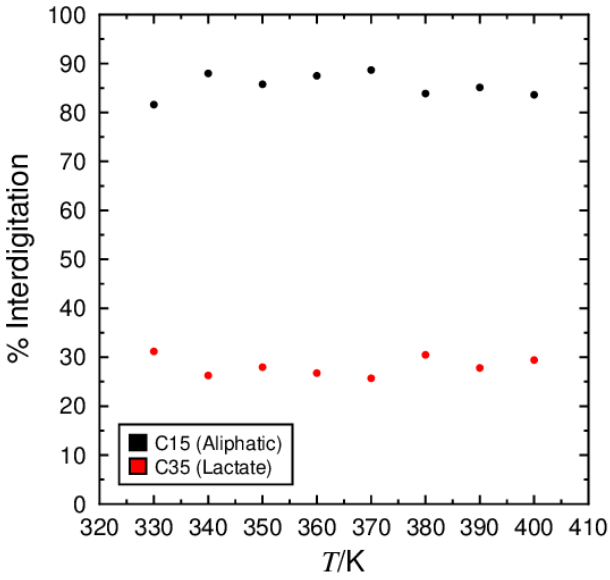

Figure 3.10 Degree of interdigitation of the lactate end-groups and aliphatic end-groups calculated over 50 ns windows.

Figure 3.10 shows that the percentage interdigitation of the aliphatic chains is consistently *ca*. 85% across the 330-400 K temperature range. This high value indicates significant interdigitation between the aliphatic chains in oppositely orientated molecules within the layer structure. In comparison, the degree of overlap is considerably less for the lactate chains with a much lower value of *ca*. 25%, indicating that only around a quarter of the lactate chains overlap with the equivalent groups in oppositely orientated molecules, and again the values are relatively consistent across the simulated temperature range.

In the case of the layer shrinkage caused by molecular tilt being compensated by a change in interdigitation, a general decrease in interdigitation would be expected upon cooling, i.e. with increasing molecular tilt, which is not apparent in Figure 3.10. Furthermore, a sudden decrease would be expected between 350 K and 360 K where the tilt angle, θ, and cos(θ) are calculated to change significantly. This decrease is also not evident in Figure 3.10, indicating that any shift in molecular interdigitation is minimal in these simulations and is not calculated to significantly affect the layer thickness or de Vries characteristics of the simulated 9HL systems.

3.3.7 Sub-Unit Analysis

Given the clear separation between the aromatic and lactate sub-layers in Figure 3.4, in addition to the distinct character of the sub-layers, emphasised by the different degrees of interdigitation shown in Figure 3.10, further analysis was performed on the different structural groups of 9HL in an effort to provide further insight into the simulated phases. Several experimental studies have reported that the tilt angle in the SmC phase may not be uniform across the whole molecule in de Vries materials, as some molecular sub-units may exhibit different tilt behaviour at the SmA-SmC* transition.[108,109] The ODFs of the minimum moment of inertia axes of the atoms comprising the aliphatic chain, the aromatic core and the lactate chain are shown in Figure 3.11, and their corresponding order parameters are presented in Table 3.2, which enabled the tilt behaviour of different molecular sub-units and their contributions to the overall tilt behaviour to be investigated across the simulated temperature range.

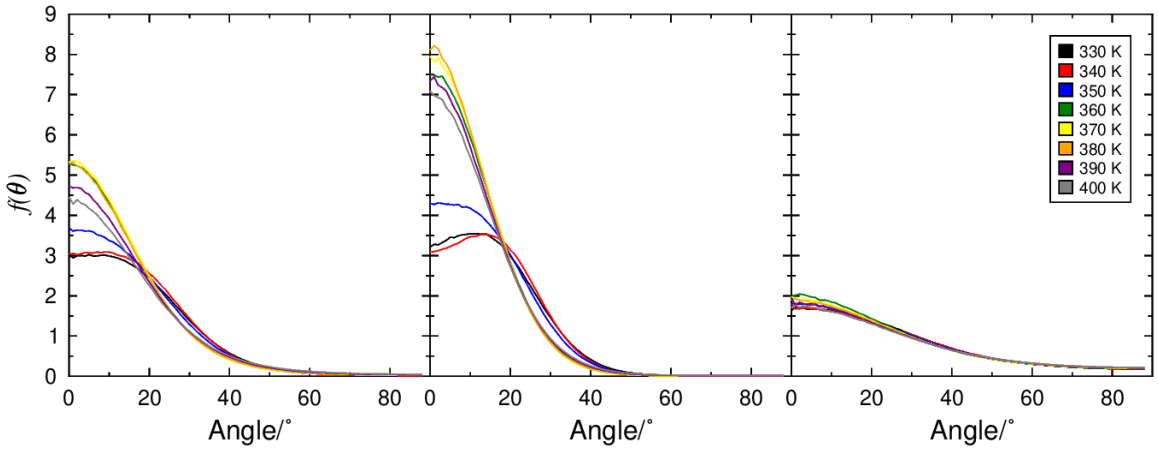

Figure 3.11 Orientational distribution functions (ODFs) of minimum MOI vectors of the achiral aliphatic chain (left), the aromatic core (centre), and the lactate chain (right), determined from simulations of 9HL at 10 K intervals between 330K and 400 K.

Table 3.2 Average P_2 values, with respect to **k**, determined from the aliphatic, aromatic, and lactate sub-units of 9HL at 10 K intervals between 330 K and 400 K.

	Aliphatic		Aromatic		Lactate	
T / K	P_2	+/-	P_2	+/-	P_2	+/-
330	0.625	0.002	0.728	0.002	0.295	0.004
340	0.651	0.004	0.733	0.002	0.284	0.004
350	0.638	0.006	0.778	0.002	0.285	0.005
360	0.699	0.006	0.818	0.002	0.287	0.006
370	0.691	0.005	0.799	0.002	0.276	0.003
380	0.659	0.006	0.805	0.002	0.269	0.003
390	0.633	0.004	0.776	0.004	0.305	0.002
400	0.606	0.013	0.756	0.015	0.291	0.003

The ODFs clearly show that different molecular sub-units do not exhibit identical tilt behaviour in the SmA and SmC phases, emphasised by their substantially different distribution functions. In the SmC phase (330 K – 350 K), the aromatic groups exhibit a 'volcano-like' distribution function, with a non-zero maximum, and the aliphatic chains exhibit more of a 'sugarloaf-like' distribution. In contrast, the lactate groups show a broad SmA-like distribution function, with a maximum at 0°, which exhibits minimal change from the distribution functions exhibited in the simulated SmA phase. In addition, the lactate groups are calculated to be significantly less orientationally ordered with respect to the layer normal than the aromatic and aliphatic groups at all temperatures. As the lactate sub-unit comprises a significant fraction of the molecular length of the 9HL molecule, this data implies that a sizable portion of the molecule remains non-tilted, with respect to the layer normal, even in the SmC phase.

The distinct tilting behaviour exhibited by individual molecular sub-units provides a potential explanation for the 'de Vries-like' character of the 9HL simulations: if the ODF of a section of the molecule does not change significantly at the SmA-SmC transition, i.e. it remains essentially untilted, the overall layer thickness will not contract to the extent predicted by the rigid-rod model. Such an

explanation for de Vries behaviour has been examined previously in the study of a perfluoropolyether-terminated compound, but in this case the model was considered inadequate to explain the behaviour.[84] The orientational behaviour of individual molecular sub-units has also previously been investigated in siloxane-terminated liquid crystals.[224,225] Siloxane sub-units are reported to be significantly less orientationally ordered and exhibit a drastically reduced tilt relative to the rest of the molecule. Finally, the orientational order of individual sub-units has been considered previously in the case of 9HL, but it was determined that their contribution to de Vries behaviour could not be clearly defined.[87]

The general effect of partial molecular tilt on the layer thickness of a smectic material is shown schematically below. Figure 3.12 demonstrates that when a tilt angle of 25° is assumed, if merely ⅓ or ⅔ of a molecule is tilted in the SmC phase, the overall layer thickness reduces by just 3.1% (R = 0.57) or 6.2% (R = 0.81), respectively, relative to the SmA phase as opposed to a 9.4% reduction if the whole molecule tilts by the same angle. More generally, for a given tilt angle, in this simplified representation, the overall layer contraction is simply proportional to the fraction of the overall molecular length that tilts.

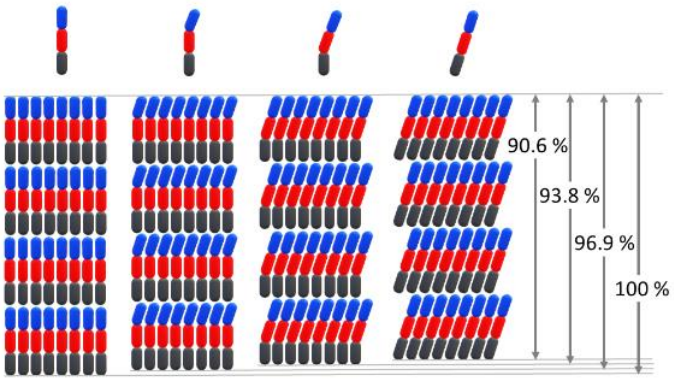

Figure 3.12 Schematic diagram illustrating differences in layer thickness when different fractions of the molecule (left to right: 0, ⅓, ⅔, 1) tilt by 25 degrees. Percentage layer thicknesses relative to the un-tilted (SmA) configuration are also given.

3.4 Conclusions

Fully atomistic MD simulations of 9HL were shown to have the capacity to reproduce numerous experimental observables, such as orientational and translational order parameters, layer spacings and tilt angles over a wide temperature range. This analysis, paired with the calculation of *R* values, revealed that the layer contraction observed in the simulated phases of 9HL was significantly reduced relative to that expected by the rigid-rod model, suggesting that the MD simulations successfully replicated the de Vries character exhibited by 9HL. Further characterisation of the phase structure through the calculation of molecular ODFs, molecular lengths and interdigitation percentages indicated that the observed reduction in layer shrinkage could not be entirely rationalised by any of the established models commonly applied to materials that exhibit de Vries character, and while the change in molecular conformation with temperature to a more elongated structure partially explained the small layer contraction, the effect was calculated to be insufficient to be the only contribution.

Analysis of the molecular sub-units provided a greater insight into the structures of the simulated phases of 9HL. ODFs of the sub-units indicated that molecules do not tilt uniformly in the SmC* phase. Aromatic and aliphatic units display fairly 'conventional' tilting behaviour, with a significant change in the distribution function resulting in a broad 'sugarloaf-like' or 'volcano-like' distribution upon transition to the SmC* phase. In contrast, the tilt behaviour of lactate units was not calculated to vary significantly between the SmA and SmC* phases, displaying a very broad zero-centred distribution across all simulated temperatures.

Experimentally, tilt angles are typically determined by methods that probe a single part of the molecule, such as vibrational spectroscopy, NMR spectroscopy, or birefringence measurements that rely on the anisotropy of the polarisability along a conjugated region of a molecule. Therefore, these measurements are usually dependent only on the angle that the aromatic core of a mesogen makes with the director. Consequently, the partial tilt behaviour exhibited in this work by 9HL enables a potential explanation as to why layer shrinkage at the SmA-SmC transition may not appear consistent with the measured tilt angle.

The de Vries behaviour exhibited by 9HL may be regarded as odd due to the absence of chemically immiscible sub-units, which are typically considered necessary for a mesogen to possess significant de Vries character,.[92,226,227] However, despite this apparent lack of chemical incompatibility, the simulations of 9HL clearly show a clear separation between lactate sub-layers and aromatic sublayers, as well as a high translational order parameter. This behaviour is consistent with the well-defined layers reported to be exhibited by perfluoropolyether and siloxane-containing mesogens, but in the case of 9HL, the behaviour may be a geometric effect rather than purely a chemical effect.[175]

This study of 9HL also demonstrates further similarities with siloxane-based mesogens, as siloxane and hydrocarbon sub-units have been shown to exhibit different orientational order parameters in

cases where x-ray scattering has enabled the resolution of peaks arising from the different sub-units.[224,225] It has also been reported that the orientational order of siloxane sub-units does not necessarily show any change across the SmA/SmC transition,[224] again consistent with the behaviour of the lactate chains exhibited in these simulations of 9HL. Given these similarities, it may be that the partial tilt behaviour described here may apply to a greater or lesser extent to other materials that exhibit de Vries behaviour.

Chapter 4 – Force Constant Parameterisation for Accurate Simulations of Perfluoropolyether and Trisiloxane-Based Materials

This chapter focuses on the parameterisation procedures utilised in an effort to improve the ability of MD simulations to model certain liquid crystals, relative to those simulations employing default force constants provided by general force fields. The work centres on the optimisation of parameters for perfluoropolyether and trisiloxane-based compounds that, like 9HL, are reported to exhibit substantial de Vries behaviour.[83,84] Recent efforts to parameterise both perfluorinated and siloxane-based liquid crystals for use in standard force fields are discussed here, in addition to the parameterisation methods that have been utilised in this process. The parameterisation of the force constants for several aspects of the perfluorinated- and siloxane-chains is outlined, including initial potential energy scans, single point energy calculations and the weighted fitting of force constants based on a Boltzmann distribution. The results of the parameterisation are then evaluated through comparison with the default force constants provided by the standard GAFF force field. Additionally, the parameterisation performed in this chapter forms the basis of the subsequent atomistic MD simulations of 3M 8422 and TSiKN65, which are described in Chapters 5 and 6, respectively.

4.1 Introduction

This section provides a brief background on the parameterisation of standard force fields in general, as well as an overview of the parameterisation methods commonly used to capture the behaviour of specific systems through MD simulations. Additionally, this introduction offers a summary of the previously published work relevant to MD simulations of perfluorinated and siloxane-based materials, and the issues associated with the use of standard force fields in both cases. Finally, this section concludes by stating the aims of the work presented in this chapter and its relevance to the subsequent simulation work discussed throughout the rest of this thesis.

4.1.1 Parameterisation of Standard Force Fields

Numerous force fields have been developed that are suitable for modelling a wide range of organic molecules.[180,181] As these general force fields aim to accurately model many different chemical groups, they contain a large number of atom types, making them an appropriate choice for the simulation of compounds containing less ‘conventional’ moieties, such as perfluoro- or siloxane-based segments. However, even these general force fields often lack the ability to capture the more unusual behaviours exhibited by such compounds. As a result, bespoke parameterisation to augment standard force fields has become increasingly necessary as the focus of many modelling studies turns to the investigation of relatively unusual material characteristics.

A variety of different methods exist for force field parameterisation, which may use data derived from both experimental techniques and electronic structure calculations.[180,181,228,229] Data obtained by employing *ab initio* techniques is particularly useful in cases where experimental data is in relatively

short supply, as is often the case for many less conventional chemical groups, or for properties such as torsional potentials, which can be difficult to determine experimentally. However, limits on computational feasibility mean a combination of experimental techniques and quantum mechanical methods are frequently used to derive optimised force field parameters that allow accurate predictions of material properties.

The majority of standard force fields aim to accurately model the structure and properties of small organic molecules. Additionally, a significant amount of work has been dedicated to the parameterisation of force fields such as OPLS and GAFF,[180,181] which has focused on improving their ability to predict many of the properties associated with liquid crystal phases. For example, the parameterisation of an AMBER-like UA force field was reported by Tiberio *et al*.,[156] in which Lennard-Jones parameters for aromatic and aliphatic carbons were optimised to predict the nematic-isotropic transition temperature in a series of cyano-biphenyl compounds. Another notable example of such a parameterisation procedure is described in work by Boyd and Wilson,[168,186] which focuses on optimisation of the standard GAFF force field for several key liquid crystal fragments, and provides modified parameters for a variety of torsional potentials obtained via the fitting of *ab initio* data. Likewise, optimisation of the torsional potential related to thiophene-thiophene rotation was carried out in work by Pizzirusso *et al*.,[230] which enabled the prediction of order parameters and diffusion coefficients in simulated phases composed of sexithiophene. Such parameterisation methods have enabled the prediction of liquid crystal phase structures and properties, providing an excellent precedent for the parameterisation of standard force fields, such as GAFF,[181] for the accurate modelling of more complex behaviours exhibited by liquid crystal phases.

4.1.2 MD Simulation of Perfluorinated Compounds

Liquid crystal materials containing a perfluorinated segment are fairly widely reported and the presence of a perfluoroalkane terminal chain is known to have a significant effect on mesophase properties.[231–233] Computational modelling of semi-perfluorinated liquid crystals, therefore, appears to have the potential to provide an insight into the mesophase structure and properties of semi-perfluorinated materials. However, while the application of simulation techniques may prove beneficial and MD simulations have been reported previously, employing standard force fields, several issues associated with the accurate replication of key properties in perfluorinated materials have limited the effectiveness of computational methods.[234]

The inability of standard force fields to reproduce many of the behaviours associated with perfluorinated compounds has led to several studies focused on improving the capacity of the MD simulations to replicate the properties of perfluoro-based materials. Some investigations have attempted to optimise the standard combining rules utilised in force fields such as OPLS-AA and AMBER,[234,235] in an effort to reproduce the observed immiscibility in mixtures of alkanes and

perfluoroalkanes. A more recent study, performed by Träg and Zahn,[236] focuses on the development and optimisation of the GAFF parameters used to describe the torsional potential in perfluoro-based molecules, while simultaneously introducing a new atom type specifically for use in perfluorinated compounds.

In addition to perfluorinated alkanes, perfluoropolyether (PFPE) materials have attracted considerable attention due to their potential for use in a variety of applications, and several liquid crystal compounds have also been reported that contain a PFPE segment.[84,111] Although numerous simulation studies have endeavoured to explore the properties of PFPEs,[237–248] not many force fields have been systemically parameterised specifically to model these compounds. One notable example can be seen in the work of Li *et al*.,[249,250] in which a UA model was parameterised to better reproduce experimental quantities of PFPEs by optimising the associated torsional potentials and partial charges. A more recent example can be found in work performed by Black *et al*.,[251] reporting on the development of a fully atomistic force field for PFPEs based on the OPLS-AA force field. In this work, Black and co-workers used a combination of experimental techniques and *ab initio* calculations to optimise both bonded and nonbonded parameters, which offered a drastic improvement in the prediction of experimental observables. This previously published work provides an encouraging starting point for further parameterisation of standard force fields and their ability to realistically model PFPE structural fragments in an expanded range of materials.

4.1.3 MD Simulation of Siloxane-Based Compounds

Liquid crystals that contain a siloxane-based chain are commonly reported to exhibit unique properties and are well-known for their demonstration of nanophase separation.[83,112,216,252] These complex behaviours make siloxane-based liquid crystals an appealing target for MD simulations, which can provide an atomic-level description of mesophase structure. However, despite this, a comprehensive computational study of organosiloxane liquid crystals has not materialised, perhaps due to the difficulties associated with the use of standard force fields in the simulation of siloxane compounds.

The widespread application of siloxanes in various areas of industry has resulted in several attempts to develop a force field model that can accurately predict their key properties. An early example is provided by Sok *et al*.,[253] reporting on a UA simulation of a polydimethylsiloxane (PDMS) that utilised parameters specifically derived for siloxane materials. A second example of such force field development was reported by Sun and Rigby,[254] who utilised *ab initio* calculations and experimental data in the parameterisation of a consistent force field for the purposes of modelling siloxane and siloxane compounds. Likewise, in work carried out by Smith *et al*.,[176] a fully atomistic force field suitable for simulation of siloxane-based materials was also developed on the basis of *ab initio* calculations on model PDMS compounds. This comprehensive parameterisation, performed by

Smith and co-workers, involved calculation of parameters for all bonded and nonbonded interactions within PDMS, and evaluation of the results produced from numerous different basis sets. The subsequent validation of this quantum chemistry-based force field featured a direct comparison of the simulated results with experimentally derived thermophysical, structural and dynamic properties, with MD simulations employing the optimised parameters shown to closely replicate experimental trends observed in single molecule systems and multi-chain polymer melts. The optimisation of a UA force field for siloxane-based materials is described in work by Makrodimitri *et al*.,[255] which focuses on the use of experimental thermodynamic data to obtain more realistic models that can reproduce the physical properties of PDMS melts. A series of more recent articles by Shi *et al*.,[256,257] reports on the development of separate UA and AA models employing parameters obtained from Sok[253] and Smith[176], respectively. In the work performed by Shi and co-workers, optimised Lennard-Jones parameters for Si, C and O atoms were also obtained through fitting of the potential developed by Smith *et al*.[176] The work summarised above emphasises the depth of published research related to the parameterisation of standard force fields that aim to accurately model siloxane-based materials. Such reports provide a reliable basis for the application and further parameterisation of standard force fields, such as GAFF,[181] to liquid crystals that contain a siloxane-based terminal chain.

4.2 Aims

The aim of the work presented in this chapter was to develop an effective parameterisation methodology for the materials 3M 8422[84] and TSiKN65[83], shown in Figure 4.1, which contain a perfluoropolyether and siloxane unit, respectively. This parameterisation procedure would, in combination with optimised parameters obtained from the published literature,[176,251] allow for the extension of the GAFF force field to the liquid crystal materials shown in Figure 3.1, which are often stated as benchmarks for de Vries behaviour. The force constant parameterisation performed here aimed to provide further optimisation of the angle bending and torsional potentials via a weighted fitting procedure based on the Boltzmann distribution at 298 K.

A clear corollary aim of the parameterisation work reported in the results section below was to investigate the capacity of MD simulations to replicate complex mesophase behaviours, such as that exhibited by 3M 8422 and TSiKN65, which are discussed in Chapters 5 and 6, respectively, with the ultimate objective of providing additional insight into the mesophase behaviour of materials that exhibit de Vries character.

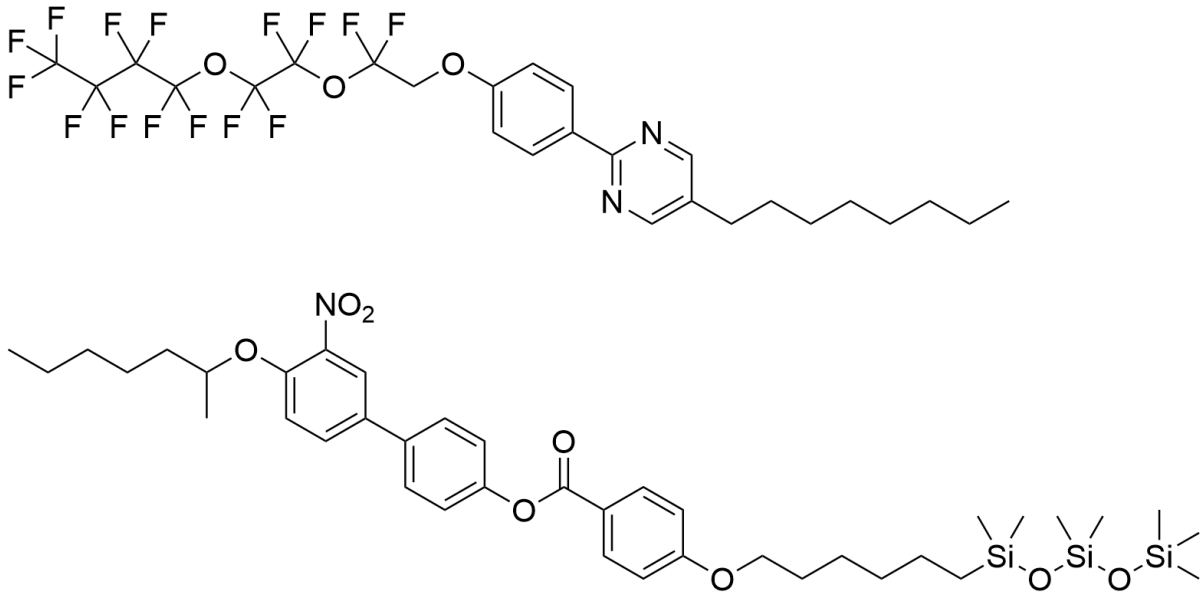

Figure 4.1 Chemical structure of the liquid crystalline compounds 3M 8422[84] (top) and TSiKN65[83] (bottom), which are the focus of the work presented in this chapter.

4.3 Results and Discussion

4.3.1 Perfluoropolyether Parameterisation

The suitability of the parameters supplied by standard force fields for MD simulations of semi-perfluorinated compounds has been assessed in multiple different studies,[234–236,251,258] which have generally reported that the default parameters fail to reproduce the realistic behaviour of perfluorinated systems. General force fields such as GAFF aim to be able to simulate a wide variety of materials, however the lack of suitable parameters for simulations of perfluorinated compounds has been emphasised in recent literature.[236] Such reports indicate that the successful simulation of 3M 8422 is likely to require optimised parameters for both bonded and non-bonded interactions.

The development of a force field for perfluoropolyethers based on OPLS-AA[180] has been reported previously in the literature,[251] and provides several new non-bond parameters, shown in Table 4.1, optimised for perfluoropolyether compounds such as 3M 8422. Notably, the OPLS[180] and GAFF[181] force fields utilise identical non-bond potentials, and as a result, the errors associated with the transfer of parameters between these force fields are expected to be minimal. Consequently, the work of Black *et al*.,[251] lays an excellent foundation for the parameterisation reported in the sections below. More specifically, the parameters associated with the van der Waals interactions and partial charges for C, O and F atoms within the perfluoropolyether chain were obtained from the report by Black *et al*.,[251] who themselves utilised a mixture of newly fitted parameters, default OPLS parameters and those established in previous computational studies of perfluoroalkanes.[180,258] These optimised values for non-bond interactions were employed throughout all of the MD simulations that comprised the parameterisation of the perfluoropolyether chain described in this section.

Table 4.1 Comparison of the non-bonded parameters from the GAFF and OPLS-AA force fields, as well as the optimised parameters provided by Black *et al*.,[251] for all of the atom types within the perfluoropolyether chain.

	GAFF		OPLS-AA			Black *et al*.		
Atom Type	ε/kJ mol^{-1}	σ/nm	ε/kJ mol^{-1}	σ/nm	*q*/*e*	ε/kJ mol^{-1}	σ/nm	*q*/*e*
R**C**F$_3$	0.45773	0.339967	0.276144	0.350	+0.36	0.276144	0.350	+0.36
R**C**F$_2$R	0.45773	0.339967	0.276144	0.350	+0.24	0.276144	0.350	+0.24
R**C**F$_2$O	0.45773	0.339967	0.276144	0.350	+0.44	0.276144	0.350	+0.44
CF*n***O**CF*n*	0.71128	0.300001	0.585760	0.290	-0.40	0.635968	0.279	-0.40
C**F**$_n$	0.255224	0.311815	0.221752	0.295	-0.12	0.221752	0.295	-0.12

Three initial structures (shown in Figure 4.2) corresponding to separate structural fragments of the perfluoropolyether chain in 3M 8422 were obtained via a geometry optimisation at the B3LYP/6-31G(d)[131,189] level. Subsequently, relaxed potential energy scans were performed on these structural fragments in Gaussian 09.[187] Using Fragment 1, three non-equivalent dihedrals were parameterised namely those corresponding to CF_3-CF_2-CF_2-CF_2 (D1), CF_2-CF_2-CF_2-O (D2) and CF_2-CF_2-O-CF_2

(D3) in the perfluoropolyether chain. Likewise, Fragment 2 was used to parameterise a single dihedral, that of O-CF_2-CF_2-O (D4) in 3M 8422. Fragment 3 enabled the parameterisation of the CF_2-O-CF_2 (A1) angle, which was applied to both equivalent angles in the partially fluorinated chain.

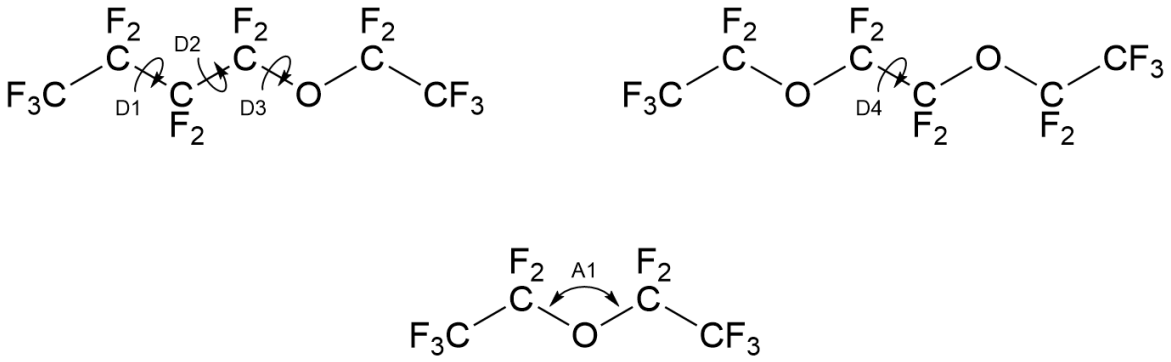

Figure 4.2 Structural representations of the three fragments used to parameterise the perfluoropolyether chain of 3M 8422, referred to in the text as Fragment 1 (top left), Fragment 2 (top right) and Fragment 3 (bottom).

Once an optimised geometry had been obtained for all three fragments, potential energy scans were performed on individual dihedrals during which all other non-fluorine-containing dihedrals within the perfluoropolyether chain were fixed. The constraint of these dihedrals meant that the energy variation observed throughout the potential energy scans were a consequence of the variation in the dihedral angle being analysed. All the potential energy scans on the dihedrals were performed with a 5° interval. The scan of D1 consisted of 72 steps, corresponding to a 360° rotation, which allowed the energy profile to be fully calculated. In contrast, all other dihedral scans consisted of 36 steps, corresponding to a 180° rotation, due to their symmetric nature about 180°. The potential energy scan performed on A1 consisted of 60 steps and utilised a 1° interval, which corresponded to an analysis of the energy of A1 between the angles of 90° and 150°. After the potential energy scans, single point energy calculations were subsequently performed at the MP2/6-31G(d) level at every step of each scan. This method of performing the potential energy scan using a lower level of theory, before calculating the energy at each interval using a higher level of theory allows a sufficient degree of confidence in the accuracy of the results, while avoiding the extended time scales usually required when carrying out a potential energy scan at a more computationally intensive level.

The default GAFF parameters for the bonded interactions discussed above were evaluated within the GROMACS 5.1.2 software,[191–195] via determination of the structural fragments' MD energy at each frame of the potential energy scan. To do so, the necessary parameters for MD simulation of Fragments 1-3 were generated using the Antechamber software package,[259] while the initial partial charges were calculated via the RESP method.[197] Where relevant, the default nonbonded GAFF parameters were then substituted for the values proposed in the literature,[180,251,258] enabling the change to be accounted for when calculating the MD energy. After this initial setup, the coordinates of each fragment at each frame of the potential energy scan were used as an input, allowing the MD

energy to be determined for these structures. The results from this analysis were compared with the MP2 energies to evaluate whether the default GAFF parameters were able to accurately model the angle and torsional potentials in 3M 8422.

4.3.1.1 Angle Parameterisation

The A1 angle of Fragment 3 was the first to be investigated, with the MD energy using default force constants plotted along with the equivalent MP2 energy in Figure 4.3. The data presented in the figure below reveals that the default force constants do not accurately model the behaviour of the CF_2-O-CF_2 bond angle in Fragment 3, deviating significantly from the relative energies calculated at the MP2 level. In Figure 4.3, the default force constants appear to underestimate the equilibrium bond angle by suggesting a value of *ca*. 116°, which in inconsistent with the MP2 value of *ca*. 122°. Likewise, the relative energy values are shown to deviate significantly at angles ≥ 120°, with the use of default force constants resulting in a higher energy barrier at larger angles, in comparison to the MP2 calculations. In addition, Figure 4.3 shows that while the MD energy is initially inconsistent with the MP2 energy at angles ≤ 120°, they become increasingly more alike as the bond angle decreases, perhaps unsurprisingly due to the exponentially large repulsion associated with atoms being in very close proximity.

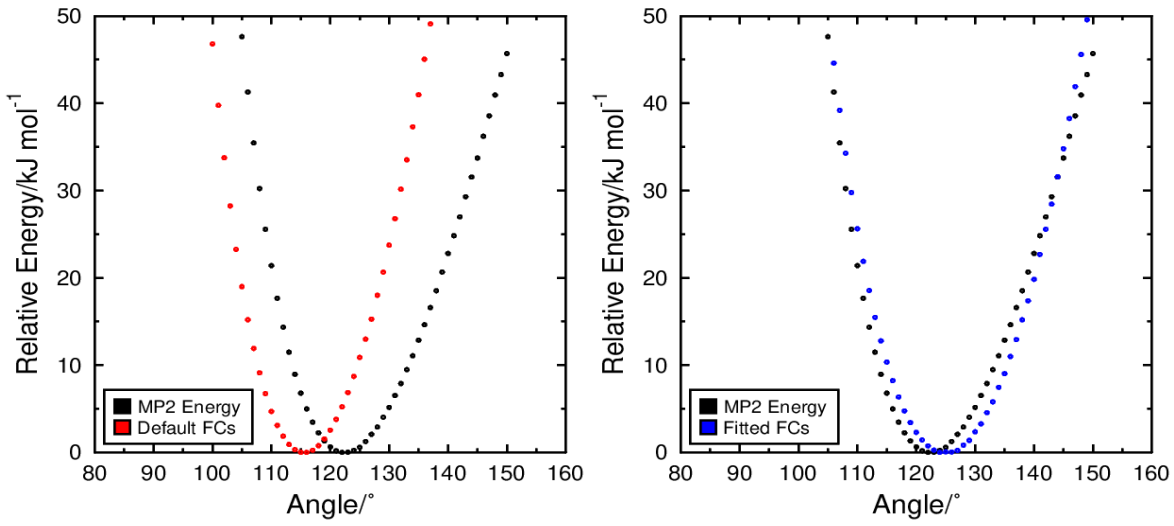

Figure 4.3 A graphical comparison of the MP2 energy versus the MD energy while employing default GAFF force constants (left) and fitted force constants (right) for angle A1, carried out using 1° intervals between 90° and 150°.

Upon taking all information provided by Figure 4.3 into consideration, it was clear that default force constants could not accurately capture the behaviour of the CF_2-O-CF_2 angle in perfluoropolyethers. As a result, more appropriate values were obtained by fitting to the energy values calculated at the MP2 level. This procedure involved calculation of the MD energy with all force constants for angle A1 set to zero, allowing the relative energy difference between this MD energy and the MP2 energy to be determined. Subsequently, the force constants were fitted to correct for this difference, in an effort to more closely reproduce the realistic behaviour of A1 in perfluoropolyether chains. The MD

energy calculated using the newly fitted force constants can also be seen in Figure 4.3, displaying much greater consistency with the MP2 energy data. Most notably, the equilibrium bond angle of *ca*. 123° when employing the fitted force constants is much more consistent with the MP2 derived value of *ca*. 122°. Additionally, the two sets of relative energy values show an excellent consistency as A1 approaches 150°, in contrast to the default parameters, which considerably overestimated the energy barrier at equivalent angles. As a consequence of the clearly improved angle potential when employing the fitted force constants, these newly developed parameters were applied to Fragments 1 and 2 throughout the remainder of the parameterisation procedure.

4.3.1.2 Dihedral Parameterisation

An equivalent parameterisation method to that described above was then applied to the D1 dihedral of Fragment 1, enabling the suitability of the default dihedral force constants to be evaluated. Initially, the MD energy was calculated while employing the default parameters and compared to the MP2 energies. The comparison shown in Figure 4.4 indicates that while the default force constants capture some elements of the torsional potential, they fail to accurately predict several key features that may have a significant effect on the overall conformation of the perfluoropolyether chain. Most notably, the MD energy in Figure 4.4 implies that in the lowest energy structure D1 sits at *ca*. 50-60°, inconsistent with the MP2 energy, which suggests the lowest energy structure occurs when D1 is at 160-170°. Likewise, the default force constants fail to correctly reproduce additional local energy minima between -90° and -45° that, while unlikely to heavily impact the molecular geometry, may subtly contribute to the preferred chain conformation.

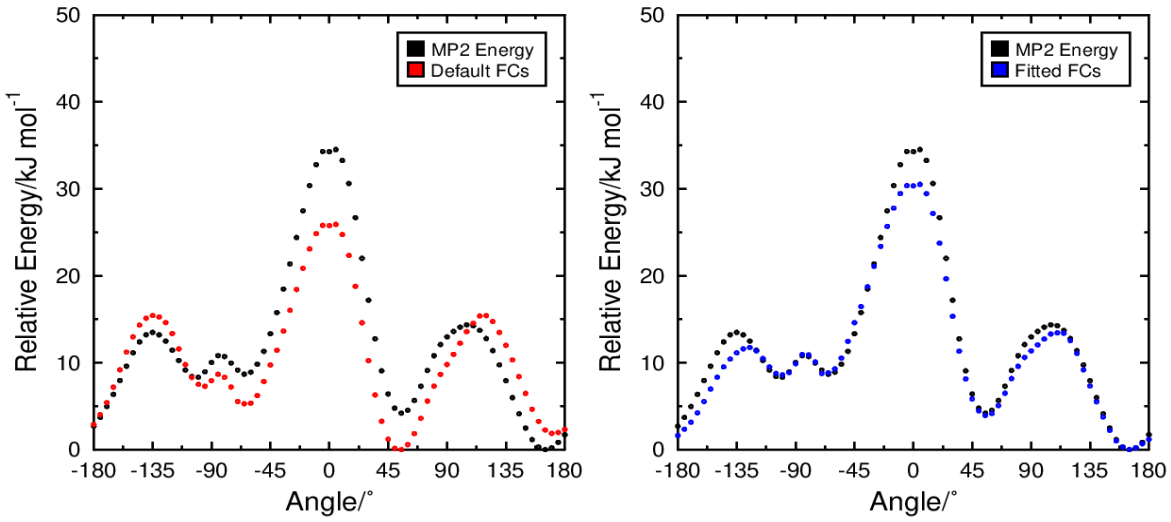

Figure 4.4 A graphical comparison of the MP2 energy versus the MD energy while employing default GAFF force constants (left) and fitted force constants (right) for dihedral D1, performed using 5° intervals between 0° and 180°.

For D1 it was concluded that the default force constants assigned by GAFF did not adequately model the torsional potential predicted by the *ab initio* methods. As a result, an analogous parameterisation method to that described for A1 was applied to D1, but with a few key distinctions. The initial fitting

procedure, similarly, consisted of the calculation of the MD energy with all force constants specific to D1 set to zero and the force constants fitted to minimise the difference in the relative energy between the MD and MP2-derived values. However, in the case of D1, a weighted fit was employed due to issues associated with unnecessary over prioritisation of high energy structures. In order to properly weight the fitting procedure, a Boltzmann distribution at 298 K was calculated, using the MP2 energy values and the weighting for each data point was set equal to the relative population. Figure 4.4 shows a graphical comparison of the MD energy calculated using the newly fitted parameters, and the MP2 energy. The data presented demonstrates that the parameters developed for D1 more accurately reproduce the torsional potential derived at the MP2 level, and clearly predict that the lowest energy structure arises when D1 sits at an angle of *ca*. 160-170°.

Initial assessment of the force constants for D2 followed a method to that equivalent to that described for D1. The data presented in Figure 4.5 highlights that when employing the default GAFF parameters, the relative energy is underestimated at angles close to 0°. However, despite this divergence, the energy minimum is well reproduced at *ca*. 50°, consistent with the MP2-derived values. Additionally, the default force constants significantly overestimate the energy between *ca*. 120-180°, which could have major implications for the overall conformation adopted by molecules in the subsequent MD simulations.

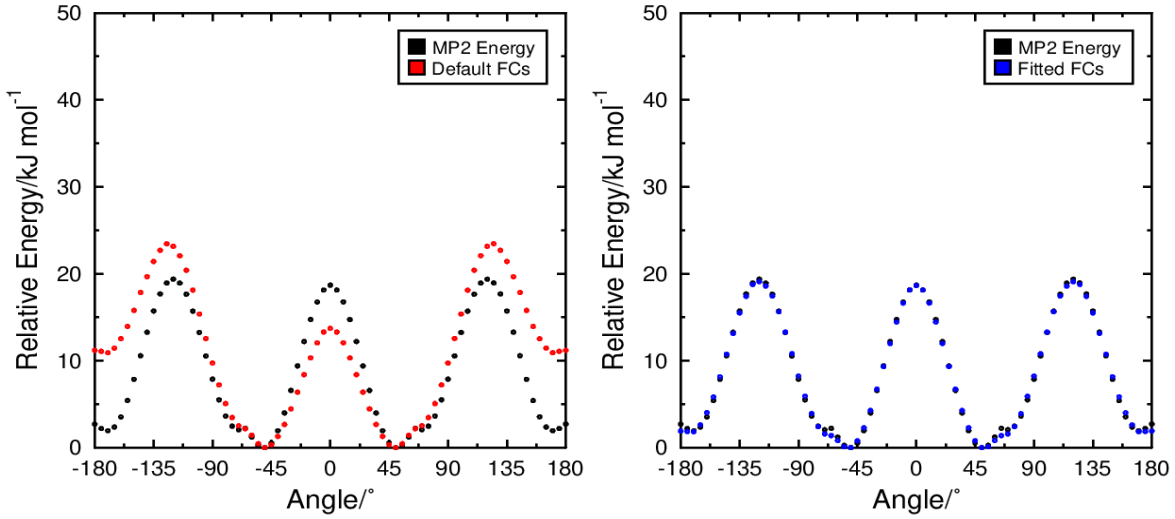

Figure 4.5 A graphical comparison of the MP2 energy versus the MD energy while employing default GAFF force constants (left) and fitted force constants (right) for dihedral D2, performed using 5° intervals between 0° and 180°.

The inability of the default parameters to accurately reproduce the torsional potential predicted by the *ab initio* calculations necessitated an optimised set of force constant, which were obtained by applying the weighted fitting procedure outlined above. The MD energy calculated while employing the newly developed parameters is also presented in Figure 4.5, displaying an improved replication of the values determined at the MP2 level. Significantly, the fitted values accurately predict the low energy at *ca*. 170-180°, which was not well reproduced using the default GAFF parameters. These

optimised force constants for D2, shown below in Table 4.2, should contribute to a more realistic representation of the perfluoropolyether chain geometry within the MD simulations performed in later work.

The default force constants applied to D3 were similarly assessed via the calculation of the MD energy, and comparison with the torsional potential predicted by MP2 calculations. This analysis, shown on the left in Figure 4.6, revealed that the auto-assigned GAFF parameters deviated significantly from the MP2-derived energy. Most notably, the default force constants result in an energy minimum at *ca.* 180°, inconsistent with the MP2 energy that displays a minimum value closer to *ca.* 160°. Likewise, the relative energy calculated from the default parameters indicates that major a local minimum exists between 45° and 90°, while this minimum is almost entirely smoothed out in the MP2 calculations, displaying only a small reduction in relative energy.

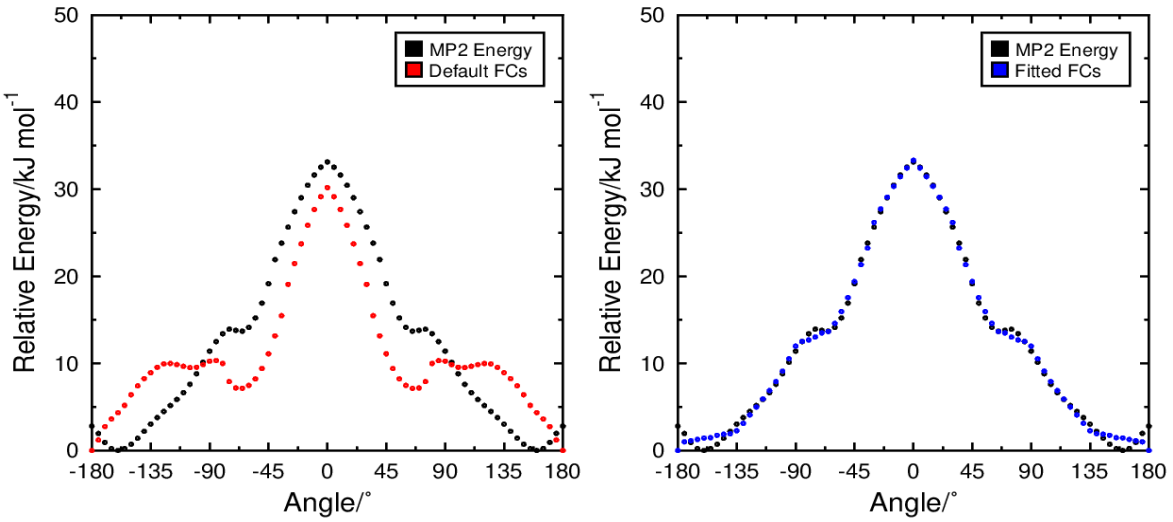

Figure 4.6 A graphical comparison of the MP2 energy versus the MD energy while employing default GAFF force constants (left) and fitted force constants (right) for dihedral D3, performed using 5° intervals between 0° and 180°.

Figure 4.6 also presents a comparison between the MD energy calculated from the fitted force constants and the relative energy determined at the MP2 level of theory, and this data demonstrates that the MD energy is more consistent with the MP2 values. The newly developed parameters still show an energy minimum at *ca.* 180°, rather than at *ca.* 160° as predicted by the MP2 data, but despite this, the optimised force constants, presented in Table 4.2, do offer a significantly improved representation of the MP2-derived torsional potential than the default GAFF parameters at almost all angles, and hence were adjudged to be more suitable for application in the subsequent MD simulations of 3M 8422.

Finally, the default force constants used to describe dihedral D4 were evaluated through application of the parameterisation procedure to Fragment 2. The MD energy calculated from the GAFF parameters is shown on the left in Figure 4.7, together with the MP2 energy corresponding to the equivalent structures. The default force constants are shown to generally match the torsional potential

when D4 sits at an angle between 0° and 100°, but the relative energy at higher angles appears to differ significantly from the values determined at the MP2 level. This can be seen most clearly at *ca*. 180°, where the relative energy is predicted to be close to 0 kJ mol^{-1} by the *ab initio* calculations but appears to be ≥ 15 kJ mol^{-1} when applying the default force constants.

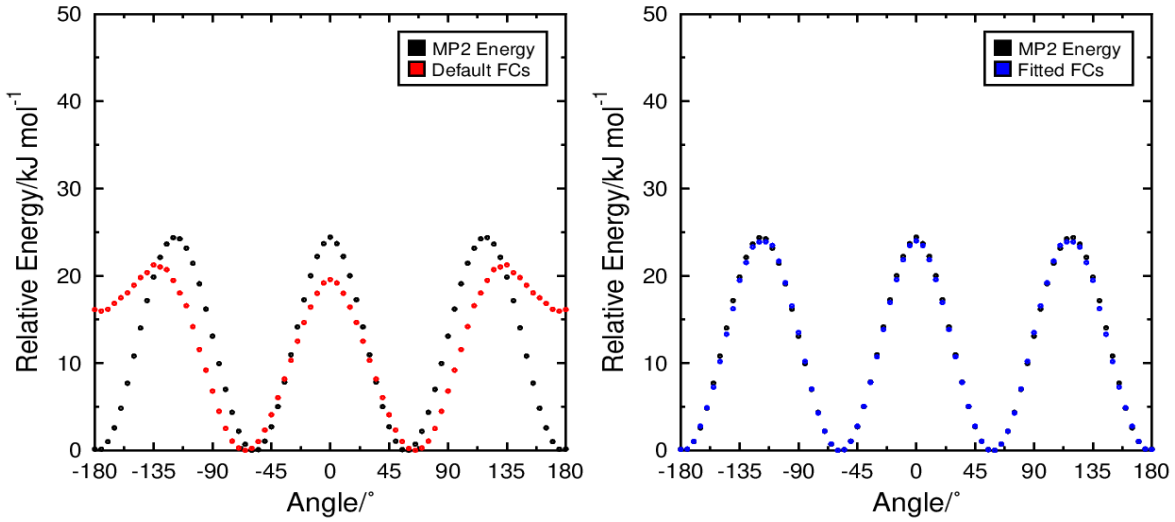

Figure 4.7 A graphical comparison of the MP2 energy versus the MD energy while employing default GAFF force constants (left) and fitted force constants (right) for dihedral D4, performed using 5° intervals between 0° and 180°.

The obvious lack of consistency between the MP2 energy and the MD energy that resulted from the use of the default GAFF parameters, meant the parameterisation method described previously was applied to D4. The MD energy between 0-180° was calculated using the newly developed force constants and is also shown on the right in Figure 4.7, which demonstrates that the fitted parameters generally resulted in a closer match between the two data sets. This is emphasised by the significant reduction in the relative energy approaching 180°, while employing the optimised parameters, down to a value of *ca*. 0 kJ mol^{-1}, consistent with the MP2 energy at an equivalent angle. Due to the improved description of D4, the force constants developed by the parameterisation of Fragment 2, shown in Table 4.2, were applied to the relevant dihedrals in the perfluoropolyether chain throughout future MD simulations of 3M 8422.

Table 4.2 The optimised force constants corresponding to dihedrals D1-D4, applied to all appropriate torsions throughout subsequent simulations of 3M 8422.

Dihedral	C0	C1	C2	C3	C4	C5
D1	3.78850	1.86350	8.64010	11.61890	6.69490	10.70990
D2	-0.88460	-0.62060	-4.28590	-5.79680	3.60580	-1.33440
D3	4.12940	-6.87740	-4.27880	-12.10870	3.29110	15.81960
D4	5.04920	11.43130	-10.62844	-22.34955	7.96144	0.081990

4.3.2 Siloxane Parameterisation

A number of studies have tried to optimise standard force fields for simulation of siloxane compounds,[176,253,256,260] often relying on quantum chemistry methods in an attempt to explore their unique properties on a molecular level. Significantly, several reports have focused on the extension of AMBER-like force fields,[256,260] providing various improved parameters that offer a potential path to capturing the behaviour of materials such as TSiKN65.

As discussed above, studies reporting on the development of an AMBER-like force field to simulate various polydimethylsiloxane species,[176,256,257,260] provided an initial start point for the work performed in this section. The relevant parameters associated with non-bond interactions, shown in Table 4.3, employed in these investigations,[256,260] many of which were established in previous computational studies of siloxane-based compounds,[176,253] were applied to the Si, C, O and H atoms within the trisiloxane molecular fragment on which this parameterisation was based. The modified values for non-bonded parameters were employed where appropriate in all of the MD analysis performed in the parametrisation of the siloxane chain, as well as in the subsequent MD simulation of TSiKN65.

Table 4.3 Optimised non-bond parameters, ε and σ, provided by Shi *et al*.,[256] applied to all atoms within the siloxane chain.

Atom Type	ε/kJ mol^{-1}	σ/nm
R**Si**$(CH_3)_2$	0.996210	0.3759
Si**O**Si	0.835545	0.2815
R**C**H_3	0.337900	0.3345
RC**H**$_n$	0.038284	0.2650

An initial structure, a representation of which is provided in Figure 4.8, corresponding to the trisiloxane fragment of the siloxane-based chain in TSiKN65 was obtained via a geometry optimisation at the B3LYP/6-311(d,p) level. A number of relaxed potential energy scans were then performed on this structural fragment in Gaussian 09. In total, seven dihedrals were parameterised, corresponding to CH_3-Si-O-Si (D1), Si-O-Si-CH_2 (D2), Si-O-Si-O (D3), O-Si-O-Si (D4) and O-Si-CH_2-CH_3 (D5) on the backbone of the chain, as well as the two Si-O-Si-CH_3 (D6, D7) dihedrals, those involving the methyl groups located on the central silicon atom in Figure 4.8. Additionally, the fragment shown below enabled the parameterisation of the Si-CH_2-CH_3 (A1) angle, while the parameters, shown in Table 4.4, for angles and bonds that included silicon were obtained from the work of Smith *et al*.,[176] utilising only the quadratic terms to maintain consistency with the force field used in studies by Shi *et al*.[256,257]

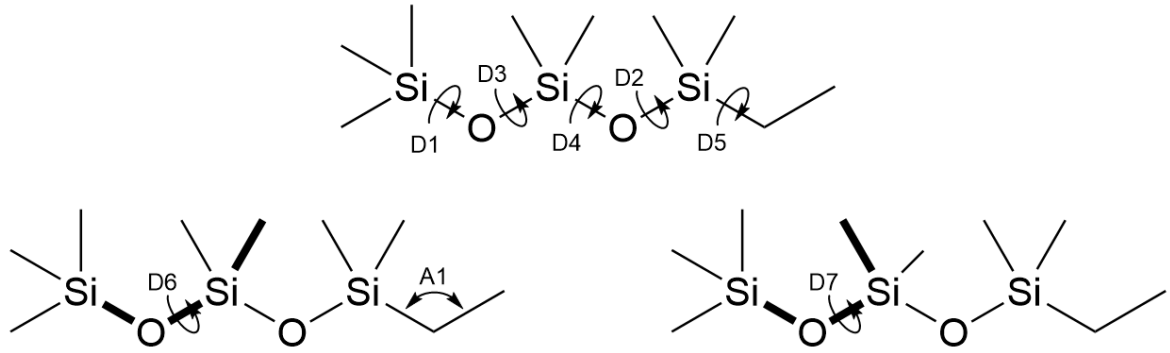

Figure 4.8 A structural representation of the trisiloxane fragment used to parameterise the siloxane-based chain of TSiKN65, highlighting the relevant angles and dihedrals.

Table 4.4 Optimised bonded parameters for atoms linked to silicon in the siloxane chain, reported in Sok *et al.*[253] and Smith *et al.*,[176] in this work only the quadratic terms were utilised.

Bond Type	K_b/kJ mol^{-1} nm^{-2}	b_0/nm
Si-O	292880.0	0.1651
Si-C	158990.0	0.1878
Angle Type	K_θ/kJ mol^{-1} rad^{-2}	θ/°
Si-O-Si	86.232	137.63
O-Si-O	768.480	105.56
O-Si-C	192.650	109.82
C-Si-C	303.000	112.44
Si-C-H	240.740	111.09

After an optimised structure for the trisiloxane fragment had been obtained, potential energy scans were carried out on all relevant angles and dihedrals, during which all other angles and dihedrals within the fragment were fixed. As described in the previous section, fixing the dihedrals not under investigation at a constant angle avoids the potential for large discontinuous jumps in energy caused by the shifting positions of other angles within the molecule, and avoids the need to fit all the dihedrals concurrently. The potential energy scan performed on A1 consisted of 70 steps with a 1° interval, resulting in an analysis of the energy between 90° and 160°. all of the potential energy scans performed on the dihedrals in this section used a 5° interval over 72 steps, corresponding to a full 360° rotation of the torsional angle. After the potential energy scans were fully completed, single point energy calculations were performed at the MP2/6-311G(d,p) level at every step of each scan, consistent with that applied previously..

The effectiveness of the default GAFF parameters used to describe the bonded interactions highlighted in Figure 4.8 were probed by analysing the MD energy of the structural fragment for each geometry of the potential energy scans. However, before this could be done, the necessary parameters for the MD simulation of the siloxane fragment had to be assigned within the Antechamber software package, and the partial charges were calculated using the RESP method. The default bond and non-bond parameters provided by GAFF were subsequently substituted for the optimised values offered by the literature.[176,253,256,257] After this initial setup, the MD energy could be

determined for each structure at each frame of the potential energy scans performed previously. These results were then compared with the MP2 energy values, so that the ability of the default GAFF parameters to correctly model the angle and torsional potentials in TSiKN65 could be evaluated.

4.3.2.1 Angle Parameterisation

The A1 angle was investigated through calculation of the MD energy using the default force constants, and these values are plotted alongside the equivalent MP2 energies in Figure 4.9. The clear deviation between the two data sets presented below implies that the GAFF parameters do not accurately describe the behaviour of the Si-CH_2-CH_3 bond in the siloxane fragment. In Figure 4.9, the default force constants seem to greatly overestimate the energy as the bend angle approaches 160°, while the relative energy at values close to 90° also appears to diverge, although to a much lesser extent. In contrast, the standard parameters are shown to fairly closely reproduce the equilibrium angle predicted by the MP2 calculations, with the lowest energy structure predicted to exist at angles of *ca*. 114° and 116°, respectively.

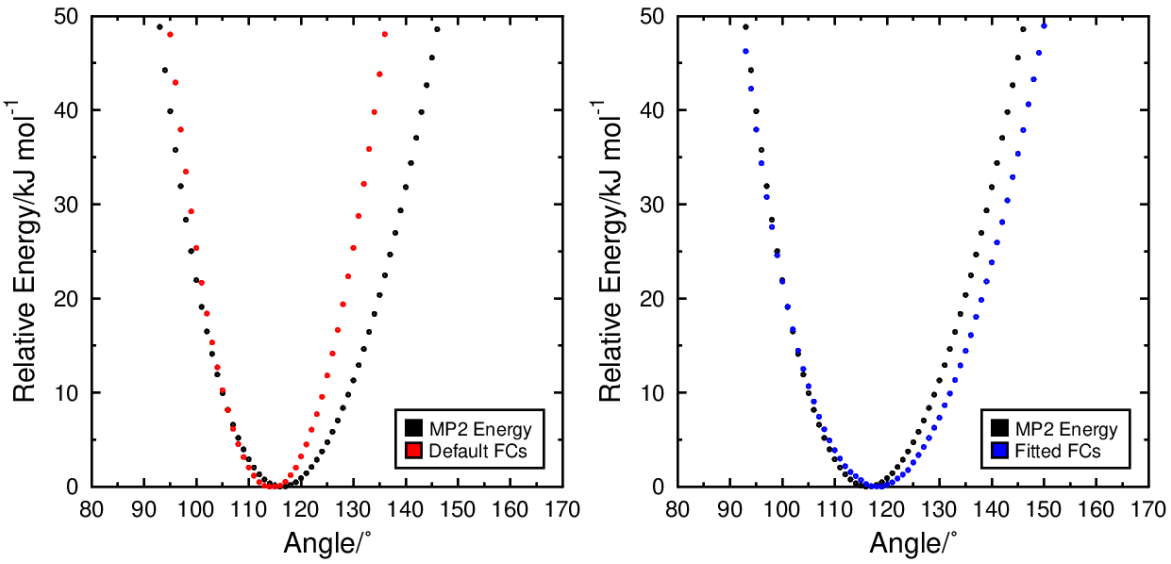

Figure 4.9 A graphical comparison of the MP2 energy versus the MD energy while employing default GAFF force constants (left) and fitted force constants (right) for angle A1, carried out using 1° intervals between 90° and 160°.

Despite the similarity between the equilibrium angle predicted by the default parameters and the MP2 calculations, optimisation of force constants for A1 was still judged necessary due to the large disparity in relative energy at angles ≥ 120°, which may be particularly relevant to chain conformation in siloxanes because of their flexibility. Accordingly, an improved set of force constants had to be obtained by fitting to the energy values determined at the MP2 level. This fitting procedure was identical to that described for the perfluoropolyether parameterisation in the section above, The MD energy calculated using the fitted force constants is shown in Figure 4.9, exhibiting

a closer agreement with the MP2-derived values at all angles. Most noticeably, while the energy remains slightly overestimated at angles approaching 160°, the fitted values are significantly more consistent with MP2 energy, relative to the default GAFF force constants. Likewise, the optimised parameters appear to closely reproduce the equilibrium angle, indicating the lowest energy structure possesses an Si-CH_2-CH_3 bend angle of 117°, in good agreement with MP2-derived values of 116°. As a result, the newly developed parameters for A1 described here were subsequently applied to the trisiloxane fragment throughout the parameterisation of the torsional potentials, discussed below.

4.3.2.2 Dihedral Parameterisation

As the siloxane fragment contains several seemingly comparable dihedrals, the parameterisation method used previously was slightly modified so that the force constants would be fitted using two separate sets of data. This alteration of the parameterisation procedure enabled the number of newly optimised parameters to be reduced, while also maintaining consistency between the behaviour of equivalent torsional angles. Initially, the dihedrals corresponding to CH_3-Si-O-Si (D1) and Si-O-Si-CH_2 (D2) in Figure 4.8 were analysed.

The parameterisation procedure applied to the D1 and D2 dihedrals followed a similar method to that described previously, with the MD energy determined after assigning all of the relevant force constants a value of zero. However, in this case, the parameters were optimised by fitting to the MP2 energy of D1 and D2 simultaneously, in an effort to maintain a degree of consistency between equivalent dihedrals. This was achieved by calculating the difference between the MD energy, while employing zero force constants, and the MP2-derived energy, before the fit was performed within *R*. The parameters were obtained via a weighted fit, which was calculated from the Boltzmann distribution of D1 and D2 at 298 K. Figure 4.10 shows the MD energy calculated using the newly derived parameters, together with the MP2 energy. The data indicates that the optimised force constants result in a reasonable replication of torsional behaviour for D1. Most notably, the energy maxima are fairly well represented, while the energy minima predicted by the *ab initio* calculations are closely reproduced by the parameters developed here. Although Figure 4.10 reveals that the fitted force constants fail to perfectly replicate the relative energy values for D1, they do predict the particularly low torsional energy barrier typically associated with siloxane chains. As a result, these improved parameters, summarised in Table 4.4, were adjudged to be suitable for the subsequent MD simulations of TSiKN65.

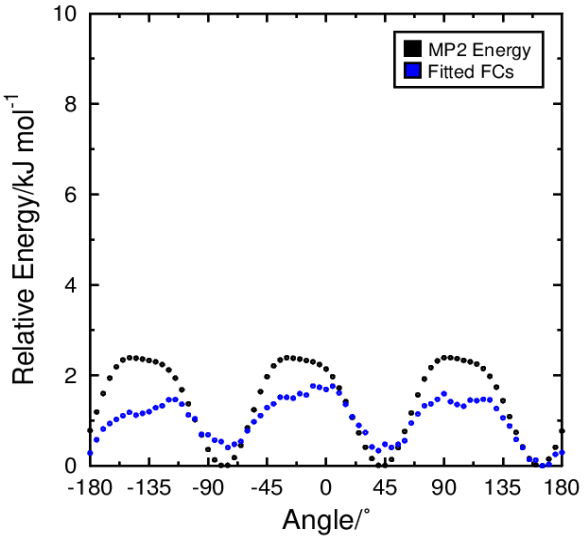

Figure 4.10 A graphical comparison of the MP2 energy (black) versus the MD energy employing fitted force constants (blue) for dihedral D1, performed with 5° intervals between -180° and 180°.

In Figure 4.11, the equivalent comparison from the analysis of D2 is plotted, highlighting the MP2 energy from the potential energy scan of D2, as well as the MD energy determined while employing the force constants derived above. Much like for D1, the D2 torsional potential appears to be fairly accurately reproduced by the newly developed parameters. While the MD energy is shown to be slightly overestimated at most points between -180° and 180°, relative to the MP2 energy, the energy minima seem to be closely replicated by the optimised parameters. In addition, the relative energy appears not to exceed 4 kJ mol^{-1}, which is consistent with the low torsional energies observed in Figure 4.10.

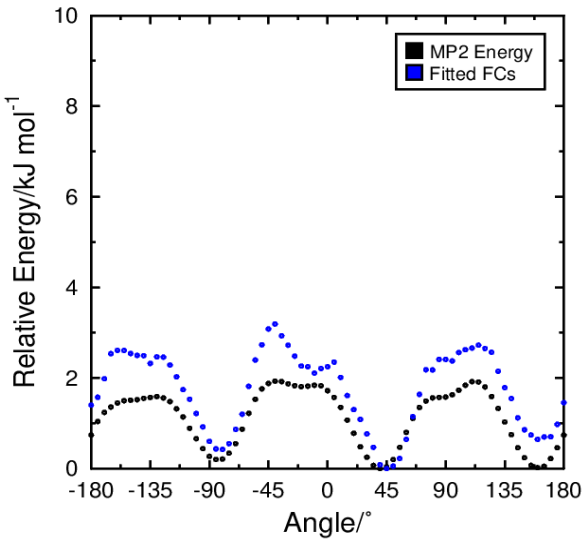

Figure 4.11 A graphical comparison of the MP2 energy (black) versus the MD energy employing fitted force constants (blue) for dihedral D2, performed with 5° intervals between -180° and 180°.

The implementation of the optimised force constants for D1 and D2 can reasonably be expected to provide an improved description of the torsional potentials, with the relatively low energy barriers

involved in dihedral rotation a well-known characteristic of siloxane chains. This feature appears to be successfully captured by the MD energy while employing the fitted parameters and may have a substantial influence on the overall conformation and dynamics adopted by the siloxane chain in MD simulations of TSiKN65.

An identical parameterisation procedure was then applied to dihedrals D3 and D4, corresponding to the Si-O-Si-O and O-Si-O-Si dihedrals in Figure 4.8. Figure 4.12 shows the fitted MD energy through a 360° rotation of D3, suggesting that the optimised parameters provide a relatively close description of the MP2 energy at the majority of angles. Notably, while the relative energies are well-matched between -180° and 0°, the energy minimum is predicted to exist at *ca*. -80° by the new force constants, slightly lower than the minimum at *ca*. -65° exhibited by *ab initio* calculations. At higher angles, the MD energy shows a nice consistency with the MP2 values, with the shape of the torsional potential largely comparable. As a result, the parameters developed here, also presented in Table 4.4, could be applied throughout subsequent MD simulations of siloxane materials.

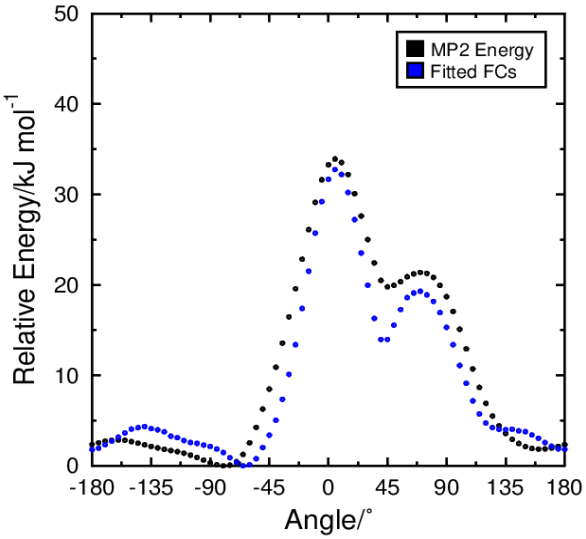

Figure 4.12 A graphical comparison of the MP2 energy (black) versus the MD energy employing fitted force constants (blue) for dihedral D3, performed with 5° intervals between -180° and 180°.

Figure 4.13 shows a comparison of the MP2 energy, and the MD energy determined from the fitted force constants described above. The two data sets deviate from one another in several key aspects, most significantly, the highest energy structure is predicted to exist at *ca*. 80° when employing the optimised parameters, inconsistent with that predicted by the *ab initio* calculations, in which the relative energy maximum occurs at *ca*. 40°. Additionally, the MD energy diverges from the MP2-derived energy in a number of more subtle ways. A small increase in the relative energy is predicted between -180° and -165°, which appears to be underestimated relative to the MP2 values throughout the equivalent range. Nevertheless, despite these inconsistencies, the parameterised force constants capture many crucial features of the torsional potential. Significantly, the relative energies between -150° and -30° including the energy minimum, as well as between 120° and 180° appear to be well

replicated by the new parameters. The clear similarities between the predicted torsional potential of D4, provided by the fitted constants, suggests that utilisation of the dihedral parameters developed here would likely result in a superior description of TSiKN65 throughout the subsequent MD simulations of the material.

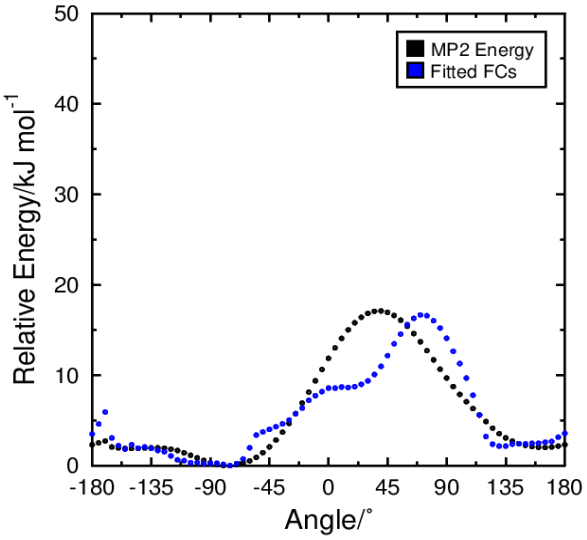

Figure 4.13 A graphical comparison of the MP2 energy (black) versus the MD energy employing fitted force constants (blue) for dihedral D4, performed with 5° intervals between -180° and 180°.

The next set of dihedrals to be simultaneously parameterised were those referred to as D6 and D7, in Figure 4.8, corresponding to the two Si-O-Si-CH_3 dihedrals where the methyl carbon is bonded to the silicon atom attached to only one other CH_3 group. A parameterisation procedure identical to that described above was employed on dihedrals D6 and D7, which involved the calculation of the MD energy after all applicable force constants has been set to zero, before a weighted fit was subsequently performed within *R*. The MD energy determined via the resultant force constants is presented in Figure 4.14, and indicates that the MP2 energy is fairly well replicated at all dihedral angles. There appears to be little discrepancy between the MD and MP2 values in the region of -90-90°, where the relative energy is at its lowest. Likewise, the local maxima predicted by the *ab initio* calculations at -170° and 120° are maintained by the newly developed parameters. As a consequence, it can be confidently stated that the parameterised force constants, shown in Table 4.4, do provide an improved description of D6, which could improve any future simulations of siloxane-base materials.

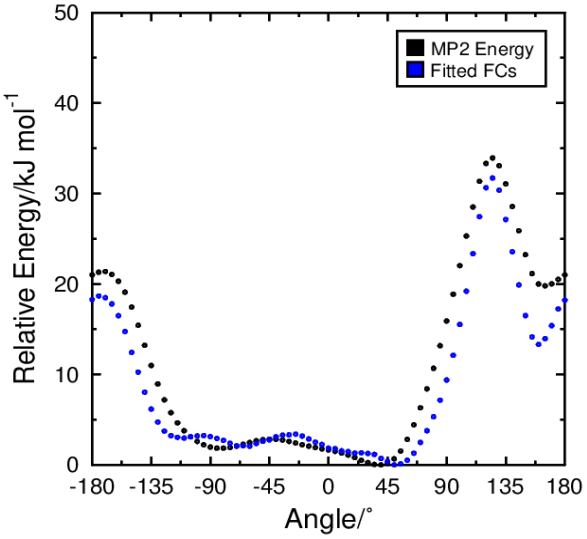

Figure 4.14 A graphical comparison of the MP2 energy (black) versus the MD energy employing fitted force constants (blue) for dihedral D6, performed with 5° intervals between -180° and 180°.

In Figure 4.15, the force constants fitted to D6 and D7 are assessed via a comparison with the MP2-derived values calculated for D7. The MD energy shows reasonable consistency with the *ab initio* calculations at most points in 360° range. The most noticeable differences between the two data sets appears between -180° and -120°, where the energy is slightly underestimated, and between -80° and -20°, where the relative energy is shown to be significantly lower than the energy calculated at the MP2 level. However, while these inconsistencies are important to note, they are unlikely to majorly influence the overall chain conformation due to the relatively high energy at which these deviations occur. In contrast, the newly developed parameters offer a good description of the torsional potential at lower relative energy values. This prioritisation of the fit towards points of lower energy highlights the advantage of the weighting method used throughout this section.

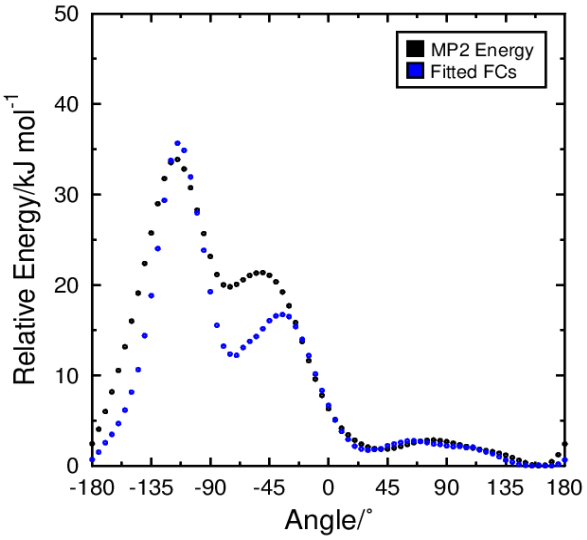

Figure 4.15 A graphical comparison of the MP2 energy (black) versus the MD energy employing fitted force constants (blue) for dihedral D7, performed with 5° intervals between -180° and 180°.

Finally, the O-Si-CH_2-CH_3 dihedral, referred to as D5 in Figure 4.8, was analysed in order to evaluate the newly derived force constants. The parameterisation procedure applied to D5 involved no other dihedrals, due to a lack of equivalent dihedrals within the structure of TSiKN65. In Figure 4.16, a comparison of the MP2 energy and the MD energy determined while employing the optimised parameters is presented, highlighting that the two data sets are consistent at most angles between -180° and 180°. Significantly, the MD and MP2 energy values are well matched at *ca*. -70° and *ca*. 70°, corresponding to the minimum energy structures. Overall, the force constants developed for D5, which are presented in Table 4.4, provide a suitable model of the true torsional potential, making them particularly appropriate for the MD simulation of materials that contain a trisiloxane moiety.

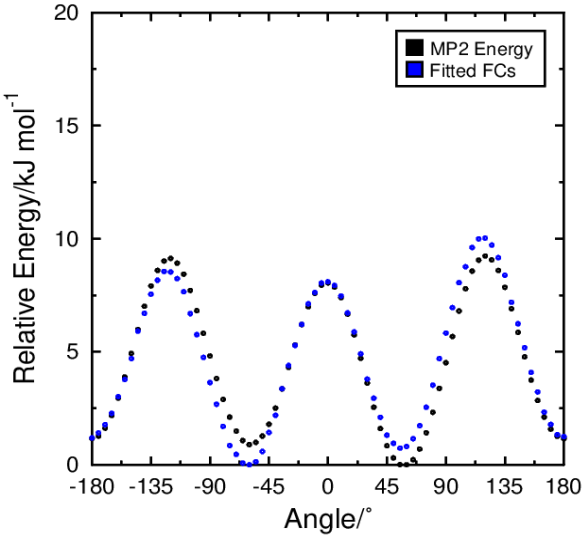

Figure 4.16 A graphical comparison of the MP2 energy (black) versus the MD energy employing fitted force constants (blue) for dihedral D5, performed with 5° intervals between -180° and 180°.

Table 4.5 The optimised force constants corresponding to dihedrals D1-D7, applied to all appropriate torsions throughout subsequent simulations of TSiKN65.

Dihedral	C0	C1	C2	C3	C4	C5
D1/D2	-2.40458	-9.44726	-1.99490	12.45323	0.90290	-0.15392
D3/D4	-1.95827	-9.83635	-6.43318	30.06072	2.88523	-15.70235
D6/D7	0.80740	2.30550	-0.92220	-0.96250	-0.44471	-2.61280
D5	-0.36983	-2.65653	-3.03071	3.72594	0.74706	0.50434

4.4 Conclusions

Force constant parameterisation was performed making use of several different molecular fragments in an effort to more realistically model the perfluoropolyether and trisiloxane chains of 3M 8422[84] and TSiKN65,[83] respectively, using the GAFF force field.[181] The research performed in this section forms the basis of the MD simulation work described within Chapter 5 and Chapter 6.

For the parameterisation of the perfluoropolyether chain, a total of one angle and four dihedrals were studied, initially through the running of potential energy scans, and later the use of single point energy calculations at an MP2 level of theory. The relevant van der Waal's and electrostatic parameters, specific to perfluoropolyether compounds, were obtained from the work of Black *et al*.,[251] and utilised throughout the entire parameterisation procedure. Analysis of the fitted force constants demonstrated that they provided a significantly improved description of the angle and torsional potentials predicted by the *ab initio* calculations relative to the default force constants. Such results imply that the optimised parameters would offer a fairly realistic representation of the chain conformation within 3M 8422, highlighting the value of the force constant parameterisation method employed within this section.

In the parameterisation of the trisiloxane chain, one angle and seven dihedrals were investigated by employing potential energy scans, and subsequent single point energy calculations at an MP2 level of theory. A number of parameters related to both the bonded and non-bonded interactions of siloxane compounds were obtained from the work of Sok *et al*.[253] and Smith *et al*.,[176] before they were applied to the trisiloxane fragment utilised throughout the parameterisation process. Optimisation of the force constants followed a very similar method to the perfluoropolyether parameterisation. However, in the case of the TSiKN65 fragment, dihedrals adjudged to be equivalent were fitted simultaneously, resulting in a single set of parameters that were applied to two torsional angles. Evaluation of the force constants fitted in this way, comparing them with those supplied by the default GAFF force field, showed they provided a superior description of the torsional potential. These results indicated that the optimised force constants derived in this work would likely provide a reasonable representation of the trisiloxane chain within TSiKN65.

The work performed here on 3M 8422 and TSiKN65 demonstrates the ability of force constant parameterisation methods based on *ab initio* data, which can be fairly easily obtained, to provide an improved description of bonded interactions that may be outside the scope of common general force fields. Likewise, the weighting method used in this section based on the calculation of a Boltzmann distribution from *ab initio*-derived energy values is not commonly reported in the literature, yet such a technique enables the fitting procedure to prioritise points on the potential energy surface at which the highest molecular populations are likely to exist. Finally, the parameterisation methodology

employed above has the potential to be used in computational studies of other ‘unconventional’ chemical moieties, many of which regularly appear as key elements liquid crystalline materials.

Chapter 5 – Molecular Dynamics Study of Perfluoropolyether-Based 3M 8422

This chapter focuses on the molecular dynamics study of the semi-perfluorinated material 3M 8422, reported in the literature to exhibit substantial de Vries behaviour. The parameterisation procedures that enabled a suitably accurate simulation of this perfluoropolyether-based liquid crystal are outlined, while the MD techniques employed throughout the study are also reported. The analysis performed on the simulated phases of 3M 8422 is described, quantifying order parameters, tilt angles and layer spacings. All further analysis is also discussed, providing an assessment of molecular behaviour in phases of 3M 8422 over a wide temperature range, in addition to molecular-level characterisation of the smectic layer structure. The results of this analysis are then interpreted, and comparisons are made where possible with several experimental studies of 3M 8422, reported in the literature, as well as with the MD simulations of 9HL reported in Chapter 3.

5.1 Introduction

This section provides a short introduction to MD simulations of perfluorinated compounds, as well as the common issues encountered when modelling such materials. The development of improved force fields for the simulation of perfluoropolyether-based compounds is also discussed. Several experimental studies investigating semi-perfluorinated liquid crystals that reportedly exhibit de Vries character are reviewed before the section concludes with an outline of the initial aims of the work presented within this chapter.

5.1.1 Issues Associated with MD Simulations of Perfluoro-Compounds

As discussed previously, compounds that are wholly or partially perfluorinated have attracted interest from numerous different fields due to their distinctive properties and their usefulness in a variety of applications. Their remarkable diversity of functions is illustrated by the use of perfluoro-based compounds as surfactants and solvents,[261–263] as microfluidics,[264] as well as their use in power generation and for biomedical applications.[265–268] Additionally, a number of liquid-crystalline compounds also contain perfluorinated structural elements, most often in the form of perfluorinated terminal chains, which have been reported to have a significant effect on liquid-crystalline phase behaviour, giving rise to several unconventional material properties.[111,269–272] The mesomorphic properties exhibited by semi-perfluorinated liquid crystals would likely benefit from computational study at an atomistic level, allowing the behaviour of the perfluoro-based molecular sub-units to be probed. However, while such an investigation may potentially provide valuable insight into the overall mesophase behaviour of perfluorinated materials, atomistic MD simulations employing standard force field parameters has proved largely ineffective at accurately predicting the chemical properties of perfluoro-based compounds.[234]

As computational techniques have become increasingly widespread and have been applied to an ever-expanding range of chemical systems, a considerable amount of research has been devoted to

improving the capacity of MD simulations to describe several of the key characteristics of perfluorinated compounds. The ability of the OPLS-AA force field to reproduce the immiscibility observed in mixtures of alkanes and perfluoroalkanes has been considered in a study by Song *et al.*,[234] which found that the Lennard-Jones and Coulomb interactions, in combination with the commonly used Lorentz-Berthelot combining rules,[273] substantially overestimate the interactions between alkane and perfluoroalkane molecules, leading to substantial deviations from the experimentally observed properties of such mixtures. However, the report concluded that a reasonable agreement with many experimental quantities could be obtained by reducing the strength of the Lennard-Jones interactions between hydrogen and fluorine atoms by ~ 25% relative to that predicted by the geometric Lorentz-Berthelot combining rules. More recently, a study carried out by Nikitin *et al.*,[235] has similarly examined the ability of the AMBER force field to model perfluoroalkane/alkane mixtures, reporting once more that the Lorentz-Berthelot combining rules inadequately describe many of their properties. In the study, several quantities were re-parameterised through high-level ab initio calculations to more accurately model the conformational properties of perfluorinated alkanes. In addition, the Waldmann-Hagler combining rules were preferred for all elements except hydrogen. This newly developed force field was validated by comparing the results with experimental measurements, showing a significant improvement in the ability to describe perfluoroalkanes relative to the parameters supplied by the standard AMBER force field. While such studies indicate that the modification of the standard Lorentz-Berthelot rules can indeed improve the accuracy of MD simulations that aim to model material properties of perfluorinated compounds, several other studies have focused on improving the ability of some force fields to reproduce physical properties, while employing the standard combination rules for Lennard-Jones interactions.

As mentioned above, the potential to accurately model perfluoropolyether materials with standard force fields has also attracted interest due to their blend of useful properties, most notably their high stability, nontoxicity, nonflammability and high viscosity. Consequently, numerous theoretical studies, employing a variety of different representations, have attempted to elucidate the molecular-level behaviour of perfluoropolyethers. Many of the earliest studies utilised a course-grained description of perfluoropolyether molecules,[237,238,241,242] typically based on a bead-spring model developed by Guo *et al.*,[237] and provided various valuable insights into the material properties of these compounds. Several more recent studies have used a higher-resolution approach to investigating perfluoropolyethers,[239,240,243–248] employing force fields such as the universal force field,[246] and the DREIDING force field.[247,248] Additionally, a united atom force field, specifically for the molecular simulation of perfluoropolyethers, has been developed by Li *et al.*,[249,250] primarily from *ab initio* calculations, which shows significantly improved predictions of critical temperature and density in short-chain perfluoropolyethers. As discussed in the previous chapter, work by Black *et al.*,[251] has provided a new force field for such compounds that implements an atomistic potential

and is based on OPLS-AA.[274] Derived from a combination of experimental and *ab initio* quantum mechanical results, this force field utilises several additional parameters to account for interactions specific to perfluoropolyethers, which were shown to provide an improved consistency with experimental measurements of vapour pressure and liquid density. This expansion of an AMBER-based force field has resulted in an improved capacity to reproduce key properties associated with perfluoropolyether compounds via an atomistic potential model, with perfluoropolyether-based liquid crystals an appealing target due to their reported ability to exhibit de Vries character.[84,111]

5.1.2 Experimental Investigations of 3M 8422

Partial perfluorination of a liquid crystalline material often significantly impacts its mesophase character. For example, the introduction of semi-perfluorinated chains typically promotes the formation of smectic layers while also having noticeable effects on properties such as viscosity and birefringence.[232,275] These factors make liquid crystals incorporating perfluorinated sections particularly appealing for applications in SSFLC-based devices.[50] As a result, numerous studies have been published attempting to characterise the phase behaviour of perfluorinated compounds, some of which are reported to exhibit unusual material properties.[78,84,111] Some of the earliest studies to report on the perfluoropolyether-based de Vries compound referred to as 3M 8422, shown in Figure 5.1, were performed by Mach *et al*.,[269,276] investigating the properties of free-standing liquid crystal films and showing that a significant negative thermal expansion in the layer spacing could be observed across a wide temperature range, encompassing both the SmA and SmC phases.

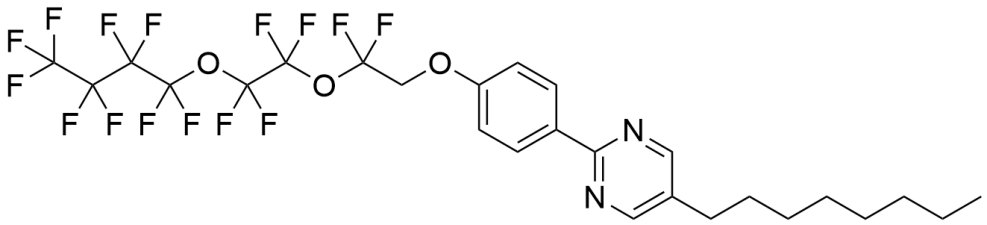

Figure 5.1 The chemical structure of the liquid crystalline compound 3M 8422 (Cr 8.00°C SmC 49.00°C SmA 70°C I).[84]

A second study, probing the layer thickness and tilt behaviour of 3M 8422, was carried out by Radcliffe *et al*.[84] In this study, it was found that 3M 8422 exhibits a remarkably consistent layer spacing across the SmA-SmC transition, indicating a considerable degree of de Vries character. Additionally, the tilt angle derived from x-ray diffraction experiments was demonstrated to be significantly lower than that observed through optical measurements, implied to be caused by an increase in the tilt exhibited by the mesogenic core, relative to the rest of the 3M 8422 molecule. In considering the results, the report also outlines several mechanisms that may explain an absence of observed layer shrinkage in 3M 8422, including non-uniform molecular tilt behaviour, changes in molecular interdigitation or perfluoroether tail flexibility, as well as the possibility of a ‘de Vries-

like' tilted SmA phase. However, the study ultimately concludes that further work is required to provide a more definitive insight into the minimal layer shrinkage exhibited by 3M 8422.

A chiral analogue of 3M 8422, referred to as 3M 8422[2F3], was characterised in a more recent study carried out by Lagerwall *et al*.[111] In this investigation, x-ray diffraction was used to determine the layer spacing exhibited by 3M 8422[2F3], which showed minimal change between the SmA* and SmC* phases. Likewise, x-ray data was used to probe the orientational distribution function, from which the orientational order and molecular tilt were obtained, exhibiting values fairly typical of de Vries materials. In addition, birefringence and optical tilt measurements suggested that the SmA*-SmC* transition was second-order in nature, while the birefringence also indicated that the orientational order increased from the SmA* into the SmC* phase. The study concluded that these results revealed that the reduction in layer contraction demonstrated by 3M 8422[2F3] was likely due to the existence of a 'diffuse cone' molecular arrangement in the SmA* phase.

5.2 Aims

The ultimate aim of the research described in this chapter was to examine the de Vries behaviour of the perfluoropolyether-based compound 3M 8422, shown in Figure 4.1, through the use of MD simulations. The intention was to carry out MD simulations at various points across the experimentally reported SmA and SmC temperature range, while identifying any simulated smectic phases and quantifying any potential de Vries character. A further aim was to characterise the underlying causes of de Vries behaviour on a molecular level and subsequently compare the results to those observed in simulated phases of 9HL, considered in Chapter 2. This comparison is of particular relevance due to the clear difference between the structural features present in the two molecules, the nature of which are commonly reported to play a vital role in the promotion of de Vries character.

5.3 Results and Discussion

A DFT optimisation of 3M 8422 at the B3LYP/6-31G(d) level[131,189] was performed, providing a low-energy geometry from which the initial system utilised in subsequent MD simulations could be constructed. Partial charges were derived for atoms in the non-perfluorinated sub-units by applying the RESP method,[197] whereas the charges within the perfluoropolyether chain were obtained from the study by Black *et al*.,[251] which, as discussed previously, is reported show an improved consistency with several key experimental measurements. Subsequently, the partial charges of the non-perfluorinated sub-units were adjusted by a value of ≈0.0005 to ensure the overall charge of 3M 8422 molecules was effectively zero, preventing any potential simulation artefacts related to the presence of molecular species with a non-zero charge. Additionally, several non-bond parameters, presented in Table 3.1, reported to capture the behaviour of perfluoropolyether compounds more accurately, were used in place of the default non-bond parameters supplied by the GAFF force field.

In this chapter, the total simulation time varied between a minimum of 500 ns and a maximum of 900 ns across all the simulations performed here. In total, six fully atomistic MD simulations were performed on systems of pure 3M 8422 at 10 K intervals between 280 K and 330 K. This simulated temperature range fully encompasses the experimentally reported SmA and SmC phase ranges, and provides several data points either side of the experimentally-derived SmA-SmC transition of 48.0-49.0°C.[84,277]

The sections that follow describe the analysis of these simulations, including the calculation of both orientational and translational order parameters, quantification of de Vries behaviour and consideration of associated molecular distributions. Additionally, the discussion below focuses on potential explanations for any observed reduction in layer contraction and makes comparisons with the work performed on the de Vries material 9HL, described in Chapter 3.

5.3.1 Determination of Order Parameters

Molecules of 3M 8422 were confirmed to exhibit considerable orientational order, typically indicative of mesophase formation, at each simulated temperature. The P_2 values associated with the orientational order are plotted for each temperature in Figure 5.2, which reveals an overall decrease in orientational order as the temperature is increased, consistent with the behaviour of conventional liquid crystal materials. P_2 values of 0.80-0.95 indicate a high degree of orientational order is present within the simulated systems, but a direct comparison to real systems is difficult due to the lack of order parameter data available for the non-chiral 3M 8422 in the literature. Nevertheless, the simulated values of 0.80-0.95 are considerably higher than those of *ca*. 0.56, derived from x-ray scattering experiments carried out on a chiral analogue of 3M 8422, referred to as 3M 8422[2F3].[88,111]

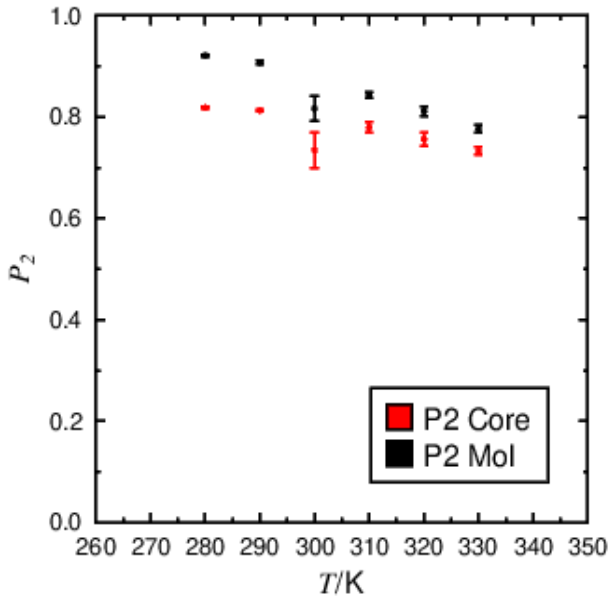

Figure 5.2 Plot of the average orientational order parameter (P_2), for the mesogenic core (red) and the whole molecule (black), with respect to **n**, determined from simulations between 280 K and 330 K, with associated error bars.

In this work, P_2 values were calculated for two different axes within the molecule, which are shown as separate data sets in Figure 5.2. The principle molecular axis, representative of the whole molecule, was defined as that calculated from the minimum moment of inertia (MOI) of the entire 3M 8422 structure, while the second axis was determined from the minimum MOI of only those atoms in the aromatic core. The clear separation between the P_2 values plotted in Figure 5.2 implies that molecular sub-units within 3M 8422 do not exhibit an identical amount of orientational order. More explicitly, the data presented in Figure 5.2 indicates that the aromatic cores are on average less orientationally ordered than the molecule as a whole at all simulated temperatures. In addition, the terminal chains of 3M 8422 seem to become increasingly more ordered, relative to the order exhibited by the aromatic cores, as the temperature decreases. These trends observed in the simulated data appear to be consistent with experimental studies,[88,111] which have reported on the orientational distribution functions of several de Vries materials, including the perfluorinated compound 3M 8422[2F3].

The final frames of the simulations performed at 280 K and 330 K are visualised in Figure 5.3, with each snapshot displaying a substantial level of orientational order and the existence of a distinct layer structure. In Figure 5.3, the visualisation of the phase at 280 K also appears significantly more ordered than that at 330 K, consistent with the P_2 values plotted in Figure 5.2. Additionally, the snapshots indicate that molecules are, on average, tilted relative to the layer normal at 280 K, whereas this seems not to be the case at 330 K, indicating that a simulated SmA-SmC transition likely exists between these temperatures.

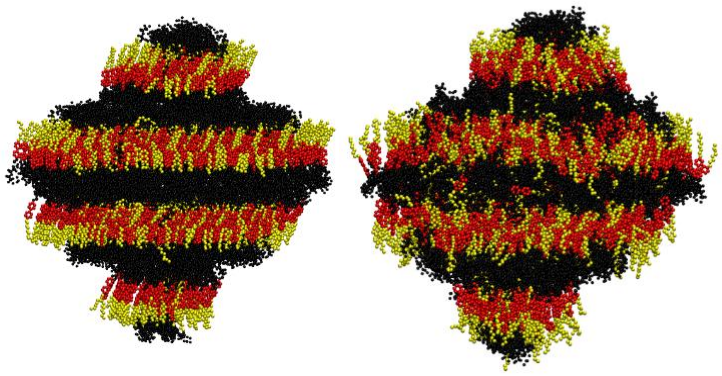

Figure 5.3 Visualisation of the simulations of 3M 8422, showing the aliphatic chains (yellow), aromatic cores (red), and perfluoropolyether chains (black), at 280 K (left) and 330 K (right), respectively.

The τ values corresponding to each simulated temperature are plotted in Figure 5.4, and show a general decrease between 280 K and 330 K. Average values of *ca*. 0.60-0.80 suggest the development of a well-defined layer structure at all temperatures, while the slightly elevated values associated with the simulations carried out at 290 K and 280 K are consistent with the visualisations discussed above. The simulated values below correspond well to those derived from an x-ray study of 3M 8422, in which τ was determined to be between *ca*. 0.70-0.80 in the SmA phase.[30] In addition, the relatively high value of τ exhibited by 3M 8422, both computationally and experimentally, is fairly typical of materials reported to exhibit de Vries character,[30] in which micro-phase separation of chemically incompatible sub-units has been reported to act as the primary driver of mesophase formation.[222,278]

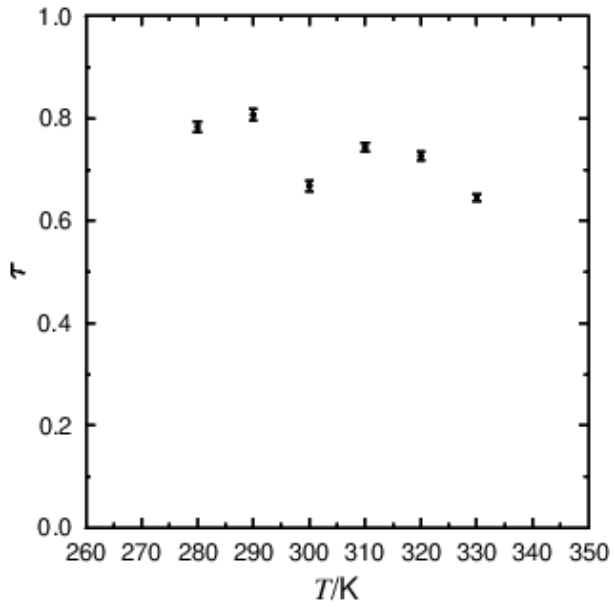

Figure 5.4 Plot of the average translational order (τ) determined from simulations between 280 K and 330 K, with associated error bars.

The upper limits of the data presented in Figure 5.2 and Figure 5.4 correspond to the simulated phase structure at 330 K, however, in performing the work reported on within this chapter equivalent simulations were performed at 340 K. At this higher temperature orientational and translational order

was calculated to be minimal, i.e., ≤ 0.2, across the phase structure. This observation of 'melting behaviour' approaching 340 K compares favourably with experimental studies of 3M 8422,[84,277] suggesting that the simulations performed in this work have the capacity to accurately reproduce the key characteristics associated with phase transitions, and further evidenced by their ability to correctly predict the direct smectic-isotropic transition observed experimentally in 3M 8422.

5.3.2 Tilt Angles and Layer Spacings

As discussed in Chapter 3, at the SmA-SmC transition the director tilts relative to the layer normal, and this tilt can be quantified through measurement of the angle between vectors **n** and **k**. The average tilt exhibited by the equilibrated phases at each temperature are shown in 5.5, revealing an overall decrease in tilt with increasing temperature. Most noticeably, a significant shift in the tilt angle occurs between 290 K and 300 K, indicating that the simulated SmA-SmC transition is located between these two temperatures. This simulated transition lies approximately 20-30 K lower than the experimentally reported transition temperature at 321 K.[277] Similar to in the analysis of orientational order, two sets of tilt measurements are displayed in Figure 5.5, representing the MOI axis of the whole molecule and the MOI axis of only the aromatic core unit. Although the difference between the tilt of these two vectors appears to be minimal in the SmA phase, in the SmC phase the tilt of the molecular axis is shown to be considerably lower than that of the aromatic core axis. This clear difference, consistent with the orientational order data presented in Figure 5.2, indicates that parts of the molecule may not tilt in a uniform manner as assumed when molecules are approximated to behave as 'rigid-rods'. When comparisons are made to experimentally derived values, it is apparent that the simulated tilt of the aromatic cores of *ca*. 21° in the SmC phase corresponds well with an optical tilt of 25° reported within the scientific literature.[84] Likewise, the molecular tilt of *ca*. 13-15° is consistent with the experimentally measured tilt of *ca*. 10-15°, determined from x-ray diffraction data presented in the same paper.

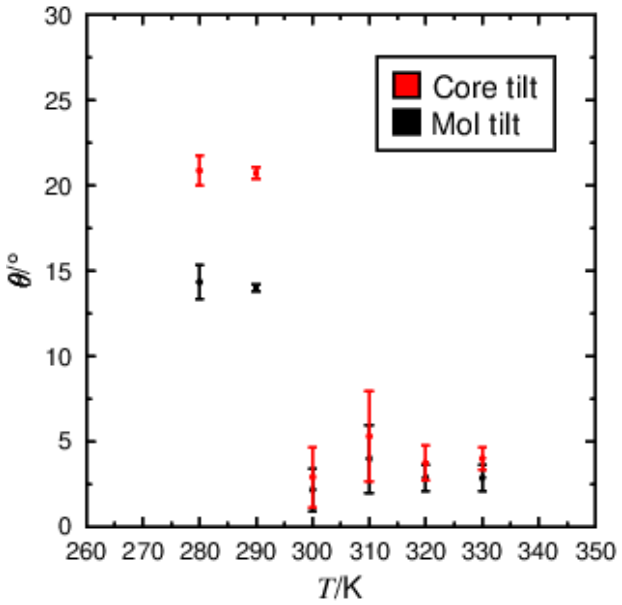

Figure 5.5 The average tilt between the layer normal (**k**) and the director (**n**), for the mesogenic core (red) and the whole molecule (black), determined from simulations between 280 K and 330 K.

It is clear from Figure 5.5 that both the molecule as a whole and the aromatic core exhibit a small but non-zero tilt angle ($\leq 5°$) in the SmA phase. This observation is consistent with the behaviour of 9HL, and, as discussed previously, may be explained by the existence of tilt fluctuations in the SmA phase.[97,111] A non-zero tilt in the SmA phase may also be a simulation artefact caused by the inherent limitations on system size. Like in the study of 9HL, the small size of the simulated systems studied here, relative to the dimensions of an experimental liquid crystal sample, has the potential to result in minor fluctuations in the layer structure appearing more significant in the simulation analysis.

The relationship between the tilt angle and layer thickness is the primary factor that influences whether a material may be referred to as 'de Vries'. The average layer thickness calculated within the equilibrated phases of 3M 8422 is plotted in Figure 5.6, showing a remarkable consistency across all simulated temperatures. The layer thickness appears to experience a decrease from 3.39 nm at 290 K down to 3.36 nm at 300 K, which is the opposite behaviour to that observed upon the conventional SmA-SmC transition. Nevertheless, these values are consistent with those reported experimentally, where values of *ca*. 3.20 nm[84] and 3.30 nm[78,88] were measured across the SmA-SmC temperature range using x-ray scattering experiments. The overall trend in layer thickness measurements reported experimentally also appear to support that exhibited in Figure 5.6, providing evidence that the layer thickness indeed increases in the SmA phase closer to the SmA-SmC transition, likely a cause of the decrease in temperature resulting in the flexible terminal chains adopting a more extended conformation. Measurement of the smectic layer shrinkage, commonly used to quantify a material's de Vries character, results in a negative value due to the smaller layer thickness in the SmA phase relative to that in the SmC phase. Therefore, it can be stated that the simulated phases of 3M 8422 reported on here exhibit a layer shrinkage significantly lower than the

generally quoted value of ≤ 1%, which is frequently used as the benchmark for materials displaying de Vries behaviour.

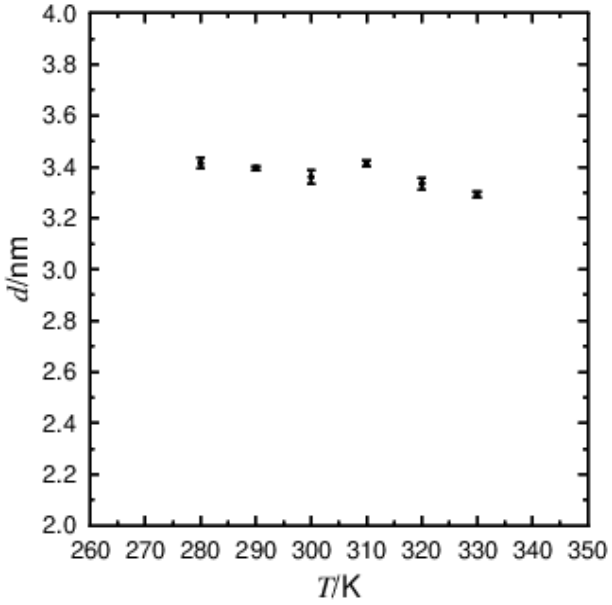

Figure 5.6 The average layer thickness determined from simulations of 3M 8422 between 280 K and 330 K, with associated error bars.

5.3.3 Quantification of de Vries Character

To further probe the tilt behaviour exhibited by 3M 8422 across the simulated temperature range, histograms were plotted from measurements of the angle between the layer normal and the director vectors at each frame, and these are presented in Figure 5.7. The data highlights a significant shift in the tilt angle populations between 290 K and 300 K, consistent with the tilt angle values shown in Figure 4.5. In addition, the smaller spread of data at 280 K and 290 K in Figure 5.7 indicates that tilt fluctuations are greatly reduced in the SmC phase compared to the SmA phase, potentially as a natural consequence of the temperature difference. The non-zero tilt angle values of ≤ 10° measured in the SmA phase could be the result of small layer fluctuations. However, as highlighted in the discussion of Figure 5.5, it is difficult to fully differentiate between small simulation artefacts and legitimate features of the system. Nevertheless, the data presented in Figure 5.5 and 5.7 clearly implies that a transition from a phase with minimal tilt at ≥ 300 K to a phase with significant tilt at ≤ 290 K is captured by the MD simulations.

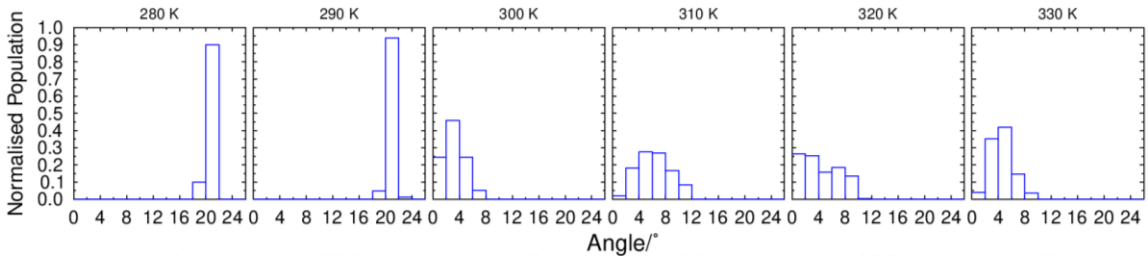

Figure 5.7 Normalised histograms of the angle formed by the vectors **n** and **k** over the final 100 ns of simulations of 3M 8422, performed at 10 K intervals between 280 K and 330 K, shown from left to right, respectively, and determined with bin-widths of 2°.

5.3.4 Orientational Distribution Functions

A subtle change in the orientation of molecules within a lamellar phase can drastically impact the overall layer thickness. However, the slight increase in the orientational order parameter, shown in Figure 5.2, at the simulated SmA-SmC transition is insufficient to rationalise the significant anomaly associated with an increase in molecular tilt. This observation is also consistent with the behaviour of several siloxane-based compounds, in which orientational order is reported to increase upon transition to the SmC phase.[90,279,280]

ODFs representing the minimum MOI axis of the entire 3M 8422 molecule are presented in Figure 5.8, providing a direct comparison to the analysis performed on 9HL. Figure 5.8 clearly exhibits two differently shaped distributions, in the SmA phase (≥ 300 K), the ODFs are centred on 0°, while in the SmC phase (≤ 290 K), the ODFs are noticeably broader and are not centred on 0°. The ODFs indicate that the most probable molecular orientation is parallel to the layer normal above the SmA-SmC transition, corresponding well with the conventional model of the SmA phase. Furthermore, the most probable orientation for individual molecules is tilted away from the layer normal below the SmA-SmC transition, which is also typical of a conventional SmC phase.

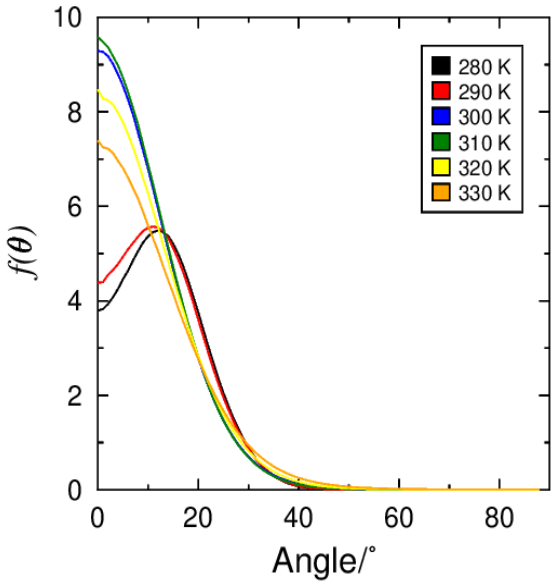

Figure 5.8 Orientational distribution functions, $f(\theta)$, of the minimum MOI vector of the molecules vs **k**, determined from simulations of 3M 8422 at 10 K intervals between 280 K and 330 K. Data was normalised according to $\int_0^{\pi} f(\theta)\sin(\theta)\,d\theta = 1$.

The zero-centred ODFs presented above appear to be inconsistent with the presence of a diffuse cone SmA phase, in which the molecules are tilted but azimuthally disordered. However, these observations are consistent with the results of the 9HL simulations, described in Chapter 3. Furthermore, visualisations of the SmA phase structure, an example of which is shown in Figure 5.3, indicate only minimal molecular tilt, supported by the high P_2 values derived from MD simulations performed at ≥ 300 K.

5.3.5 Molecular Length

As mentioned previously, the thickness of the smectic layers is inherently determined by the effective molecular length. In Chapter 3, analysis of 9HL revealed that the average molecular length increased upon transition to the SmC phase, partly compensating for the layer contraction expected due to the onset of molecular tilt. With this in mind, the calculated molecular lengths, defined as the length of the vector between the terminal CH_3 carbon on the C_8 aliphatic chain and the terminal CF_3 carbon on the perfluoropolyether chain, associated with each simulated temperature are plotted in Figure 5.9. From this data, it is clear that the length of molecules increases as the temperature is decreased, both in terms of the average values and the length distributions. An increase in average molecular length at lower temperatures has the potential to subtly influence the layer thickness, consistent with the idea that molecules are more likely to adopt an extended conformation as the phase is cooled down. The observed increase in length observed here is comparable in extent to that exhibited by 9HL, discussed in detail in Chapter 3. With this in mind, while an increase in the length of 3M 8422 molecules may partially explain the reduction in layer shrinkage it is unlikely to be the only contributor to de Vries character.

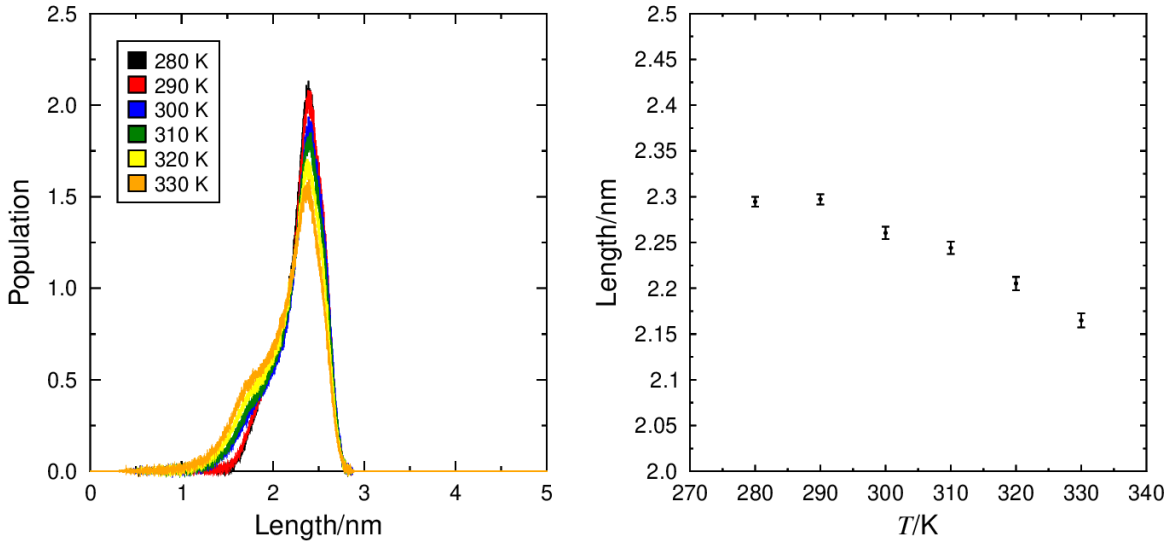

Figure 5.9 The distribution of molecular lengths (left), and the mean molecular lengths of 3M 8422 plotted against temperature (right), determined from simulations of 3M 8422 at 10 K intervals between 280 K and 330 K.

5.3.6 Molecular Interdigitation

The distribution of positions occupied by atoms within 3M 8422 parallel to the layer normal, **k**, at 280 K and 330 K are presented in Figure 5.10. The molecules are defined as "up" or "down" corresponding to whether the projection of the vector derived from the principle molecular axis on **k** is positive or negative. As shown in Figure 5.11, the atoms selected are those located at each end of the molecule, as well as those at the boundaries between the aromatic and aliphatic sub-units, and between the aromatic and perfluorinated sub-units. Figure 5.10 demonstrates that the C26 (CF_3 carbons) and C11 (CH_2 carbons adjacent to the pyrimidine) are roughly coincident for parallel or anti-parallel molecules, supporting the existence of a bilayer structure, also evident within the snapshots shown in Figure 5.3. Likewise, the layer projections indicate that the C26 and C11 atoms are roughly coincident with the centre of the perfluorinated and aromatic/aliphatic sub-layers, respectively. In contrast, the O1 (conjugated oxygens) and C18 (CH_3 carbons) in anti-parallel molecules are out of phase, implying these atoms are located roughly at the interface between the perfluorinated and aromatic/aliphatic sub-layers. The distributions derived from 280 K and 330 K are generally alike, indicative of only very minimal shifts in the position of molecules within the layer structure between the SmA phase and SmC phase.

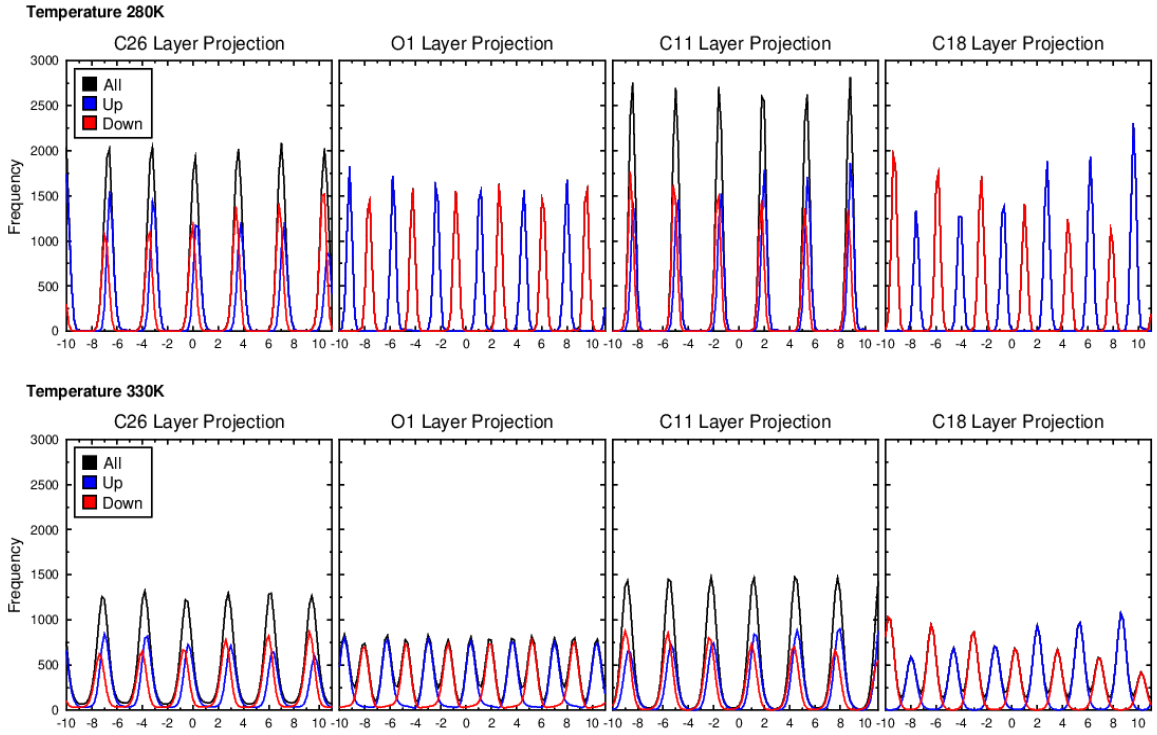

Figure 5.10 Layer projections for atoms C26, O1, C11 and C18 shown from left to right, respectively, for the simulations at 280 K (top) and 330 K (bottom).

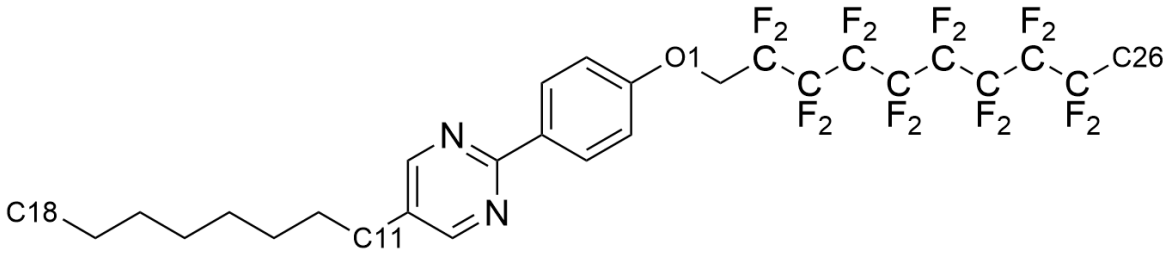

Figure 5.11 The structure of 3M 8422 highlighting the position of the projection atoms C26, O1, C11 and C18.

Further analysis of the layer structure is presented in Figure 5.12, which shows the extent to which the two end groups of 3M 8422, defined as the CH_3 carbon on the C_8 aliphatic chain and the CF_3 carbon on the perfluoropolyether chain, are interdigitated. These values were determined in accordance with the method laid out in previous work, where an atom is interdigitated if it lies beyond the overall layer position, defined by all molecules within a layer.[175] Figure 5.12 shows that while the percentage interdigitation of the aliphatic chains appears to experience an overall decrease with increasing temperature, the values consistently remain between *ca*. 90-100%. These high values indicate significant interdigitation between the aliphatic chains in oppositely orientated molecules within the layer structure. In contrast, the degree of interdigitation is comparatively lower for the perfluoropolyether chains, showing a value of *ca*. 20-30% across the temperature range, indicating that significantly fewer perfluorinated chains overlap with the corresponding groups in oppositely orientated molecules. Additionally, Figure 5.12 reveals that the interdigitation of the CF_3 atoms increases with increased temperature. Nevertheless, the combination of data presented in Figure 5.10

and Figure 5.12 suggest that the expected layer contraction at the SmA-SmC transition is not significantly compensated by a corresponding decrease in the level of interdigitation.

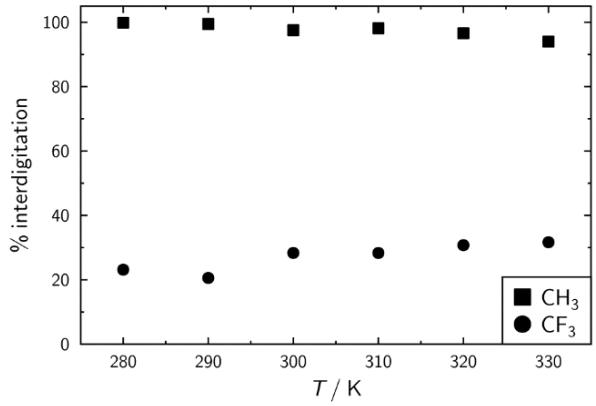

Figure 5.12 Degree of interdigitation of the perfluorinated end-groups and aliphatic end-groups calculated over 50 ns windows of the simulations.

5.3.7 Sub-Unit Analysis

To this point the results in this chapter indicate that the behaviour of 3M 8422 is largely consistent with the equivalent study of de Vries character in 9HL, discussed in Chapter 3. In the study of 9HL, it was found that the lactate chains exhibited a SmA-like distribution even in the SmC phase. For this reason, and to provide a fuller picture of molecular orientation, sub-unit analysis was carried out on 3M 8422 in an equivalent manner to 9HL.

The nano-segregation of immiscible chemical domains into distinct sub-layers is a commonly reported feature of many smectic liquid crystal materials. However, in the case of de Vries materials, it has been proposed that the behaviour of these sub-layers may not be entirely uniform, opening the possibility that individual molecular sub-units may contribute differently to the overall layer thickness.[108,109] 3M 8422 contains a flexible perfluoropolyether tail and an inflexible aromatic core, which may be expected to promote phase separation, supported by the clear aromatic and perfluoropolyether layers discussed above. Several studies of de Vries materials have reported that tilt is not typically uniform across the whole molecule, as molecular sub-units may exhibit different tilt behaviour either side of the SmA-SmC transition.[78,84,108] The ODFs determined from the MOI axes of all atoms that comprise the aliphatic chains, aromatic cores, and the perfluoropolyether chains are presented in Figure 5.13, and their corresponding order parameters are listed below in Table 5.1, enabling a comparison of the tilt behaviour of the different molecular sub-units at all simulated temperatures.

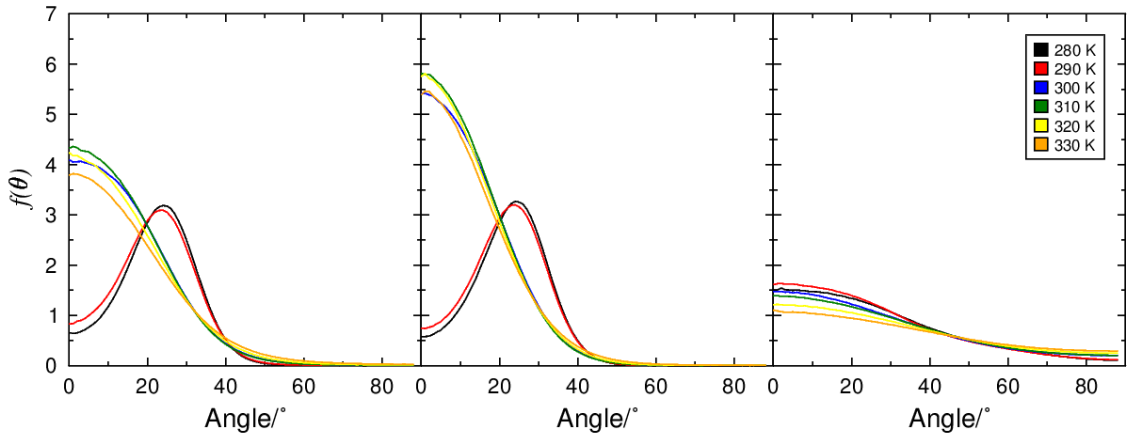

Figure 5.13 Orientational distribution functions, $f(\theta)$, of minimum MOI vectors of the aliphatic chain (left), the aromatic core (centre), and the perfluoropolyether chain (right), determined from simulations of 3M 8422 at 10 K intervals between 280 K and 330 K. Data are normalised according to $\int_0^{\pi} f(\theta)\sin(\theta)\,d\theta = 1$.

Table 5.1 Orientational order parameter, P_2, determined with respect to **k**, of the aliphatic chain, aromatic core, and the perfluoropolyether chain from simulations of 3M 8422 at 10 K intervals between 280 K and 330 K.

	Aliphatic		Aromatic		Perfluoro	
T / K	P_2	+/-	P_2	+/-	P_2	+/-
280	0.6947	0.0153	0.7032	0.0160	0.3694	0.0052
290	0.6904	0.0034	0.6977	0.0038	0.3752	0.0050
300	0.7146	0.0072	0.7691	0.0098	0.3104	0.0043
310	0.7250	0.0070	0.7884	0.0102	0.2845	0.0027
320	0.6902	0.0066	0.7719	0.0087	0.2358	0.0048
330	0.6434	0.0048	0.7421	0.0058	0.1947	0.0037

Consistent with analysis of 9HL, the ODFs presented above show that molecules exhibit a non-uniform tilt in the SmA phase and SmC phase, emphasised by the three sub-units displaying orientational distributions with very different overall shapes. In the SmC phase (280-290 K), the aromatic and aliphatic sub-units exhibit a conventional 'volcano-like' distribution function with a non-zero maximum probability. However, the perfluoropolyether sub-unit exhibits a much broader distribution with a maximum at 0° even at temperatures ≤ 290 K, characterised previously as the SmC phase. Such distributions cannot be differentiated from the ODFs in the simulated SmA phase, which indicates that the perfluoropolyether sub-unit remains untilted, with respect to **k**, in the SmC phase and, therefore, does not contribute to the layer contraction expected at the SmA-SmC transition.

The observed differences in tilt behaviour between the perfluoropolyether sub-unit and the remainder of the molecule in 3M 8422 has obvious parallels to the behaviour exhibited by the lactate sub-unit in simulations of 9HL. This behaviour provides a clear rationale for the de Vries exhibited by 3M 8422, as a substantial proportion of the layer structure remains untilted in the SmC phase, consequently the layers will contract to a lesser extent than predicted by the 'rigid-rod' approximation.

An illustration of the layer structure in the simulated phases of 3M 8422 is presented in Figure 5.14, based on the layer projections shown in Figure 5.10, which illustrate the sub-layer separation that occurs between the perfluorinated chains and the rest of the molecule. The behaviour of these sub-units was further examined by analysing the lengths alongside the tilts of the aromatic and perfluoropolyether segments. Values of $l \cos(\theta)$, where l is the length of the sub-unit and θ is the angle between the axis defined by the average orientation of the sub-units and the layer normal, **k**, reveal the thickness of the sub-layers themselves, measured parallel to **k**. The values of $l \cos(\theta)$, corresponding to each simulated temperature, are plotted in Figure 5.15, and clearly show that the thickness of the sub-layer that contain the aromatic sub-units displays fairly conventional behaviour, as it exhibits a reduction at the SmA-SmC transition upon cooling from 300 K to 290 K. However, the sub-layers overwhelmingly composed of perfluorinated sub-units exhibit the inverse behaviour, with the layer thickness expanding on cooling through the SmA phase, consistent with the ODFs and the P_2 values presented in Figure 5.13 and Table 5.1, respectively. In contrast to the aromatic sub-layers, the increase in the thickness of the perfluorinated sub-layers is maintained upon transition to the SmC phase at 290 K, in which the sub-layer remains essentially SmA-like in structure. This increase in the sub-layer thickness appears to counteract the shrinkage exhibited by the aromatic sub-layer, providing a remarkably straightforward explanation for the de Vries behaviour of simulated 3M 8422.

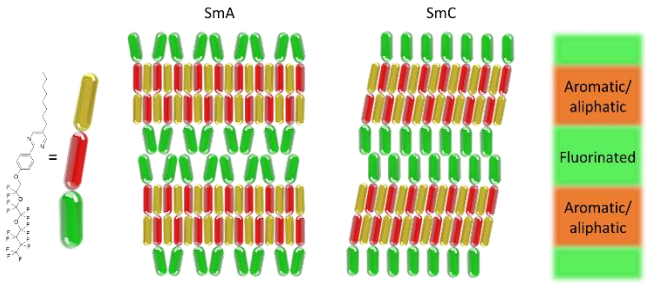

Figure 5.14 Schematic illustration of the SmA and SmC phases of 3M 8422 based on the layer projections and orientational distribution functions from the MD simulations. Aliphatic, aromatic and perfluorinated regions are shown in yellow, red and green, respectively.

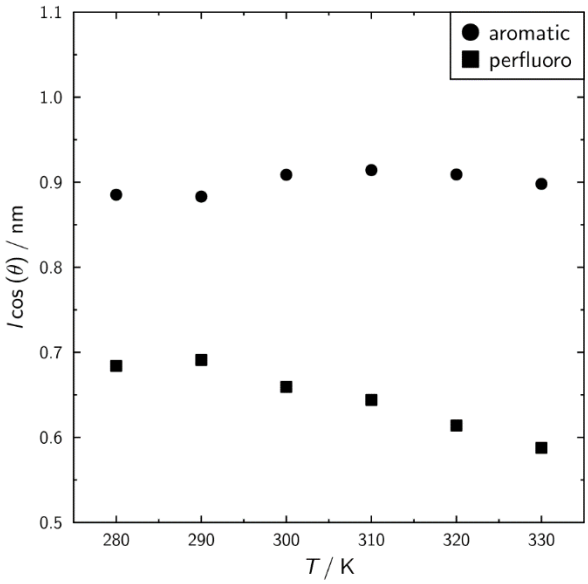

Figure 5.15 Plot of $l \cos\langle\theta\rangle$ for the aromatic and perfluoro subunits where l is the average length of the sub-unit, and the value of $\cos\langle\theta\rangle$ was calculated from the respective average P_2 values in Table 5.1.

5.4 Conclusions

Atomistic MD simulations of the compound 3M 8422 were shown to replicate properties such as orientational and translational order parameters, layer spacings and tilt angles in generally good agreement with experimentally reported values. Analysis of the simulated phases demonstrated that de Vries behaviour was captured by the MD simulations, which provided an insight into both the phase structure and behaviour of 3M 8422. In this material, the shift in average molecular tilt observed at the SmA-SmC transition did not coincide with a reduction in the layer thickness, which appeared to be largely independent of tilt. The models typically invoked to account for de Vries behaviour could not individually explain the results of the analysis. While a slight increase in the average molecular length of 3M 8422 was found to influence the layer thickness upon cooling, this could not fully explain the lack of observed layer contraction, and no meaningful change in molecular interdigitation was identified between the temperatures chosen for this study.

Analysis of the behaviour of molecular sub-units, equivalent to that carried out in Chapter 3, provided further details about the simulated phase structure of 3M 8422. The ODFs and tilt exhibited by individual sub-units indicated that molecules do not tilt uniformly, but rather only partially tilt upon transition to the SmC phase. The aromatic cores and aliphatic chains of 3M 8422 appear to tilt in a manner consistent with conventional SmA-SmC transitions, with a clear shift in tilt between 290 K and 300 K. In contrast, the ODFs of the perfluoropolyether chains were shown to remain remarkably consistent either side of 290-300 K. Much like in 9HL, a combination of the factors outlined above are likely to result in the minimal layer contraction observed in simulations of 3M 8422, as well as those reported in experimental studies of the same and similar compounds.[78,84] The sub-unit

behaviour reported in these simulations is consistent with experimental studies,[108,224] which focus on several siloxane-terminated liquid crystals that show very minimal change in orientational order of certain sub-units at the SmA-SmC transition. It is important to note that the simulations of 3M 8422 did not provide evidence of any net sub-unit tilt in the SmA phase, which has been reported in some siloxane-based materials, but despite this, indicated that the expansion of the perfluoropolyether sub-layers was sufficient to entirely offset the contraction of the aromatic/aliphatic sub-layers.

De Vries behaviour is often stated to be caused by the incompatibility of sub-units, such as the flexible perfluoropolyether chain and rigid aromatic core in 3M 8422. The phase separation of molecular sub-units is clearly evident in the simulations of 3M 8422 with distinct perfluoropolyether and aromatic sub-layers present at all simulated temperatures. However, the formation of such sub-layers is not exclusively observed within perfluorinated liquid crystals as similar sub-unit behaviour was reported in Chapter 2, which centred on lactated-based 9HL. This consistency between the behaviour of 3M 8422 and 9HL seems peculiar due to the lack of groups that promote nanophase separation in 9HL, seemingly at odds with the notion that de Vries behaviour is a result of sub-unit incompatibility However, the lactate units within 9HL appear to play a similar role to the perfluoropolyether chains in 3M 8422, perhaps due to their kinked orientation, relative to the aromatic core unit.

The work performed in this chapter further illustrates the ability of atomistic MD simulations to capture complex phase behaviours. It is evident that multiple effects contribute to the layer thickness in 3M 8422, which leads to the development of de Vries behaviour. The computational study of such materials has helped to further elucidate the behaviour, and the extension of computational methods to similar compounds seems likely to afford even greater insight into the phase behaviour of liquid crystal materials.

Chapter 6 – Molecular Dynamics Study of Trisiloxane-Based TSiKN65

The primary focus of this chapter is the molecular dynamics simulation of the trisiloxane-based mesogen TSiKN65, which is commonly cited in the literature to be the benchmark for de Vries behaviour.[83] This work, therefore, details the MD simulation methodology applied in the course of studying this siloxane-based liquid crystal, as well as providing a short overview of the simulation setup. The initial analysis carried out on the partially ordered phases of TSiKN65, including orientational and translational order parameters, tilt angles and layer spacings, is reported on and additional analysis, such as molecular lengths, orientational distribution functions and the probing of sub-unit behaviour is described in detail. These results are subsequently compared with experimental data available within the literature. Additionally, the findings of this study are evaluated alongside the MD simulations of 9HL and 3M 8422, previously discussed in Chapters 3 and 5, respectively.

6.1 Introduction

The intent of this introduction is to provide a brief overview of the MD simulation work performed on polysiloxane compounds. Additionally, it aims to provide further details on the currently published work related to the optimisation of standard force fields attempting to more realistically model materials that contain siloxane or silane structural features, as well as discuss the numerous issues that have been problematic for simulations which include such chemical moieties. A variety of studies investigating siloxane and silane-based liquid crystals using experimental techniques are touched upon in this section, including those focused on the propensity of these materials to exhibit de Vries-like behaviour. Lastly, the introduction is concluded by laying out the aims of the work presented in this chapter.

6.1.1 MD Simulation of Silicon-Based Materials

Compounds that are based primarily on polysiloxane or polysilane structures are often reported to exhibit many unique and potentially useful properties, a fact illustrated by their widespread applications in industry.[281–286] Likewise, liquid crystalline materials that contain such elements are fairly abundant, with the insertion of a siloxane- or silane-based terminal chain commonly reported to have a substantial effect on mesophase character.[83,113,216,287,288] The prevalence of these materials in a wide array of chemical settings make them an attractive target for computational analysis methods, such as MD simulations, which have the potential to provide detailed insights into mesophase structure that could potentially lead to a more comprehensive explanation of their fairly unique properties.

Early attempts to study silicon-based materials using MD methods had varying degrees of success but highlighted their utility for studying physical properties within organosiloxane compounds. One example, investigating the intramolecular interactions between biphenyl and cholesterol mesogenic units in a siloxane-based liquid crystal polymer, *in silico*, enabled various molecular associations to

be studied in excellent detail.[289] In another case, MD simulations were used to study the bulk phase behaviour of a cyclic siloxane-based mesogen,[290] probing the major structural conformations adopted by the molecules under several different simulation conditions. Such work has provided the basis for further applications of MD simulations to silicon-based materials. For example, on study reported slightly more recently focused on evaluation of the specific volume near the glass transition temperature in a functionalised polysiloxane material.[291]

Even more recent studies have attempted to utilise MD simulation to study some rather unusual properties exhibited siloxane- and carbosilane-based dendrimers. One such report, which represented a poly(butyl)carbosilane dendrimer by employing a coarse-grained potential, outlined the MD simulation and subsequent analysis of the dendrimer melt.[292] A second computational study investigating the structure of poly(butyl)carbosilane has been reported,[293] in which the dendrimers were represented via a UA potential and simulated using the AMBER force field, with supplementary parameters corresponding to the Si atoms and CH_2 methylene groups.[294] Additionally, a series of reports have been published, which utilise UA MD simulations to study molecular organisation and dynamics in siloxane- and carbosilane-based dendrimers.[295–297] The wide variety of studies described above highlights the wide range of research that attempted to exploit MD simulations to probe the bulk character and structural features exhibited by polysiloxane and polysilane materials, with the ultimate aim of providing a greater understanding of their unique properties.

6.1.2 Force Field Parameterisation for Silicon-Based Materials

Many of the computational studies concerning the modelling of siloxane- and carbosilane-based materials have utilised force fields such as PCFF[298–301] and COMPASS,[142] which are described by a functional form that includes additional energy contributions from cross terms. These force fields are particularly popular for polymer simulations, typically the main context in which siloxane are studied. However, as the use of additional terms can make simulations more computationally intensive, several attempts have been made to optimise standard force fields, such as OPLS[180] and GAFF,[181] improving their ability to predict various key properties associated with compounds based primarily on silicon moieties.

An early attempt to develop a force field that can accurately model polysiloxane materials is outlined in work performed by Sok *et al.*,[253] focusing on a MD simulation of polydimethylsiloxane using a UA representation. In this study, the derivation of bonded and nonbonded parameters, specific to polysiloxane materials, enabled an AMBER-like force field to model the transport of small molecules across a polymer membrane. A later study concerning the optimisation of a general force field targeted towards improved modelling of siloxane-based compounds was reported by Sun and Rigby,[254] which outlined the parameterisation of a CFF-type force field using a combination of *ab initio* calculations and experimentally derived data. Likewise, the parameterisation of a UA-type

force field aimed at more realistically modelling the thermodynamic and structural properties of polydimethylsiloxane melts is expanded upon in work by Makrodimitri *et al*.,[255] which utilises experimental thermodynamics data throughout the fitting procedure. Alternatively, an example of a fully atomistic force field developed primarily using QM calculations is that described in the work of Smith *et al*.,[176] in which parameters related to polydimethylsiloxane were determined from a variety of basis sets, and subsequently validated by comparing the results derived from MD simulations to experimentally measured density values and heats of vaporisation. A more recent series of studies by Shi *et al*.,[256,257] outlines the development of UA and AA models, utilising many of the parameters derived in previous publications.[176,253] In these studies, further optimised Lennard-Jones parameters for Si, C and O atoms were obtained by fitting to the potential developed by Smith *et al*.[176] The work discussed above illustrates the significant amount of research effort that has been devoted to the parameterisation of standard force fields aimed towards more accurately modelling polysiloxane compounds, as well as the wide variety of models that have been applied to silicon-based materials.

6.1.3 Experimental Investigations of Siloxane-Based Mesogens

Liquid-crystalline materials that exhibit the SmA* and SmC* phases at or close to room temperature have attracted significant interest due to their potential suitability in electro-optic devices. However, as FLCs typically exhibit the SmA* and SmC* phases at temperatures well in excess of 25°, their use in devices has remained limited. As a consequence, numerous studies have been reported focusing on exploring the effect of various structural changes in previously established FLC materials on key mesophase properties. One such change that is reported to have showed excellent capacity in lowering the relative temperature of the SmC* phase range is partial substitution of the hydrocarbon terminal chains with significantly more bulky polysiloxane end groups.[302–305] These units are noted to reduce the phase transition temperatures and enhance the thermal stability of liquid-crystalline materials, attributed to their increased bulk and greater flexibility relative to alkyl chains.[302] As a result of these valuable properties, numerous examples of FLC materials containing siloxane units have been reported in the literature, [302–305] some of which are noted to exhibit unusual mesogenic properties that have been subsequently investigated using a wide range of experimental techniques.[83]

The first study to report on the trisiloxane-based de Vries compound TSiKN65, shown in Figure 6.1, was performed by Naciri *et al*.,[83] reviewing the synthesis of a series of novel FLCs that contained a polysiloxane terminal group, specifically, a chain composed of between one and three dimethylsiloxane units. In this report, the electro-optic characteristics of the synthesised FLCs were also investigated, displaying a significant sensitivity to the number of siloxane units comprising the polysiloxane end chain, and exhibiting unusually large electroclinic tilt angles across the SmA* temperature range. A second study was reported by Naciri *et al*.,[306] concerning with the synthesis of a number of TSiKN65 derivatives, in which a similarly high electroclinic tilt was observed,

ultimately concluding that the materials possess de Vries-like character in the SmA* phase. The earliest study to focus specifically on the potential de Vries behaviour exhibited by TSiKN65 was performed by Spector *et al.*,[96] reporting a detailed electro-optic and x-ray investigation of the material. In this study, a substantial electric field induced optical tilt was observed without a corresponding contraction of the smectic layers, and while the authors propose several potential explanations to account for these results, the behaviour is concluded to most likely arise due to existence of tilted molecules in the SmA* phase, consistent with the diffuse cone model.

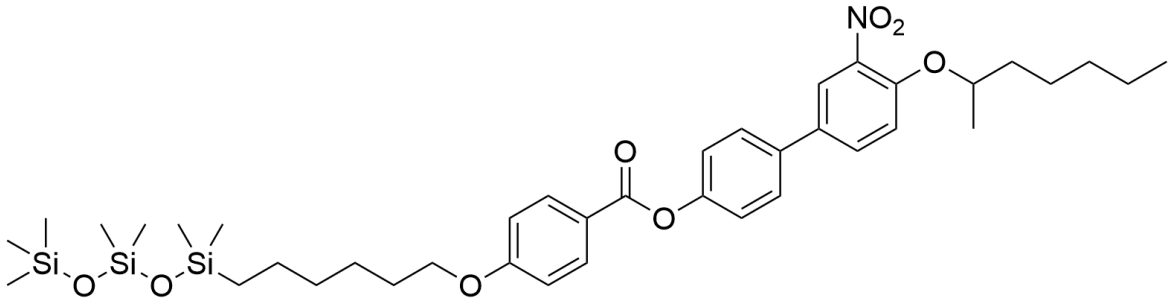

Figure 6.1 The chemical structure of the liquid crystalline compound TSiKN65 (SmC 23.00°C SmA 55.50°C I).[83]

Subsequent studies of TSiKN65 have covered a wide array of experimental methods in an effort to quantify important mesophase properties, as well as investigating the underlying reason behind de Vries character. Second and fourth rank orientational order parameters obtained from polarised Raman experiments were found to be very low, providing evidence for the existence of a de Vries SmA* phase.[89] Further studies focused on the orientational distribution of TSiKN65 molecules have utilised infrared and polarised Raman spectroscopy to measure a significant molecular tilt above the SmA*-SmC* transition.[90] These results show excellent consistency with earlier work,[226] in which the order parameters of dichroic dyes dissolved in TSiKN65 were determined, and found to be consistent with models proposing a 'tilted' SmA* phase, in which molecules are azimuthally disordered. Additionally, the proposal of a de Vries SmA* phase is consistent with an experimental investigation of optical tilt and birefringence,[95] which took into consideration both the di- and tri-siloxy liquid crystals, referred to as DSiKN65 and TSiKN65, respectively. The dielectric response of the de Vries SmA* phase believed to be formed by TSiKN65 was investigated in a set of studies,[94,307] which reported that an increase in dielectric strength and a decrease in relaxation frequency observed upon cooling over a large temperature range is incompatible with a 'conventional' SmA phase, but could be explained by molecules adopting a configuration reminiscent of a de Vries SmA* phase.

Several more recent experimental investigations of TSiKN65 have focused on studying the molecular-level contributions to minimal layer shrinkage, exploring how individual structural features influence mesophase behaviour. A significant decrease in birefringence ~15-20° above the SmA*-SmC* transition was observed in one report,[308] which also measured the tilt angle associated

with TSiKN65. In this study, the behaviour exhibited by the tilt angle and birefringence was found to be consistent with the mean field theory proposed by Saunders *et al*.,[278,309] related to the SmA-SmC transition in de Vries materials. In a second study, four compounds, referred to as 'high electroclinic' materials, were studied by dielectric spectroscopy, as well as through calculation of their birefringence and tilt angle.[310] The assessment of these quantities indicated that compounds that contain a siloxane tail showed significant de Vries characteristics in their dielectric spectra, while the non-siloxane materials could be described as displaying a conventional SmA phase. The study, therefore, concludes that the flexible siloxane fragment causes molecules to possess a fairly a 'non-calamitic' shape, resulting in a diffuse-cone arrangement in the SmA* phase.

In addition to work described above on TSiKN65, a number of experimental studies have also centred on attempts to synthesise similar liquid crystalline materials that exhibit some degree of de Vries character. Most commonly, these investigations have involved the synthesis of compounds designed around a 5-phenylpyrimidine core attached to either a siloxane- or carbosilane-based terminal chain. Some instances of such an investigation can be seen in work performed by Roberts *et al*.,[117,118] concerned with developing a design strategy for materials displaying 'de Vries-like' properties by considering which structural elements promote the formation of the SmA and SmC phases. Furthermore, several studies have been reported, which detail the synthesis, and subsequent analysis, of carbosilane-terminated compounds showing various degrees of de Vries character.[218,311] More recently, the design and characterisation of various of silicon moieties for applications in SSFLCs has been reported on.[113,312]

A vast amount of published research has focused on siloxane-based liquid crystals, providing an in-depth understanding of their thermodynamic and mesogenic properties. Additionally, as discussed above, many studies have also investigated their propensity to exhibit de Vries character without a clear consensus on the underlying causes of such a behaviour. As a result, siloxane-terminated liquid crystalline materials can be considered an attractive target for further studies, perhaps those making use of computational techniques, which may have the ability to provide an atomistic view of mesophase phenomena. More specifically, the experimentally obtained results published thus far on TSiKN65 provide an excellent comparison tool for any potential simulation studies of the material.

6.2 Aims

The primary aim of the work presented in this chapter was to investigate the de Vries behaviour reported to be exhibited by the trisiloxane-based material TSiKN65,[83,96] shown in Figure 6.1, through the application of MD simulations. The initial aim was to parameterise the polysiloxane chain of TSiKN65 in an effort to provide a more realistic model of the SmA* and SmC* phases beginning from a fully disordered system. The objective was then to measure relevant properties, such as

orientational and translational order parameters, tilt angles and layer spacings; enabling any potential de Vries character captured by the MD simulations to be quantified.

In the case of these goals being accomplished, a periphery aim was to investigate how structural elements promote de Vries character exhibited by compounds similar to TSiKN65, as well as compare the results of this analysis with that from simulations of 9HL and 3M 8422, reported in Chapter 3 and Chapter 5, respectively.

6.3 Results and Discussion

A geometry optimisation performed via DFT calculations at the B3LYP/6-311G(d) level provided a low energy structure of TSiKN65 that could be utilised in the subsequent MD simulations. Similar to the study of 9HL, partial charges were derived for all atoms in the molecule by employing the RESP method,[197] including those in the trisiloxane chain. As discussed in Chapter 3, a number of bonded and non-bonded parameters were assigned to the relevant groups of atoms within TSiKN65, which were developed specifically for polysiloxane systems,[176] and had been reported to work reasonably well in MD simulations performed using an AMBER-like force field.[256] Where relevant, the default GAFF parameters were substituted for these improved values. Additionally, optimised parameters for several dihedrals within the siloxane sub-unit, derived from the force constant parameterisation outlined in Chapter 3, were used throughout all of the simulations described below.

MD simulations were ran until the liquid crystalline phase structure was adjudged to be fully equilibrated at each temperature. The overall simulation time required to achieve these equilibrated systems, varied between 900 ns and 1,400 ns in the simulations performed here.

In this work, four fully atomistic MD simulations were carried out on systems composed of 1024 molecules of TSiKN65. These four simulations correspond to a 20 K interval between 340 K and 400 K, significantly above the experimentally determined $T_{A\text{-}C}$ of 296-297 K and slightly above the $T_{A\text{-}I}$ of 328-329 K.[83,90] Despite this, the simulations encompass a wide temperature range, which should provide a useful measure of any potential temperature effects on the phase structure. The analysis performed on these systems is reported below, and outlines the methods used to evaluate orientational and translational order, layer spacings and tilt angles. Additionally, this work discusses the extent of de Vries character exhibited by the simulated phases of TSiKN65 and considers several measures that provide a more in-depth examination of molecular behaviour in such systems.

6.3.1 Determination of Order Parameters

A primary indicator of mesophase formation in simulated systems is the development of orientational order. Orientational order was observed at all simulated temperatures, clearly evident from the calculated P_2 values plotted in Figure 5.2. The simulated values here show an overall decrease as the temperature is increased, which is largely consistent with the behaviour of conventional liquid crystalline materials, while the P_2 values of 0.40-0.60 appear in close accord with experimentally-derived values of 0.40-0.65, calculated from infrared absorbance data for temperatures 15°C either side of the SmA-SmC transition.[90] Moreover, the P_2 values shown in Figure 6.2 are only slightly lower than those of 0.6-0.8, measured using Raman spectroscopy.[89]

Like in Chapter 5, P_2 values were calculated for two distinct axes within TSiKN65 and these are presented as two separate data sets in Figure 6.2. The primary molecular axis, representing the complete molecule, was determined as the minimum MOI of the TSiKN65 structure, while the

second axis was also calculated as the MOI of the atoms located in the aromatic core. The clear disparity between the P_2 values calculated from the different axes is evident in Figure 6.2, and reveals that the molecules likely do not behaviour as rigid rods. The P_2 values indicate that the full molecule exhibits, on the whole, slightly more orientational order than the aromatic cores, and this trend holds across the entire temperature range. The data in Figure 6.2 shows a noticeable likeness to the equivalent analysis the previous chapter, corresponding to Figure 5.2, implying that the orientational behaviour displayed by molecules of TSiKN65 and 3M 8422 exhibits a clear similarity.

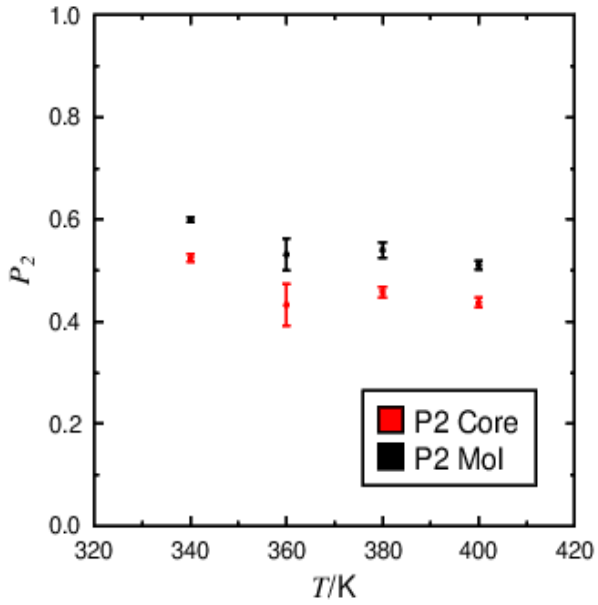

Figure 6.2 Plot of the average orientational order parameter (P_2), for the mesogenic core (red) and the whole molecule (black), with respect to **n**, determined from simulations between 340 K and 400 K, with associated error bars.

To serve as comparison of the TSiKN65 system at different temperatures, visualisations of the simulations performed at 340 K and 400 K are shown in Figure 6.3. Noticeably, it is clear that both snapshots demonstrate a significant degree of orientational order, as well as the presence of a well-defined layer structure. In these images, the phase at 340 K appears substantially more ordered than that at 400 K, which is consistent with the P_2 values in Figure 6.2. In comparison to the equivalent snapshots in previous chapters, the visualisation of the phase at the lower temperature does not indicate that the molecules are clearly tilted relative to the layer normal. However, in order to accurately gauge the average molecular tilt in such phases, additional analysis is necessary.

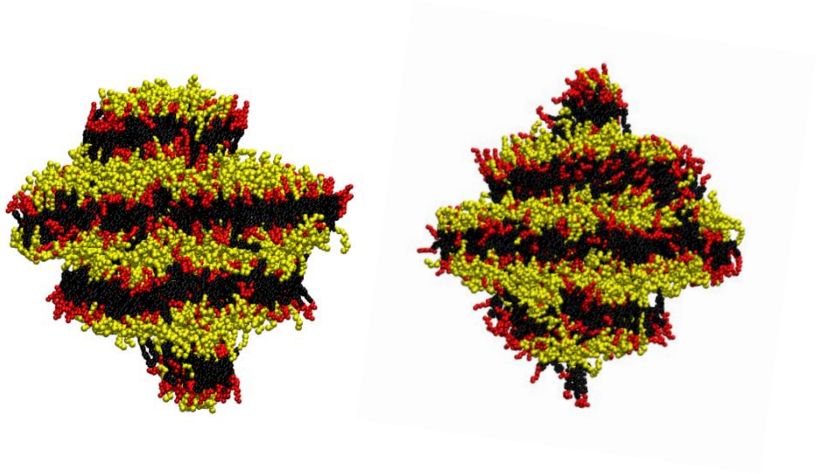

Figure 6.3 Visualisation of the simulations of TSiKN65, showing the aliphatic chains (yellow), aromatic cores (red), and siloxane chains (black), at 340 K (left) and 400 K (right), respectively.

As in previous chapters, the translational order exhibited by the simulated systems was also quantified, with the τ values associated with each simulated temperature plotted in Figure 6.4. The four data points are very similar, with average values of between 0.70-0.80, signifying the formation of a distinct layer structure, across the whole temperature range. The simulated values of 0.70-0.80 are also fairly well matched by values of *ca*. 0.80-0.90, extracted from x-ray measurements in the SmA* phase.[313] Likewise, the τ values plotted in Figure 6.4 are consistent with those from x-ray scattering experiments on similar liquid crystalline compounds, containing a trisiloxy terminal chain.[117] Interestingly, the results presented in Figures 6.2 and 6.4 appear consistent with several theoretical models focused on smectic ordering in de Vries materials, which state the combination of low orientational and high translational order are common features of compounds that exhibit minimal layer shrinkage.[222,309] However, this observation of low orientational order in TSiKN65 is inconsistent with the analysis performed in previous chapters, which showed P_2 values of *ca*. 0.80-0.90 are exhibited by 9HL and 3M 8422 in both the SmA and SmC phases.

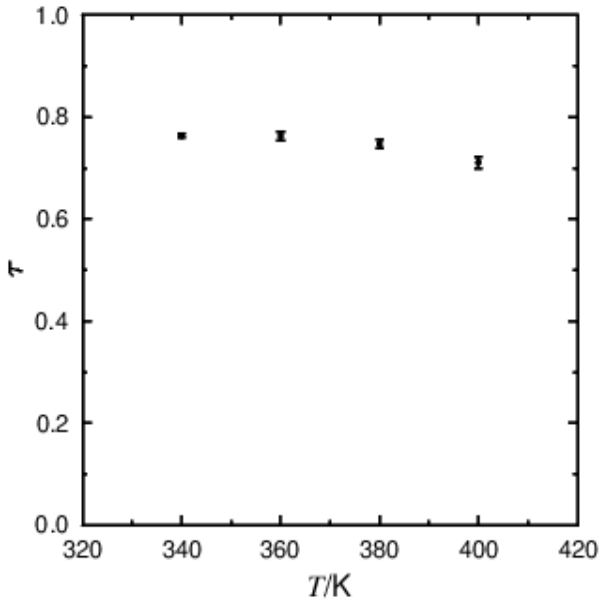

Figure 6.4 Plot of the average translational order (τ) determined from simulations between 340 K and 400 K, with associated error bars.

6.3.2 Tilt Angle Measurements

As mentioned previously, the average molecular tilt exhibited by smectic phases may be calculated via measurement of the angle between vectors **n** and **k**. With this method, the average tilt angle exhibited by simulated molecules at each temperature was computed and plotted in Figure 6.5, revealing that the average tilt varies significantly between 340-400 K. An overall trend in the data is difficult to discern, however, the highest tilt is exhibited at 340 K, corresponding to the lowest temperature simulation performed in this work. A noticeable decrease in the tilt occurs between 340 K and 360 K, implying that a tilt transition may occur between these two temperatures, and consistent with the results presented in previous chapters. However, despite this observation, it cannot be stated with absolute confidence that a simulated SmA*-SmC* transition is located within this temperature range and as a result, further analysis is required.

In Figure 6.5, two separate sets of tilt measurements are plotted, corresponding to the minimum MOI axis of the whole molecule, shown in black, and the minimum MOI axis of only the aromatic core, shown in red. While the difference between these two data sets is not as pronounced as seen previously, the average optical tilt is higher than the average molecular tilt at all simulated temperatures, consistent with observations in the simulated SmA phases of 9HL and 3M 8422. Comparing the simulated tilt to that measured experimentally, the optical tilt angle of *ca*. 12-13° at 340 K is substantially lower than the optical tilt of *ca*. 30° near to the transition to the SmC* phase, determined by Hayashi *et al*..[90] In contrast, the simulated molecular tilt of *ca*. 9-10° is fairly consistent with an x-ray derived tilt angle of *ca*. 6-8°, however, the core tilt is once again significantly lower than that calculated in the same experimental study.[96]

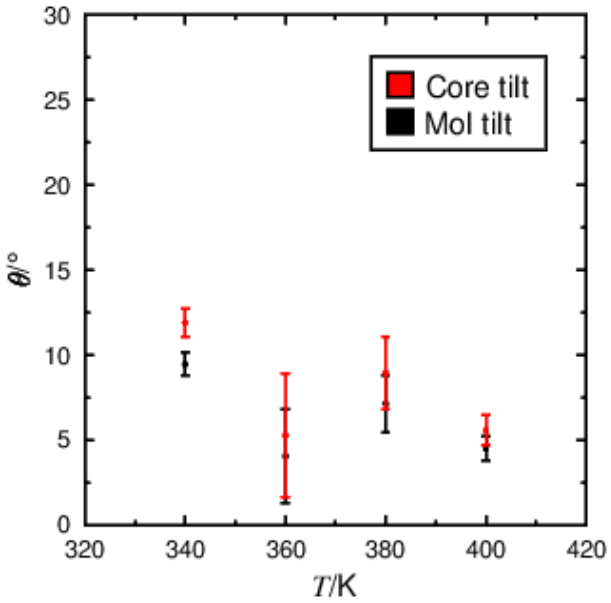

Figure 6.5 The average tilt between the layer normal (**k**) and the director (**n**), for the mesogenic core (red) and the whole molecule (black), determined from simulations between 340 K and 400 K.

Further characterisation of the molecular tilt behaviour exhibited by TSiKN65 is presented in Figure 6.6, with the histograms showing the normalised population of the tilt angles measured at each frame contained within the final 100 ns of simulation time. Most strikingly, the data shows that a seemingly discontinuous shift in the tilt angle population occurs between 340 K and 360 K, consistent with the average tilt values shown in Figure 6.5. Furthermore, the distribution of tilt angles appears to be slightly tighter at 340 K, with the average tilt at every simulation frame calculated to be between 8° and 12°. This contrasts with the histograms representing 360 K, 380 K and 400 K, in which the distribution is seen to be much broader. All of these observations indicate that the simulated phase at 340 K does possess some degree of SmC* character. Although, it is difficult to definitively state that this temperature corresponds fully to the SmC* phase in these simulations of TSiKN65.

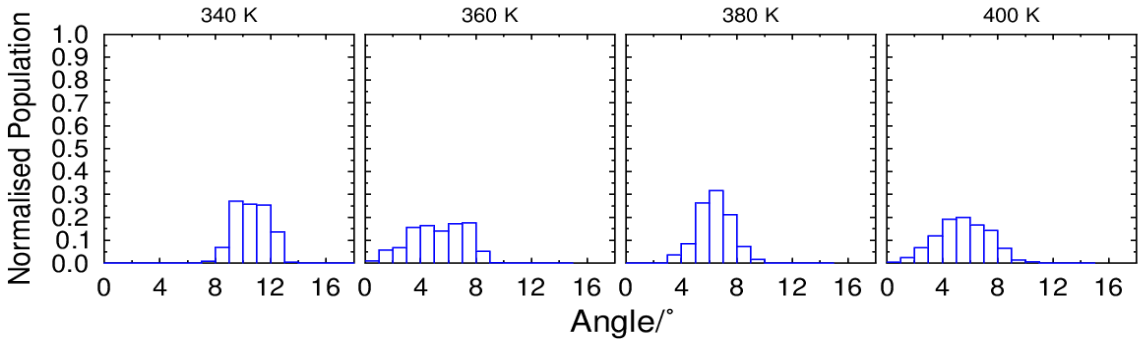

Figure 6.6 Normalised histograms of the angle formed by vectors **n** and **k** over the final 100 ns of simulations of TSiKN65, performed at 20 K intervals between 340 K and 400 K, shown from left to right, respectively, and determined with bin-widths of 1°.

6.3.3 Quantification of de Vries Character

The primary marker of de Vries character in smectic liquid-crystalline materials is the observation of minimal layer shrinkage upon the transition to the SmC* phase. The thickness of the smectic layers at each temperature interval is plotted in Figure 6.7, appearing generally consistent across the simulated temperature range. The layer thickness does, however, decrease slightly from *ca*. 3.80 nm at 340 K to *ca*. 3.67 nm at 360 K. Such an observation is perhaps surprising, due to the sudden decrease in molecular tilt between 340 K and 360 K, as illustrated in Figures 6.5 and 6.6, which is most often associated with an increase in the layer thickness. In comparison with experimentally derived layer spacings, the simulated values are slightly overestimated, relative to values of *ca*. 3.57 nm and *ca*. 3.60 nm, determined in the SmC* phase and SmA phase, respectively.[96] The behaviour exhibited by the simulated phases of TSiKN65 is, however, largely consistent with the results in Chapter 5, showing the layer thickness increases in the SmA phase, approaching the SmA-SmC transition. Likewise, the measurements of the smectic layer thickness at 340 K and 360 K also suggest a negative layer shrinkage, upon transition to the SmC*-like phase. Consequently, although it is still unclear if the simulated phases of TSiKN65 truly display de Vries behaviour, they possess many characteristics typically associated with non-layer shrinkage materials.

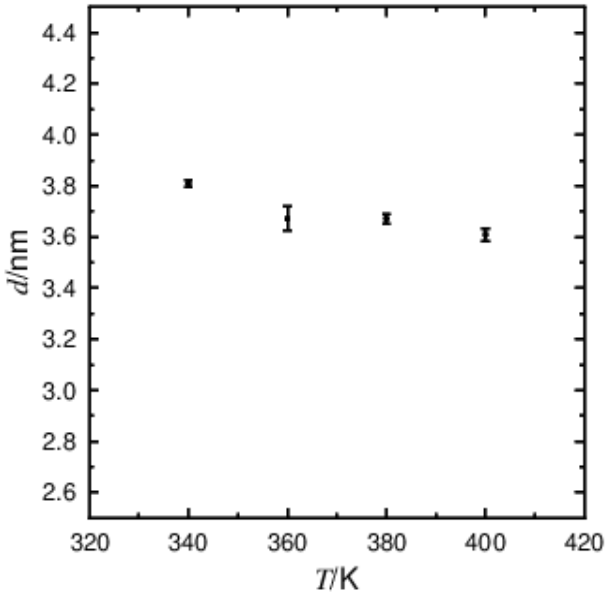

Figure 6.7 The average layer thickness determined from simulations of TSiKN65 between 340 K and 400 K, with associated error bars.

6.3.4 Orientational Distribution Functions

It can often be difficult to attribute any observed change in layer thickness to any one effect as the overall layer thickness results from an interplay between3333 numerous potential factors. However, a fairly simple explanation for a change in layer thickness is a shift in the average molecular orientation, which can drastically impact the smectic layer structure. While P_2 values, such as those plotted in Figure 6.2, provide a method to evaluate orientational order, the modest increase observed

at the potential SmA-SmC transition may not fully offset the layer contraction caused by an increase in molecular tilt. This shift in orientational order between 340 K and 360 K is also consistent with behaviour of several other siloxane-based compounds,[94,279,280] and shows a similarity to the behaviour of the perfluoropolyether-terminated compound analysed in Chapter 5.

To gain a more comprehensive understanding of the molecular distribution adopted by any liquid crystal material is it useful to determine ODFs. In Figure 6.8, four ODFs are shown, corresponding to the four temperature intervals, which were calculated using the MOI axis of the whole TSiKN65 molecule. While the ODFs below exhibit fairly similar shaped distributions, several differences are highlighted when compared side by side. Most notably, the ODF determined at 340 K is clearly not centred on 0°, in agreement with the phase's slightly higher molecular tilt of 12-13° at this temperature, as seen in Figure 6.5. Although not as pronounced in simulations of TSiKN65, this demonstration of a "volcano-like" distribution at relatively low temperatures is consistent with previous ODF analysis of 9HL and 3M 8422. Unexpectedly, the ODF corresponding to 360 K also appears not to be zero-centred, despite its apparent low molecular tilt. However, this may be explained by a particularly broad distribution of molecular tilts around 0°, which would be consistent with the large error values associated with 360 K in Figure 6.5. In contrast, the ODFs determined at 380 K and 400 K are clearly centred on 0°, which indicates that at these temperatures the most probable molecule orientation is that aligned along the layer normal.

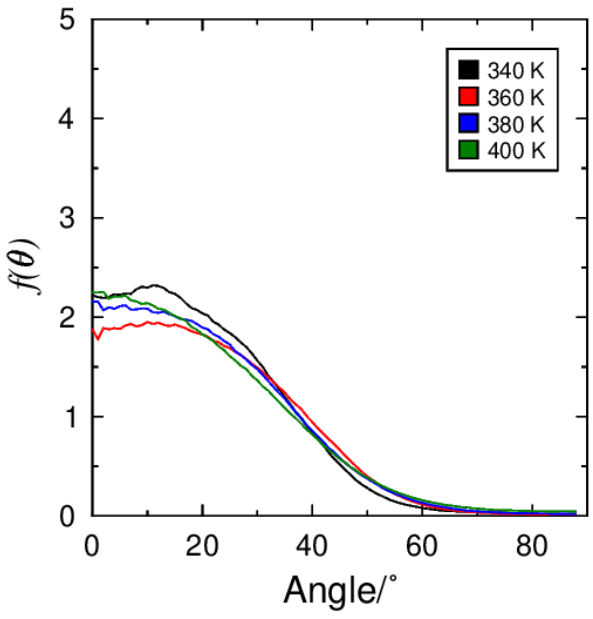

Figure 6.8 Orientational distribution functions, $f(\theta)$, of the minimum MOI vector of the molecules vs **k**, determined from simulations of TSiKN65 at 20 K intervals between 340 K and 400 K. Data was normalised according to the equation $\int_0^{\pi} f(\theta)\sin(\theta)\,d\theta = 1$.

6.3.5 Molecular Lengths

A shift in the molecular length naturally impacts the thickness of the smectic layers, and this effect is often invoked in the case of de Vries materials to explain the absence of layer shrinkage at the

SmA-SmC transition.[78,103] In order to evaluate the length of molecules at all simulated temperatures, the distributions of the molecular lengths in TSiKN65, defined as the length of the vector between the terminal CH_3 carbon atom on the chiral C_5 aliphatic chain and the $Si(CH_3)_3$ silicon atom on the tri-siloxy chain, were calculated and are shown in Figure 6.9. The average molecular lengths, calculated from the same vector, are also presented in Figure 6.9, showing an overall decrease as the temperature is increased. Consistent with previous chapters, the data below reveals that any expected reduction in layer thickness, due to an increase in molecular tilt, is likely to be compensated, to some extent, by elongation of the constituent molecules. The molecular length distributions also appear to marginally broaden as the temperature is increased, implying an extension of the molecule at lower temperatures. However, the degree of elongation observed here is comparable to that exhibited by 9HL and 3M 8422, which could not fully rationalise the lack of layer contraction in either material.

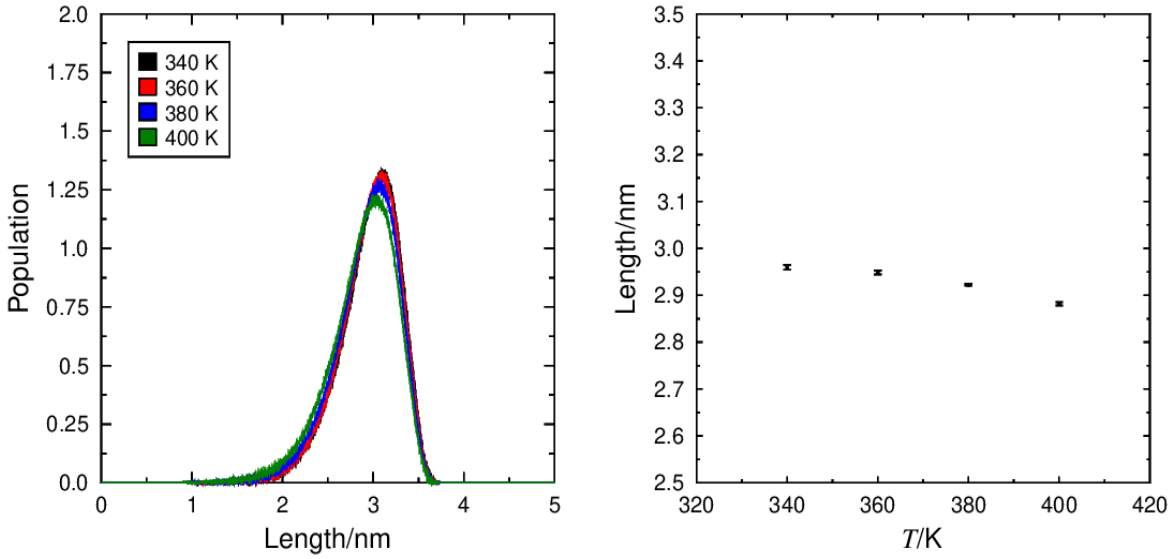

Figure 6.9 The distribution of molecular lengths (left), and the mean molecular lengths of TSiKN65 plotted against temperature (right), determined from simulations of TSiKN65 at 20 K intervals between 340 K and 400 K.

6.3.6 Molecular Interdigitation

Figure 6.10 reveals the distribution of positions occupied by atoms in TSiKN65 parallel to the layer normal, **k**, at 340 K and 400 K. As before, the 'up' and 'down' in Figure 6.10 indicates whether the projection of the vector is derived from the principle molecular axis orientated parallel or antiparallel to the layer normal, **k**. In order to preserve consistency with previous analysis, the atoms selected are those positioned at either end of the molecule, in addition to those at the border of the aromatic and aliphatic sub-units, and between the aromatic and siloxane-terminated sub-units, all of which are highlighted in Figure 6.11. In Figure 6.10, it can be seen that C25 (CH_3 atoms) and O3 (oxygens joining the aromatic and siloxane sub-units) in anti-parallel molecules are largely out of phase at 340 K, signifying that these atoms are typically located at the interface between the siloxane and the aromatic/aliphatic domains. In comparison, the projections show that O1 (oxygens joining the aromatic and aliphatic sub-units) and Si3 ($Si(CH_3)_3$ atoms) in anti-parallel molecules are generally

much more closely positioned, characteristic of a bilayer arrangement, supporting the visualisations presented in Figure 6.3. While the layer projections determined at 340 K and 400 K exhibit several common features, those derived at the higher temperature show significantly broader, consistent with the lesser order demonstrated by Figures 6.2 to 6.4. Additionally, the position of O3 atoms in anti-parallel molecules appear more closely aligned at 400 K, suggesting that the bilayer structure may be less defined, relative to at lower temperatures.

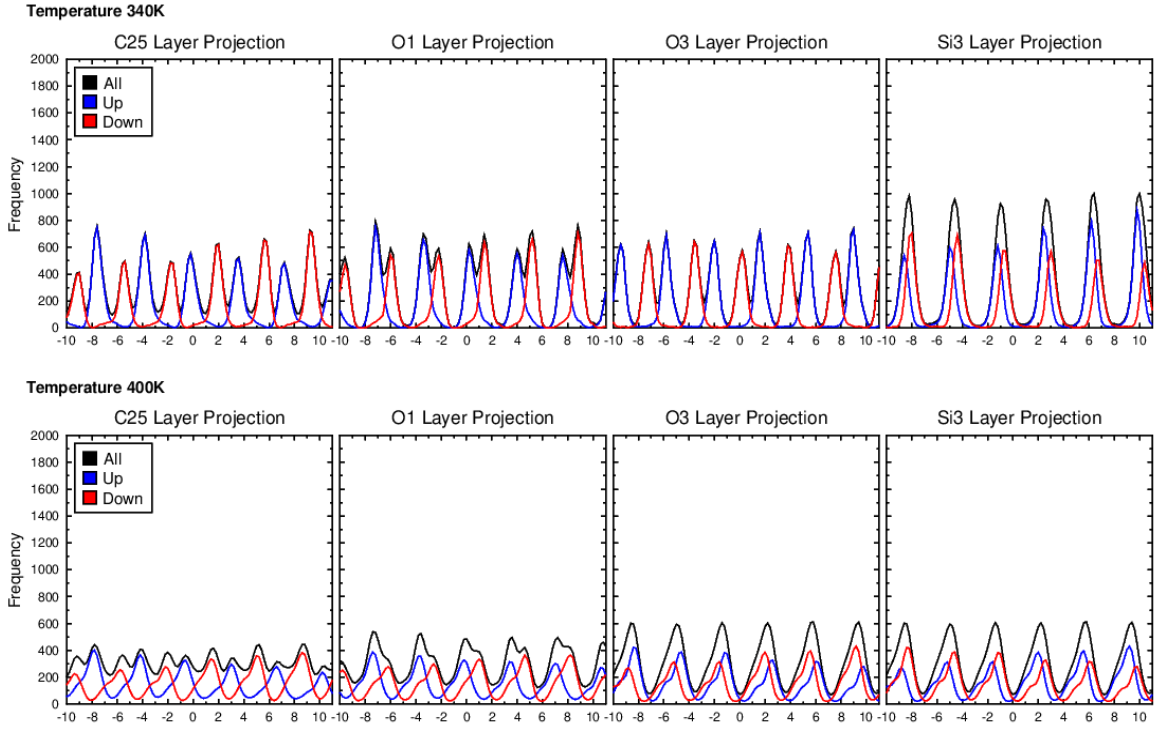

Figure 6.10 Layer projections for atoms C25, O1, O3 and Si3 shown from left to right, respectively, for the simulations at 340 K (top) and 400 K (bottom).

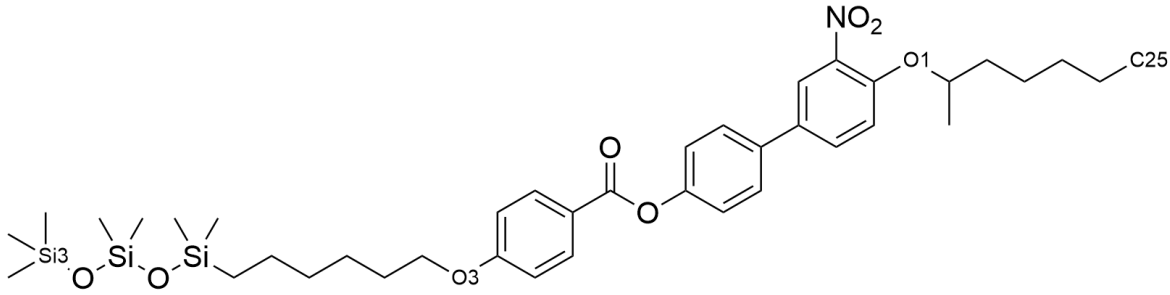

Figure 6.11 The structure of TSiKN65 highlighting the position of the projection atoms C25, O1, O3 and Si3.

6.3.7 Sub-Unit Analysis

The results reported so far in this chapter reveal that the behaviour of TSiKN65 exhibits several features in common with 9HL and 3M 8422, considered in Chapter 3 and Chapter 5, respectively. However, in other important ways, the behaviour of TSiKN65 deviates significantly from these compounds, most clearly in its lower orientational order. Due to this, it was considered useful to

analyse the behaviour of individual sub-units in an equivalent manner to previous chapters, in an effort to further elucidate the molecular behaviour of TSiKN65.

The partial or full separation of chemically distinct molecular fragments, leading to the formation of smectic sub-layers has been discussed previously. Several publications have highlighted the tendency of de Vries materials to contain immiscible sub-units, resulting in microphase separation, and suggesting that sub-layers within the smectic layer structure may contribute differently to the layer thickness.[108,109,314] TSiKN65 is characteristic of de Vries compounds, containing a fairly rigid aromatic core and a flexible siloxane end group, the combination of which would be expected to promote phase segregation. Accordingly, the formation of defined sub-layers is evident from the clear separation between the aromatic/aliphatic and siloxane sub-units in Figure 6.3, as well as the high translational order values in Figure 6.4. A number of studies have also reported that the tilt of individual sub-units may not be uniform across the SmA-SmC transition in de Vries materials.[84,108,109] Therefore, in order to assess the behaviour of different sub-units in TSiKN65, the ODFs calculated using the MOI axes of all atoms comprising the aliphatic chains, aromatic cores and the siloxane-terminated chains are shown in Figure 6.12. Similarly, the orientational order parameters derived from these ODFs are presented in Table 6.1 to provide a comparison of the tilt behaviour of the individual molecular sub-unit at all simulated temperatures.

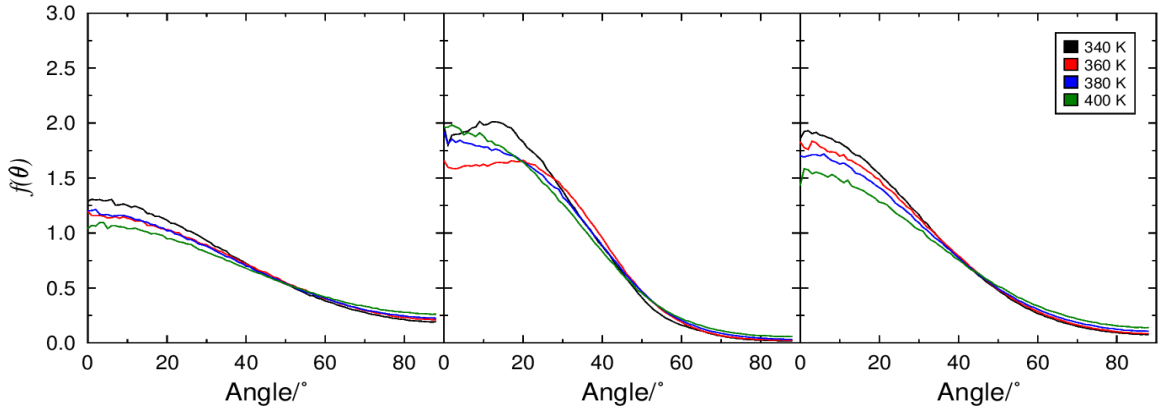

Figure 6.12 Orientational distribution functions, $f(\theta)$, of minimum MOI vectors of the aliphatic chain (left), the aromatic core (centre), and the siloxane chain (right), determined from simulations of TSiKN65 at 20 K intervals between 340 K and 400 K. Data are normalised according to $\int_0^{\pi} f(\theta)\sin(\theta)\,d\theta = 1$.

Table 6.1 Orientational order parameter, P_2, determined with respect to **k**, of the aliphatic chain, aromatic core, and the siloxane chain from simulations of TSiKN65 at 20 K intervals between 340 K and 400 K.

	Aliphatic		Aromatic		Siloxane	
T / K	P_2	+/-	P_2	+/-	P_2	+/-
340	0.2596	0.0028	0.5400	0.0170	0.4138	0.0142
360	0.2264	0.0048	0.4622	0.0324	0.3976	0.0044
380	0.2176	0.0028	0.4720	0.0102	0.3728	0.0062
400	0.1872	0.0034	0.4476	0.0080	0.3314	0.0048

The sub-unit analysis, in Figure 6.12, shows that the aliphatic, aromatic and siloxane ODFs demonstrate rather different shapes, indicative that the simulated TSiKN65 molecules adopt a non-uniform conformation in both the SmA and SmC*-like phases. Noticeably, the ODFs corresponding to the aromatic cores clearly exhibit different shape distributions at different temperature intervals. Interestingly, the ODF at 360 K appears significantly broader than the other temperatures, with a maximum away from 0°, inconsistent with the average tilt shown in Figure 6.5. The ODF corresponding to the aromatic cores at 340 K exhibits a clear "volcano-like" distribution, consistent with the analysis of 9HL and 3M 8422. In contrast, the non-aromatic units exhibit a maximum centred on 0° at all temperatures. The zero-centred distributions evident at 340 K for the aliphatic and siloxane fragments, despite their measured tilt in Figure 6.5, may indicate that one or both of these sub-layers remains untilted even in a SmC*-like phase. This behaviour is remarkably similar to that displayed by the lactate and perfluoropolyether sub-layers observed in 9HL and 3M 8422, respectively.

6.4 Conclusions

MD simulations of the siloxane-terminated liquid crystal TSiKN65, performed at a fully atomistic resolution, demonstrated a fine ability to replicate several experimental observables associated with smectic mesophases, namely orientational and translational order parameters. However, the calculated tilt behaviour and layer thickness across the SmA-SmC* transition were less consistent with experiment. Despite their shortcomings, the MD simulations provided a molecular-level insight into the general phase structure and composition in the SmA phase. Analysis of the layer spacing across the simulated temperature range revealed that the smectic layers expanded upon transition from a less-tilted to a more-tilted phase, in general agreement with the results in Chapter 5, and consistent with de Vries behaviour. Despite a lack of definitive results, the phases were examined in an identical way to previous chapters, which indicated that no significant change in molecular length or molecular interdigitation likely occurs between the temperatures of 340 K and 400 K.

The behaviour of the molecular sub-units was investigated using a similar method to that set out in Chapters 3 and 5, which allowed for a deeper understanding of the orientational distributions adopted by TSiKN65 molecules. As before, the ODFs corresponding to different sub-units exhibited very different overall shapes, suggesting that tilt behaviour is not uniform across molecules of TSiKN65. Significantly, the ODFs corresponding to the aromatic sub-units calculated at 340 K appeared to possess a maximum probability away from 0°, consistent with its relatively high average tilt. The ODFs associated with the siloxane-based terminal chains showed very little variation across the simulated temperature range, while the distributions corresponding to the chiral aliphatic chains exhibited only minimal changes between 340 K and 400 K. The clear difference in orientational behaviour exhibited by the aromatic and siloxane sub-units at lower temperatures is largely consistent with the distinct behaviour of the aromatic and lactate/perfluorinated sub-units in Chapter 3 and

Chapter 5, respectively. This observation that sub-layers within de Vries materials appear to behave in a non-uniform manner has also been proposed in previous experimental studies of siloxane-based compounds.[108,109]

The formation of a strongly defined layer structure due to the incompatibility of different molecular sub-units is often considered a necessity for compounds to display de Vries behaviour, and consistent with the notion that translational order is the primary driver of mesophase formation in de Vries materials.[116] Therefore, the immiscibility of the flexible trisiloxane end group and the inflexible aromatic core in TSiKN65 is coherent with the observation of distinct aromatic and siloxane sub-layers at all simulated temperatures. The formation of such nano-segregated layers can not only be seen in polysiloxane liquid crystalline materials, but also in perfluorinated- and lactate-based compounds. Despite the issues associated with the simulation of de Vries character in TSiKN65, the consistency between many behaviours exhibited by TSiKN65 and that of 9HL and 3M 8422, supports the view that nanophase separation is a crucial component for the promotion of de Vries character.

Chapter 7 – Conclusions and Further Work

The materials chosen for study in this work offered an excellent opportunity to explore the de Vries behaviour exhibited by compounds that contain very different structural features. It was found that many of the characteristics associated with de Vries behaviour were successfully captured by MD simulations, yielding additional insights into the potential mechanisms that contribute to minimal layer contraction in smectic materials. The aim of this chapter is to discuss the overall conclusions that can be drawn from the work performed throughout this project and consider how the work could be expanded in an effort to provide a more comprehensive picture of de Vries behaviour and the materials that exhibit it.

7.1 MD Simulations

7.1.1 Prediction of Experimental Trends

The initial aim of the MD simulations described in this thesis was to accurately model the SmA and SmC phases formed by molecules of 9HL, 3M 8422 and TSiKN65. In this project, a key indicator of MD simulation success was their ability to replicate experimental trends in orientational and translational order parameters, layer spacing and molecular tilt across a wide temperature range, with the simulations found to be largely effective at replicating the trends in these observables. Measurement of the P_2 values exhibited by the simulations at each temperature revealed that all of the phases were orientationally ordered and that the orientational order decreased as the temperature increased for all three compounds, consistent with the results of experimental studies. Likewise, the calculation of the simulated τ values showed that all three materials formed phases with a defined layer structure across the entire simulated temperature range, which was confirmed by visualisations of the SmA and SmC phases and consistent with experimental reports.

The ability of the MD simulations to accurately replicate experimentally observed trends in layer spacing and tilt angle measurements was particularly relevant, due to the focus on de Vries character. In this work, the average molecular tilt was determined at all simulated temperatures as the angle between the vectors **n** and **k**, and significantly, was shown to increase as the temperature is decreased in all materials. Phases of 9HL and 3M 8422 displayed a sizable increase in tilt upon transition to the SmC phase, consistent with experimental results. However, in contrast, the simulations of TSiKN65 exhibited only a relatively small increase in tilt upon transition to a SmC-like phase, which is at odds with experimental studies of the same material. In addition, as the materials studied in this work are reported to exhibit minimal variation in layer spacing at the SmA-SmC transition, the thickness of the smectic layers was quantified at all simulated temperatures. The MD simulations were shown to accurately reproduce the experimental trend in layer spacing for each material. Most notably, simulations of 9HL exhibited only a minimal reduction in layer thickness at the SmA-SmC transition,

while the simulations of 3M 8422 and TSiKN65 demonstrated no layer shrinkage, despite the onset of molecular tilt.

Although the MD simulations performed in this work do remarkably well to reproduce the experimental trends associated with each of the studied materials, they commonly either under- or overestimate the value of important observables, relative to experimental reports. As a result, further work in this area could focus on improving the prediction of absolute values for several key mesogenic properties. For example, P_2 values were substantially overestimated at all temperatures in the simulations of 3M 8422, relative to experimental studies, inconsistent with the idea that low orientational order is a fundamental feature of materials that exhibit de Vries character. However, curiously, low orientational order, i.e. P_2 values between 0.40-0.60, consistent with experiment, was observed in the simulations of TSiKN65, despite the clear parallels between the two compounds. A potential explanation for the inconsistency between the orientational order exhibited by simulations of 3M 8422 and TSiKN65 lies in the application of several optimised parameters, intended to improve the prediction of the nematic-isotropic transition in atomistic simulations of liquid crystals,[168] which were utilised in the simulations of 3M 8422 but not in the simulations of TSiKN65. As a result, further work could centre on additional simulations of 3M 8422 that do not employ these optimised parameters, probing whether the de Vries behaviour exhibited by the simulated phases is significantly affected by this change.

MD simulations generally reproduced the layer spacings and tilt angles to within an acceptable degree of accuracy. Simulations of 9HL exhibited an average tilt angle between 15-18° in the SmC phase, and a layer spacing between 4.08-4.25 nm across the simulated temperature range, both consistent with experimental studies.[85,87,219,220] Equivalent analysis performed on simulated phases of 3M 8422 revealed an average tilt angle of 21°and 15° for the aromatic cores and whole molecule, respectively, as well as a layer spacing between 3.36-3.39 nm either side of the SmA-SmC transition, which are in good agreement with those values observed from experiment.[78,84,88] Furthermore, simulations of TSiKN65 exhibited a tilt between 9-13° in the SmC phase, which, while considerably lower than the value of 30° often stated for the polarisable aromatic cores,[90] closely matches the experimentally-derived tilt of the whole molecules in the SmC phase.[96] However, despite this success, improving the capacity of MD simulations to predict absolute experimental values for layer spacings and tilt angles, two crucial aspects of smectic liquid crystals, would certainly provide an expanded ability to explore individual contributions to de Vries behaviour. This observation presents another potential route for future work, which could focus on the optimisation of a standard force field for the realistic prediction of key properties in smectic liquid crystals.

A crucial property for liquid crystals used in device applications is the thermal stability of the liquid-crystalline phase, i.e. the temperature at which the material becomes fully isotropic. Consequently,

in computational studies, this temperature point is frequently used as a simple benchmark or check for judging the accuracy of MD simulations. In this work, due to the primary focus on molecular behaviour close to the SmA-SmC transition, the ultimate transition to an isotropic phase was not studied in any considerable detail nor considered a quantity of interest in the parameterisation work. Despite this, a few of the simulated materials did exhibit some degree of 'melting-like' behaviour close to their experimentally reported clearing point. As discussed briefly in Chapter 5, in simulations of 3M 8422, a substantial reduction in order was observed between simulations performed at 330 K and 340 K, consistent with experimentally reported transition temperatures.[84,277] Likewise, simulations of 9HL carried out above 400 K exhibited increasingly less order, in keeping with earlier studies of *n*HL materials.[219] In contrast, all of the work performed on simulations of TSiKN65 was clearly above the reported SmA-I transition of 329 K,[83,90] potentially due to the lack of suitable GAFF force field parameters for Si atoms, even after the optimisation performed in this work. Due to this mixed success, an obvious route for future work could focus on improving the ability of MD simulations to accurately predict the temperature of the transition to the isotropic phase in these materials. Furthermore, work could centre on exploring the direct SmA-I transition more generally, due to its seemingly vital importance to de Vries behaviour.

7.1.2 Quantification of de Vries Character

The work reported in this thesis focuses on the simulation of de Vries behaviour in materials that are known to exhibit minimal layer contraction at the SmA-SmC transition. As a result, the ability to quantify the relationship between the layer spacing and the tilt angle was an important factor in judging whether the MD simulations performed had been successful in capturing de Vries behaviour. In the analysis of 9HL, *R* values provided a means to quantify the reduction in layer contraction relative to that expected if molecules behaved as rigid-rods and indicated that the simulated phases of 9HL exhibited clear de Vries character. The equivalent analysis performed on phases of 3M 8422 and TSiKN65 was hindered by the smectic layers expanding upon transition to the SmC phase, highlighting that the layer shrinkage was not only significantly lower than expected from the measurement of the molecular tilt, but negative. In addition, analysis of the tilt angle populations over the final 100 ns of simulation time, at each temperature, revealed that a seemingly discontinuous increase in tilt occurs upon transition to the SmC-like phase, and that this increase does not correspond to a simultaneous decrease in layer thickness. In this work, each series of simulations utilised a 10 K or 20 K temperature interval, which enabled the properties of the phases to be studied over a fairly wide temperature range. However, future work could aim to explore de Vries character with a series of MD simulations more closely interspaced around the SmA-SmC transition, potentially providing further insight into the behaviour of individual molecules and the layer structure more generally at temperatures close to the tilt transition.

7.1.3 Analysis of de Vries Behaviour

As atomistic MD simulations have the ability to provide a sub-molecular level view of the liquid crystal phase structure, simulations can often be a useful way to obtain an insight into the behaviour of individual molecules, as well as their contributions to macroscopic properties. In addition, MD simulations are particularly suited to probing properties, such as de Vries character, which may be caused by the combination of multiple factors, each partially offsetting the layer contraction expected due to the tilt transition. In this work, the potential mechanisms behind de Vries behaviour were considered, and comparisons were made with the results of the MD simulations performed on 9HL, 3M 8422 and TSiKN65.

ODFs based on the MOI axis of the whole molecule enabled the molecular distribution of tilt directions to be probed in both the tilted and non-tilted phases. The ODFs determined from simulations of 9HL and 3M 8422 indicated a very clear shift occurs at the SmA-SmC transition, as molecules adopted a 'volcano-like' distribution in the SmC phase and a distribution centred on zero in the SmA phase. Simulations of TSiKN65 exhibited much broader distributions due to the lower orientational order observed in these phases, likewise, displaying a non-zero-centred and zero-centred distribution in the SmC and SmA phase, respectively, but to a much less obvious extent. These observations indicated that all of the materials studied in this work possess a fairly conventional SmA phase, in which molecules remain untilted relative to **k**. This in itself is noteworthy due to the number of models of de Vries behaviour that propose the existence of a uniquely tilted 'de Vries-type' SmA phase, however, the ODFs determined from simulations of all three materials appear to be inconsistent with the presence of such an extensive molecular tilt in the SmA phase.

The impact of molecular length on the overall layer spacing was assessed via measurement of the average length of molecules at all simulated temperatures. This was important as several models that attempt to provide an explanation for de Vries behaviour propose that the extension of molecules upon transition to the SmC phase offset the layer contraction expected from the increased tilt. In this work, the average molecular length was observed to increase as the temperature was decreased for all three compounds, consistent with the idea that the terminal chains of molecules adopt a more extended conformation as the temperature is reduced. However, in all cases, the molecular elongation was determined to be insufficient to fully account for the decrease in layer contraction. In addition, molecular length distributions were also calculated at each simulated temperature, suggesting that molecules do indeed take on a more extended conformation as the phase is cooled down. The calculation of this contribution from molecular elongation, whilst being insufficient to fully explain de Vries behaviour in all cases, perhaps indicates that molecules adopting a more extended conformation can be considered a minor effect more broadly. Furthermore, it would seem extremely doubtful that any material should not exhibit such an effect, implying that the distinction between

materials with and without de Vries character likely does not arise due to the extension of molecules alone.

Various models for de Vries behaviour reference a shift in interdigitation as the primary factor that leads to minimal layer contraction, proposing that the degree of overlap between molecules in adjacent smectic layers changes significantly at the SmA-SmC transition. In this work, the extent to which molecules were interdigitated within the simulated phases was probed by analysing the positions of key atoms located at the border between different structural fragments. Layer projections, described in previous chapters focused on 3M 8422 and TSiKN65, provided several important insights into the smectic layer structure formed by these compounds, but no substantial differences in the molecular positions were observed in either compound at temperatures above and below the transition to the SmA/SmC phase. Analysis performed on 9HL and 3M 8422 included calculation of the percentage of the end groups considered to be interdigitated, which revealed that the aliphatic sub-units of both materials remained almost fully overlapped with their equivalents in oppositely orientated molecules across the entire simulated temperature range. In contrast, the lactate sub-units in 9HL and the perfluorinated sub-units in 3M 8422 were shown to possess a degree of interdigitation of 20-30 %, implying significantly less overlap occurs between sub-units in adjacent layers. This observation is especially noteworthy as, despite their clear structural differences, both lactate and perfluoropolyether sub-units appear to strongly promote phase-segregation, perhaps due to the considerable flexibility that each of these elements possess. In addition, the interdigitation analysis indicated that the perfluorinated sub-units of 3M 8422 become increasingly overlapped at higher temperatures, a trend not exhibited by the lactate units of 9HL. Such behaviour leads to a potential explanation for de Vries behaviour, in which layer shrinkage is fully or partially offset by a decrease in molecular overlap close to the SmA-SmC transition. However, given the absence of clear shift in the layer projections at low and high temperatures, this increase in interdigitation was considered to be insufficient to compensate the layer shrinkage expected upon transition to the SmC phase.

The materials studied in this work possess several parallels in their structural composition. Notably, they contain an inflexible aromatic core in combination with highly flexible terminal chains, which could be expected to induce a degree of nano-segregation that would result in the formation of distinct sub-layers. However, despite these loose parallels, all three materials possess very dissimilar chemical structures, composed of groups that would be expected to contribute rather differently to mesophase behaviour. For example, the lactate sub-unit of 9HL contains a seemingly conventional 6-carbon aliphatic chain, and does not possess any highly electronegative atoms, such as fluorine in 3M 8422, or any bulky substituents, such as siloxane in TSiKN65. Likewise, the aromatic cores of 9HL and TSiKN65 appear to be three ring systems based on phenyl benzoate, but the aromatic core of 3M 8422 is based on shorter and more rigid 2-phenylpyrimidine group. Consequently, it is quite

remarkable that the overall combination of structural elements in 9HL, 3M 8422 and TSiKN65 results in largely comparable mesophase behaviour. The formation of distinct perfluoropolyether and siloxane sub-layers in simulations of 3M 8422 and TSiKN65, respectively, may be expected due to the clear contrast between the flexibility and bulky character of these units, and the rest of the molecule. However, surprisingly, a similar behaviour is exhibited by 9HL, in which it would be anticipated that the hexyl lactate unit would be largely miscible with the 9-carbon aliphatic chain, yet these elements can be seen to be quite well separated in the phase structure.

Many models that attempt to measure the expected layer shrinkage upon transition to the SmC phase assume that the whole molecule behaves uniformly in both the SmA and SmC phases. However, several studies of de Vries materials have reported that different parts of the molecule potentially display very different tilt behaviour. The possibility that individual molecular sub-units may contribute differently to the overall layer thickness was probed in this work via the calculation of ODFs based on the MOI axis of only those atoms in each distinct molecular sub-unit. The ODFs indicated that molecules of 9HL, 3M 8422 and TSiKN65 exhibited a non-uniform tilt in the SmA phase and the SmC phase, with clear differences in the shapes of the orientational distributions across the entire temperature range. The lack of similarity between the ODFs representing different molecular sub-units was most obvious in simulations of 9HL and 3M 8422, due to the higher orientational order, relative to the simulations of TSiKN65. Crucially, all of the materials appear to possess at least one sub-layer that remains untilted, even in the SmC phase. The sub-layers composed of the lactate, perfluoropolyether and siloxane sub-units in 9HL, 3M 8422 and TSiKN65, respectively, happen to exhibit very similar characteristics, most obviously in their low orientational order and minimal tilt, relative to the aromatic and aliphatic sub-units in the same phase. This analysis presented a remarkably simple and consistent rationalisation for the reduction in layer contraction observed in simulations of three de Vries materials, as a considerable proportion of the layer structure remains untilted in the SmC phase.

7.1.4 Periodic System Properties

In this work, the periodic box setup remained consistent across simulations performed at different temperatures. In addition, the replication procedure used to create each of the final systems was identically applied in every case. Such an approach enabled a direct comparison between results extracted from separate simulation runs and provided a level of confidence that any differences in observed were not caused by inconsistencies in the system ‘build up’ phase. A potential avenue for future work could, therefore, be the examination of factors such as box shape dependency, which may be used to further validate the results presented in the previous chapters, as well as explore how the development of liquid-crystalline order is affected by employing a non-cubic periodic boundary condition.

A second aspect of system setup that could be studied in any corollary work is the effect of ultimate system size on simulation accuracy. Until recently, the computational cost of studying positionally ordered materials, such as smectic liquid crystals, has been prohibitive due to the perceived need for sizeable systems, i.e., ≥ 1000 molecules, as well as extended timescales associated with the development of a layer structure. In this work, system setup was achieved via a 2 × 2 × 2 replication procedure that started with an isotropic 16-molecule system, used to construct fully equilibrated 128- and 1024-molecule systems. While this method substantially reduced the time necessary to produce a stable liquid-crystalline phase, the requirement to simulate systems composed of *ca.* 1000 molecules in order to probe translational order has not been fully established. Therefore, a comprehensive study of system size dependency for simulation results could prove to be valuable, potentially expediating MD studies by allowing for smaller system sizes without much loss in simulation accuracy.

Appendix

A.1 Supplementary information relating to Chapter 3

A.1.1 Geometry optimised structures

Table A.1 Coordinates of each atom within the optimised geometry of 9HL, derived from DFT calculations at the B3LYP/6-31G(d) level and used as the initial geometry of 9HL molecules in the MD simulation performed in this work.

C	-5.64433	-0.00711	-1.68312
C	-6.41048	0.42647	-0.59378
C	-6.2746	-0.7246	-2.71691
C	-7.77438	0.15252	-0.52508
H	-5.93662	0.9816	0.20777
C	-7.62828	-1.00181	-2.65919
H	-5.67703	-1.05781	-3.55895
C	-8.39147	-0.5678	-1.5596
H	-8.34433	0.49942	0.32862
H	-8.12714	-1.55577	-3.44785
O	-9.70626	-0.89549	-1.59295
C	-10.55116	-0.5193	-0.5003
H	-10.56765	0.57581	-0.40491
H	-10.15201	-0.93556	0.43558
C	-11.94419	-1.06307	-0.78374
H	-11.87446	-2.15085	-0.91195
H	-12.29361	-0.65501	-1.74075
C	-12.94346	-0.72695	0.33082
H	-13.00942	0.36449	0.45005
H	-12.56908	-1.11659	1.28904
C	-14.3453	-1.29367	0.06979
H	-14.27627	-2.3845	-0.05239
H	-14.72177	-0.90416	-0.88739
C	-15.35161	-0.97032	1.1814
H	-15.42611	0.12098	1.2989
H	-14.96906	-1.35296	2.13937
C	-16.74927	-1.54968	0.92698
H	-16.67241	-2.64053	0.8064
H	-17.13302	-1.16576	-0.02998
C	-17.75665	-1.23357	2.0397
H	-17.83707	-0.14274	2.15942
H	-17.37221	-1.61541	2.99741
C	-19.15249	-1.81795	1.78716
H	-19.07158	-2.90758	1.66576
H	-19.53792	-1.43443	0.83161
C	-20.15225	-1.50189	2.9042
H	-20.28149	-0.41937	3.0264
H	-21.13769	-1.93269	2.69324
H	-19.81206	-1.90419	3.86642

O	-3.71833	0.96503	-0.72563
C	-2.37765	1.28561	-0.59006
C	-1.33746	0.40172	-0.89257
C	-2.11522	2.54224	-0.03696
C	-0.02569	0.79376	-0.64216
H	-1.5495	-0.56658	-1.3245
C	-0.80328	2.92246	0.21141
H	-2.94652	3.20146	0.19083
C	0.25483	2.0525	-0.09095
H	0.78788	0.11642	-0.87402
H	-0.57733	3.89323	0.6394
O	2.56289	1.56469	-0.1385
C	3.9269	1.77679	0.01631
C	4.56035	2.97958	-0.30909
C	4.65933	0.66533	0.43892
C	5.94455	3.05677	-0.19488
H	3.98306	3.83441	-0.6339
C	6.04261	0.75231	0.54877
H	4.13337	-0.25503	0.6711
C	6.69441	1.95376	0.23469
H	6.46542	3.97576	-0.44239
H	6.62333	-0.10605	0.86718
O	8.75507	0.98552	0.8312
C	10.18591	0.97764	0.90496
H	10.58795	1.5799	0.08477
C	10.65954	1.55148	2.2423
H	11.74984	1.50371	2.30759
H	10.34614	2.59591	2.31908
H	10.22765	0.98701	3.07506
O	11.95891	-0.54001	0.62765
C	12.52159	-1.86135	0.44035
H	12.09565	-2.29711	-0.46974
H	12.22153	-2.49473	1.28211
C	14.03184	-1.71348	0.34695
H	14.27132	-1.02164	-0.47107
H	14.40459	-1.25027	1.2699
C	14.73179	-3.0597	0.11515
H	14.34535	-3.51837	-0.8067
H	14.47651	-3.75236	0.93047
C	16.25764	-2.93452	0.01647
H	16.64622	-2.48438	0.94188
H	16.51252	-2.23384	-0.79231
C	16.96487	-4.27296	-0.23201
H	16.57573	-4.72092	-1.15736
H	16.70894	-4.97349	0.57559
C	18.48803	-4.14073	-0.32998

H	18.91104	-3.72978	0.59496
H	18.96281	-5.11184	-0.5102
H	18.77588	-3.4718	-1.15034
C	-4.19337	0.24431	-1.8039
C	1.63334	2.52051	0.19646
C	8.17031	2.1	0.32409
C	10.61388	-0.47664	0.71102
O	-3.49364	-0.11983	-2.72265
O	1.91521	3.59788	0.67116
O	8.79252	3.08931	-0.01323
O	9.87689	-1.43185	0.64533

A.1.2 9HL MD Simulation Data

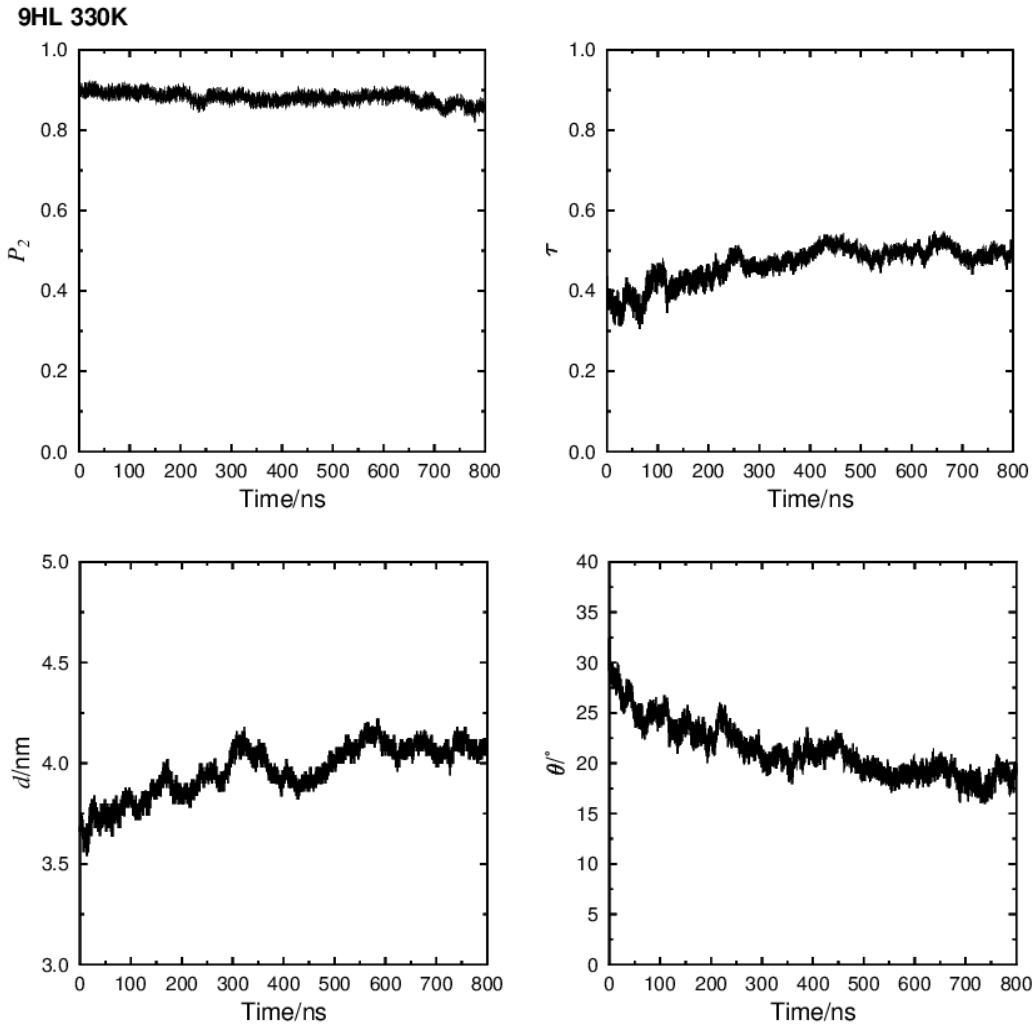

Figure A.1 Measurements of P_2, τ, d and Θ at each timestep of the MD simulation, comprising 1024 molecules of 9HL and performed at 330 K.

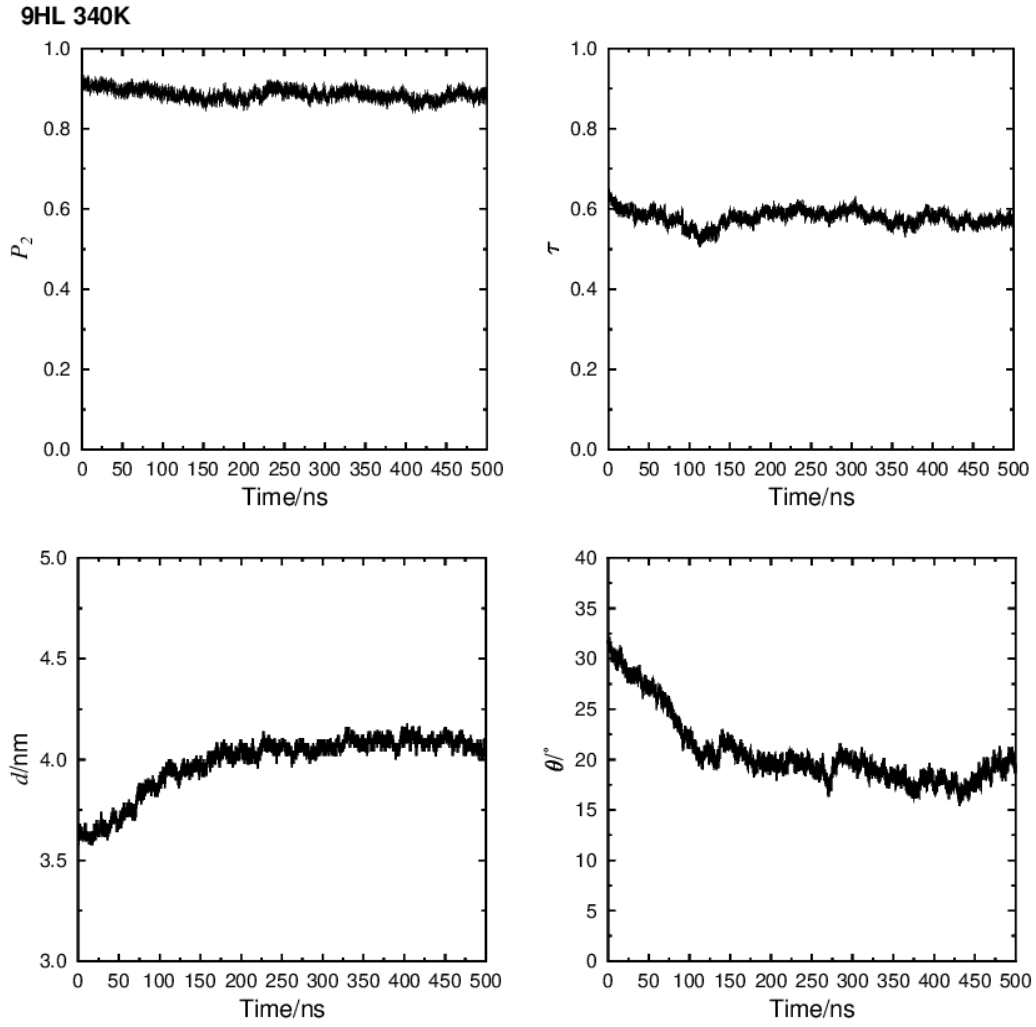

Figure A.2 Measurements of P_2, τ, d and Θ at each timestep of the MD simulation, comprising 1024 molecules of 9HL and performed at 340 K.

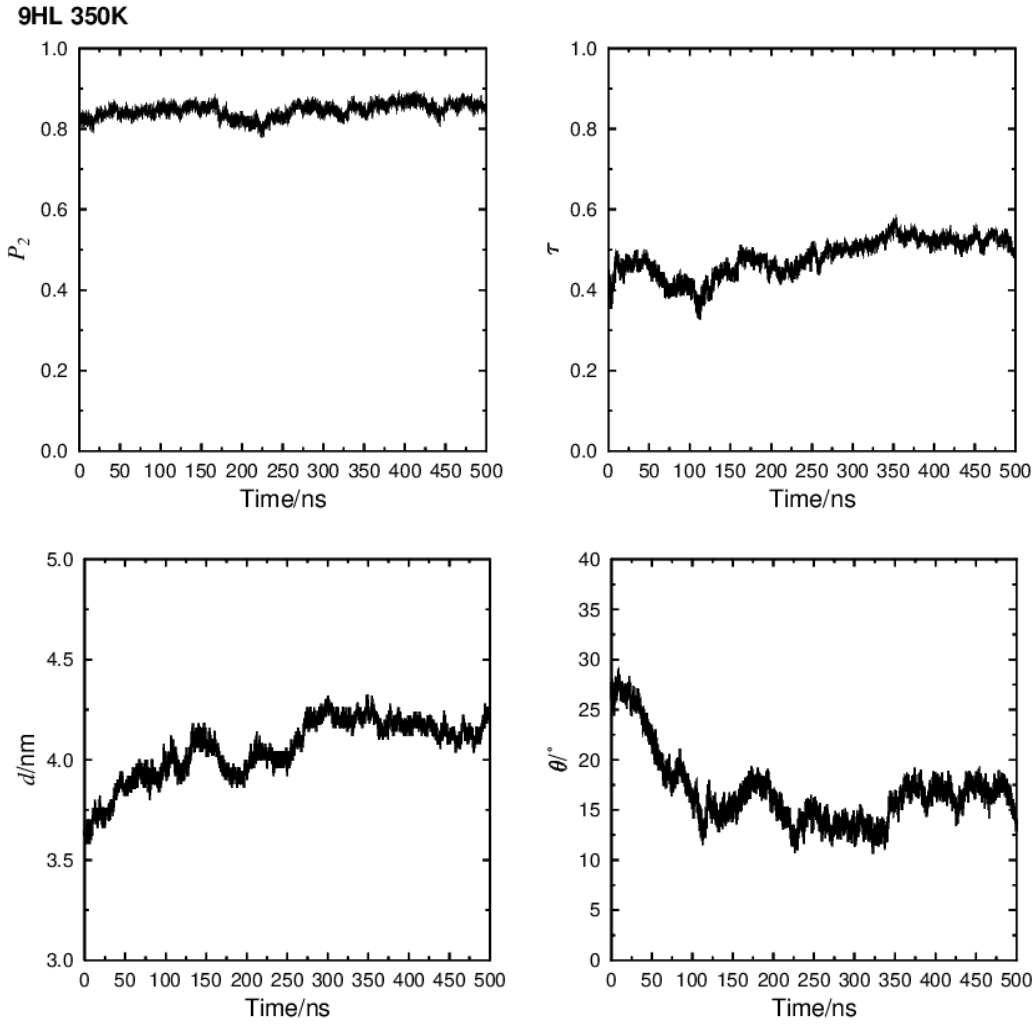

Figure A.3 Measurements of P_2, τ, d and Θ at each timestep of the MD simulation, comprising 1024 molecules of 9HL and performed at 350 K.

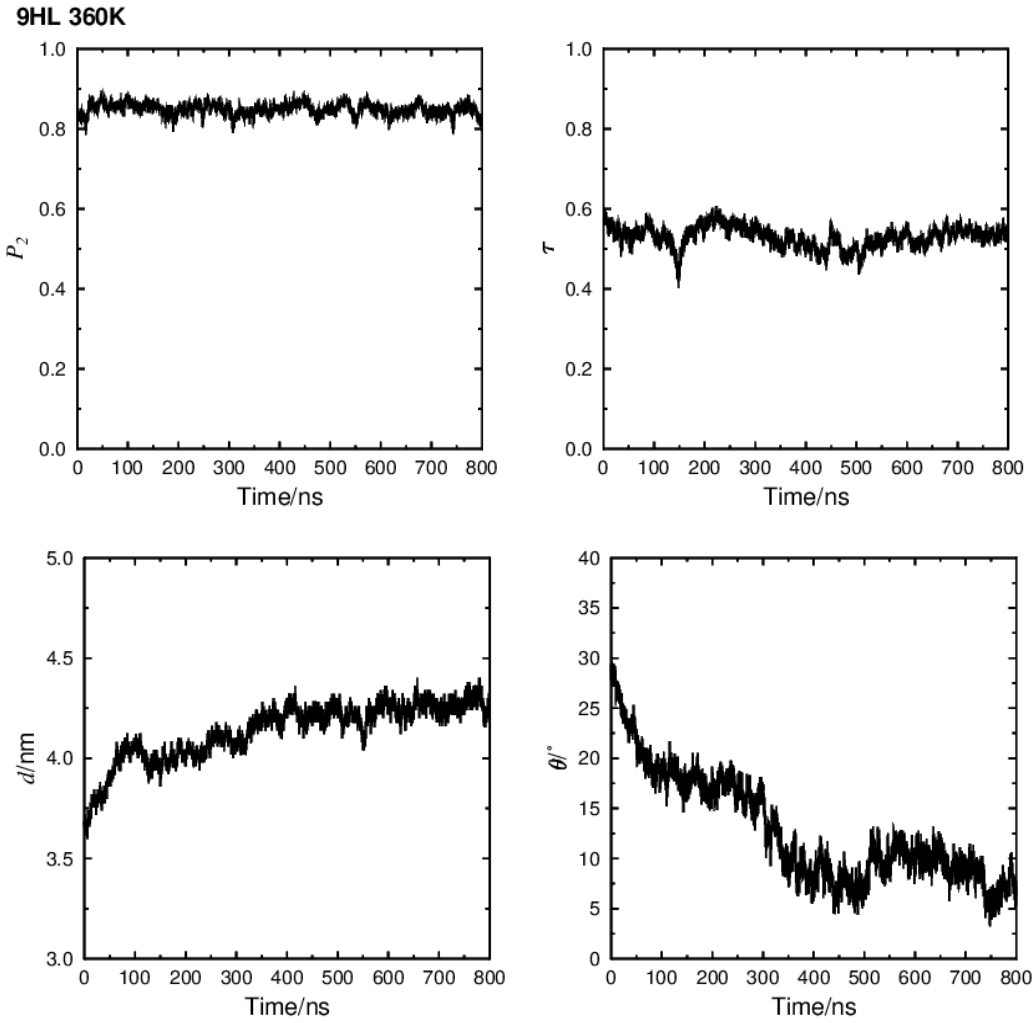

Figure A.4 Measurements of P_2, τ, d and Θ at each timestep of the MD simulation, comprising 1024 molecules of 9HL and performed at 360 K.

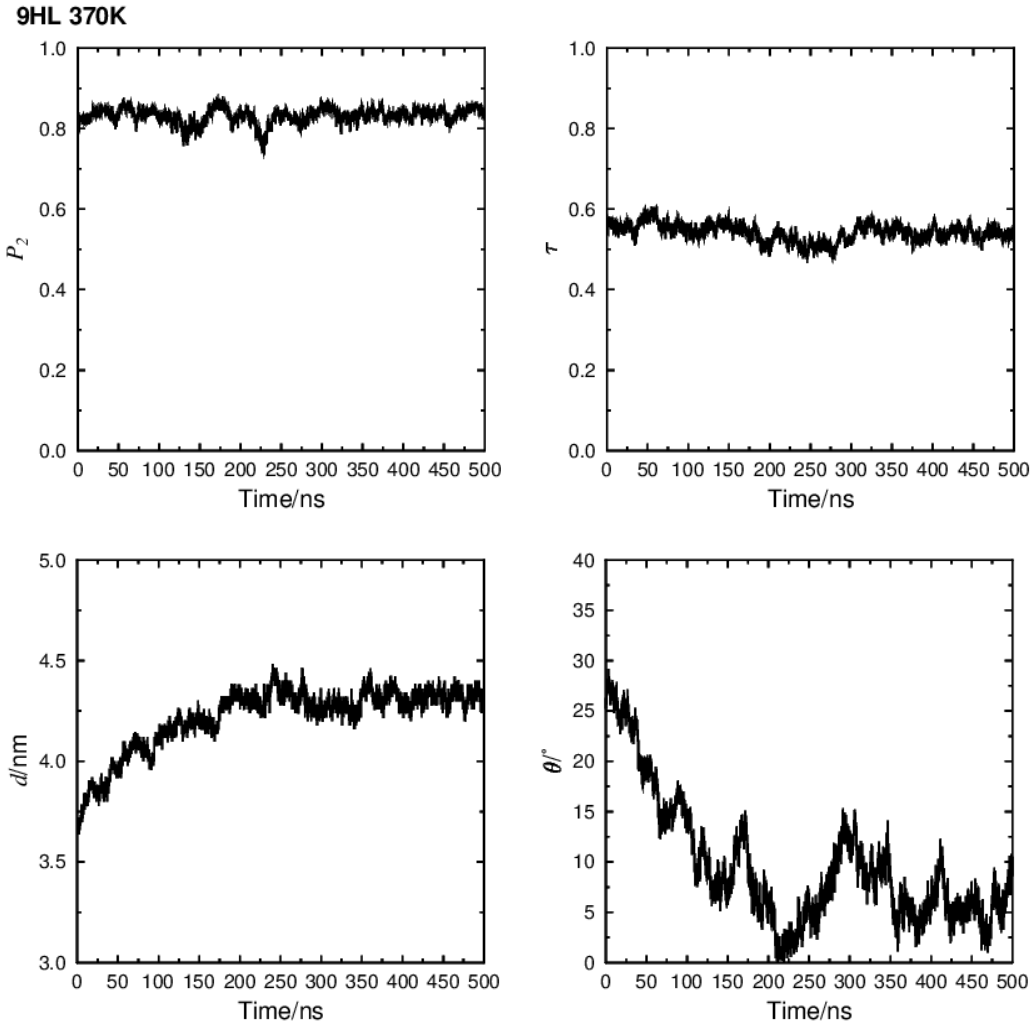

Figure A.5 Measurements of P_2, τ, d and Θ at each timestep of the MD simulation, comprising 1024 molecules of 9HL and performed at 370 K.

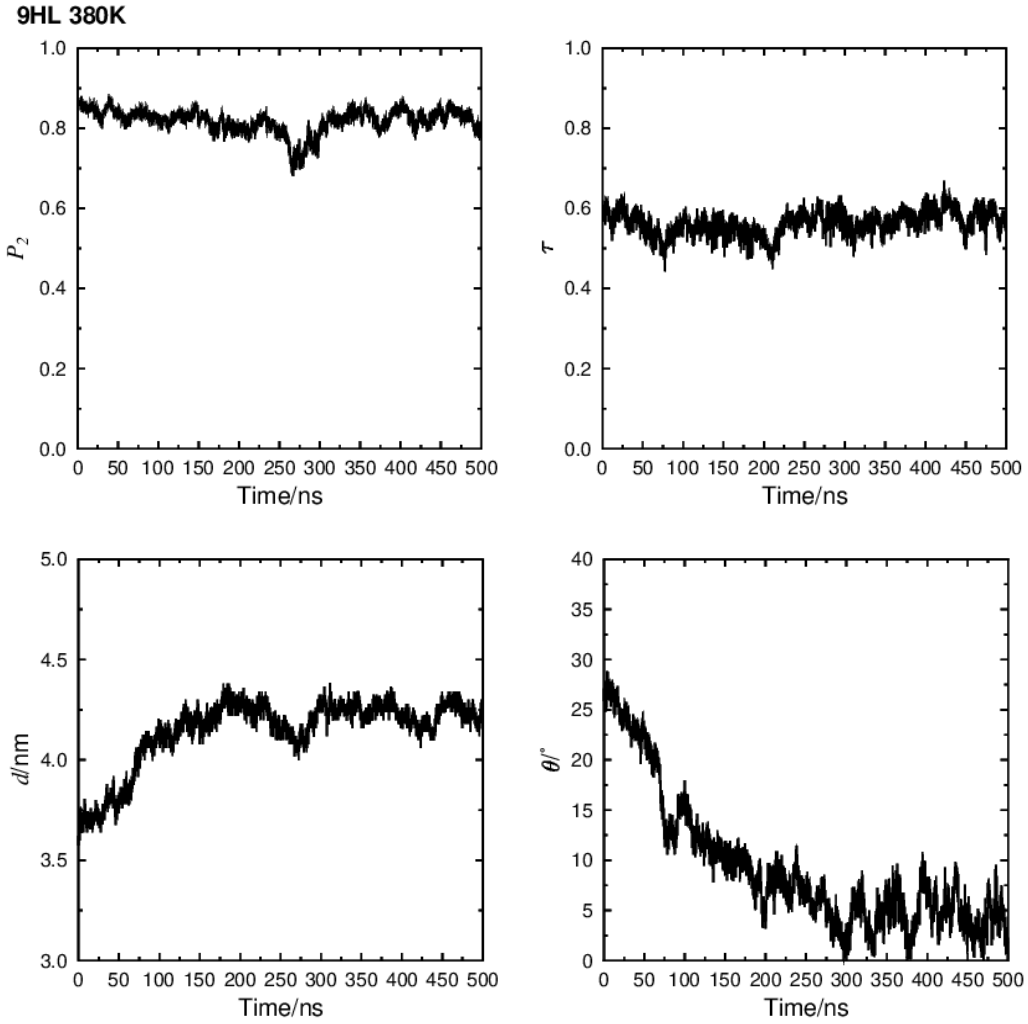

Figure A.6 Measurements of P_2, τ, d and Θ at each timestep of the MD simulation, comprising 1024 molecules of 9HL and performed at 380 K.

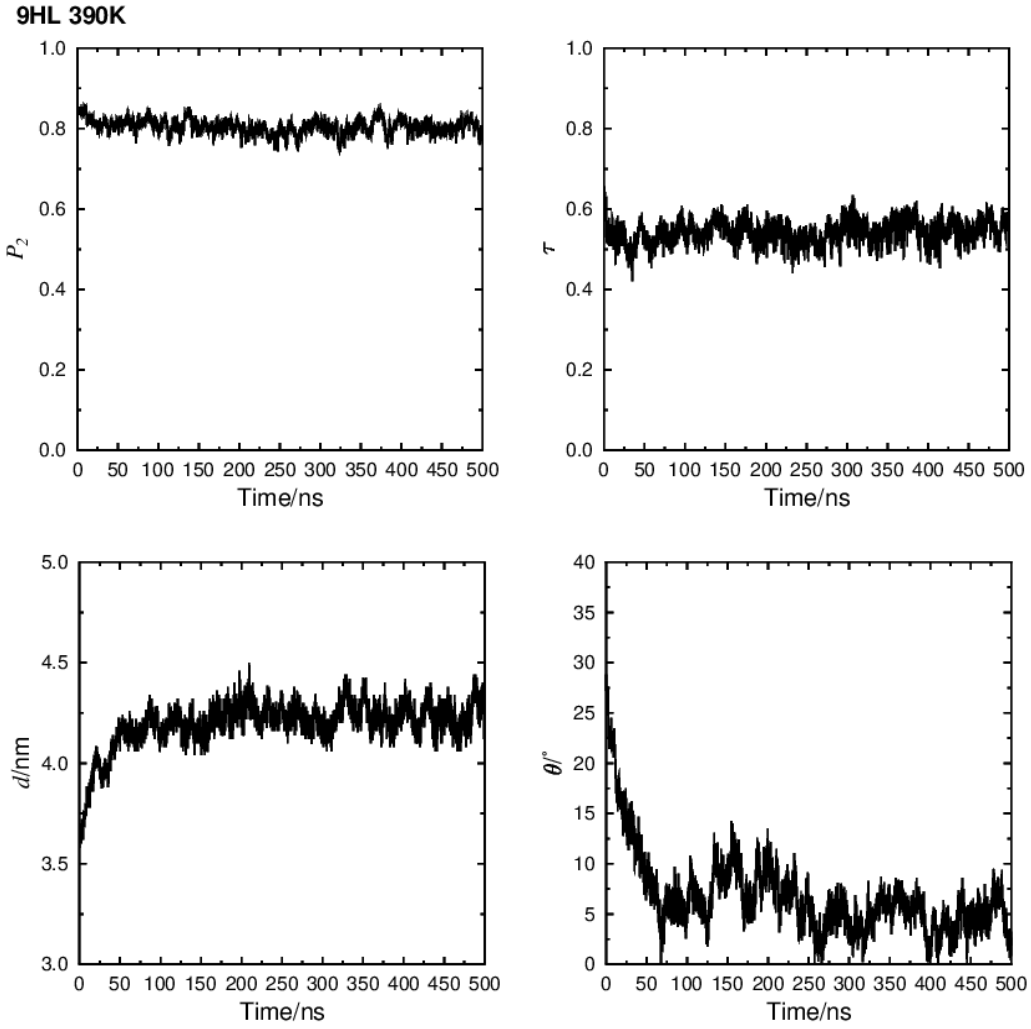

Figure A.7 Measurements of P_2, τ, d and Θ at each timestep of the MD simulation, comprising 1024 molecules of 9HL and performed at 390 K.

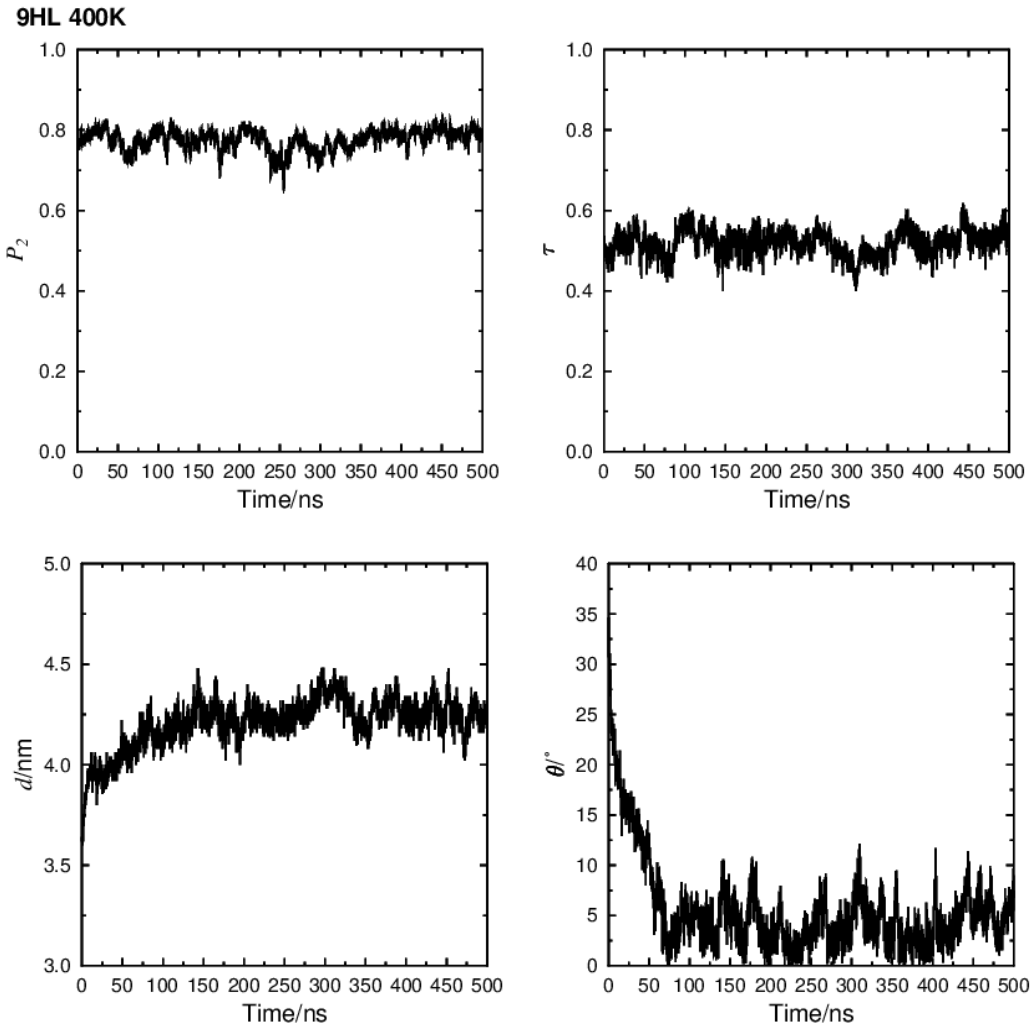

Figure A.8 Measurements of P_2, τ, d and Θ at each timestep of the MD simulation, comprising 1024 molecules of 9HL and performed at 400 K.

A.2 Supplementary information relating to Chapter 5

A.2.1 Geometry optimised structures

Table A.2 Coordinates of each atom within the optimised geometry of 3M8422, derived from DFT calculations at the B3LYP/6-31G(d) level and used as the initial geometry of 3M8422 molecules in the MD simulation performed in this work.

C	1.82491	1.7656	0.32927
C	2.75461	2.61318	0.94084
C	4.10123	2.48444	0.65133
C	4.55405	1.51026	-0.25351
C	3.6126	0.67389	-0.85855
C	2.25464	0.79305	-0.5755
H	2.39467	3.35976	1.63792
H	4.82723	3.13462	1.12122
H	3.95726	-0.07685	-1.55741
H	1.55404	0.12813	-1.06317
C	5.99641	1.36982	-0.55647
N	6.36165	0.42221	-1.4358

N	6.84938	2.20035	0.06449
C	7.66095	0.30122	-1.69076
C	8.14296	2.056	-0.20923
C	8.64046	1.0989	-1.09545
H	7.93962	-0.46586	-2.41147
H	8.82038	2.74153	0.29723
C	10.11168	0.92271	-1.36627
H	10.61664	1.89045	-1.27198
H	10.25415	0.59944	-2.40346
C	10.78644	-0.0935	-0.42366
H	10.63973	0.22883	0.61403
H	10.27719	-1.06015	-0.51628
C	12.28263	-0.27003	-0.70271
H	12.78575	0.70085	-0.60787
H	12.42199	-0.58363	-1.74532
C	12.96077	-1.2843	0.22536
H	12.81944	-0.97172	1.26784
H	12.45781	-2.25499	0.12888
C	14.45822	-1.46112	-0.05091
H	14.59922	-1.77056	-1.09459
H	14.96125	-0.49055	0.04813
C	15.13735	-2.47818	0.87301
H	14.99619	-2.17029	1.91723
H	14.63578	-3.44962	0.77342
C	16.63513	-2.6545	0.5983
H	16.77639	-2.96118	-0.44522
H	17.13679	-1.68445	0.69962
C	17.30522	-3.67368	1.52413
H	18.37113	-3.77487	1.30247
H	17.2112	-3.37668	2.57338
H	16.84916	-4.66315	1.41946
O	0.51718	1.96782	0.68517
C	-0.46635	1.13676	0.11955
H	-0.53451	1.25709	-0.96686
H	-0.30207	0.08073	0.35823
C	-1.79727	1.55202	0.72325
O	-2.75578	0.67439	0.19268
C	-4.09513	0.96498	0.24576
C	-4.85387	-0.36982	-0.00411
O	-6.20664	-0.08259	0.04362
C	-7.13373	-0.95702	-0.48281
C	-8.51002	-0.57492	0.14788
C	-9.73602	-1.27068	-0.52133
C	-11.05243	-1.19513	0.31012
F	-2.10729	2.83246	0.42456
F	-1.78299	1.45044	2.06856

F	-4.44529	1.84825	-0.71159
F	-4.4711	1.47367	1.43326
F	-4.49242	-0.88057	-1.19575
F	-4.51877	-1.259	0.94673
F	-7.20066	-0.83823	-1.82337
F	-6.83477	-2.23629	-0.19537
F	-8.67392	0.75807	0.04251
F	-8.4685	-0.91108	1.45648
F	-9.9659	-0.68102	-1.71228
F	-9.45935	-2.57803	-0.72622
F	-12.06558	-1.62102	-0.4495
F	-10.97456	-1.97175	1.39238
F	-11.29827	0.06283	0.69034

A.2.2 3M 8422 MD Simulation Data

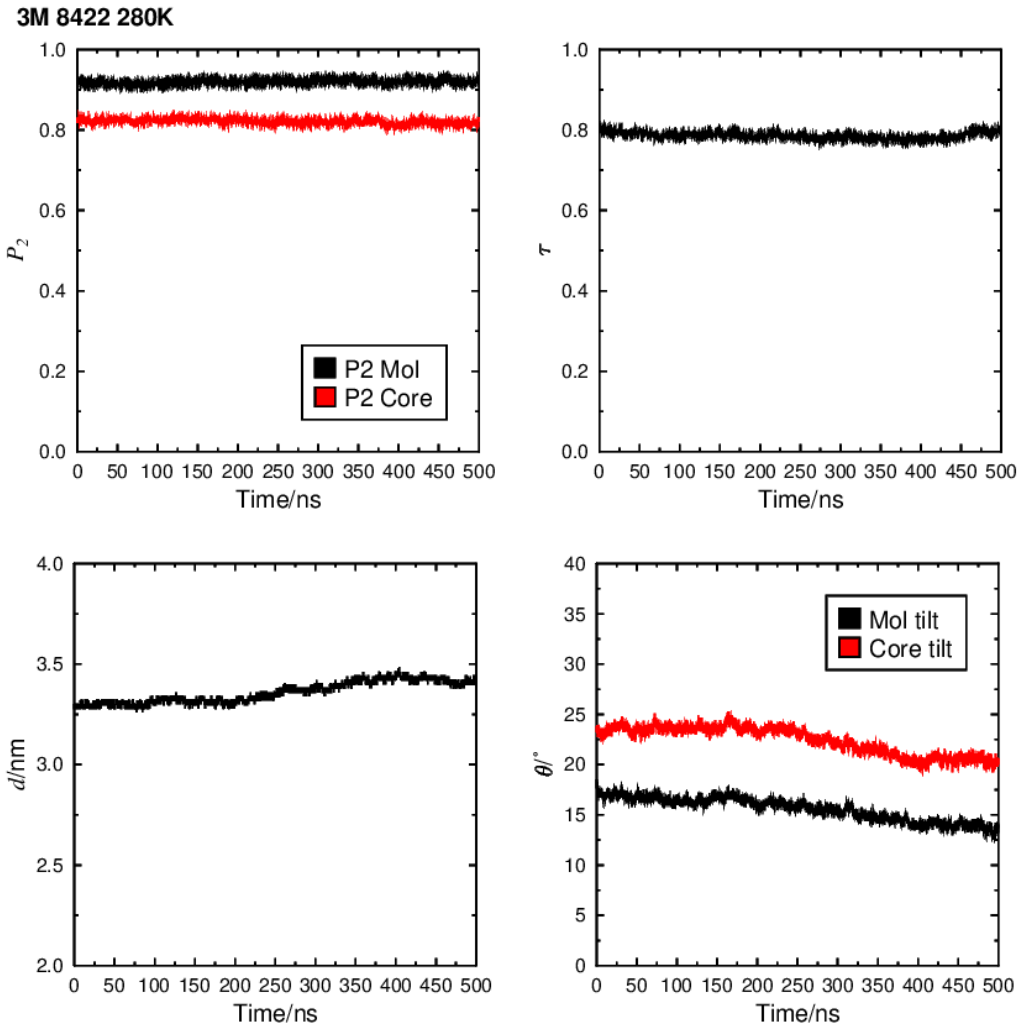

Figure A.9 Measurements of P_2, τ, d and Θ at each timestep of the MD simulation, comprising 1024 molecules of 3M 8422 and performed at 280 K.

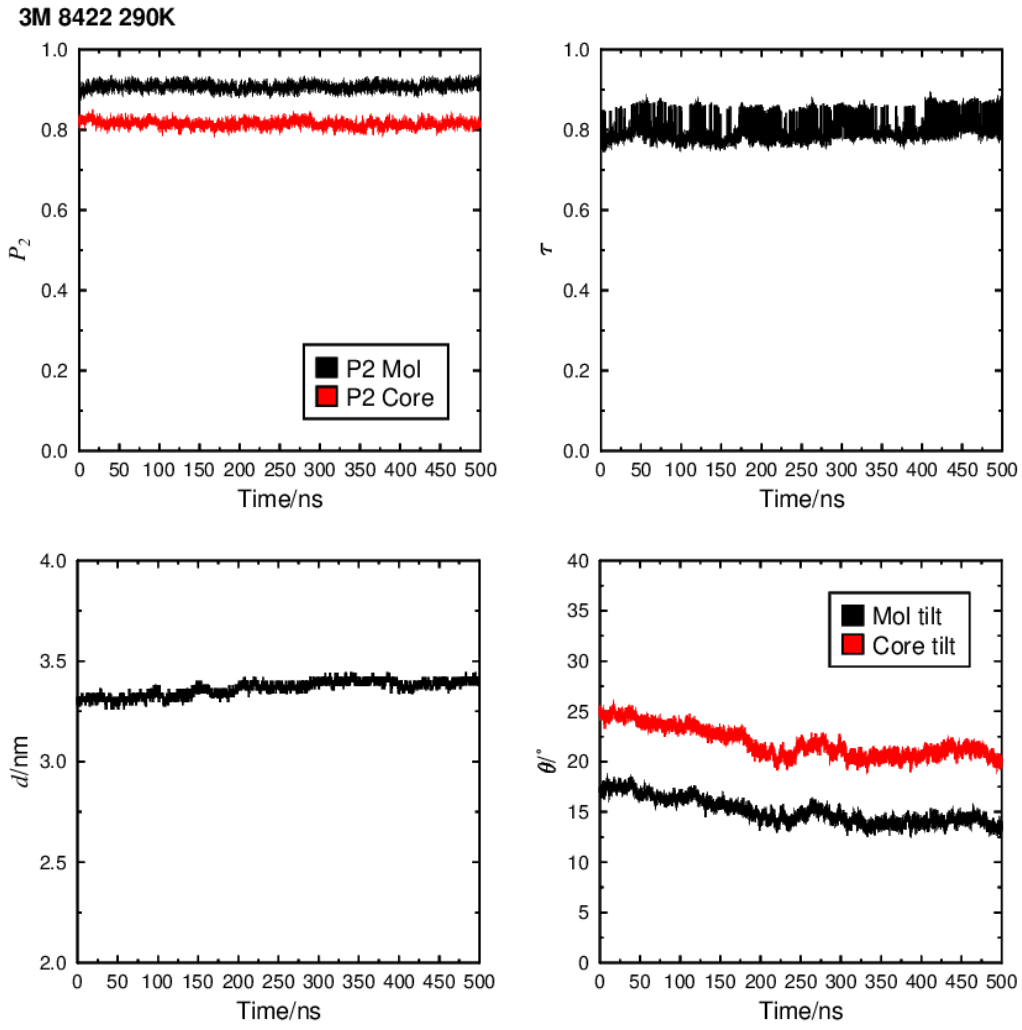

Figure A.10 Measurements of P_2, τ, d and Θ at each timestep of the MD simulation, comprising 1024 molecules of 3M 8422 and performed at 290 K.

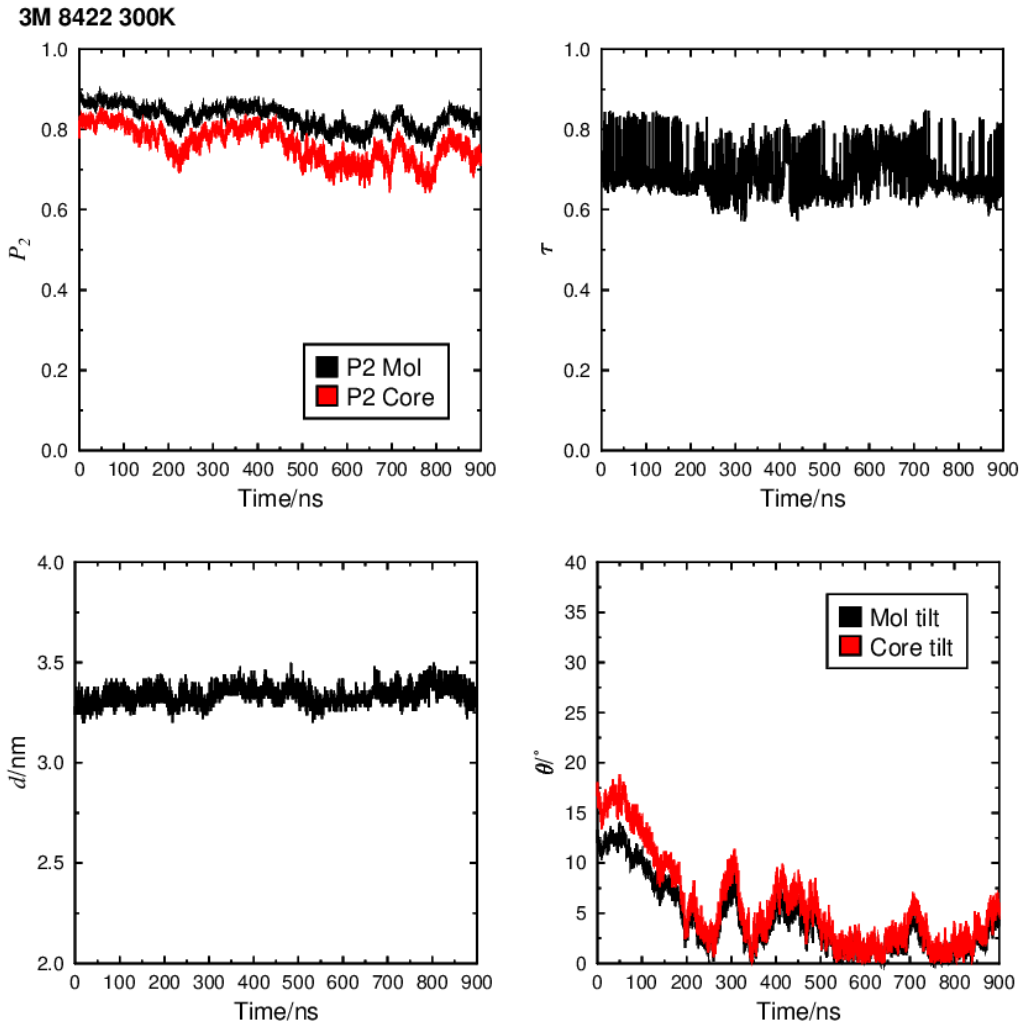

Figure A.11 Measurements of P_2, τ, d and Θ at each timestep of the MD simulation, comprising 1024 molecules of 3M 8422 and performed at 300 K.

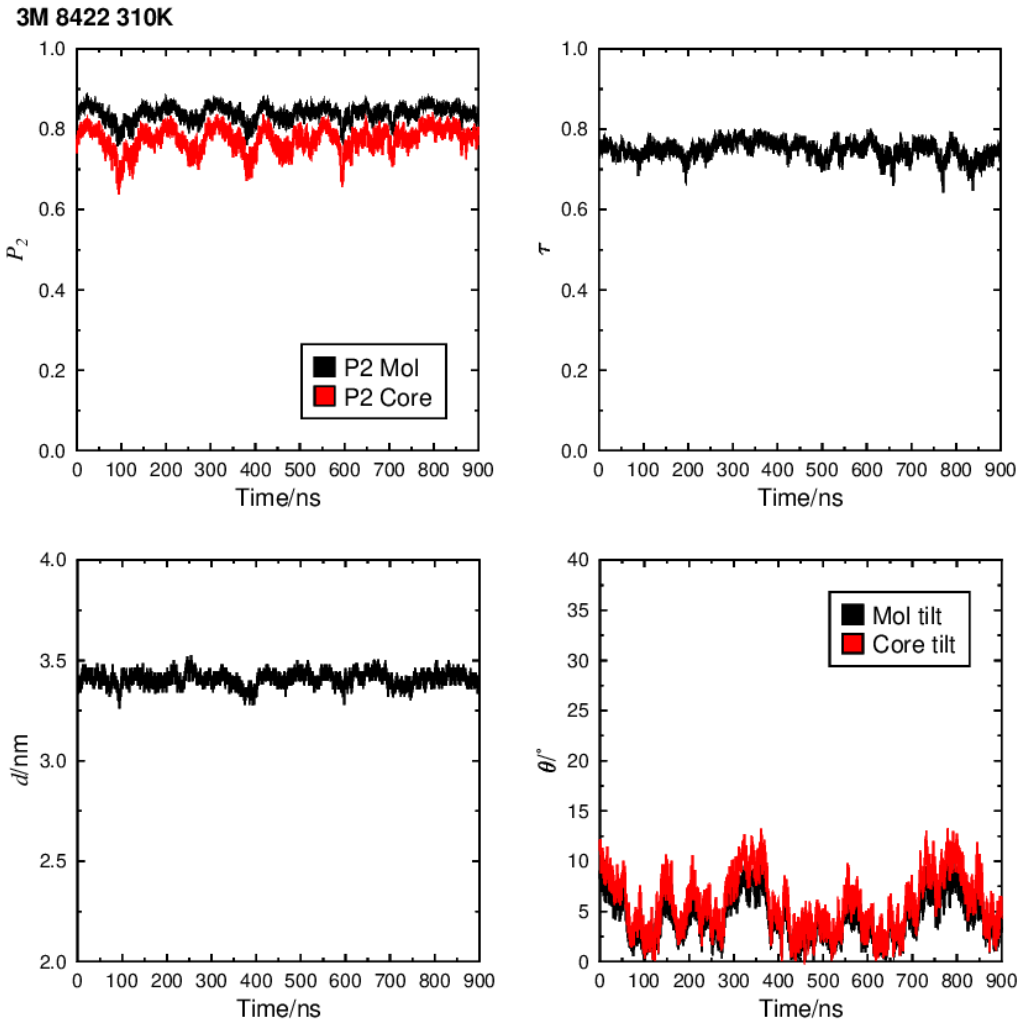

Figure A.12 Measurements of P_2, τ, d and Θ at each timestep of the MD simulation, comprising 1024 molecules of 3M 8422 and performed at 310 K.

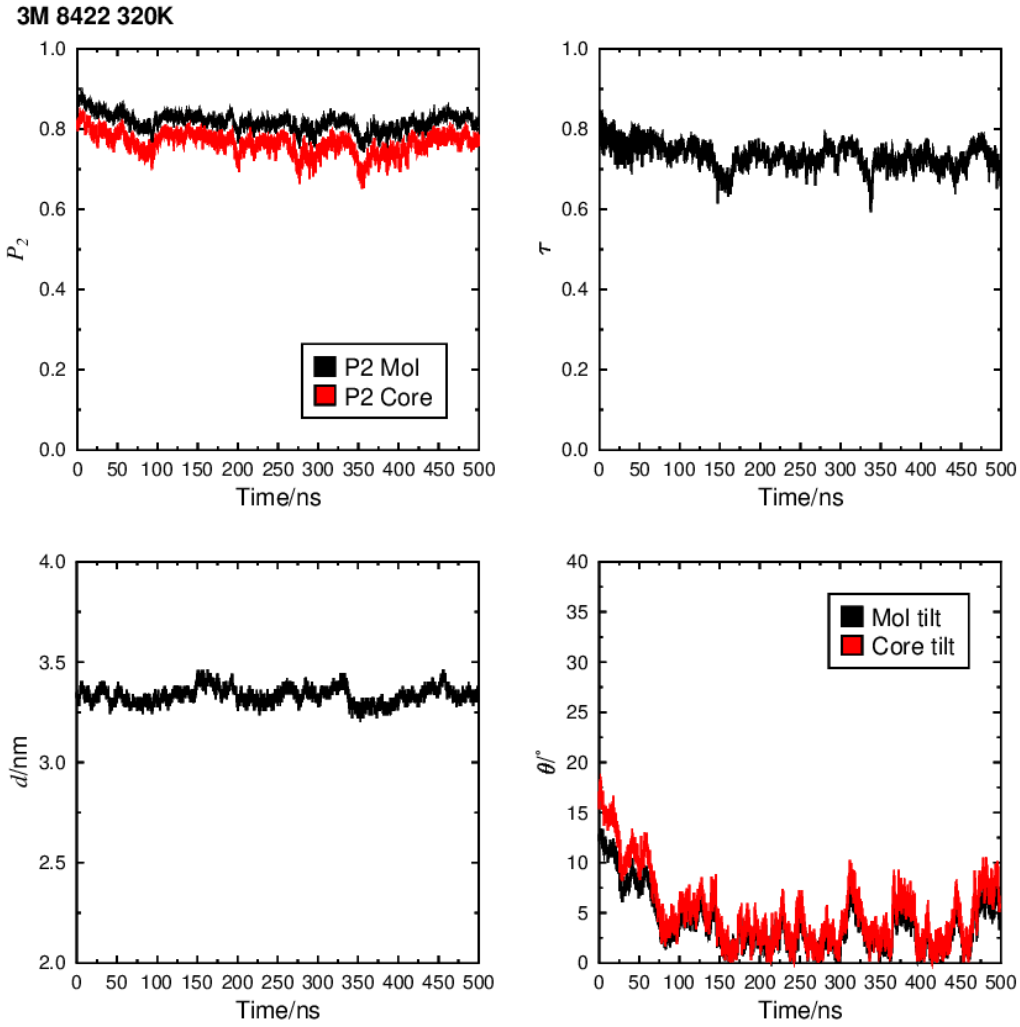

Figure A.13 Measurements of P_2, τ, d and Θ at each timestep of the MD simulation, comprising 1024 molecules of 3M 8422 and performed at 320 K.

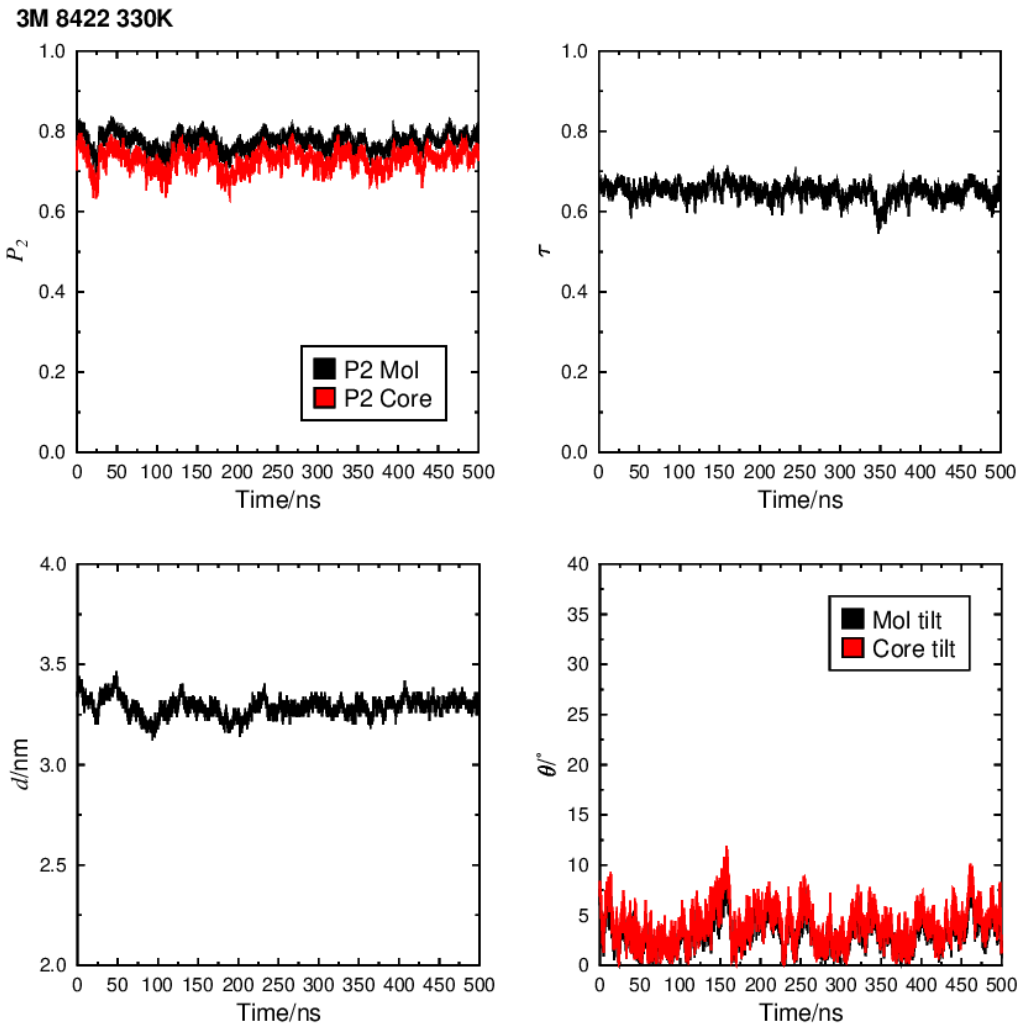

Figure A.14 Measurements of P_2, τ, d and Θ at each timestep of the MD simulation, comprising 1024 molecules of 3M 8422 and performed at 330 K.

A.3 Supplementary information relating to Chapter 6

A.3.1 Geometry optimised structures

Table A.3 Coordinates of each atom within the optimised geometry of TSiKN65, derived from DFT calculations at the B3LYP/6-311G(d) level and used as the initial geometry of TSiKN65 molecules in the MD simulation performed in this work.

C	9.60084	-1.71164	0.32827
C	10.96877	-1.54798	0.47149
C	11.5488	-0.28117	0.57229
C	10.67146	0.8163	0.56631
C	9.29642	0.65328	0.44716
C	8.73253	-0.61201	0.30314
H	9.19415	-2.71396	0.26982
H	11.6205	-2.40881	0.54151
H	8.67744	1.53956	0.45064
C	7.26855	-0.7863	0.15007
C	6.36764	0.00149	0.87705
C	6.74761	-1.74462	-0.72548

C	4.9965	-0.15808	0.73872
H	6.74193	0.73534	1.58046
C	5.37676	-1.91352	-0.8699
H	7.41879	-2.35198	-1.32056
C	4.50959	-1.11935	-0.13594
H	4.31006	0.44701	1.31535
H	4.97415	-2.6487	-1.55507
O	12.87983	-0.16608	0.8136
O	3.14398	-1.26081	-0.36995
C	2.33349	-1.67685	0.66177
C	0.91583	-1.74727	0.25077
C	0.47579	-1.39369	-1.02452
C	-0.02418	-2.18821	1.19297
C	-0.86871	-1.47376	-1.36448
H	1.19001	-1.0509	-1.76057
C	-1.36081	-2.27355	0.8669
H	0.31972	-2.46134	2.18212
C	-1.79671	-1.91641	-0.4169
H	-1.18056	-1.19208	-2.35974
H	-2.09403	-2.61443	1.58673
O	-3.12689	-2.03532	-0.64095
C	13.78849	-0.00369	-0.32742
H	13.32248	0.70393	-1.01598
C	15.04917	0.62043	0.25771
H	15.4938	-0.08625	0.9675
H	14.74087	1.49643	0.83303
C	16.08718	1.03862	-0.78801
H	15.61297	1.69349	-1.52879
H	16.44791	0.16264	-1.33761
C	17.28651	1.76476	-0.17225
H	17.75505	1.11751	0.57913
H	16.93324	2.65034	0.36875
C	18.33883	2.18703	-1.20029
H	17.86981	2.83298	-1.95105
H	18.69186	1.30114	-1.74054
C	19.53253	2.91317	-0.57823
H	20.04339	2.27986	0.15256
H	20.26455	3.20118	-1.33649
H	19.21538	3.82284	-0.06079
C	14.01463	-1.34053	-1.01795
H	14.46715	-2.05997	-0.33101
H	13.08001	-1.75734	-1.39679
H	14.68242	-1.21276	-1.87221
C	-3.65399	-1.69713	-1.93053
H	-3.42213	-0.6493	-2.15355
H	-3.17921	-2.32652	-2.69054

C	-5.15477	-1.92536	-1.90713
H	-5.52125	-1.79041	-2.93095
H	-5.34537	-2.97063	-1.64323
C	-5.9167	-0.99665	-0.9584
H	-5.52698	-1.11961	0.05633
H	-5.71982	0.04519	-1.23998
C	-7.42646	-1.24693	-0.96123
H	-7.62209	-2.28888	-0.68105
H	-7.8159	-1.12944	-1.97991
C	-8.20359	-0.32196	-0.01837
H	-7.80416	-0.43838	0.99563
H	-8.00466	0.71817	-0.30191
C	-9.71786	-0.58258	-0.0163
H	-9.91277	-1.62578	0.26162
H	-10.11383	-0.47224	-1.03338
Si	-10.75617	0.50535	1.11771
O	-12.31744	-0.01945	0.93708
Si	-13.91195	0.30358	1.17516
O	-14.41666	1.4471	0.10747
Si	-14.87245	1.77891	-1.45087
C	-10.6204	2.31406	0.62545
H	-10.9056	2.46356	-0.41891
H	-11.27073	2.94251	1.23951
H	-9.59714	2.67995	0.74851
C	-10.23583	0.29191	2.91039
H	-10.85965	0.89195	3.57795
H	-10.32111	-0.7522	3.2231
H	-9.19837	0.6025	3.06224
C	-14.19677	0.99822	2.88671
H	-13.84214	0.31268	3.66048
H	-13.67933	1.95225	3.01601
H	-15.26159	1.17666	3.05764
C	-14.83271	-1.30165	0.9118
H	-14.63238	-1.71322	-0.08071
H	-14.52112	-2.04897	1.6462
H	-15.91244	-1.16385	1.01014
C	-14.83594	3.64306	-1.64257
H	-15.51318	4.12213	-0.93084
H	-13.83226	4.03696	-1.46357
H	-15.13989	3.94431	-2.64905
C	-16.61121	1.13056	-1.7398
H	-16.65835	0.04424	-1.62862
H	-17.31702	1.57022	-1.03015
H	-16.95707	1.37575	-2.74817
C	-13.67905	0.97428	-2.6587
H	-13.66078	-0.11248	-2.54241

H	-13.96685	1.19236	-3.69131
H	-12.66005	1.3412	-2.51274
O	2.75564	-1.94972	1.75585
N	11.1576	2.19417	0.72288
O	10.43819	2.9746	1.33736
O	12.23505	2.49178	0.22198

A.3.2 TSiKN65 MD Simulation Data

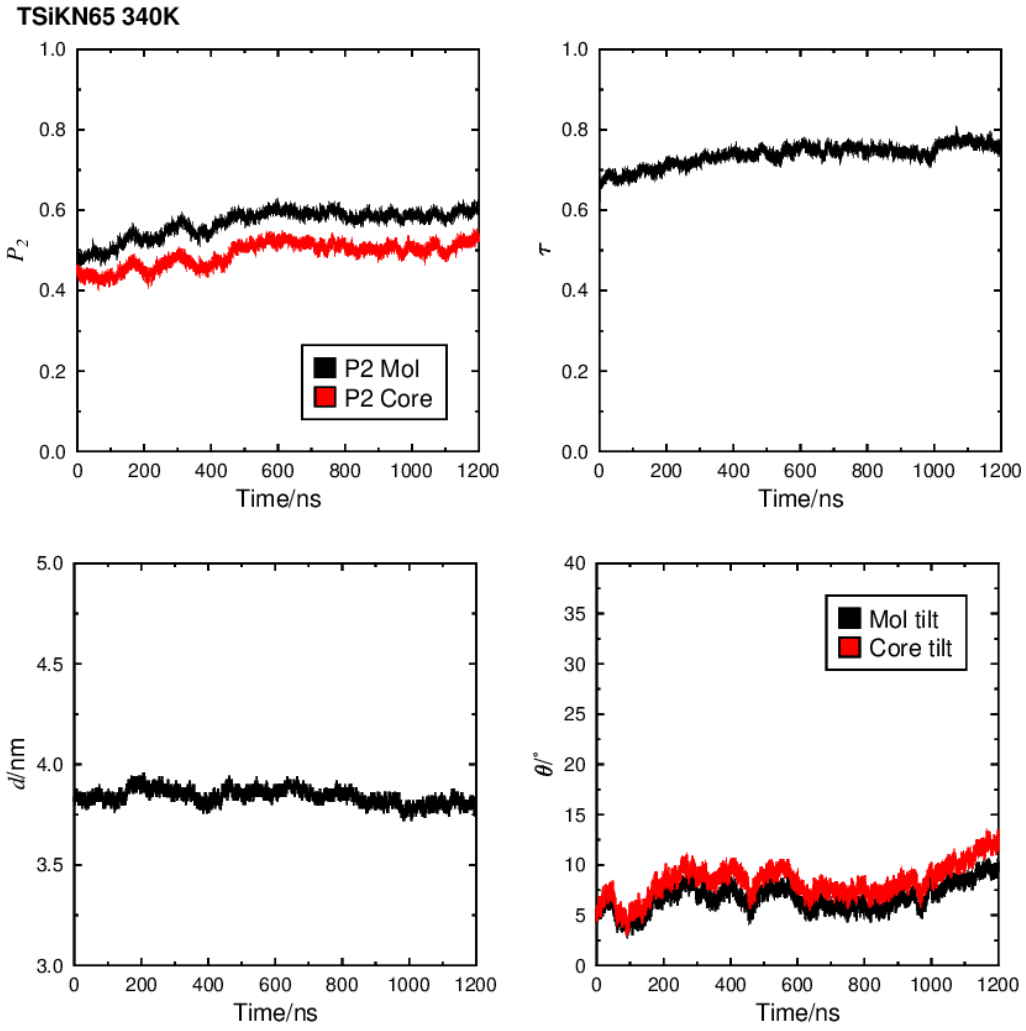

Figure A.15 Measurements of P_2, τ, d and Θ at each timestep of the MD simulation, comprising 1024 molecules of TSiKN65 and performed at 340 K.

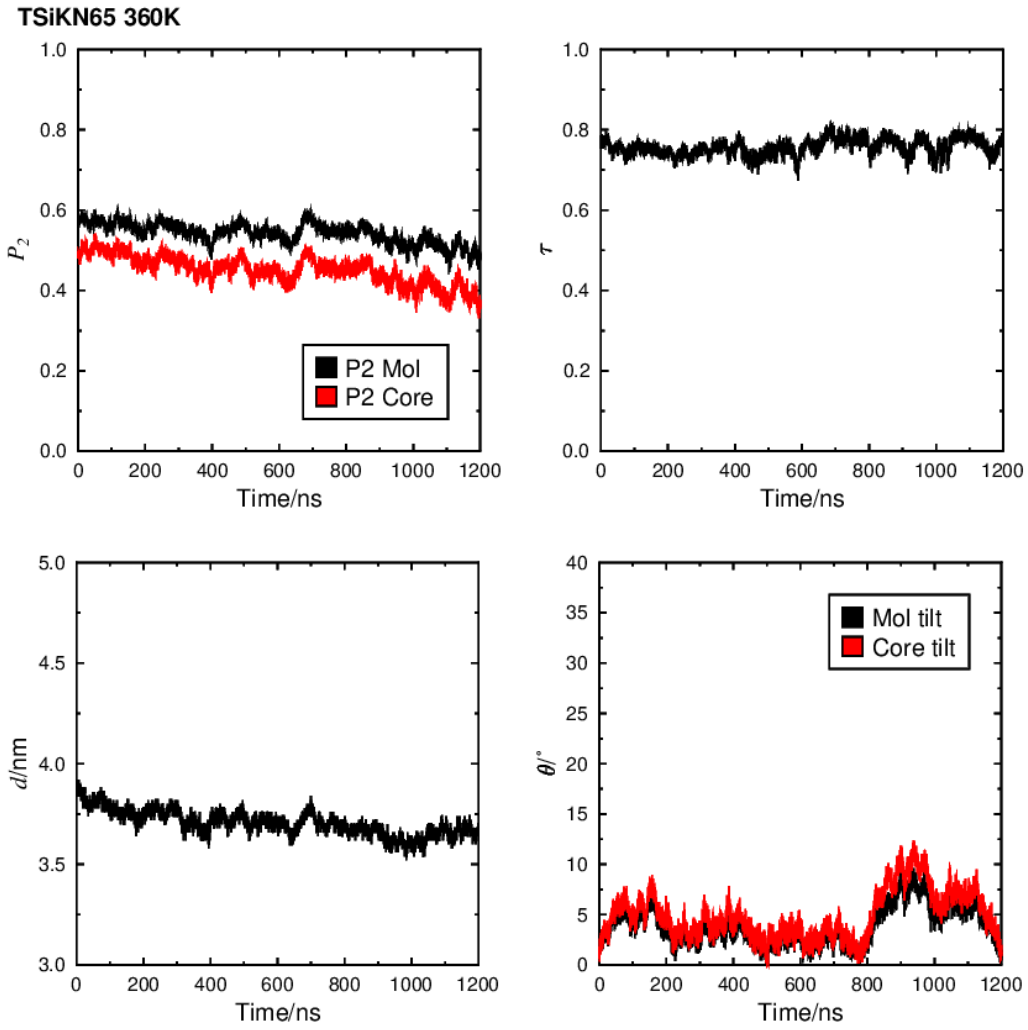

Figure A.16 Measurements of P_2, τ, d and Θ at each timestep of the MD simulation, comprising 1024 molecules of TSiKN65 and performed at 360 K.

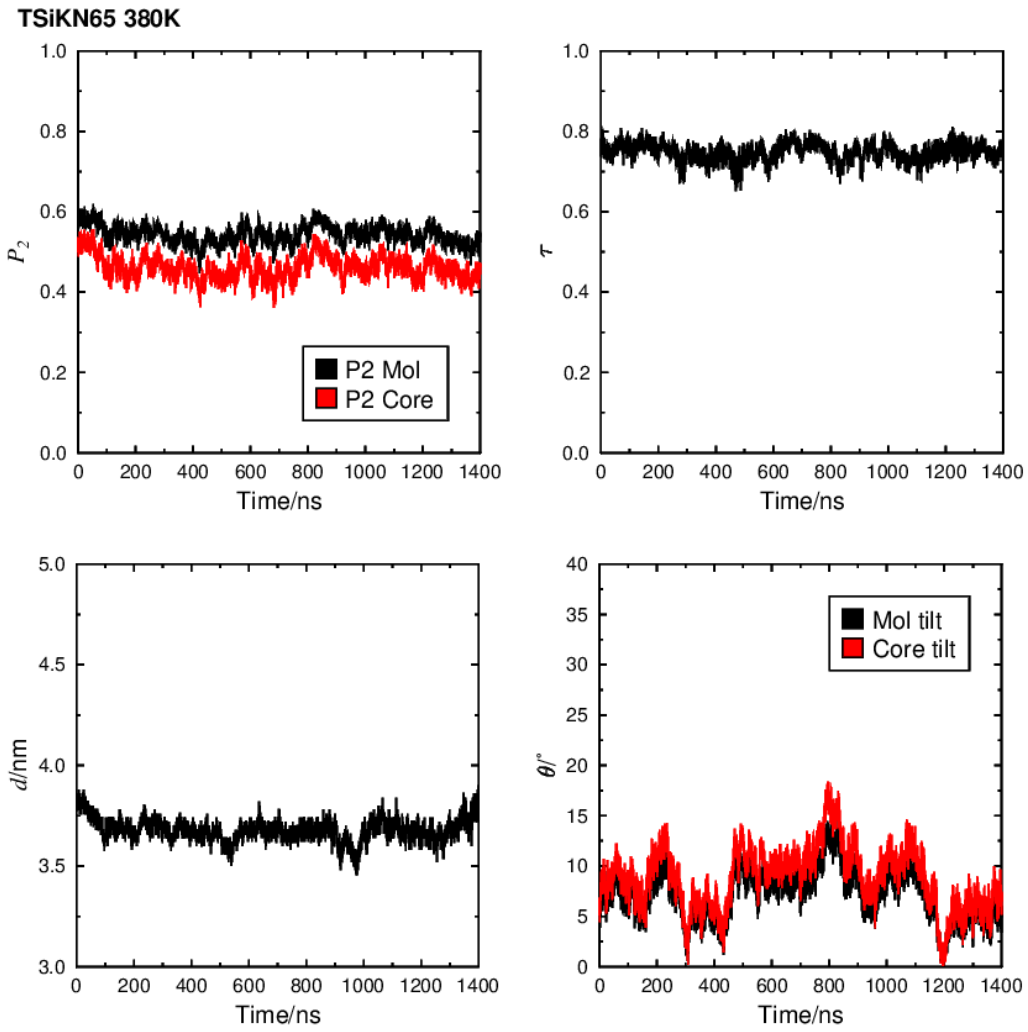

Figure A.17 Measurements of P_2, τ, d and Θ at each timestep of the MD simulation, comprising 1024 molecules of TSiKN65 and performed at 380 K.

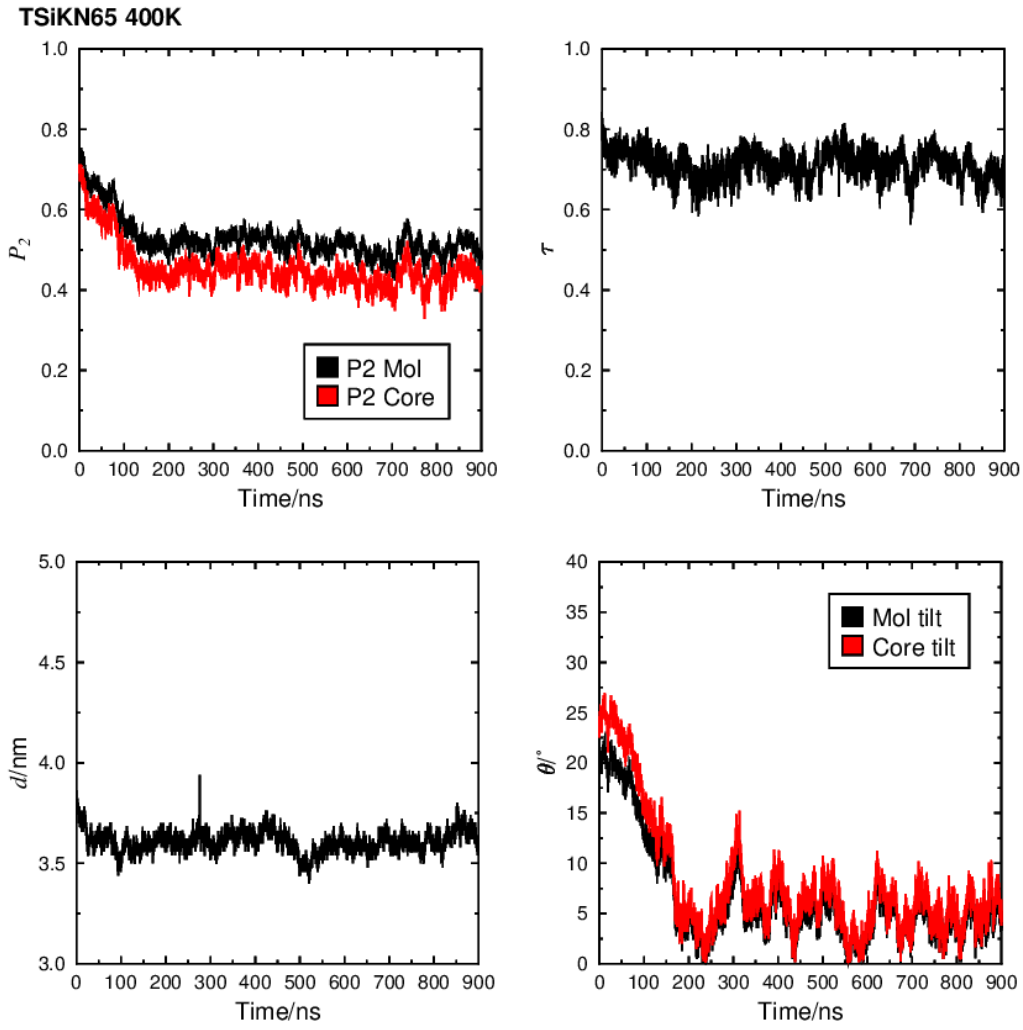

Figure A.18 Measurements of P_2, τ, d and Θ at each timestep of the MD simulation, comprising 1024 molecules of TSiKN65 and performed at 400 K.

Definitions

α – Euler angle describing initial rotation about the principal axis of the Cartesian reference frame.

β **–** Euler angle describing the rotation about the y-axis after rotation, α.

DFT – Density Functional Theory

d – Layer spacing

d_{A} – Layer spacing in SmA phase

$d_{\mathrm{A\text{-}C}}$ – Layer spacing at SmA-SmC transition

d_{C} – Layer spacing in SmC phase

DHF – Deformed Helix Ferroelectric

ESHFLC – Electrically supressed helix ferroelectric liquid crystal

EPR – Electron paramagnetic resonance

$f(\alpha, \beta, \gamma)$ – Full orientational distribution function

FLC – Ferroelectric Liquid Crystal

FLCOS – Ferroelectric liquid crystal on silicon

γ **–** Euler angle describing the rotation about the z-axis after rotations described by α and β.

HF – Hartree Fock

I – Isotropic

IPS – In-plane Switching

k – Layer normal

LC – Liquid Crystal

LCD – Liquid crystal display

LED – Light emitting diode

MC – Monte Carlo

MD – Molecular dynamics

MM – Molecular mechanics

MOI – Moment of inertia

n – Director

N – Nematic

NMR – Nuclear magnetic resonance

ODF – Orientational distribution function

$\boldsymbol{\Omega}$ – Abbreviation of Euler angles, α, β, γ

P_2 – Second-rank orientational order parameter

P_4 – Fourth-rank orientational order parameter

PDMS - Polydimethylsiloxane

PFPE - Perfluoropolyether

P_n – n^{th}-rank orientational order parameter

QM – Quantum mechanics

RESP – Restrained electrostatic resonance

SmA – Smectic A

SmA* – Chiral Smectic A

SmC – Smectic C

SmC* – Chiral Smectic C

SLM – Spatial light modulator

SSFLC – Surface Stabilised Ferroelectric Liquid Crystal

τ – Translational order parameter

$T_{A\text{-}C}$ – Temperature of SmA-SmC transition

θ – Tilt angle

$T_{I\text{-}A}$ – Temperature of I-SmA transition

TN – Twisted Nematic

References

1 F. Reinitzer, *Monatshefte für Chemie*, 1888, **9**, 421–441.

2 O. Lehmann, *Zeitschrift für Phys. Chemie*, 1899, **4**, 462–472.

3 M. Mitov, *ChemPhysChem*, 2014, **15**, 1245–1250.

4 H. Kawamoto, *Proc. IEEE*, 2002, **90**, 460–500.

5 S. Garoff and R. B. Meyer, *Phys. Rev. A*, 1979, **19**, 338–347.

6 R. B. Meyer, L. Liebert, L. Strzelecki and P. Keller, *J. Phys. Lettres*, 1975, **36**, 69–71.

7 P. J. Collings and M. Hird, in *Introduction to Liquid Crystals Chemistry and Physics*, Taylor & Francis, London, 1997, pp. 43–79.

8 S. Singh, in *Liquid Crystal Fundamentals*, World Scientific Publishing Co., Singapore, 2002, pp. 1–28.

9 S. Singh, in *Liquid Crystal Fundamentals*, World Scientific Publishing Co., Singapore, 2002, pp. 57–92.

10 C. Zannoni, in *The Molecular Dynamics of Liquid Crystals*, eds. G. R. Luckhurst and C. A. Veracini, Springer, New York, 1994, pp. 11–40.

11 G. R. Luckhurst, in *Physical Properties of Liquid Crystals: Nematics*, eds. D. A. Dunmur, A. Fukuda and G. R. Luckhurst, IET, London, 2001, pp. 57–88.

12 P. J. Collings and M. Hird, in *Introduction to Liquid Crystals Chemistry and Physics*, Taylor & Francis, London, 1997, pp. 17–43.

13 A. F. Runge, S. S. Saavedra and S. B. Mendes, *J. Phys. Chem. B*, 2006, **110**, 6721–6731.

14 M. van Gurp, *Colloid Polym. Sci.*, 1995, **273**, 607–625.

15 I. W. Hamley, S. Garnett, G. R. Luckhurst, S. J. Roskilly, J. M. Sedon, J. S. Pedersen and R. M. Richardson, *J. Chem. Phys.*, 1996, **104**, 10046–10054.

16 M. T. Sims, L. C. Abbott, R. M. Richardson, J. W. Goodby and J. N. Moore, *Liq. Cryst.*, 2019, **46**, 11–24.

17 S. Limmer, *Fortschritte der Phys.*, 1989, **37**, 879–931.

18 W. Kuczyński, B. Żywucki and J. Małecki, *Mol. Cryst. Liq. Cryst.*, 2002, **381**, 1–19.

19 S. Jen, N. A. Clark, P. S. Pershan and E. B. Priestley, *J. Chem. Phys.*, 1977, **66**, 4635–4661.

20 W. Jeremy Jones, D. K. Thomas, D. W. Thomas and G. Williams, *J. Mol. Struct.*, 2004, **708**, 145–163.

21 A. Arcioni, R. Tarroni and C. Zannoni, *Nuovo Cim. D*, 1988, **10**, 1409–1426.

22 J. G. Kirkwood and E. Monroe, *J. Chem. Phys.*, 1941, **9**, 514–526.

23 K. K. Kobayashi, *J. Phys. Soc. Japan*, 1970, **29**, 101–105.

24 K. K. Kobayashi, *Mol. Cryst. Liq. Cryst.*, 1971, **13**, 137–148.

25 W. L. McMillan, *Phys. Rev. A*, 1971, **4**, 1238–1246.

26 W. L. McMillan, *Phys. Rev. A*, 1972, **6**, 936–947.

27 A. J. Leadbetter and E. K. Norris, *Mol. Phys.*, 1979, **38**, 669–686.

28 Y. Takanishi, A. Ikeda, H. Takezoe and A. Fukuda, *Phys. Rev. E*, 1995, **51**, 400–406.

29 E. F. Gramsbergenf and W. H. De Jeu, *Liq. Cryst.*, 1989, **4**, 449–455.

30 N. Kapernaum and F. Giesselmann, *Phys. Rev. E - Stat. Nonlinear, Soft Matter Phys.*, 2008, **78**, 1–3.

31 G. G. Alexander, S. M. King, R. M. Richardson and H. Zimmermann, *Liq. Cryst.*, 2010, **37**, 961–968.

32 G. H. Heilmeier, *Sci. Am.*, 1970, **222**, 100–107.

33 M. Oh-e and K. Kondo, *Appl. Phys. Lett.*, 1995, **67**, 3895–3897.

34 M. F. Moreira, I. C. S. Carvalho, W. Cao, C. Bailey, B. Taheri and P. Palffy-Muhoray, *Appl. Phys. Lett.*, 2004, **85**, 2691–2693.

35 M. F. O. Hameed, M. Y. Azab, A. M. Heikal, S. M. El-Hefnawy and S. S. A. Obayya, *IEEE Photonics Technol. Lett.*, 2015, **28**, 59–62.

36 S. J. Woltman, G. D. Jay and G. P. Crawford, *Nat. Mater.*, 2007, **6**, 929–938.

37 J. Stasiek, M. Jewartowski and T. Aleksander Kowalewski, *J. Cryst. Process Technol.*, 2014, **04**, 46–59.

38 H. F. Gleeson, in *Handbook of Liquid Crystals*, eds. D. Demus, J. W. Goodby, G. W. Gray, H. W. Spiess and V. Vill, Wiley-VCH, Weinheim, 1998, pp. 823–838.

39 H.-K. Liu, J. A. Davis and R. A. Lilly, *Opt. Lett.*, 1985, **10**, 635.

40 F. Mok, J. Diep, H.-K. Liu and D. Psaltis, *Opt. Lett.*, 1986, **11**, 748.

41 P. M. Birch, R. Young, D. Budgett and C. Chatwin, *Opt. Lett.*, 2000, **25**, 1013.

42 J. A. Davis, D. E. McNamara, D. M. Cottrell and T. Sonehara, *Appl. Opt.*, 2000, **39**, 1549.

43 J. A. Davis, I. Moreno, T. M. Hernandez, D. M. Cottrell and D. Sand, *Front. Opt. FIO 2012*, 2012, **20**, 812–816.

44 S. Manzanera, P. M. Prieto, D. B. Ayala, J. M. Lindacher and P. Artal, *Opt. Express*, 2007, **15**, 16177.

45 J. P. F. Lagerwall and G. Scalia, *Curr. Appl. Phys.*, 2012, **12**, 1387–1412.

46 J. Valasek, *Phys. Rev.*, 1921, **17**, 475–481.

47 S. Singh, in *Liquid Crystal Fundamentals*, World Scientific Publishing Co, Singapore, 2002, pp. 404–419.

48 H. Stegemeyer, R. Meister, U. Hoffmann, A. Sprick and A. Becker, *J. Mater. Chem.*, 1995, **5**, 2183–2193.

49 P. Mach, R. Pindak, A.-M. Levelut, P. Barois, H. T. Nguyen, H. Baltes, M. Hird, K. Toyne, A. Seed, J. W. Goodby, C. C. Huang and L. Furenlid, *Phys. Rev. E*, 1999, **60**, 6793–6802.

50 N. A. Clark and S. T. Lagerwall, *Appl. Phys. Lett.*, 1980, **36**, 899.

51 R. B. Meyer, *Mol. Cryst. Liq. Cryst.*, 1977, **40**, 33–48.

52 S. T. Lagerwall, N. A. Clark, J. Dijon and J. F. Clerc, *Ferroelectrics*, 1989, **94**, 3–62.

53 S. T. Lagerwall, *Ferroelectrics*, 2004, **301**, 15–45.

54 A. K. Srivastava, V. G. Chigrinov and H. S. Kwok, *J. Soc. Inf. Disp.*, 2015, **23**, 253–272.

55 S. T. Lagerwall, *Ferroelectrics*, 1984, **59**, 25–67.

56 W. J. A. M. Hartmann, *Ferroelectrics*, 1991, **122**, 1–26.

57 L. A. Beresnev, V. G. Chigrinov, D. I. Dergachev, E. P. Poshidaev, J. Fünfschilling and M. Schadt, *Liq. Cryst.*, 1989, **5**, 1171–1177.

58 G. B. Cohen, R. Pogreb, K. Vinokur and D. Davidov, *Appl. Opt.*, 1997, **36**, 455.

59 D. V. Wick, T. Martinez, M. V. Wood, J. M. Wilkes, M. T. Gruneisen, V. A. Berenberg, M. V. Vasil'ev, A. P. Onokhov and L. A. Beresnev, *Appl. Opt.*, 1999, **38**, 3798.

60 G. Hegde, P. Xu, E. Pozhidaev, V. Chigrinov and H. S. Kwok, *Liq. Cryst.*, 2008, **35**, 1137–1144.

61 A. K. Srivastava, M. C. Tseng, V. G. Chigrinov and H. S. Kwok, *Dig. Tech. Pap. - SID Int. Symp.*, 2015, **23**, 176–181.

62 Guo, Yan, Chigrinov, Zhao and Tribelsky, *Crystals*, 2019, **9**, 470.

63 B. Löfving and S. Hård, *Opt. Lett.*, 1998, **23**, 1541.

64 D. C. O'Brien, R. J. Mears, T. D. Wilkinson and W. A. Crossland, *Appl. Opt.*, 1994, **33**, 2795.

65 K. M. Johnson and G. Moddel, *Appl. Opt.*, 1989, **28**, 4888.

66 M. Hird, *Liq. Cryst.*, 2011, **38**, 1467–1493.

67 D. Vettese, *Nat. Photonics*, 2010, **4**, 752–754.

68 Z. Zhang, Z. You and D. Chu, *Light Sci. Appl.*, 2014, **3**, 1–10.

69 T. D. Wilkinson, *Liq. Cryst. Today*, 2012, **21**, 34–41.

70 M. J. O'Callaghan, R. Ferguson, R. Vohra, W. Thurmes, A. W. Harant, C. S. Pecinovsky, Y. Zhang, S. Yang, M. O'Neill and M. A. Handschy, *J. Soc. Inf. Disp.*, 2009, **17**, 369.

71 N. A. Clark, C. Crandall, M. A. Handschy, M. R. Meadows, R. M. Malzbender, C. Park and J. Z. Xue, *Ferroelectrics*, 2000, **246**, 97–110.

72 S. Hasegawa and Y. Hayasaki, *Adv. Opt. Technol.*, 2016, **5**, 39–54.

73 Y. S. Zhang, C. Y. Liu, A. V. Emelyanenko and J. H. Liu, *Adv. Funct. Mater.*, 2018, **28**, 1–8.

74 W. L. McMillan, *Phys. Rev. A*, 1973, **8**, 1921.

75 A. Wulf, *Phys. Rev. A*, 1975, **11**, 365.

76 T. Sakurai, K. Sakamoto, M. Honma, K. Yoshino and M. Ozaki, *Ferroelectrics*, 1984, **58**, 21–32.

77 T. Sakurai, N. Mikami, M. Ozaki and K. Yoshino, *J. Chem. Phys.*, 1986, **85**, 585–590.

78 J. P. F. Lagerwall and F. Giesselmann, *ChemPhysChem*, 2006, **7**, 20–45.

79 T. P. Rieker, N. A. Clark, G. S. Smith, D. S. Parmar, E. B. Sirota and C. R. Safinya, *Phys. Rev. Lett.*, 1987, **59**, 2658–2661.

80 N. A. Clark and T. P. Rieker, *Phys. Rev. A*, 1988, **37**, 1053–1056.

81 Y. Ouchi, H. Takano, H. Takezoe and A. Fukuda, *Jpn. J. Appl. Phys.*, 1988, **27**, 1–7.

82 A. de Vries, *Mol. Cryst. Liq. Cryst.*, 1970, **11**, 361–383.

83 J. Naciri, J. Ruth, G. Crawford, R. Shashidhar and B. R. Ratna, *Chem. Mater.*, 1995, **7**, 1397–1402.

84 M. D. Radcliffe, M. L. Brostrom, K. A. Epstein, A. G. Rappaport, B. N. Thomas, R. Shao and N. A. Clark, *Liq. Cryst.*, 1999, **26**, 789–794.

85 F. Giesselmann, P. Zugenmaier, I. Dierking, S. T. Lagerwall, B. Stebler, M. Kaš, V. Hamplová and M. Glogarová, *Phys. Rev. E*, 1999, **60**, 598–602.

86 N. A. Clark, T. Bellini, R. F. Shao, D. Coleman, S. Bardon, D. R. Link, J. E. MacLennan, X. H. Chen, M. D. Wand, D. M. Walba, P. Rudquist and S. T. Lagerwall, *Appl. Phys. Lett.*, 2002, **80**, 4097–4099.

87 A. Sanchez-Castillo, M. A. Osipov, S. Jagiella, Z. H. Nguyen, M. Kašpar, V. Hamplová, J. MacLennan and F. Giesselmann, *Phys. Rev. E - Stat. Nonlinear, Soft Matter Phys.*, 2012, **85**, 1–18.

88 P. Rudquist, M. A. Osipov and F. Giesselmann, *Liq. Cryst.*, 2018, **45**, 2097–2108.

89 N. Hayashi, T. Kato, A. Fukuda, J. K. Vij, Y. P. Panarin, J. Naciri, R. Shashidhar, S. Kawada and S. Kondoh, *Phys. Rev. E - Stat. Nonlinear, Soft Matter Phys.*, 2005, **71**, 1–8.

90 N. Hayashi, A. Kocot, M. J. Linehan, A. Fukuda, J. K. Vij, G. Heppke, J. Naciri, S. Kawada and S. Kondoh, *Phys. Rev. E - Stat. Nonlinear, Soft Matter Phys.*, 2006, **74**, 1–11.

91 A. de Vries, *Mol. Cryst. Liq. Cryst.*, 1985, **131**, 125–145.

92 Y. Takanishi, Y. Ouchi, H. Takezoe, A. Fukuda, A. Mochizuki and M. Nakatsuka, *Jpn. J. Appl. Phys.*, 1990, **29**, L984–L986.

93 R. B. Meyer and R. A. Pelcovits, *Phys. Rev. E - Stat. Physics, Plasmas, Fluids, Relat. Interdiscip. Top.*, 2002, **65**, 1–6.

94 U. Manna, J. K. Song, J. K. Vij and J. Naciri, *Appl. Phys. Lett.*, 2009, **94**, 2007–2010.

95 J. V. Selinger, P. J. Collings and R. Shashidhar, *Phys. Rev. E - Stat. Physics, Plasmas, Fluids, Relat. Interdiscip. Top.*, 2001, **64**, 9.

96 M. S. Spector, P. A. Heiney, J. Naciri, B. T. Weslowski, D. B. Holt and R. Shashidhar, *Phys. Rev. E - Stat. Physics, Plasmas, Fluids, Relat. Interdiscip. Top.*, 2000, **61**, 1579–1584.

97 M. Buivydas, S. T. Lagerwall, I. Dierking, F. Gouda and A. Mochizuki, *Ferroelectrics*, 1998, **212**, 67–78.

98 M. Krueger and F. Giesselmann, *Phys. Rev. E - Stat. Nonlinear, Soft Matter Phys.*, 2005, **71**, 1–8.

99 A. de Vries, *Mol Cryst Liq Cryst*, 1977, **41**, 27–31.

100 A. de Vries, A. Ekachai and N. Spielberg, *Mol Cryst Liq Cryst*, 1979, **49**, 143–152.

101 Y. P. Panarin, V. Panov, O. E. Kalinovskaya and J. K. Vij, *J. Mater. Chem.*, 1999, **9**, 2967–2970.

102 A. de Vries, *Mol Cryst Liq Cryst*, 1979, **49**, 179–185.

103 V. Domenici, M. Lelli, M. Cifelli, V. Hamplová, A. Marchetti and C. A. Veracini, *ChemPhysChem*, 2014, **15**, 1485–1495.

104 A. Marchetti, V. Domenici, V. Novotná, M. Lelli, M. Cifelli, A. Lesage and C. A. Veracini, *ChemPhysChem*, 2010, **11**, 1641–1645.

105 V. Domenici, M. Cifelli, A. Marchetti, M. Lelli, V. Hamplová, M. Kaspar and C. A. Veracini, *Mol. Cryst. Liq. Cryst.*, 2012, **553**, 103–110.

106 A. Gradišek, V. Domenici, T. Apih, V. Novotná and P. J. Sebastião, *J. Phys. Chem. B*, 2016, **120**, 4706–4714.

107 D. J. Photinos and E. T. Samulski, *Science (80-.).*, 1995, **270**, 783–786.

108 K. Merkel, A. Kocot, J. K. Vij, P. J. Stevenson, A. Panov and D. Rodriguez, *Appl. Phys. Lett.*, 2016, **108**, 243301.

109 K. Merkel, *Phase Transitions*, 2018, **91**, 1000–1006.

110 Z. Ahmed, C. Müller, J. J. Johnston, K. Nguyen, C. P. J. Schubert, K. Abitaev, S. Marino, F. Giesselmann and R. P. Lemieux, *Liq. Cryst.*, 2019, **46**, 896–904.

111 J. P. F. Lagerwall, F. Giesselmann and M. D. Radcliffe, *Phys. Rev. E - Stat. Physics, Plasmas, Fluids, Relat. Interdiscip. Top.*, 2002, **66**, 1–11.

112 G. Galli, M. Reihmann, A. Crudeli, E. Chiellini, Y. P. Panarin, J. Vij, C. Blanc, V. Lorman and N. Olsson, *Mol. Cryst. Liq. Cryst.*, 2005, **439**, 245–257.

113 S. P. Sreenilayam, D. Rodriguez-Lojo, D. M. Agra-Kooijman, J. K. Vij, V. P. Panov, A. Panov, M. R. Fisch, S. Kumar and P. J. Stevenson, *Phys. Rev. Mater.*, 2018, **2**, 025603.

114 V. Novotná, V. Hamplová, A. Bubnov, M. Kapar, M. Glogarová, N. Kapernaum, S. Bezner and F. Giesselmann, *J. Mater. Chem.*, 2009, **19**, 3992–3997.

115 M. V. Gorkunov, M. A. Osipov, J. P. F. Lagerwall and F. Giesselmann, *Phys. Rev. E - Stat. Nonlinear, Soft Matter Phys.*, 2007, **76**, 1–16.

116 S. T. Lagerwall, P. Rudquist and F. Giesselmann, *Mol. Cryst. Liq. Cryst.*, 2009, **510**, 148–157.

117 J. C. Roberts, N. Kapernaum, Q. Song, D. Nonnenmacher, K. Ayub, F. Giesselmann and R. P. Lemieux, *J. Am. Chem. Soc.*, 2010, **132**, 364–370.

118 J. C. Roberts, N. Kapernaum, F. Giesselmann and R. P. Lemieux, *J. Am. Chem. Soc.*, 2008, **130**, 13842–13843.

119 S. P. Sreenilayam, D. Rodriguez-Lojo, V. P. Panov, V. Swaminathan, J. K. Vij, Y. P. Panarin, E. Gorecka, A. Panov and P. J. Stevenson, *Phys. Rev. E*, 2017, **96**, 042701.

120 Q. Song, A. Bogner, F. Giesselmann and R. P. Lemieux, *Chem. Commun.*, 2013, **49**, 8202–8204.

121 P. Pasini, C. Zannoni and S. Žumer, Eds., *Computer Simulations of Liquid Crystals and Polymers*, Springer Netherlands, Dordrecht, 2005, vol. 177.

122 C. J. Cramer, *Essentials of Computational Chemistry*, Wiley, Chichester, 2004.

123 J. B. Foresman and Æ. Frisch, in *Exploring Chemistry with Electronic Structure Methods*, Gaussian. Inc., Wallingford, CT., Third., 2015, pp. 463–499.

124 R. Ditchfield, W. J. Hehre and J. A. Pople, *J. Chem. Phys.*, 1971, **54**, 724–728.

125 C. C. J. Roothaan, *Rev. Mod. Phys.*, 1951, **23**, 69–89.

126 G. G. Hall, in *Proceedings of the Royal Society of London. Series A. Mathematical and Physical Sciences*, 1951, vol. 205, pp. 541–552.

127 C. Møller and M. S. Plesset, *Phys. Rev.*, 1934, **46**, 618–622.

128 D. Cremer, *Wiley Interdiscip. Rev. Comput. Mol. Sci.*, 2011, **1**, 509–530.

129 M. Dragoman and D. Dragoman, in *Encyclopedia of Condensed Matter Physics*, Elsevier, 2005, pp. 415–423.

130 W. Kohn and L. J. Sham, *Phys. Rev.*, 1965, **140**, 1133–1138.

131 A. D. Becke, *J. Chem. Phys.*, 1993, **98**, 5648–5652.

132 P. J. Stephens, F. J. Devlin, C. F. Chabalowski and M. J. Frisch, *J. Phys. Chem.*, 1994, **98**, 11623–11627.

133 B. J. Alder and T. E. Wainwright, *J. Chem. Phys.*, 1957, **27**, 1208–1209.

134 B. J. Alder and T. E. Wainwright, *J. Chem. Phys.*, 1959, **31**, 459–466.

135 F. H. Stillinger and A. Rahman, *J. Chem. Phys.*, 1974, **60**, 1545–1557.

136 A. Rahman and F. H. Stillinger, *J. Chem. Phys.*, 1971, **55**, 3442–3449.

137 F. H. Stillinger and A. Rahman, *J. Chem. Phys.*, 1972, **57**, 1281–1292.

138 L. Verlet, *Phys. Rev.*, 1967, **159**, 98–103.

139 R. . Hockney, S. . Goel and J. . Eastwood, *J. Comput. Phys.*, 1974, **14**, 148–158.

140 C. Zannoni, *Liq. Cryst.*, 2018, **45**, 1880–1893.

141 M. P. Allen, *Mol. Phys.*, 2019, **117**, 2391–2417.

142 H. Sun, *Comput. Theor. Polym. Sci.*, 1998, **8**, 229–246.

143 S. B. Sinnott and D. W. Brenner, *MRS Bull.*, 2012, **37**, 469–473.

144 P. H. Hünenberger, in *Advanced Computer Simulation. Advances in Polymer Science*, eds. C. Holm and K. Kremer, Springer, Berlin, 2005, pp. 105–149.

145 W. Yang, R. Bitetti-Putzer and M. Karplus, *J. Chem. Phys.*, 2004, **120**, 2618–2628.

146 J. D. Chodera, *J. Chem. Theory Comput.*, 2016, **12**, 1799–1805.

147 M. P. Allen and D. J. Tildesley, *Computer simulation of liquids: Second edition*, Oxford University Press, Oxford, 2017.

148 C. Zannoni, *J. Mater. Chem.*, 2001, **11**, 2637–2646.

149 C. M. Care and D. J. Cleaver, *Reports Prog. Phys.*, 2005, **68**, 2665–2700.

150 M. R. Wilson, *Int. Rev. Phys. Chem.*, 2005, **24**, 421–455.

151 D. Frenkel and B. M. Mulder, *Mol. Phys.*, 1985, **55**, 1171–1192.

152 D. Frenkel, *Mol. Phys.*, 1987, **60**, 1–20.

153 G. R. Luckhurst and S. Romano, *Proc. R. Soc. London. A. Math. Phys. Sci.*, 1980, **373**, 111–130.

154 J. G. Gay and B. J. Berne, *J. Chem. Phys.*, 1981, **74**, 3316–3319.

155 I. Cacelli, G. Prampolini and A. Tani, *J. Phys. Chem. B*, 2005, **109**, 3531–3538.

156 G. Tiberio, L. Muccioli, R. Berardi and C. Zannoni, *ChemPhysChem*, 2009, **10**, 125–136.

157 J. Peláez and M. R. Wilson, *Phys. Chem. Chem. Phys.*, 2007, **9**, 2968–2975.

158 M. F. Palermo, A. Pizzirusso, L. Muccioli and C. Zannoni, *J. Chem. Phys.*, 2013, **138**, 204901.

159 R. Berardi, L. Muccioli and C. Zannoni, *ChemPhysChem*, 2004, **5**, 104–111.

160 E. Kuprusevicius, R. Edge, H. Gopee, A. N. Cammidge, E. J. L. McInnes, M. R. Wilson and V. S. Oganesyan, *Chem. - A Eur. J.*, 2010, **16**, 11558–11562.

161 F. Chami, M. R. Wilson and V. S. Oganesyan, *Soft Matter*, 2012, **8**, 6823–6833.

162 D. Chen, J. H. Porada, J. B. Hooper, A. Klittnick, Y. Shen, M. R. Tuchband, E. Korbloèa, D. Bedrov, D. M. Walba, M. A. Glaser, J. E. Maclennan and N. A. Clark, *Proc. Natl. Acad. Sci. U. S. A.*, 2013, **110**, 15931–15936.

163 M. T. Sims, L. C. Abbott, S. J. Cowling, J. W. Goodby and J. N. Moore, *Chem. - A Eur. J.*, 2015, **21**, 10123–10130.

164 M. T. Sims, L. C. Abbott, S. J. Cowling, J. W. Goodby and J. N. Moore, *Phys. Chem. Chem. Phys.*, 2016, **18**, 20651–20663.

165 P. Styring, *Mol. Cryst. Liq. Cryst. Sci. Technol. Sect. A Mol. Cryst. Liq. Cryst.*, 1999, **332**, 199–206.

166 Y. Lansac, M. A. Glaser and N. A. Clark, *Phys. Rev. E - Stat. Physics, Plasmas, Fluids, Relat. Interdiscip. Top.*, 2001, **64**, 12.

167 D. L. Cheung, S. J. Clark and M. R. Wilson, *Phys. Rev. E*, 2002, **65**, 051709.

168 N. J. Boyd and M. R. Wilson, *Phys. Chem. Chem. Phys.*, 2015, **17**, 24851–24865.

169 J. Ilnytskyi and M. R. Wilson, *Comput. Phys. Commun.*, 2001, **134**, 23–32.

170 M. R. Wilson, M. P. Allen, M. A. Warren, A. Sauron and W. Smith, *J. Comput. Chem.*, 1997, **18**, 478–488.

171 I. T. Todorov, W. Smith, K. Trachenko and M. T. Dove, *J. Mater. Chem.*, 2006, **16**, 1911–1918.

172 A. Pizzirusso, M. E. Di Pietro, G. De Luca, G. Celebre, M. Longeri, L. Muccioli and C. Zannoni, *ChemPhysChem*, 2014, **15**, 1356–1367.

173 Y. Olivier, L. Muccioli and C. Zannoni, *ChemPhysChem*, 2014, **15**, 1345–1355.

174 M. Fujiwara, K. Satoh and S. Mita, *Mol. Cryst. Liq. Cryst.*, 2005, **441**, 307–317.

175 M. T. Sims, L. C. Abbott, J. W. Goodby and J. N. Moore, *Soft Matter*, 2019, **15**, 7722–7732.

176 J. S. Smith, O. Borodin and G. D. Smith, *J. Phys. Chem. B*, 2004, **108**, 20340–20350.

177 M. Bizzarri, I. Cacelli, G. Prampolini and A. Tani, *J. Phys. Chem. A*, 2004, **108**, 10336–10341.

178 I. Cacelli, C. F. Lami and G. Prampolini, *J. Comput. Chem.*, 2008, **30**, 366–378.

179 I. Cacelli, A. Cimoli, L. De Gaetani, G. Prampolini and A. Tani, *J. Chem. Theory Comput.*, 2009, **5**, 1865–1876.

180 W. L. Jorgensen, D. S. Maxwell and J. Tirado-Rives, *J. Am. Chem. Soc.*, 1996, **118**, 11225–11236.

181 J. Wang, R. M. Wolf, J. W. Caldwell, P. A. Kollman and D. A. Case, *J. Comput. Chem.*, 2004, **25**, 1157–1174.

182 M. J. Cook and M. R. Wilson, *Mol. Cryst. Liq. Cryst. Sci. Technol. Sect. A. Mol. Cryst. Liq. Cryst.*, 2001, **363**, 181–193.

183 D. L. Cheung, S. J. Clark and M. R. Wilson, *J. Chem. Phys.*, 2004, **121**, 9131–9139.

184 M. R. Wilson and M. P. Allen, *Mol. Cryst. Liq. Cryst.*, 1991, **198**, 465–477.

185 J. Peláez and M. R. Wilson, *Phys. Rev. Lett.*, 2006, **97**, 1–5.

186 N. J. Boyd and M. R. Wilson, *Phys. Chem. Chem. Phys.*, 2018, **20**, 1485–1496.

187 M. J. Frisch, G. W. Trucks, H. B. Schlegel, G. E. Scuseria, M. A. Robb, J. R. Cheeseman, G. Scalmani, V. Barone, B. Mennucci, G. A. Petersson, H. Nakatsuji, M. Caricato, X. Li, H. P. Hratchian, A. F. Izmaylov, J. Bloino, G. Zheng, J. L. Sonnenberg, M. Hada, M. Ehara, K. Toyota, R. Fukuda, J. Hasegawa, M. Ishida, T. Nakajima, Y. Honda, O. Kitao, H. Nakai, T. Vreven, J. J. A. Montgomery, J. E. Peralta, F. Ogliaro, M. Bearpark, J. J. Heyd, E. Brothers, K. N. Kudin, V. N. Staroverov, R. Kobayashi, J. Normand, K. Raghavachari, A. Rendell, J. C. Burant, S. S. Iyengar, J. Tomasi, M. Cossi, N. Rega, J. M. Millam, M. Klene, J. E. Knox, J. B. Cross, V. Bakken, C. Adamo, J. Jaramillo, R. Gomperts, R. E. Stratmann, O. Yazyev, A. J. Austin, R. Cammi, C. Pomelli, J. W. Ochterski, R. L. Martin, K. Morokuma, V. G. Zakrzewski, G. A. Voth, P. Salvador, J. J. Dannenberg, S. Dapprich, A. D. Daniels, Ö. Farkas, J. B. Foresman, J. V. Ortiz, J. Cioslowski and D. J. Fox, Gaussian 09, Revision B.01, Gaussian Inc., Wallingford CT, 2009.

188 A. D. Becke, *J. Chem. Phys.*, 1993, **98**, 5648–5652.

189 C. Lee, W. Yang and R. G. Parr, *Phys. Rev. B*, 1988, **37**, 785–789.

190 M. Head-Gordon, J. A. Pople and M. J. Frisch, *Chem. Phys. Lett.*, 1988, **153**, 503–506.

191 H. J. C. Berendsen, D. van der Spoel and R. van Drunen, *Comput. Phys. Commun.*, 1995, **91**, 43–56.

192 E. Lindahl, B. Hess and D. van der Spoel, *J. Mol. Model.*, 2001, **7**, 306–317.

193 D. van Der Spoel, E. Lindahl, B. Hess, G. Groenhof, A. E. Mark and H. J. C. Berendsen, *J. Comput. Chem.*, 2005, **26**, 1701–1718.

194 B. Hess, C. Kutzner, D. van der Spoel and E. Lindahl, *J. Chem. Theory Comput.*, 2008, **4**, 435–447.

195 S. Pronk, S. Páll, R. Schulz, P. Larsson, P. Bjelkmar, R. Apostolov, M. R. Shirts, J. C. Smith, P. M. Kasson, D. Van Der Spoel, B. Hess and E. Lindahl, *Bioinformatics*, 2013, **29**, 845–854.

196 M. J. Abraham, T. Murtola, R. Schulz, S. Páll, J. C. Smith, B. Hess and E. Lindah, *SoftwareX*, 2015, **1**–**2**, 19–25.

197 C. I. Bayly, P. Cieplak, W. D. Cornell and P. A. Kollman, *J. Phys. Chem.*, 1993, **97**, 10269–10280.

198 B. Hess, H. Bekker, H. J. C. Berendsen and J. G. E. M. Fraaije, *J. Comput. Chem.*, 1997, **18**, 1463–1472.

199 T. A. Darden, D. York and L. Pedersen, *J. Chem. Phys.*, 1993, **98**, 10089–10092.

200 S. Nosé, *Mol. Phys.*, 1984, **52**, 255–268.

201 S. Nosé, *J. Chem. Phys.*, 1984, **81**, 511–519.

202 M. Parrinello and A. Rahman, *J. Appl. Phys.*, 1981, **52**, 7182–7190.

203 I. M. Withers, C. M. Care and D. J. Cleaver, *J. Chem. Phys.*, 2000, **113**, 5078–5090.

204 R. Pecheanu and N. M. Cann, *Phys. Rev. E - Stat. Nonlinear, Soft Matter Phys.*, 2010, **81**, 1–17.

205 R. Core Team (2014), R: A Language and Environment for Statistical Computing, R Foundation for Statistical Computing, Vienna, Austria, Available online at https://www.Rproject.org/.

206 W. Humphrey, A. Dalke and K. Schulten, *J. Mol. Graph.*, 1996, **14**, 33–38.

207 M. R. Wilson, *Chem. Soc. Rev.*, 2007, **36**, 1881–1888.

208 Z. Wang, J. A. Lupo, S. Patnaik and R. Pachter, *Comput. Theor. Polym. Sci.*, 2001, **11**, 375–387.

209 A. J. McDonald, S. Hanna and H. H. Wills, *Mol. Cryst. Liq. Cryst.*, 2004, **413**, 135–144.

210 A. J. McDonald and S. Hanna, *J. Chem. Phys.*, , DOI:10.1063/1.2193154.

211 M. R. Wilson, *J. Mol. Liq.*, 1996, **68**, 23–31.

212 C. McBride, M. R. Wilson and J. A. . Howard, *Mol. Phys.*, 1998, **93**, 955–964.

213 D. L. Cheung, S. J. Clark and M. R. Wilson, *Chem. Phys. Lett.*, 2002, **356**, 140–146.

214 E. D. Gerts, A. V. Komolkin, V. A. Burmistrov, V. V. Alexandriysky and S. V. Dvinskikh, *J. Chem. Phys.*, 2014, **141**, 074503.

215 F. Jenz, M. A. Osipov, S. Jagiella and F. Giesselmann, *J. Chem. Phys.*, 2016, **145**, 134901.

216 L. Li, C. D. Jones, J. Magolan and R. P. Lemieux, *J. Mater. Chem.*, 2007, **17**, 2313–2318.

217 F. Goc, C. Blanc, V. Lorman, M. Nobili, S. Samaritani, G. Galli and W. Kuczyński, *Ferroelectrics*, 2006, **343**, 101–110.

218 C. P. J. Schubert, A. Bogner, J. H. Porada, K. Ayub, T. Andrea, F. Giesselmann and R. P. Lemieux, *J. Mater. Chem. C*, 2014, **2**, 4581–4589.

219 M. Kaspar, V. Hamplová, S. A. Pakhomov, A. Bubnov, F. Guittard, H. Sverenyak, I. Stibor, P. Vanek and M. Glogarova, *Liq. Cryst.*, 1998, **24**, 599–605.

220 S. Bezner, M. Krueger, V. Hamplová, M. Glogarová and F. Giesselmann, *J. Chem. Phys.*, 2007, **126**, 1–7.

221 C. Zannoni, in *The Molecular Dynamics of Liquid Crystals*, eds. G. R. Luckhurst and C. A. Veracini, Kluwer Academic, Dordrecht, 1994, pp. 11–40.

222 M. V. Gorkunov, M. A. Osipov, N. Kapernaum, D. Nonnenmacher and F. Giesselmann, *Phys. Rev. E - Stat. Nonlinear, Soft Matter Phys.*, 2011, **84**, 1–13.

223 L. De Gaetani and G. Prampolini, *Soft Matter*, 2009, **5**, 3517–3526.

224 H. Yoon, D. M. Agra-Kooijman, K. Ayub, R. P. Lemieux and S. Kumar, *Phys. Rev. Lett.*, 2011, **106**, 1–4.

225 D. M. Agra-Kooijman, H. Yoon, S. Dey and S. Kumar, *Phys. Rev. E - Stat. Nonlinear, Soft Matter Phys.*, 2014, **89**, 1–6.

226 P. J. Collings, B. R. Ratna and R. Shashidhar, *Phys. Rev. E - Stat. Physics, Plasmas, Fluids, Relat. Interdiscip. Top.*, 2003, **67**, 8.

227 T. Murias, A. C. Ribeiro, D. Guillon, D. Shoosmith and H. J. Coles, *Liq. Cryst.*, 2002, **29**, 627–633.

228 T. a Halgren, *J. Comput. Chem.*, 1996, **17**, 490–519.

229 C. S. Ewig, R. Berry, U. Dinur, J. R. Hill, M. J. Hwang, H. Li, C. Liang, J. Maple, Z. Peng, T. P. Stockfisch, T. S. Thacher, L. Yan, X. Ni and A. T. Hagler, *J. Comput. Chem.*, 2001, **22**, 1782–1800.

230 A. Pizzirusso, M. Savini, L. Muccioli and C. Zannoni, *J. Mater. Chem.*, 2011, **21**, 125–133.

231 S. Diele, D. Lose, H. Kruth, G. Pelzl, F. Guittard and A. Cambon, *Liq. Cryst.*, 1996, **21**, 603–608.

232 H. Liu and H. Nohira, *Liq. Cryst.*, 1996, **20**, 581–586.

233 Y. Yang, B. Chen and J. Wen, *Liq. Cryst.*, 1999, **26**, 893–896.

234 W. Song, P. J. Rossky and M. Maroncelli, *J. Chem. Phys.*, 2003, **119**, 9145–9162.

235 A. Nikitin, Y. Milchevskiy and A. Lyubartsev, *J. Phys. Chem. B*, 2015, **119**, 14563–14573.

236 J. Träg and D. Zahn, *J. Mol. Model.*, , DOI:10.1007/s00894-018-3911-5.

237 Q. Guo, S. Izumisawa, D. M. Phillips and M. S. Jhon, *J. Appl. Phys.*, 2003, **93**, 8707–8709.

238 H. Chen, Q. Guo and M. S. Jhon, *IEEE Trans. Magn.*, 2007, **43**, 2247–2249.

239 L. Dai, N. Satyanarayana, S. K. Sinha and V. B. C. Tan, *Tribol. Int.*, 2013, **60**, 53–57.

240 L. Dai, V. Sorkin, Z. D. Sha, Q. X. Pei, P. S. Branicio and Y. W. Zhang, *Langmuir*, 2014, **30**, 1573–1579.

241 M. Fukuda, H. Zhang, T. Ishiguro, K. Fukuzawa and S. Itoh, *Tribol. Lett.*, 2013, **51**, 479–487.

242 H. Zhang, M. Fukuda, H. Washizu, T. Kinjo, H. Yoshida, K. Fukuzawa and S. Itoh, *Tribol. Int.*, 2016, **93**, 163–171.

243 S. Senapati and M. L. Berkowitz, *J. Phys. Chem. B*, 2003, **107**, 12906–12916.

244 L. Lu and M. L. Berkowitz, *J. Phys. Chem. B*, 2005, **109**, 21725–21731.

245 D. Kamei, H. Zhou, K. Suzuki, K. Konno, S. Takami, M. Kubo and A. Miyamoto, *Tribol. Int.*, 2003, **36**, 297–303.

246 B. Jiang, D. J. Keffer and B. J. Edwards, *J. Fluor. Chem.*, 2006, **127**, 787–795.

247 H. Tani, K. Sakamoto and N. Tagawa, *IEEE Trans. Magn.*, 2009, **45**, 5050–5054.

248 H. Tani, T. Shimizu, N. Kobayashi, Y. Taniike, K. Mori and N. Tagawa, *IEEE Trans. Magn.*, 2010, **46**, 1420–1423.

249 H. C. Li, C. McCabe, S. T. Cui, P. T. Cummings and H. D. Cochran, *Mol. Phys.*, 2002, **100**, 265–272.

250 H. Li, C. McCabe, S. T. Cui, P. T. Cummings and H. D. Cochran, *Mol. Phys.*, 2003, **101**, 2157–2169.

251 J. E. Black, G. M. C. Silva, C. Klein, C. R. Iacovella, P. Morgado, L. F. G. Martins, E. J. M. Filipe and C. McCabe, *J. Phys. Chem. B*, 2017, **121**, 6588–6600.

252 D. J. Gardiner and H. J. Coles, *J. Phys. D. Appl. Phys.*, 2006, **39**, 4948–4955.

253 R. M. Sok, H. J. C. Berendsen and W. F. Van Gunsteren, *J. Chem. Phys.*, 1992, **96**, 4699–4704.

254 H. Sun and D. Rigby, *Spectrochim. Acta - Part A Mol. Biomol. Spectrosc.*, 1997, **53**, 1301–1323.

255 Z. A. Makrodimitri, R. Dohrn and I. G. Economou, *Macromolecules*, 2007, **40**, 1720–1729.

256 W. Shi, N. S. Siefert and B. D. Morreale, *J. Phys. Chem. C*, 2015, **119**, 19253–19265.

257 W. Shi, N. S. Siefert, H. O. Baled, J. A. Steckel and D. P. Hopkinson, *J. Phys. Chem. C*, 2016, **120**, 20158–20169.

258 E. K. Watkins and W. L. Jorgensen, *J. Phys. Chem. A*, 2001, **105**, 4118–4125.

259 J. Wang, W. Wang, P. A. Kollman and D. A. Case, *J. Mol. Graph. Model.*, 2006, **25**, 247–260.

260 P. H. Lin and R. Khare, *Macromolecules*, 2009, **42**, 4319–4327.

261 P. Lo Nostro, *Adv. Colloid Interface Sci.*, 1995, **56**, 245–287.

262 P. Mukerjee, *Colloids Surfaces A Physicochem. Eng. Asp.*, 1994, **84**, 1–10.

263 A. Maciejewski, *J. Photochem. Photobiol. A Chem.*, 1990, **51**, 87–131.

264 Y. Wang, S. Chen, H. Sun, W. Li, C. Hu and K. Ren, *Microphysiological Syst.*, 2018, **2**, 1–1.

265 M. Salado, F. J. Ramos, V. M. Manzanares, P. Gao, M. K. Nazeeruddin, P. J. Dyson and S.

Ahmad, *ChemSusChem*, 2016, **9**, 2708–2714.

266 Y. Sakane, Y. Suzuki and N. Kasagi, *J. Micromechanics Microengineering*, 2008, **18**, 104011.

267 M. Krafft, *Adv. Drug Deliv. Rev.*, 2001, **47**, 209–228.

268 M. K. Pandey, R. Tyagi, K. Yang, R. J. Fisher, C. K. Colton, J. Kumar, V. S. Parmar, E. Aiazian and A. C. Watterson, *Polymer (Guildf).*, 2011, **52**, 4727–4735.

269 P. Mach, P. M. Johnson, E. D. Wedell, F. Lintgen and C. C. Huang, *Europhys. Lett.*, 1997, **40**, 399.

270 D. Goswami, D. Sinha, A. Debnath, P. K. Mandal, S. K. Gupta, W. Haase, D. Ziobro and R. Dabrowski, *J. Mol. Liq.*, 2013, **182**, 95–101.

271 L. Zohrabyan, A. Zohrabyan and T. Galstian, *Opt. Mater. (Amst).*, 2009, **31**, 1189–1193.

272 S. Marzouk, A. Khalfallah, B. Heinrich, J. E. Khiari, A. Kriaa and S. Méry, *J. Fluor. Chem.*, 2017, **197**, 15–23.

273 H. A. Lorentz, *Ann. Phys.*, 1881, **248**, 127–136.

274 M. J. Cook and M. R. Wilson, *Mol. Cryst. Liq. Cryst. Sci. Technol. Sect. A. Mol. Cryst. Liq. Cryst.*, 2001, **357**, 149–165.

275 P. Kromm, M. Cotrait and H. T. Nguyen, *Liq. Cryst.*, 1996, **21**, 95–102.

276 P. Mach, C. C. Huang, T. Stoebe, E. D. Wedell, T. Nguyen, W. H. De Jeu, F. Guittard, J. Naciri, R. Shashidhar, N. Clark, I. M. Jiang, F. J. Kao, H. Liu and H. Nohira, *Langmuir*, 1998, **14**, 4330–4341.

277 G. S. Iannacchione, *Liq. Cryst.*, 1999, **26**, 51–55.

278 K. Saunders, *Phys. Rev. E - Stat. Nonlinear, Soft Matter Phys.*, 2008, **77**, 1–13.

279 R. Korlacki, V. P. Panov, A. Fukuda, J. K. Vij, C. M. Spillmann and J. Naciri, *Phys. Rev. E - Stat. Nonlinear, Soft Matter Phys.*, 2010, **82**, 1–7.

280 D. Nonnenmacher, S. Jagiella, Q. Song, R. P. Lemieux and F. Giesselmann, *ChemPhysChem*, 2013, **14**, 2990–2995.

281 C.-C. Sun and J. E. Mark, *Polymer (Guildf).*, 1989, **30**, 104–106.

282 K. E. Polmanteer, *Rubber Chem. Technol.*, 1988, **61**, 470–502.

283 H. Cochrane and C. S. Lin, *Rubber Chem. Technol.*, 1993, **66**, 48–60.

284 Q. W. Yuan and J. E. Mark, *Macromol. Chem. Phys.*, 1999, **200**, 206–220.

285 K. S. Kwan, D. A. Harrington, P. A. Moore, J. R. Hahn, J. V. Degroot and G. T. Burns, *Rubber Chem. Technol.*, 2001, **74**, 630–644.

286 G. Pan, J. E. Mark and D. W. Schaefer, *J. Polym. Sci. Part B Polym. Phys.*, 2003, **41**, 3314–3323.

287 I.-H. Chiang, W.-T. Chuang, C.-L. Lu, M.-T. Lee and H.-C. Lin, *Chem. Mater.*, 2015, **27**, 4525–4537.

288 C. Racles and V. Cozan, *High Perform. Polym.*, 2002, **14**, 169–181.

289 G. M. Podojil, B. L. Farmer and W. W. Adams, *Polymer (Guildf).*, 1996, **37**, 1825–1832.

290 S. S. Patnaik, R. Pachter, S. Plimpton and W. WADE ADAMS, *MRS Proc.*, 1993, **328**, 711.

291 J. Pozuelo and J. Baselga, *Polymer (Guildf).*, 2002, **43**, 6049–6055.

292 A. N. Shishkin, D. A. Markelov and V. V. Matveev, *Russ. Chem. Bull.*, 2016, **65**, 67–74.

293 N. K. Balabaev, M. A. Mazo and E. Y. Kramarenko, *Macromolecules*, 2017, **50**, 432–445.

294 S. J. Weiner, P. A. Kollman, U. C. Singh, D. A. Case, C. Ghio, G. Alagona, S. Profeta and P. Weiner, *J. Am. Chem. Soc.*, 1984, **106**, 765–784.

295 A. Kurbatov, N. Balabaev, M. Mazo and E. Kramarenko, *Polymers (Basel).*, 2018, **10**, 838.

296 A. O. Kurbatov, N. K. Balabaev, M. A. Mazo and E. Y. Kramarenko, *J. Chem. Phys.*, 2018, **148**, 014902.

297 A. O. Kurbatov, N. K. Balabaev, M. A. Mazo and E. Y. Kramarenko, *Soft Matter*, 2020, **16**, 3792–3805.

298 H. Sun, S. J. Mumby, J. R. Maple and A. T. Hagler, *J. Am. Chem. Soc.*, 1994, **116**, 2978–2987.

299 H. Sun, *Macromolecules*, 1995, **28**, 701–712.

300 M. J. Hwang, T. P. Stockfisch and A. T. Hagler, *J. Am. Chem. Soc.*, 1994, **116**, 2515–2525.

301 H. Sun, *Macromolecules*, 1993, **26**, 5924–5936.

302 K. Sunohara, K. Takatoh and M. Sakamoto, *Liq. Cryst.*, 1993, **13**, 283–294.

303 H. J. Coles, H. Owen, J. Newton and P. Hodge, *Liq. Cryst.*, 1993, **15**, 739–744.

304 J. Newton, H. Coles, H. Owen and P. Hodge, *Ferroelectrics*, 1993, **148**, 379–387.

305 J. Newton, H. Coles, P. Hodge and J. Hannington, *J. Mater. Chem.*, 1994, **4**, 869–874.

306 J. Naciri, C. Carboni and A. K. George, *Liq. Cryst.*, 2003, **30**, 219–225.

307 U. Manna, J. K. Song, J. K. Vij and J. Naciri, *Phys. Rev. E - Stat. Nonlinear, Soft Matter Phys.*, 2008, **78**, 1–5.

308 J. Fernsler, D. Wicks, D. Staines, A. Havens and N. Paszek, *Liq. Cryst.*, 2012, **39**, 1204–1215.

309 K. Saunders, D. Hernandez, S. Pearson and J. Toner, *Phys. Rev. Lett.*, 2007, **98**, 1–4.

310 O. E. Panarina, Y. P. Panarin and J. K. Vij, *Mol. Cryst. Liq. Cryst.*, 2015, **610**, 193–200.

311 C. P. J. Schubert, C. Müller, A. Bogner, F. Giesselmann and R. P. Lemieux, *Soft Matter*, 2017, **13**, 3307–3313.

312 V. Swaminathan, V. P. Panov, Y. P. Panarin, S. P. Sreenilayam, J. K. Vij, A. Panov, D. Rodriguez-Lojo, P. J. Stevenson and E. Gorecka, *Liq. Cryst.*, 2018, **45**, 513–521.

313 S. Krishna Prasad, D. S. . Rao, S. Sridevi, C. V. Lobo, B. R. Ratna, J. Naciri and R. Shashidhar, *Phys. Rev. Lett.*, 2009, **102**, 1–4.

314 M. Rössle, L. Braun, D. Schollmeyer, R. Zentel, J. P. F. Lagerwall, F. Giesselmann and R. Stannarius, *Liq. Cryst.*, 2005, **32**, 533–538.